

The Quark Gluon Plasma probed by
Low Momentum Direct Photons in Au+Au Collisions
at $\sqrt{s_{NN}} = 62.4$ GeV and $\sqrt{s_{NN}} = 39$ GeV beam energies

A Dissertation presented

by

Vladimir Khachatryan

to

The Graduate School

in Partial Fulfillment of the

Requirements

for the Degree of

Doctor of Philosophy

in

Physics

(Heavy Ion Physics)

Stony Brook University

December 2017

Copyright by
Vladimir Khachatryan
2017

Stony Brook University

The Graduate School

Vladimir Khachatryan

We, the dissertation committee for the above candidate for the

Doctor of Philosophy degree, hereby recommend

acceptance of this dissertation

Thomas K. Hemmick – Dissertation Advisor
Professor, Department of Physics and Astronomy

Axel Drees – Dissertation Co-advisor
Professor, Department of Physics and Astronomy

Alan Calder – Chairperson of Defense
Professor, Department of Physics and Astronomy

Dmitri Kharzeev
Professor, Department of Physics and Astronomy

Mickey Chiu
Doctor, Physics Department, Brookhaven National Laboratory

This dissertation is accepted by the Graduate School

Charles Taber
Dean of the Graduate School

Abstract of the Dissertation

The Quark Gluon Plasma probed by
Low Momentum Direct Photons in Au+Au Collisions
at $\sqrt{s_{NN}} = 62.4 \text{ GeV}$ and $\sqrt{s_{NN}} = 39 \text{ GeV}$ beam energies

by

Vladimir Khachatryan

Doctor of Philosophy

in

Physics

(Heavy Ion Physics)

Stony Brook University

2017

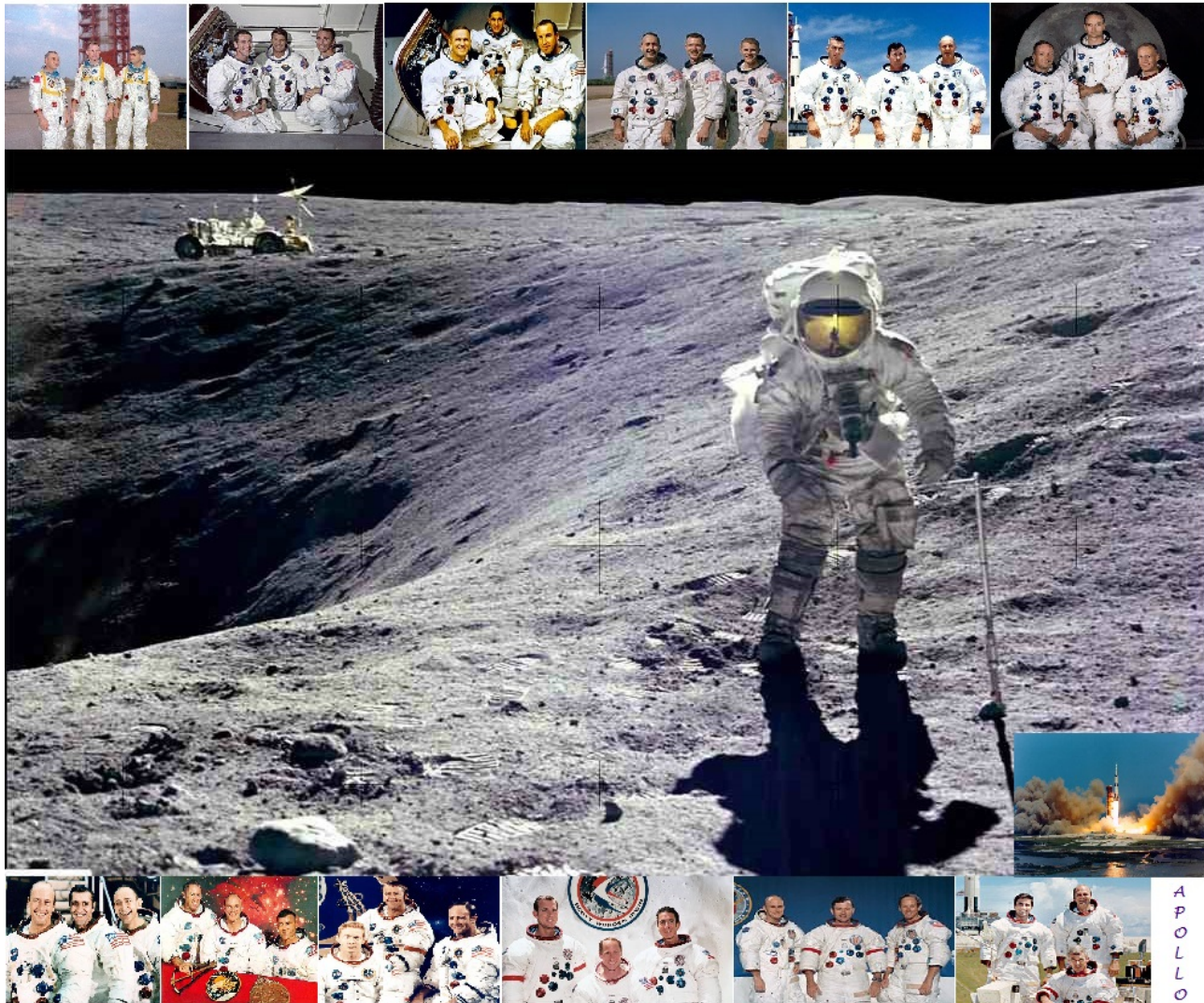
One of the main purposes of (ultra)relativistic heavy ion collisions is to study the non-perturbative aspects of QCD. It has been established by experiments at RHIC and LHC facilities that a colored medium is formed. Direct photons are an important tool with unique capabilities to study the created medium in relativistic heavy ion collisions. The photons do not participate in strong interactions with the hot and dense medium produced in these collisions due to a large mean free path and small cross-section. Therefore they leave the interaction region unmodified. The large yield and large anisotropy of low momentum direct photons, observed by PHENIX experimental collaboration at RHIC in Au+Au collisions at $\sqrt{s_{NN}} = 200 \text{ GeV}$, pose a significant challenge to theoretical models commonly referred to as “thermal photon puzzle”. Measurements at lower collision energies may provide new insight on the origin of the low momentum direct photons, which might be an additional piece of information in understanding and solving this puzzle.

In our analysis we utilize the previous photon measurement from 200 GeV via external conversion method, which gives a very good purity in photon identification and virtually eliminates the particle contamination from non-photonic sources. We map out the low momentum direct photon observables and present the results of the measurements in Au+Au collisions at $\sqrt{s_{NN}} = 62.4$ GeV and $\sqrt{s_{NN}} = 39$ GeV, using data samples of externally converted photons. The observed direct photon excess yield at these low energies can be interpreted as a sign of thermal radiation from the Quark Gluon Plasma, in addition to the PHENIX previous result. Moreover, we have found that the yields of direct photons from heavy ion collisions follow a universal scaling as a function of the charged particle multiplicity, where we combine various collision systems at four center-of-mass energies. The observed scaling properties of direct photons from these systems imply that the strength of the thermal radiation source grows faster than the volume of the thermal medium.

Dedicated to my father, mother and brother.

I am very grateful to my advisor Thomas K. Hemmick and co-advisor Axel Drees as well as Stony Brook relativistic heavy ion group members Norbert Novitzky, Richard Petti, Gabor David and the rest of the group for supporting and helping me in accomplishing the work and getting the results of my thesis.

“Alone we can do so little, together we can do so much.” – Helen Keller



The middle large photo shows the astronaut Charles M. Duke Jr. walking on the Moon, the Lunar Module pilot of the Apollo 16 mission. Apollo 16 launched from the Kennedy Space Center on April 16, 1972 (the bottom left smaller photo).

Top photos from the left to the right: The crews of Apollo 1, 7, 8, 9, 10 and 11.
Bottom photos from the left to the right: The crews of Apollo 12, 13, 14, 15, 16 and 17.

“If everyone is moving forward together, then success takes care of itself.” – Henry Ford

Contents

I Introduction and Experiment	1
1 Introduction	1
1.1 Quantum chromodynamics	1
1.1.1 Quarks and color charge	2
1.1.2 Gluons, asymptotic freedom and confinement	4
1.2 Heavy ion collisions	9
1.2.1 Pre-collision phase: Color Glass Condensate (CGC)	10
1.2.2 Pre-thermal phase: Glasma and bottom-up thermalization scenarios	14
1.2.3 Thermal phase: Quark Gluon Plasma (QGP) and hadronic gas (HG)	18
1.3 Some mechanisms of direct photon production in heavy ion collisions	21
1.3.1 Thermal photon puzzle and recent direct photon measurements in A+A collisions	21
1.3.2 Pre-thermal and thermal photon production in the thermalizing Glasma phase	26
1.3.3 Pre-thermal and thermal photon production in the bottom-up thermalization scenario	33
1.3.4 Thermal photon production from the hadronic phase based upon a spectral function approach within a hydrodynamical description	37
1.3.5 Photon production based upon thermal fireball and hydrodynamical models .	41
2 The PHENIX Experiment	47
2.1 The PHENIX detector at RHIC Facility	47
2.2 The PHENIX coordinate system	50
2.3 The PHENIX global detectors	52
2.3.1 Beam–Beam Counters, BBCs	52
2.3.2 Zero Degree Calorimeters, ZDCs	53
2.3.3 Reaction Plane Detectors, RXPs	55
2.3.4 Determination of the reaction plane, centrality and collision vertex	55
2.4 Central arm detectors	57
2.4.1 Central arm magnets	57
2.4.2 Drift Chambers, DCs	59
2.4.3 Pad Chambers, PCs	61
2.4.4 Ring Imaging Cherenkov Detector, RICH	62
2.4.5 Hadron Blind Detector, HBD	65

2.4.6 Electromagnetic Calorimeters, EMCals	65
II Analysis	71
3 Data analysis for the relative direct photon yield, R_γ	71
3.1 The motivation and goal of the measurements and analysis of low-momentum direct photons in Au+Au collisions at $\sqrt{s_{NN}} = 62.4 \text{ GeV}$ and $\sqrt{s_{NN}} = 39 \text{ GeV}$	71
3.2 Run quality analysis (QA)	73
3.2.1 DC hitmaps/deadmaps, electron multiplicities and cluster multiplicities	78
3.2.2 EMCAL hitmaps/deadmaps	85
3.3 The cuts of the inclusive photon sample	89
3.3.1 The event cut and electron cuts	89
3.3.2 The conversion pair cuts	91
3.3.3 The EMCAL photon cuts	95
3.4 π^0 -tagged photon yield	95
4 Monte Carlo simulations	99
4.1 Pion tagging efficiency correction	99
4.1.1 Photon efficiency, ε_γ	99
4.1.2 Efficiency and conditional acceptance, $\langle \varepsilon_\gamma f \rangle$	101
4.2 Cocktail ratio from hadronic decays	107
5 Systematic Uncertainties	113
5.1 Conditional acceptance	113
5.2 Cocktail ratio	117
5.3 Background scale uncertainty in the π^0 yield extraction	117
6 The R_γ results	124
III Discussion	128
7 Discussion of the analysis results	128
7.1 Direct photon invariant yield at $\sqrt{s_{NN}} = 62.4 \text{ GeV}$ and $\sqrt{s_{NN}} = 39 \text{ GeV}$	128
7.2 Direct photon scaling	132
7.2.1 The scaling between number of binary collisions and charged particle multiplicity distribution	132
7.2.2 Calculation of the charged hadron multiplicity for peripheral A+A systems .	138

7.2.3 Integrated yield vs. charged particle multiplicity	139
8 Summary and conclusions	155
9 Appendix A1	157
10 Appendix A2	162
11 Appendix B1	167
12 Appendix B2	172
13 Appendix C1	177
14 Appendix C2	182
15 Data tables	187
15.1 The constituents of the relative direct photon yield, R_γ	187
15.2 Charged particle multiplicity data tables	195
15.3 Direct photon invariant yield data tables	197
15.4 Direct photon scaling (integrated yield) data tables	212

List of Figures

1	A diagram showing a quark changing its color from i to j by emitting or absorbing a gluon of color a	5
2	Diagrams showing three and four self-interactions of gluons.	5
3	In the left panel diagram, the coupling becomes stronger at shorter distance (screening). In the right panel diagram, the coupling becomes weaker at short distance, arising from the nonlinear interaction between gluons in QCD (which has an anti-screening effect).	6
4	The theoretically calculated $\alpha_s(Q)$ in QCD as a function of momentum transfer compared to measurements shown as data points [6].	7
5	A cartoon illustrating the quark confinement.	8
6	Schematic phase diagram of QCD based on [7, 8], as a function of temperature and baryochemical potential.	9
7	A visualization of successive phases a heavy ion collision.	10
8	Another view of a heavy ion collision, along with the most widely used approaches to describe each phase.	10
9	Parton distributions in a proton, measured in Deep Inelastic Scattering at HERA. The figure is from [18].	12
10	Increasing gluon density within a proton with increasing energy. Quarks are not displayed.	12
11	An illustration of the classical color fields inside a color glass sheet.	13
12	The collision of two color glass sheets.	14
13	The longitudinal color electric and color magnetic fields making a longitudinal color flux tube in a high energy collision of two color glass sheets.	15
14	Characteristic momentum scales in the bottom-up thermalization scenario. The figure is from [27].	17
15	(Color online) The invariant cross section ($p+p$) and the invariant yield ($Au+Au$) of direct photons as a function of p_T . The three curves on the $p+p$ data represent NLO pQCD calculations, and the dashed curves show the power-law fit to the $p+p$ data scaled by the Glauber nuclear overlap function, T_{AA} , for $Au+Au$. The black solid curves are an exponential plus the T_{AA} -scaled $p+p$ fit. The dotted (red) curve near the 0-20 % centrality data is a theory calculation [46]. This figure is from Refs. [40, 41]. .	22

- 16 Direct photon p_T spectra in centrality bins 0-20%, 20-40%, 40-60% and 60-92% in Au+Au collisions at $\sqrt{s_{NN}} = 200$ GeV. The error bars (boxes) of the data points are statistical (systematic) uncertainties. Widths of filled boxes indicate the p_T bin widths. The green bands show a N_{coll} scaled modified power-law fit to the PHENIX p+p data and its extrapolation below 1 GeV/c. The figure is from [42]. 23
- 17 Direct photon p_T spectra in centrality bins 0-20% (scaled by a factor 100), 20-40% (scaled by a factor 10) and 40-80% in Pb+Pb collisions at $\sqrt{s_{NN}} = 2760$ GeV, compared to NLO pQCD predictions for the direct photon yield in p+p collisions at the same energy, scaled by the number of binary nucleon collisions for each centrality bin. The figure is from [45]. 24
- 18 Direct photon v_2 and v_3 in centrality bins 0-20%, 20-40% and 40-60% in Au+Au collisions at $\sqrt{s_{NN}} = 200$ GeV, measured with the conversion method (solid circles, green) and calorimeter method (solid squares, black). The error bars (boxes) of the data points are statistical (systematic) uncertainties. The figure is from [48]. 25
- 19 Direct photon v_2 in centrality bins 0-40% in Pb+Pb collisions at $\sqrt{s_{NN}} = 2760$ GeV. The figure is from [49]. 25
- 20 The result from $\chi^2/d.o.f.$ analysis in the λ - η parameter space for the discussed PHENIX direct photon data in three centrality classes by fitting with the present model, with the blue, green, and red contours indicating 1-, 2-, and 3- σ errors, respectively. The figure is from Ref. [50]. 31
- 21 Comparison between the PHENIX direct photon data [40, 41] and the present model with $\lambda = 0.29$ and varied values of η for three centrality bins. The black dashed curves represent the T_{AA} -scaled p+p yield from Eq. (50), and the colorful bands represent the full yield including also the Glasma contribution from Eq. (49) with the upper and lower boundary curves for each band corresponding to the results with the parameter $\eta = 6.05$ and $\eta = 7.25$, respectively (see the text for more details). In the figure $\delta \equiv \delta'$. The figure is from Ref. [50]. 32

- 22 The comparison between the total photon yield ((**i**)+(**ii**)+(**iii**)) in the bottom-up thermalization scenario (named as Glasma), and the yield in a “hydro” scenario (that assumes early thermalization) plus the thermal QGP yield. Top: The normalization of the saturation scale Q_s is chosen such that its values in Au+Au 0-5% collisions at RHIC $\sqrt{s_{NN}} = 200 \text{ GeV}$ are 1.4 GeV and 2 GeV. Bottom: The normalization of Q_s is chosen such that its values in Pb+Pb 0-5% collisions at LHC $\sqrt{s_{NN}} = 2760 \text{ GeV}$ is 2.1 GeV and 3 GeV. The red color bands denote the uncertainty for the bottom-up total photon yield corresponding to the variation of $c_{eq} = 0.1\text{-}0.4$ (bottom edge of band to top edge). The red dashed lines correspond to $c_T = 0.18$. This figure is from Ref. [54]. 38
- 23 Direct photon spectra for PHENIX [40, 42] at $\sqrt{s_{NN}} = 200 \text{ GeV}$ in Au+Au centrality bins 0-20% (23(a)) and 20-40% (23(b)) as well as for ALICE [45] at $\sqrt{s_{NN}} = 2.76 \text{ TeV}$ in Pb+Pb centrality bins 0-20% (23(c)) and 20-40% (23(d)). One can see the sum of one- and two-pion contributions from the hadronic phase plus also the contributions from the prompt photons and from the QGP phase. The curves are obtained with different hydrodynamical parameters, which depend on the center-of-mass energy and centrality of the colliding systems. These plots are from [57]. 40
- 24 Direct photon elliptic flow v_2 for PHENIX [48] at $\sqrt{s_{NN}} = 200 \text{ GeV}$ in Au+Au centrality bins 0-20% (24(a)), 20-40% (24(b)) and 40-60% (24(c)) as well as for ALICE [49] at $\sqrt{s_{NN}} = 2.76 \text{ TeV}$ in Pb+Pb centrality bin 0-40% (24(d)). These plots are from [57]. 42
- 25 Direct photon spectra for PHENIX [40] at $\sqrt{s_{NN}} = 200 \text{ GeV}$ in Au+Au centrality bin 0-20% (25(a)) using the expanding fireball and 0-20% (25(b)) using the ideal hydrodynamics as well as for ALICE [45] at $\sqrt{s_{NN}} = 2.76 \text{ TeV}$ in Pb+Pb centrality bin 0-40% (25(c)) using the expanding fireball and 0-40% (25(d)) using the ideal hydrodynamics. The plots are from [60]. 43
- 26 Direct photon elliptic flow v_2 for PHENIX [48] at $\sqrt{s_{NN}} = 200 \text{ GeV}$ in Au+Au centrality bin 0-20% (26(a)) using the expanding fireball and 0-20% (26(b)) using the ideal hydrodynamics as well as for ALICE [49] at $\sqrt{s_{NN}} = 2.76 \text{ TeV}$ in Pb+Pb centrality bin 0-40% (26(c)) using the expanding fireball and 0-40% (26(d)) using the ideal hydrodynamics. The plots are from [60]. 44
- 27 Direct photon spectra for PHENIX [42] at $\sqrt{s_{NN}} = 200 \text{ GeV}$ in Au+Au centrality bins 0-20% (27(a)) and 20-40% (27(b)) as well as for ALICE [45] at $\sqrt{s_{NN}} = 2.76 \text{ TeV}$ in Pb+Pb centrality bins 0-20% (27(c)) and 20-40% (27(d)). The plots are from [63]. 45

28	Direct photon elliptic flow v_2 for PHENIX [48] at $\sqrt{s_{NN}} = 200 \text{ GeV}$ in Au+Au centrality bins 0-20% (28(a)) and 20-40% (28(b)) as well as for ALICE [49] at $\sqrt{s_{NN}} = 2.76 \text{ TeV}$ in Pb+Pb centrality bin 0-40% (28(c)). The plots are from [63].	46
29	The top figure shows a cross-sectional view of the PHENIX detector for the 2010 setup (in the x-y plane), displaying the PHENIX central arms. The bottom figure shows a side view, showing the forward muon arms.	48
30	Members of the PHENIX collaboration standing and sitting in front of the detector. The photo is taken in 2008.	49
31	An aerial photograph of the RHIC facility. The various colors show different sub-facilities that produce ion beams in (ultra)relativistic heavy ion collisions, and bring them up to full energy.	50
32	A cartoon illustrating the coordinate system used in the PHENIX detector. The cartoon is from [115].	51
33	The illustration of the relation between η and θ relative to the beam line z.	52
34	a) The assembly of one side of the BBCs. b) One BBC element.	53
35	A schematic of the ZDC tungsten modules. All dimensions are in mm.	54
36	a) The plan view of the collision region and particle trajectories, with the BBC and ZDC locations along the beam axis (by indicating also deflections of protons and charged fragments). b) The “beam’s eye” view (section A-A) of the ZDC location.	54
37	a) The schematic diagram of one RXP detector. The beam pipe goes through a hole in the center of the detector (perpendicular to the plane), and around it the scintillator paddles of the detector are arranged in concentric circles. The inner RXP detector is shown in red color, the outer one in blue color. The numbers give the scintillator dimensions in cm. b) One of the RXP detectors installed on the face of the central arm magnet, where the black pipe near the top right is the beam pipe.	55
38	The reaction plane, Ψ_R , defined by the impact parameter of colliding nuclei and the beam direction.	56
39	The PHENIX central magnets shown from different sides.	58
40	Calculations of the magnetic fields from a Garfield simulation: for the (++)-configuration (left panel) and for the (+−)-configuration (right panel).	58
41	The process of the DC delivery.	59
42	a) A schematic of the frame of one DC arm. The dimensions are given in meters. b) The layered wire net layout of a keystone. The dimensions are given in mm.	60

43	The wire layout of the DC sector (keystone). The left panel shows the positions of different wire planes along the beam axis: namely X1, X2, U1, U2, V1, V2 planes are indicated in the side view of a keystone. The dashed lines represent the anode plane, and the dotted lines represent the cathode plane. The right panel of the figure shows the orientation of the wire layers from the top view. In the middle , a zoom-in of single anode plane wire net is shown with different wire types. Filled circles and open squares denote the position of wires used to create or shape the electric field, open circles denote wires that are used to collect and measure the ionization.	61
44	a) The view of one of the PC1 arms. b) The relative sizes of PC1, PC2 and PC3 sectors.	62
45	A view of a vertical cut through the PC.	62
46	One arm of the RICH detector after the mirror alignment is accomplished.	63
47	a) A cut through view of the RICH detector. b) Cutaway view of one arm of the RICH detector.	64
48	a) The front view of one half of the HBD. b) The schematic view of both HBD halves.	65
49	a) The construction of one of the HBD sides. b) Visualization of a photon conversion originating in the beam pipe.	66
50	Some of the PbSc modules.	67
51	A diagram showing the interior view of the lead-scintillator calorimeter (PbSc) module.	68
52	Some of the lead-glass calorimeter (PbGl) modules.	69
53	A diagram illustrating the construction of a PbGl supermodule.	69
54	The run group details for data samples at $\sqrt{s_{NN}} = 62.4 \text{ GeV}$ and $\sqrt{s_{NN}} = 39 \text{ GeV}$. It is shown the total number of events and the number of runs in all run groups, in both used (“good”) and thrown out (“bad”) run groups.	74
55	The total number of events in 62.4 GeV data set for centrality bins in 10%.	77
56	The total number of events in 39 GeV data set for centrality bins in 10%.	77
57	A randomly chosen DC hitmaps/deadmaps from the “good” Run Group 1 corresponding to the run number 310714 at $\sqrt{s_{NN}} = 62.4 \text{ GeV}$. The vertical is α , the horizontal is the board number.	79
58	A randomly chosen DC hitmaps/deadmaps from the “good” Run Group 2 corresponding to the run number 311032 at $\sqrt{s_{NN}} = 62.4 \text{ GeV}$. The vertical is α , the horizontal is the board number.	80
59	A randomly chosen DC hitmaps/deadmaps from the “good” Run Group 3 corresponding to the run number 312691 at $\sqrt{s_{NN}} = 62.4 \text{ GeV}$. The vertical is α , the horizontal is the board number.	80

60	A randomly chosen DC hitmaps/deadmaps from the “good” Run Group 4 corresponding to the run number 311905 at $\sqrt{s_{NN}} = 62.4 \text{ GeV}$. The vertical is α , the horizontal is the board number.	81
61	A randomly chosen DC hitmaps/deadmaps from the “bad” Run Group 5 corresponding to the run number 312467 at $\sqrt{s_{NN}} = 62.4 \text{ GeV}$. The vertical is α , the horizontal is the board number.	81
62	A randomly chosen DC hitmaps/deadmaps from the “good” Run Group 1 corresponding to the run number 313725 at $\sqrt{s_{NN}} = 39 \text{ GeV}$. The vertical is α , the horizontal is the board number.	82
63	A randomly chosen DC hitmaps/deadmaps from the “good” Run Group 2 corresponding to the run number 314459 at $\sqrt{s_{NN}} = 39 \text{ GeV}$. The vertical is α , the horizontal is the board number.	82
64	A randomly chosen DC hitmaps/deadmaps from the “good” Run Group 3 corresponding to the run number 313755 at $\sqrt{s_{NN}} = 39 \text{ GeV}$. The vertical is α , the horizontal is the board number.	83
65	A randomly chosen DC hitmaps/deadmaps from the “bad” Run Group 4 corresponding to the run number 313614 at $\sqrt{s_{NN}} = 39 \text{ GeV}$. The vertical is α , the horizontal is the board number.	83
66	The integrated electron multiplicity (per number of events) vs run number for the first four run groups at $\sqrt{s_{NN}} = 62.4 \text{ GeV}$	84
67	The integrated electron multiplicity (per number of events) vs run number for the first three run groups at $\sqrt{s_{NN}} = 39 \text{ GeV}$. This difference between Run Group 1 and Run Group 2, for example, can be traced to Fig. (62) and Fig. (63). The dceast0 in Fig. (63) has a cold region cut out, which is not the case in Fig. (62). That is why the red points here are below the blue ones.	84
68	The mean value of the EMCal cluster multiplicity (per number of events) vs run number for the first four run groups at $\sqrt{s_{NN}} = 62.4 \text{ GeV}$	85
69	The mean value of the EMCal cluster multiplicity (per number of events) vs run number for the first three run groups at $\sqrt{s_{NN}} = 39 \text{ GeV}$	85
70	The fraction of the deposited energy in each tower of the PbSc by the electromagnetic shower at the impact point in $(0, 0) \text{ cm}$, and with no impact angle ($\theta = 0$). Each cell corresponds to one tower. The upper number in each cell represents the fraction of the total deposited energy (from Eq. (102)), and the lower numbers represent the energy fluctuations (from Eq. (104)) with $E_{total} = 10 \text{ GeV}$. The figure is from [133].	88
71	The EMCal hitmaps/deadmaps for the eight sectors at $\sqrt{s_{NN}} = 62.4 \text{ GeV}$	88
72	The EMCal hitmaps/deadmaps for the eight sectors at $\sqrt{s_{NN}} = 39 \text{ GeV}$	89

73	The illustration of the effect from the assumption of a track origin. For the purpose of visualization the effect is exaggerated. The true path of the e^+e^- pair through different subsystems is given by the red lines, which originate from the HBD backplane. The pair does not have an initial opening angle but the visible opening of the tracks happen further down due to the field. The yellow lines represent the wrong track projections, if we assume (incorrectly) that the particles come from the true event vertex. The cartoon is from [115].	92
74	2d mass plots for a view of the cut space used for the conversion photon identification at $\sqrt{s_{NN}} = 62.4$ GeV. The upper four plots, Figs. (74(a)), (74(b)), (74(c)), (74(d)), correspond to the north-east, south-east, north-west, south-west of the PHENIX detector, respectively. The bottom plot is the aggregation of all of them.	93
75	2d mass plots for a view of the cut space used for the conversion photon identification at $\sqrt{s_{NN}} = 39$ GeV. The differences between the plots is explained in the same way as in Fig. (74).	94
76	The converted di-photon foreground (FG) pair distribution in mass divided by the combinatorial mixed event background (BG) distribution for 20-40% centrality in the converted photon p_{Tee} bin of 1.1 - 1.3 GeV/c ($p_{Tee} \equiv p_T$) at $\sqrt{s_{NN}} = 62.4$ GeV. The region of the purple colored pion peak is excluded. The ratio is fitted with a second order polynomial (shown in red).	97
77	The di-photon foreground (blue) and normalized mixed event background (red) for 20-40% centrality in the converted photon p_{Tee} bin of 1.1 - 1.3 GeV/c ($p_{Tee} \equiv p_T$) at $\sqrt{s_{NN}} = 62.4$ GeV. The uncertainty on the background includes both background's statistical uncertainty and the uncertainty in the normalization with CL=0.66. . . .	97
78	The π^0 yield extraction for 20-40% centrality in the converted photon p_{Tee} bin of 1.1 - 1.3 GeV/c ($p_{Tee} \equiv p_T$) at $\sqrt{s_{NN}} = 62.4$ GeV. The residual background is assumed to be described by averaging the sum of the green and cyan colored lines, which is subtracted from the original blue histogram of the π^0 yield extraction (fitted by the blue Gaussian). The result is the purple histogram (fitted by the purple Gaussian). In this plot the cyan color is on top of the green color.	98
79	The single photon efficiency ε_γ (designated as $\varepsilon_{\text{PHENIX}}$) into the live detector as a function of the photon $1/p_{T\gamma}$, in the first two centrality bins, for the PbSc (blue) and PbGl (red) at $\sqrt{s_{NN}} = 62.4$ GeV and $\sqrt{s_{NN}} = 39$ GeV. Systematic uncertainties are not shown.	102

80	The single photon efficiency ε_γ (designated as $\varepsilon_{\text{PHENIX}}$) into the live detector as a function of the photon $1/p_{T\gamma}$, in the second two centrality bins, for the PbSc (blue) and PbGl (red) at $\sqrt{s_{NN}} = 62.4 \text{ GeV}$ and $\sqrt{s_{NN}} = 39 \text{ GeV}$. Systematic uncertainties are not shown.	103
81	The conditional acceptance $\langle \varepsilon_\gamma f \rangle$ at $\sqrt{s_{NN}} = 62.4 \text{ GeV}$ in the centrality bins of 0-20% (81(a)), 20-40% (81(b)), 40-60% (81(c)), 60-86% (81(d)) and minimum bias 0-86% (81(e)).	105
82	The conditional acceptance $\langle \varepsilon_\gamma f \rangle$ at $\sqrt{s_{NN}} = 39 \text{ GeV}$ in the centrality bins of 0-20% (82(a)), 20-40% (82(b)), 40-60% (82(c)), 60-86% (82(d)) and minimum bias 0-86% (82(e)).	106
83	The simulated converted photon spectra of all photons from hadronic decays (filled circles) and of photons from π^0 decays (open circles) at $\sqrt{s_{NN}} = 62.4 \text{ GeV}$ in the centrality bins of 0-20% (83(a)), 20-40% (83(b)), 40-60% (83(c)), 60-86% (83(d)) and minimum bias 0-86% (83(e)).	109
84	The simulated ratio (cocktail ratio) of all photons from hadronic decays to photons from π^0 decays at $\sqrt{s_{NN}} = 62.4 \text{ GeV}$ in the centrality bins of 0-20% (84(a)), 20-40% (84(b)), 40-60% (84(c)), 60-86% (84(d)) and minimum bias 0-86% (84(e)).	110
85	The simulated converted photon spectra of all photons from hadronic decays (filled circles) and of photons from π^0 decays (open circles) at $\sqrt{s_{NN}} = 39 \text{ GeV}$ in the centrality bins of 0-20% (85(a)), 20-40% (85(b)), 40-60% (85(c)), 60-86% (85(d)) and minimum bias 0-86% (85(e)).	111
86	The simulated ratio (cocktail ratio) of all photons from hadronic decays to photons from π^0 decays at $\sqrt{s_{NN}} = 39 \text{ GeV}$ in the centrality bins of 0-20% (86(a)), 20-40% (86(b)), 40-60% (86(c)), 60-86% (86(d)) and minimum bias 0-86% (86(e)).	112
87	The neutral and charged pion invariant yield per event for PHENIX [141] and STAR [142]. The plot is from [140].	113
88	The ratios of the fits (to the data sets shown in Fig. (87)) to the combined fit. The plot is from [140].	114
89	The neutral and charged pion invariant yield per event for PHENIX [141]. The plot is from [143].	115
90	The ratios of the fits (to the data set shown in Fig. (89)) to the combined fit. The plot is from [143].	116
91	The relative uncertainty on the cocktail ratio taking into account all hadron to π^0 production rate uncertainties (closed points), and only the uncertainty from the η/π^0 production rate (open points). The dashed line is an analytical form shown in the text. This plot is from [134].	117

92	The relative π^0 -tagged photon yield determined from assumption of varying the residual background (which comes from various polynomial fits) at $\sqrt{s_{NN}} = 62.4 \text{ GeV}$ in the centrality bins of 0-20% (92(a)), 20-40% (92(b)) and minimum bias 0-86% (92(c)).	119
93	The relative π^0 -tagged photon yield determined from assumption of varying the residual background (which comes from various polynomial fits) at $\sqrt{s_{NN}} = 39 \text{ GeV}$ in the centrality bins of 0-20% (95(a)) and minimum bias 0-86% (95(b)).	120
94	The nomenclature is the same as in Fig. (92), but the p_{Tee} binning is according to Table (8).	121
95	The nomenclature is the same as in Fig. (93), but the p_{Tee} binning is according to Table (9).	122
96	R_γ in the converted photon $p_{Tee} \equiv p_T$ bins at $\sqrt{s_{NN}} = 62.4 \text{ GeV}$ in the centrality bins of 0-20% (96(a)), 20-40% (96(b)) and minimum bias 0-86% (96(c)) as well as at $\sqrt{s_{NN}} = 39 \text{ GeV}$ in the minimum bias 0-86% (96(d)). The upper limits at $p_T = 1.6 \text{ GeV}/c$ and $p_T = 2.75 \text{ GeV}/c$ in Fig. (96(b)) are calculated with 95.4% confidence level (CL). The upper limit at $p_T = 1.7 \text{ GeV}/c$ in Fig. (96(d)) is also calculated with CL = 95.4%.	124
97	The raw inclusive photon yield at $\sqrt{s_{NN}} = 62.4 \text{ GeV}$ and 39 GeV in the centrality bins of 0-20% (97(a)), 20-40% (97(b)), 40-60% (97(c)), 60-86% (97(d)) and minimum bias 0-86% (97(e)).	125
98	The raw π^0 -tagged photon yield at $\sqrt{s_{NN}} = 62.4 \text{ GeV}$ and 39 GeV in the centrality bins of 0-20% (98(a)), 20-40% (98(b)), 40-60% (98(c)), 60-86% (98(d)) and minimum bias 0-86% (98(d)).	126
99	The ratio of the raw inclusive photon yield to the raw π^0 -tagged photon yield at $\sqrt{s_{NN}} = 62.4 \text{ GeV}$ and $\sqrt{s_{NN}} = 39 \text{ GeV}$ in the centrality bins of 0-20% (99(a)), 20-40% (99(b)), 40-60% (99(c)), 60-86% (99(d)) and minimum bias 0-86% (99(e)).	127
100	The invariant yield of direct photons at $\sqrt{s_{NN}} = 62.4 \text{ GeV}$ beam energy in the centrality bin of 0-20%. The inverse slope T_{eff} is obtained from fitting with the data in the p_T range of 0.55 GeV/c - 2.05 GeV/c.	129
101	The invariant yield of direct photons at $\sqrt{s_{NN}} = 62.4 \text{ GeV}$ beam energy in the centrality bin of 20-40%. The inverse slope T_{eff} is obtained from fitting with the data in the p_T range of 0.55 GeV/c - 2.05 GeV/c.	130
102	The invariant yield of direct photons at $\sqrt{s_{NN}} = 62.4 \text{ GeV}$ beam energy in the minimum bias 0-86%. The inverse slope T_{eff} is obtained from fitting with the data in the p_T range of 0.55 GeV/c - 2.05 GeV/c.	130

103	The invariant yield of direct photons at $\sqrt{s_{NN}} = 39$ GeV beam energy in the minimum bias 0-86%. The inverse slope T_{eff} is obtained from fitting with the data in the p_T range of 0.45 GeV/c - 1.95 GeV/c.	131
104	Data-extracted T_{eff} for four systems at four beam energies: 2760 GeV, 200 GeV and 62.4 GeV and 39 GeV.	131
105	The number of binary collisions, N_{coll} , vs. charged particle multiplicity, $dN_{\text{ch}}/d\eta$, for four datasets, individually fitted by a power-law with vertical errors, leading to four extracted powers.	132
106	The number of binary collisions, N_{coll} , vs. charged particle multiplicity, $dN_{\text{ch}}/d\eta$, for four datasets, individually fitted by a power-law with vertical and horizontal errors, leading to four extracted powers.	133
107	The number of binary collisions, N_{coll} , vs. charged particle multiplicity, $dN_{\text{ch}}/d\eta$, for four normalized and merged datasets, simultaneously fitted by a power-law with vertical errors, leading to one extracted power.	134
108	The number of binary collisions, N_{coll} , vs. charged particle multiplicity, $dN_{\text{ch}}/d\eta$, for four normalized and merged datasets, simultaneously fitted by a power-law with vertical and horizontal errors, leading to one extracted power.	135
109	The ratio of the data to the simultaneous fit obtained with horizontal errors.	136
110	The ratio of the data to the simultaneous fit obtained with vertical and horizontal errors.	136
111	The number of binary collisions, N_{coll} , vs. charged particle multiplicity, $dN_{\text{ch}}/d\eta$, for four datasets, simultaneously fitted by a power-law (with vertical errors) with the power $\alpha = 1.25$	137
112	The ratio of the charged particle multiplicity error to its central value as a function of $dN_{\text{ch}}/d\eta$ at $\sqrt{s_{NN}} = 200$ GeV (see Table 29).	138
113	The ratio of the charged particle multiplicity error to its central value as a function of N_{part} at $\sqrt{s_{NN}} = 200$ GeV (see Table 29).	139
114	The direct photon spectra normalized by $(dN_{\text{ch}}/d\eta)^{1.25}$, for Au+Au and Cu+Cu datasets at 200 GeV collision energy (left panel), and for four A+A datasets at different collision energies (right panel). The data in Au+Au at 200 GeV are from [40, 42], in Cu+Cu at 200 GeV from [44], and in Pb+Pb at 2.76 TeV from [45]. The data in Au+Au at 62.4 GeV and 39 GeV are those from Fig. (100), Fig. (101), Fig. (102) and Fig. (103) (this analysis). The 200 GeV p+p data points are from [153], the 62.4 GeV p+p and 63 GeV p+p data points are from [154, 155, 156, 157]. The statistical and systematic errors combined in quadrature, along with all upper limits are shown as well. All the corresponding direct photon invariant yield data tables can be seen in Sec. (15.2).	142

115	Another version of Fig. (114) with the same nomenclature.	143
116	A linear-log version of Fig. (115) with the same nomenclature.	143
117	The integral correction using the center p_T point (correction upward). For the exponential we use minimum $p_T = 1 \text{ GeV}/c$, for the power-law we use minimum $p_T = 5 \text{ GeV}/c$. For the exponential, the correction is independent of p_T . For the power-law, the correction depends not only on n but also on p_T	144
118	The integral correction using the mean p_T point (correction downward). For the exponential we use minimum $p_T = 1 \text{ GeV}/c$, for the power-law we use minimum $p_T = 5 \text{ GeV}/c$. For the exponential, the correction is independent of p_T . For the power-law, the correction depends not only on n but also on p_T	145
119	The direct photon integrated yield vs. charged particle multiplicity for p_T integrated from $1.0 \text{ GeV}/c$ to $1.5 \text{ GeV}/c$, for five A+A datasets and one p+p dataset. The references for Pb+Pb, Au+Au and Cu+Cu systems are shown in Fig. (114). The p+p data are from [153]. The p+p fit describing the N_{coll} scaled prompt photons is obtained using a parameterization from [42] (see Eq. (136)). Each model curve also describing these N_{coll} scaled prompt photons is the (integrated) prompt photon yield extrapolated down to $p_T = 1.0 \text{ GeV}/c$ [144], at respective beam energy. All the corresponding direct photon integrated yield points can be seen in Table 63. The power $\alpha = 1.25$ is from Fig. (111). The black colored dashed fit is described by $Fit = 0.000557 \cdot dN_{ch}/d\eta^{1.25}$. If α were not fixed, it would be $\alpha = 1.184 \pm 0.040$. . .	146
120	The direct photon integrated yield vs. charged particle multiplicity for p_T integrated from $1.0 \text{ GeV}/c$ to $5.0 \text{ GeV}/c$, for five A+A datasets and one p+p dataset. The nomenclature is the same as in Fig. 119. All the corresponding direct photon integrated yield points can be seen in Table 64. The power $\alpha = 1.25$ is from Fig. (111). The black colored dashed fit is described by $Fit = 0.000721 \cdot dN_{ch}/d\eta^{1.25}$. If α were not fixed, it would be $\alpha = 1.211 \pm 0.033$	147
121	The direct photon integrated yield vs. charged particle multiplicity for p_T integrated from $1.5 \text{ GeV}/c$ to $5.0 \text{ GeV}/c$, for four A+A datasets and one p+p dataset. The nomenclature is the same as in Fig. 119. All the corresponding direct photon integrated yield points can be seen in Table 65. The power $\alpha = 1.25$ is from Fig. (111). The black colored dashed fit is described by $Fit = 0.000165 \cdot dN_{ch}/d\eta^{1.25}$. If α were not fixed, it would be $\alpha = 1.321 \pm 0.037$	148

127	All the nomenclature is the same as in Fig. (121). However, now instead of the power-law fit (with $\alpha = 1.25$), the dashed fit is described by $Fit = 4.242 \cdot 10^{-5} \cdot (dN_{ch}/d\eta) + 9.362 \cdot 10^{-5} \cdot (dN_{ch}/d\eta)^{4/3}$	154
128	The converted di-photon foreground (FG) pair distribution in mass divided by the combinatorial mixed event background (BG) distribution for 0-20% centrality in the converted photon p_{Tee} bin of 0.9 - 1.1 GeV/c at $\sqrt{s_{NN}} = 62.4$ GeV. The region of the pion peak is excluded. The ratio is fitted with a second order polynomial (shown in red).	157
129	The FG pair distribution in mass divided by the combinatorial BG distribution for 0-20% centrality in the converted photon p_{Tee} bin of 1.9 - 2.1 GeV/c at $\sqrt{s_{NN}} = 62.4$ GeV.	157
130	The converted di-photon foreground (FG) pair distribution in mass divided by the combinatorial mixed event background (BG) distribution for 20-40% centrality in the converted photon p_{Tee} bin of 0.9 - 1.1 GeV/c at $\sqrt{s_{NN}} = 62.4$ GeV. The region of the pion peak is excluded. The ratio is fitted with a second order polynomial (shown in red).	158
131	The FG pair distribution in mass divided by the combinatorial BG distribution for 20-40% centrality in the converted photon p_{Tee} bin of 1.9 - 2.1 GeV/c at $\sqrt{s_{NN}} = 62.4$ GeV.	158
132	The converted di-photon foreground (FG) pair distribution in mass divided by the combinatorial mixed event background (BG) distribution for 40-60% centrality in the converted photon p_{Tee} bin of 0.9 - 1.1 GeV/c at $\sqrt{s_{NN}} = 62.4$ GeV. The region of the pion peak is excluded. The ratio is fitted with a second order polynomial (shown in red).	159
133	The FG pair distribution in mass divided by the combinatorial BG distribution for 40-60% centrality in the converted photon p_{Tee} bin of 1.9 - 2.1 GeV/c at $\sqrt{s_{NN}} = 62.4$ GeV.	159
134	The converted di-photon foreground (FG) pair distribution in mass divided by the combinatorial mixed event background (BG) distribution for 60-86% centrality in the converted photon p_{Tee} bin of 0.7 - 0.9 GeV/c at $\sqrt{s_{NN}} = 62.4$ GeV. The region of the pion peak is excluded. The ratio is fitted with a second order polynomial (shown in red).	160
135	The FG pair distribution in mass divided by the combinatorial BG distribution for 60-86% centrality in the converted photon p_{Tee} bin of 1.3 - 1.5 GeV/c at $\sqrt{s_{NN}} = 62.4$ GeV.	160

136	The converted di-photon foreground (FG) pair distribution in mass divided by the combinatorial mixed event background (BG) distribution for 0-86% centrality in the converted photon p_{Tee} bin of 0.9 - 1.1 GeV/c at $\sqrt{s_{NN}} = 62.4$ GeV. The region of the pion peak is excluded. The ratio is fitted with a second order polynomial (shown in red).	161
137	The FG pair distribution in mass divided by the combinatorial BG distribution for 0-86% centrality in the converted photon p_{Tee} bin of 1.9 - 2.1 GeV/c at $\sqrt{s_{NN}} = 62.4$ GeV.	161
138	The converted di-photon foreground (FG) pair distribution in mass divided by the combinatorial mixed event background (BG) distribution for 0-20% centrality in the converted photon p_{Tee} bin of 0.8 - 1.0 GeV/c at $\sqrt{s_{NN}} = 39$ GeV. The region of the pion peak is excluded. The ratio is fitted with a second order polynomial (shown in red).	162
139	The FG pair distribution in mass divided by the combinatorial BG distribution for 0-20% centrality in the converted photon p_{Tee} bin of 1.8 - 2.0 GeV/c at $\sqrt{s_{NN}} = 39$ GeV.	162
140	The converted di-photon foreground (FG) pair distribution in mass divided by the combinatorial mixed event background (BG) distribution for 20-40% centrality in the converted photon p_{Tee} bin of 0.8 - 1.0 GeV/c at $\sqrt{s_{NN}} = 39$ GeV. The region of the pion peak is excluded. The ratio is fitted with a second order polynomial (shown in red).	163
141	The FG pair distribution in mass divided by the combinatorial BG distribution for 20-40% centrality in the converted photon p_{Tee} bin of 1.8 - 2.0 GeV/c at $\sqrt{s_{NN}} = 39$ GeV.	163
142	The converted di-photon foreground (FG) pair distribution in mass divided by the combinatorial mixed event background (BG) distribution for 40-60% centrality in the converted photon p_{Tee} bin of 0.6 - 0.8 GeV/c at $\sqrt{s_{NN}} = 39$ GeV. The region of the pion peak is excluded. The ratio is fitted with a second order polynomial (shown in red).	164
143	The FG pair distribution in mass divided by the combinatorial BG distribution for 40-60% centrality in the converted photon p_{Tee} bin of 1.2 - 1.4 GeV/c at $\sqrt{s_{NN}} = 39$ GeV.	164
144	The converted di-photon foreground (FG) pair distribution in mass divided by the combinatorial mixed event background (BG) distribution for 60-86% centrality in the converted photon p_{Tee} bin of 0.4 - 0.6 GeV/c at $\sqrt{s_{NN}} = 39$ GeV. The region of the pion peak is excluded. The ratio is fitted with a second order polynomial (shown in red).	165

145	The FG pair distribution in mass divided by the combinatorial BG distribution for 60-86% centrality in the converted photon p_{Tee} bin of 0.8 - 1.0 GeV/c at $\sqrt{s_{NN}} = 39$ GeV.	165
146	The converted di-photon foreground (FG) pair distribution in mass divided by the combinatorial mixed event background (BG) distribution for 0-86% centrality in the converted photon p_{Tee} bin of 0.8 - 1.0 GeV/c at $\sqrt{s_{NN}} = 39$ GeV. The region of the pion peak is excluded. The ratio is fitted with a second order polynomial (shown in red).	166
147	The FG pair distribution in mass divided by the combinatorial BG distribution for 0-86% centrality in the converted photon p_{Tee} bin of 1.8 - 2.0 GeV/c at $\sqrt{s_{NN}} = 39$ GeV.	166
148	The di-photon foreground (blue) and normalized mixed event background (red) for 0-20% centrality in the converted photon p_{Tee} bin of 0.9 - 1.1 GeV/c at $\sqrt{s_{NN}} = 62.4$ GeV. The uncertainty on the background includes both background's statistical uncertainty and the uncertainty in the normalization with CL=0.66.	167
149	The foreground and normalized background for 0-20% centrality in the converted photon p_{Tee} bin of 1.9 - 2.1 GeV/c at $\sqrt{s_{NN}} = 62.4$ GeV.	167
150	The di-photon foreground (blue) and normalized mixed event background (red) for 20-40% centrality in the converted photon p_{Tee} bin of 0.9 - 1.1 GeV/c at $\sqrt{s_{NN}} = 62.4$ GeV. The uncertainty on the background includes both background's statistical uncertainty and the uncertainty in the normalization with CL=0.66.	168
151	The foreground and normalized background for 20-40% centrality in the converted photon p_{Tee} bin of 1.9 - 2.1 GeV/c at $\sqrt{s_{NN}} = 62.4$ GeV.	168
152	The di-photon foreground (blue) and normalized mixed event background (red) for 40-60% centrality in the converted photon p_{Tee} bin of 0.9 - 1.1 GeV/c at $\sqrt{s_{NN}} = 62.4$ GeV. The uncertainty on the background includes both background's statistical uncertainty and the uncertainty in the normalization with CL=0.66.	169
153	The foreground and normalized background for 40-60% centrality in the converted photon p_{Tee} bin of 1.9 - 2.1 GeV/c at $\sqrt{s_{NN}} = 62.4$ GeV.	169
154	The di-photon foreground (blue) and normalized mixed event background (red) for 60-86% centrality in the converted photon p_{Tee} bin of 0.7 - 0.9 GeV/c at $\sqrt{s_{NN}} = 62.4$ GeV. The uncertainty on the background includes both background's statistical uncertainty and the uncertainty in the normalization with CL=0.66.	170
155	The foreground and normalized background for 60-86% centrality in the converted photon p_{Tee} bin of 1.3 - 1.5 GeV/c at $\sqrt{s_{NN}} = 62.4$ GeV.	170

156	The di-photon foreground (blue) and normalized mixed event background (red) for 0-86% centrality in the converted photon p_{Tee} bin of 0.9 - 1.1 GeV/c at $\sqrt{s_{NN}} = 62.4$ GeV. The uncertainty on the background includes both background's statistical uncertainty and the uncertainty in the normalization with CL=0.66.	171
157	The foreground and normalized background for 0-86% centrality in the converted photon p_{Tee} bin of 1.9 - 2.1 GeV/c at $\sqrt{s_{NN}} = 62.4$ GeV.	171
158	The di-photon foreground (blue) and normalized mixed event background (red) for 0-20% centrality in the converted photon p_{Tee} bin of 0.8 - 1.0 GeV/c at $\sqrt{s_{NN}} = 39$ GeV. The uncertainty on the background includes both background's statistical uncertainty and the uncertainty in the normalization with CL=0.66.	172
159	The foreground and normalized background for 0-20% centrality in the converted photon p_{Tee} bin of 1.8 - 2.0 GeV/c at $\sqrt{s_{NN}} = 39$ GeV.	172
160	The di-photon foreground (blue) and normalized mixed event background (red) for 20-40% centrality in the converted photon p_{Tee} bin of 0.8 - 1.0 GeV/c at $\sqrt{s_{NN}} = 39$ GeV. The uncertainty on the background includes both background's statistical uncertainty and the uncertainty in the normalization with CL=0.66.	173
161	The foreground and normalized background for 20-40% centrality in the converted photon p_{Tee} bin of 1.8 - 2.0 GeV/c at $\sqrt{s_{NN}} = 39$ GeV.	173
162	The di-photon foreground (blue) and normalized mixed event background (red) for 40-60% centrality in the converted photon p_{Tee} bin of 0.6 - 0.8 GeV/c at $\sqrt{s_{NN}} = 39$ GeV. The uncertainty on the background includes both background's statistical uncertainty and the uncertainty in the normalization with CL=0.66.	174
163	The foreground and normalized background for 40-60% centrality in the converted photon p_{Tee} bin of 1.2 - 1.4 GeV/c at $\sqrt{s_{NN}} = 39$ GeV.	174
164	The di-photon foreground (blue) and normalized mixed event background (red) for 60-86% centrality in the converted photon p_{Tee} bin of 0.4 - 0.6 GeV/c at $\sqrt{s_{NN}} = 39$ GeV. The uncertainty on the background includes both background's statistical uncertainty and the uncertainty in the normalization with CL=0.66.	175
165	The foreground and normalized background for 60-86% centrality in the converted photon p_{Tee} bin of 0.8 - 1.0 GeV/c at $\sqrt{s_{NN}} = 39$ GeV.	175
166	The di-photon foreground (blue) and normalized mixed event background (red) for 0-86% centrality in the converted photon p_{Tee} bin of 0.8 - 1.0 GeV/c at $\sqrt{s_{NN}} = 39$ GeV. The uncertainty on the background includes both background's statistical uncertainty and the uncertainty in the normalization with CL=0.66.	176
167	The foreground and normalized background for 0-86% centrality in the converted photon p_{Tee} bin of 1.8 - 2.0 GeV/c at $\sqrt{s_{NN}} = 39$ GeV.	176

168	The π^0 yield extraction for 0-20% centrality in the converted photon p_{Tee} bin of 0.9 - 1.1 GeV/c at $\sqrt{s_{NN}} = 62.4$ GeV. The residual background is assumed to be described by averaging the sum of the green and cyan colored lines, which is subtracted from the original blue π^0 yield extraction (fitted by the blue Gaussian). The result is the purple histogram (fitted by the purple Gaussian).	177
169	The π^0 yield extraction for 0-20% centrality in the converted photon p_{Tee} bin of 1.9 - 2.1 GeV/c at $\sqrt{s_{NN}} = 62.4$ GeV.	177
170	The π^0 yield extraction for 20-40% centrality in the converted photon p_{Tee} bin of 0.9 - 1.1 GeV/c at $\sqrt{s_{NN}} = 62.4$ GeV. The residual background is assumed to be described by averaging the sum of the green and cyan colored lines, which is subtracted from the original blue π^0 yield extraction (fitted by the blue Gaussian). The result is the purple histogram (fitted by the purple Gaussian).	178
171	The π^0 yield extraction for 20-40% centrality in the converted photon p_{Tee} bin of 1.9 - 2.1 GeV/c at $\sqrt{s_{NN}} = 62.4$ GeV.	178
172	The π^0 yield extraction for 40-60% centrality in the converted photon p_{Tee} bin of 0.9 - 1.1 GeV/c at $\sqrt{s_{NN}} = 62.4$ GeV. The residual background is assumed to be described by averaging the sum of the green and cyan colored lines, which is subtracted from the original blue π^0 yield extraction (fitted by the blue Gaussian). The result is the purple histogram (fitted by the purple Gaussian).	179
173	The π^0 yield extraction for 40-60% centrality in the converted photon p_{Tee} bin of 1.9 - 2.1 GeV/c at $\sqrt{s_{NN}} = 62.4$ GeV.	179
174	The π^0 yield extraction for 60-86% centrality in the converted photon p_{Tee} bin of 0.7 - 0.9 GeV/c at $\sqrt{s_{NN}} = 62.4$ GeV. The residual background is assumed to be described by averaging the sum of the green and cyan colored lines, which is subtracted from the original blue π^0 yield extraction (fitted by the blue Gaussian). The result is the purple histogram (fitted by the purple Gaussian).	180
175	The π^0 yield extraction for 60-86% centrality in the converted photon p_{Tee} bin of 1.3 - 1.5 GeV/c at $\sqrt{s_{NN}} = 62.4$ GeV.	180
176	The π^0 yield extraction for 0-86% centrality in the converted photon p_{Tee} bin of 0.9 - 1.1 GeV/c at $\sqrt{s_{NN}} = 62.4$ GeV. The residual background is assumed to be described by averaging the sum of the green and cyan colored lines, which is subtracted from the original blue π^0 yield extraction (fitted by the blue Gaussian). The result is the purple histogram (fitted by the purple Gaussian).	181
177	The π^0 yield extraction for 0-86% centrality in the converted photon p_{Tee} bin of 1.9 - 2.1 GeV/c at $\sqrt{s_{NN}} = 62.4$ GeV.	181

178	The π^0 yield extraction for 0-20% centrality in the converted photon p_{Tee} bin of 0.8 - 1.0 GeV/c at $\sqrt{s_{NN}} = 39$ GeV. The residual background is assumed to be described by averaging the sum of the green and cyan colored lines, which is subtracted from the original blue π^0 yield extraction (fitted by the blue Gaussian). The result is the purple histogram (fitted by the purple Gaussian).	182
179	The π^0 yield extraction for 0-20% centrality in the converted photon p_{Tee} bin of 1.8 - 2.0 GeV/c at $\sqrt{s_{NN}} = 39$ GeV.	182
180	The π^0 yield extraction for 20-40% centrality in the converted photon p_{Tee} bin of 0.8 - 1.0 GeV/c at $\sqrt{s_{NN}} = 39$ GeV. The residual background is assumed to be described by averaging the sum of the green and cyan colored lines, which is subtracted from the original blue π^0 yield extraction (fitted by the blue Gaussian). The result is the purple histogram (fitted by the purple Gaussian).	183
181	The π^0 yield extraction for 20-40% centrality in the converted photon p_{Tee} bin of 1.8 - 2.0 GeV/c at $\sqrt{s_{NN}} = 39$ GeV.	183
182	The π^0 yield extraction for 40-60% centrality in the converted photon p_{Tee} bin of 0.6 - 0.8 GeV/c at $\sqrt{s_{NN}} = 39$ GeV. The residual background is assumed to be described by averaging the sum of the green and cyan colored lines, which is subtracted from the original blue π^0 yield extraction (fitted by the blue Gaussian). The result is the purple histogram (fitted by the purple Gaussian).	184
183	The π^0 yield extraction for 40-60% centrality in the converted photon p_{Tee} bin of 1.2 - 1.4 GeV/c at $\sqrt{s_{NN}} = 39$ GeV.	184
184	The π^0 yield extraction for 60-86% centrality in the converted photon p_{Tee} bin of 0.4 - 0.6 GeV/c at $\sqrt{s_{NN}} = 39$ GeV. The residual background is assumed to be described by averaging the sum of the green and cyan colored lines, which is subtracted from the original blue π^0 yield extraction (fitted by the blue Gaussian). The result is the purple histogram (fitted by the purple Gaussian).	185
185	The π^0 yield extraction for 60-86% centrality in the converted photon p_{Tee} bin of 0.8 - 1.0 GeV/c at $\sqrt{s_{NN}} = 39$ GeV.	185
186	The π^0 yield extraction for 0-86% centrality in the converted photon p_{Tee} bin of 0.8 - 1.0 GeV/c at $\sqrt{s_{NN}} = 39$ GeV. The residual background is assumed to be described by averaging the sum of the green and cyan colored lines, which is subtracted from the original blue π^0 yield extraction (fitted by the blue Gaussian). The result is the purple histogram (fitted by the purple Gaussian).	186
187	The π^0 yield extraction for 0-86% centrality in the converted photon p_{Tee} bin of 1.8 - 2.0 GeV/c at $\sqrt{s_{NN}} = 39$ GeV.	186

List of Tables

1	The summary of the parameters of the PHENIX EMCals. There are two types of EMCal detectors: lead-scintillator (PbSc) and lead-glass (PbGl).	67
2	The segmented p_{Tee} bins of converted photons (in GeV/c) in four centrality bins plus the minimum bias at $\sqrt{s_{NN}} = 62.4$ GeV.	78
3	The segmented p_{Tee} bins of converted photons (in GeV/c) in four centrality bins plus the minimum bias at $\sqrt{s_{NN}} = 39$ GeV.	78
4	The Hagedorn parameters of π^0 p_T spectra obtained by fitting the modified Hagedorn function (Eq. (124)) with the PHENIX data [140] at $\sqrt{s_{NN}} = 62.4$ GeV.	104
5	The Hagedorn parameters of π^0 p_T spectra obtained by fitting the modified Hagedorn function (Eq. (124) at $b = 0$) with the PHENIX data [143] at $\sqrt{s_{NN}} = 39$ GeV.	104
6	The photon production channels used in our cocktail ratio simulation. The table is from [134].	107
7	The hadron yield relative to the π^0 yield. The table is from [134].	108
8	The segmented p_{Tee} bins of converted photons (in GeV/c) in four centrality bins plus the minimum bias at $\sqrt{s_{NN}} = 62.4$ GeV. The p_{Tee} binning is different than what is used in this analysis.	118
9	The segmented p_{Tee} bins of converted photons (in GeV/c) in four centrality bins plus the minimum bias at $\sqrt{s_{NN}} = 39$ GeV. The p_{Tee} binning is different than what is used in this analysis.	118
10	The systematic uncertainties on R_γ constituents at $\sqrt{s_{NN}} = 62.4$ GeV. The type A is a source of uncertainty, which is uncorrelated between data points. The type B uncertainties are p_T -correlated.	123
11	The systematic uncertainties on R_γ constituents at $\sqrt{s_{NN}} = 39$ GeV. The type A is a source of uncertainty, which is uncorrelated between data points. The type B uncertainties are p_T -correlated.	123
12	The values of T_{AA} is obtained from [145]. T_{eff} is from Fig. (100), Fig. (101), Fig. (102) and Fig. (103).	129
13	The table for 0-20% centrality binned conditional acceptance, $\langle \varepsilon_\gamma f \rangle$, at $\sqrt{s_{NN}} = 62.4$ GeV, shown in Fig. 81(a).	187
14	The conditional acceptance $\langle \varepsilon_\gamma f \rangle$ for 20-40% centrality at $\sqrt{s_{NN}} = 62.4$ GeV, shown in Fig. 81(b).	187
15	The conditional acceptance $\langle \varepsilon_\gamma f \rangle$ for the minimum bias 0-86% at $\sqrt{s_{NN}} = 62.4$ GeV, shown in Fig. 81(e).	188
16	The conditional acceptance $\langle \varepsilon_\gamma f \rangle$ for the minimum bias 0-86% at $\sqrt{s_{NN}} = 39$ GeV, shown in Fig. 82(e).	188

17	The table for 0-20% centrality binned cocktail ratio, $Y_{cocktail}$, at $\sqrt{s_{NN}} = 62.4 \text{ GeV}$, shown in Fig. 84(a).	189
18	The cocktail ratio $Y_{cocktail}$ for 20-40% centrality at $\sqrt{s_{NN}} = 62.4 \text{ GeV}$, shown in Fig. 84(b).	189
19	The cocktail ratio $Y_{cocktail}$ for the minimum bias 0-86% at $\sqrt{s_{NN}} = 62.4 \text{ GeV}$, shown in Fig. 84(e).	190
20	The cocktail ratio $Y_{cocktail}$ for the minimum bias 0-86% at $\sqrt{s_{NN}} = 39 \text{ GeV}$, shown in Fig. 86(e).	190
21	The data table for 0-20% centrality binned $N^{incl}/N^{\pi^0,tag}$ ratio at $\sqrt{s_{NN}} = 62.4 \text{ GeV}$, shown in Fig. 99(a).	191
22	The $N^{incl}/N^{\pi^0,tag}$ ratio for 20-40% centrality at $\sqrt{s_{NN}} = 62.4 \text{ GeV}$, shown in Fig. 99(b).	191
23	The $N^{incl}/N^{\pi^0,tag}$ ratio for the minimum bias 0-86% at $\sqrt{s_{NN}} = 62.4 \text{ GeV}$, shown in Fig. 99(e).	192
24	The $N^{incl}/N^{\pi^0,tag}$ ratio for the minimum bias 0-86% at $\sqrt{s_{NN}} = 39 \text{ GeV}$, shown in Fig. 99(e).	192
25	The data table for 0-20% centrality binned relative direct photon yield, R_γ , at $\sqrt{s_{NN}} = 62.4 \text{ GeV}$, shown in Fig. 96(a).	193
26	R_γ for 20-40% centrality at $\sqrt{s_{NN}} = 62.4 \text{ GeV}$, shown in Fig. 96(b).	193
27	R_γ for the minimum bias 0-86% at $\sqrt{s_{NN}} = 62.4 \text{ GeV}$, shown in Fig. 96(c).	194
28	R_γ for the minimum bias 0-86% at $\sqrt{s_{NN}} = 39 \text{ GeV}$, shown in Fig. 96(d).	194
29	Charged particle multiplicity results for 200 GeV Au+Au collisions. The uncertainties include the total statistical and systematic uncertainties. The table is from [145] with the substitution $\langle N_{qp} \rangle \leftrightarrow \langle N_{coll} \rangle$, where $\langle N_{coll} \rangle$ is from [146].	195
30	Charged particle multiplicity results for 62.4 GeV Au+Au collisions. The uncertainties include the total statistical and systematic uncertainties. The table is from [145] with the substitution $\langle N_{qp} \rangle \leftrightarrow \langle N_{coll} \rangle$, where $\langle N_{coll} \rangle$ is from [148].	195
31	Charged particle multiplicity results for 39 GeV Au+Au collisions. The uncertainties include the total statistical and systematic uncertainties. The table is from [145] with the substitution $\langle N_{qp} \rangle \leftrightarrow \langle N_{coll} \rangle$, where $\langle N_{coll} \rangle$ is from [148].	196
32	Charged particle multiplicity results for 2760 GeV Pb+Pb collisions. The table is from [149] with the addition of $\langle N_{coll} \rangle$, which is from [147].	196
33	The data table for 0-20% centrality binned direct photon invariant yield in Au+Au at $\sqrt{s_{NN}} = 62.4 \text{ GeV}$	197
34	The data table for 20-40% centrality binned direct photon invariant yield in Au+Au at $\sqrt{s_{NN}} = 62.4 \text{ GeV}$	197

35	The data table for 0-86% centrality binned direct photon invariant yield in Au+Au at $\sqrt{s_{NN}} = 62.4 \text{ GeV}$	198
36	The data table for 0-86% centrality binned direct photon invariant yield in Au+Au at $\sqrt{s_{NN}} = 39 \text{ GeV}$	198
37	The data table for 0-20% centrality binned direct photon invariant yield in Au+Au at $\sqrt{s_{NN}} = 200 \text{ GeV}$ from [42].	199
38	The data table for 20-40% centrality binned direct photon invariant yield in Au+Au at $\sqrt{s_{NN}} = 200 \text{ GeV}$ from [42].	199
39	The data table for 40-60% centrality binned direct photon invariant yield in Au+Au at $\sqrt{s_{NN}} = 200 \text{ GeV}$ from [42].	200
40	The data table for 60-92% centrality binned direct photon invariant yield in Au+Au at $\sqrt{s_{NN}} = 200 \text{ GeV}$ from [42].	200
41	The data table for 0-20% centrality binned direct photon invariant yield in Au+Au at $\sqrt{s_{NN}} = 200 \text{ GeV}$ from [40].	201
42	The data table for 20-40% centrality binned direct photon invariant yield in Au+Au at $\sqrt{s_{NN}} = 200 \text{ GeV}$ from [40].	201
43	The data table for 0-92% centrality binned direct photon invariant yield in Au+Au at $\sqrt{s_{NN}} = 200 \text{ GeV}$ from [40].	201
44	The data table for 0-40% centrality binned direct photon invariant yield in Cu+Cu at $\sqrt{s_{NN}} = 200 \text{ GeV}$ from [44].	202
45	The data table for 0-94% centrality binned direct photon invariant yield in Cu+Cu at $\sqrt{s_{NN}} = 200 \text{ GeV}$ from [44].	202
46	The data table for 0-20% centrality binned direct photon invariant yield in Pb+Pb at $\sqrt{s_{NN}} = 2760 \text{ GeV}$ from [45].	202
47	The data table for 20-40% centrality binned direct photon invariant yield in Pb+Pb at $\sqrt{s_{NN}} = 2760 \text{ GeV}$ from [45].	203
48	The data table for 40-80% centrality binned direct photon invariant yield in Pb+Pb at $\sqrt{s_{NN}} = 2760 \text{ GeV}$ from [45].	204
49	The data table for direct photon invariant cross section in p+p at $\sqrt{s_{NN}} = 200 \text{ GeV}$ from [153].	205
50	The data table for 0-5% centrality binned direct photon invariant yield in Au+Au at $\sqrt{s_{NN}} = 200 \text{ GeV}$ from [151].	206
51	The data table for 5-10% centrality binned direct photon invariant yield in Au+Au at $\sqrt{s_{NN}} = 200 \text{ GeV}$ from [151].	206
52	The data table for 10-15% centrality binned direct photon invariant yield in Au+Au at $\sqrt{s_{NN}} = 200 \text{ GeV}$ from [151].	207

53	The data table for 15-20% centrality binned direct photon invariant yield in Au+Au at $\sqrt{s_{NN}} = 200 \text{ GeV}$ from [151].	207
54	The data table for 20-30% centrality binned direct photon invariant yield in Au+Au at $\sqrt{s_{NN}} = 200 \text{ GeV}$ from [151].	208
55	The data table for 30-40% centrality binned direct photon invariant yield in Au+Au at $\sqrt{s_{NN}} = 200 \text{ GeV}$ from [151].	208
56	The data table for 40-50% centrality binned direct photon invariant yield in Au+Au at $\sqrt{s_{NN}} = 200 \text{ GeV}$ from [151].	209
57	The data table for 50-60% centrality binned direct photon invariant yield in Au+Au at $\sqrt{s_{NN}} = 200 \text{ GeV}$ from [151].	209
58	The data table for 60-92% centrality binned direct photon invariant yield in Au+Au at $\sqrt{s_{NN}} = 200 \text{ GeV}$ from [151].	210
59	The data table for 0-92% centrality binned direct photon invariant yield in Au+Au at $\sqrt{s_{NN}} = 200 \text{ GeV}$ from [151].	210
60	The data table for direct photon invariant cross section in p+p at $\sqrt{s_{NN}} = 62.4 \text{ GeV}$ from [154, 157].	211
61	The data table for direct photon invariant cross section in p+p at $\sqrt{s_{NN}} = 63 \text{ GeV}$ from [155, 157].	211
62	The data table for direct photon invariant cross section in p+p at $\sqrt{s_{NN}} = 63 \text{ GeV}$ from [156, 157].	211
63	The data table for the integrated yield, ($1.0 \text{ GeV}/c < p_T < 1.5 \text{ GeV}/c$, Fig. (119)), all shown in Tables 33, 34, 35, 36, 37, 38, 39, 40, 41, 42, 43, 44, 45, 46, 49.	212
64	The data table for the integrated yield, ($p_T > 1.0 \text{ GeV}/c$, Fig. (120)), all shown in Tables 33, 34, 35, 36, 37, 38, 39, 40, 41, 42, 43, 44, 45, 46, 49.	212
65	The data table for the integrated yield, ($p_T > 1.5 \text{ GeV}/c$, Fig. (121)), all shown in Tables 33, 35, 37, 38, 39, 40, 41, 42, 43, 44, 45, 46, 47, 49.	213
66	The data table for the integrated yield, ($p_T > 2.0 \text{ GeV}/c$, Fig. (122)), all shown in Tables ,37, 38, 39, 40, 41, 42, 43, 46, 47, 48, 49.	213
67	The data table for the integrated yield, ($5.0 \text{ GeV}/c < p_T < 8.0 \text{ GeV}/c$, Fig. (123)), all shown in Tables 46, 47, 48, 50, 51, 52, 53, 54, 55, 56, 57, 58, 49, 60, 61.	214
68	The data table for the integrated yield, ($p_T > 5.0 \text{ GeV}/c$, Fig. (124)), all shown in Tables 46, 47, 48, 50, 51, 52, 53, 54, 55, 56, 57, 58, 49, 60.	214
69	The data table for the integrated yield, ($p_T > 8.0 \text{ GeV}/c$, Fig. (125)), all shown in Tables 46, 47, 48, 50, 51, 52, 53, 54, 55, 56, 57, 58, 49, 60.	215

70	The data table for the N_{coll} values used to obtain the model and pQCD calculations describing the N_{coll} scaled prompt photons, shown for example in Fig. (114), Fig. (120) and Fig. (124). No errors are shown.	215
----	---	-----

List of Abbreviations

- BNL - Brookhaven National Laboratory
- RHIC - Relativistic Heavy Ion Collider
- PHENIX - Pioneering High Energy Nuclear Interaction eXperiment
 - STAR - Solenoidal Tracker at RHIC
- CERN - European Organization for Nuclear Research
 - LHC - Large Hadron Collider
- ALICE - A Large Ion Collider Experiment
- GSI Helmholtzzentrum für Schwerionenforschung - GSI Helmholtz Centre for Heavy Ion Research
- HADES - High Acceptance Di-Electron Spectrometer
 - QCD - Quantum chromodynamics
 - CGC - Color Glass Condensate
 - QGP - Quark Gluon Plasma
- sQGP - strongly coupled Quark Gluon Plasma
 - HG - Hadronic gas
 - BBC - Beam-Beam Counter
- ZDC - Zero Degree Calorimeter
- RXP - Reaction Plane Detector
 - DC - Drift Chamber
 - PC - Pad Chamber
- RICH - Ring-Imaging Cherenkov Detector
 - HBD - Hadron Blind Detector
- EMCal - Electromagnetic Calorimeter
 - PbSc - Lead-Scintillator
 - PbGl - Lead-Glass
- DAQ - Data Acquisition System
 - QA - Quality Analysis
- ATM - Alternate Track Model
- PISA - PHENIX Integrated Simulation Application

Acknowledgements

This page is optional.

Part I

Introduction and Experiment

Chapter 1

1 Introduction

We start the introduction section with the concise description of quantum chromodynamics, then we discuss the physics of heavy ion collisions and direct photon production in Sec. 1.2 and Sec. 1.3, respectively.

1.1 Quantum chromodynamics

The fundamental force describing the interactions of quarks and gluons is known as the *strong force*, which make up hadronic particles such as the protons, neutrons and pions. It is one of the four fundamental forces of nature, which are used in physics in order to quantitatively describe phenomena from the small scale world of quarks and leptons (10^{-18} cm) to the large scale of the whole present-day Universe (10^{28} cm). In theoretical physics, the strong interactions are described by a quantum field theory called quantum chromodynamics, QCD [1, 2, 3]. The strong force has its carriers, the gluons, like the photons for the electromagnetic force in quantum electrodynamics, QED. The QCD analog of the electric charge is a property called *color*. The theory of QCD is an important part of the Standard Model of particle physics [4], and a large body of experimental evidence has been gathered over the years for confirmation of its outcomes.

Every field theory of particle physics is based on certain symmetries of nature, the existences of which are deduced from observations. These symmetries are

- local symmetries, which are symmetries acting independently at each point in spacetime. Each such a symmetry is the basis of a gauge theory, and requires the introduction of its own gauge bosons.
- global symmetries, which are symmetries that have operations being simultaneously applied to all points in spacetime.

The QCD is a non-abelian gauge theory of the SU(3) gauge group obtained by taking the color charge to define a local symmetry. More details are given in the following Sec. 1.1.1 and Sec. 1.1.2.

1.1.1 Quarks and color charge

The quarks, being fermions of spin-1/2, are the fundamental objects participating in strong interactions. They are the only elementary particles in the Standard Model to experience all four fundamental interactions. The quarks are described by the Dirac spinors, $\psi_\gamma(x)$, which are functions of the four-dimensional Minkowski spacetime coordinates, $x^\mu = (t, x, y, z)$, and where the spinor component accepts four values: $\gamma = 0, 1, 2, 3$. The Lagrangian is given by

$$\mathcal{L}(x) = \bar{\psi}(x)(i\gamma^\mu\partial_\mu - m_q)\psi(x). \quad (1)$$

The basic wave equation describing the dynamics of quarks is the Dirac equation. In the absence of quark interactions with other particles and fields, the Dirac equation has the following form:

$$(i\gamma^\mu\partial_\mu - m_q)\psi(x) = 0, \quad (2)$$

which in turn can be derived from the free quark Lagrangian itself. The solutions of Eq. (2) are plane waves of the form

$$\psi_{k,s}(x) = u(k, s) e^{-i(E\cdot t - \vec{x}\cdot \vec{k})}, \quad (3)$$

where $k_\mu = (E, \vec{k})$ is the four-momentum, the polarization is denoted by s , and $u(k, s)$ is the spin-dependent momentum-space wave function.

There are six types (flavors) of quarks: up (u) and down (d), charm (c) and strange (s), top (t) and bottom (b). These quarks have various intrinsic properties (described by certain quantum numbers), including electric charge, mass, color charge, and spin. Their electric charges are not integer multiples of the elementary charge. For example, the electric charges of u, c and t quarks are all 2/3 of that of proton, and the charges of d, s and b are all $-1/3$ of proton. The u and d quarks (plus the electron e^- and electron neutrino ν_e) form the first generation of matter, c and s (plus the muon μ^- and muon neutrino ν_μ) the second generation, and t and b (plus the tauon τ^- and tau neutrino ν_τ) the third one.

The u and d quarks are stable particles and have the lowest masses of all quarks. Through a particle decay a heavier quark can change into u and d quarks. The s, c quarks and b, t quarks can only be produced in high energy collisions. For every quark flavor there is a corresponding type of antiparticle, known as an antiquark, that differs from the quark only in that some of its quantum numbers have equal magnitude but opposite sign.

In Eqs. (1) and (2) the quark mass term is actually just a parameter in the Lagrangian of the theory, which describes the self-interaction of the quark, and is not directly observable. The mass parameter is dependent on the momentum scale and renormalization scheme, a scheme, which is based on dimensional regularization and modified minimal subtraction that give the $\overline{\text{MS}}$ quark masses¹. Ac-

¹See Ref. [5] for the values of the quark masses, and for more details.

cording to the Standard Model, the quark masses are generated through a symmetry breaking phase transition of the electroweak interactions (electroweak symmetry breaking, EWSB). The fermions, such as quarks and leptons, acquire masses as a result of their interaction with the Higgs field, but not in the same way as the gauge bosons. One should also distinguish between the masses of *bare* quarks (called also *naked* or *current* quarks) and *constituent* quarks. The bare quarks are defined as the constituent quark cores of valence quarks. The bare quark mass is the constituent quark mass reduced by the mass of the respective constituent quark covering. There is very small difference between bare and constituent quark masses for the heavy c, b, t quarks, however, this is not the case for the light u, d, s quarks. Since the strong interaction does not discriminate between different lighter flavors of quarks, the QCD has approximate flavor symmetry for quarks with lighter masses, which is broken by differed masses of the heavier quarks.

The participation of the quarks in strong interactions occurs because of color charge. In particular, the color charge is a “quantum vector charge”, conceptually similar to angular momentum in quantum mechanics, but different from electric charge, which is a scalar quantity in the sense that the total electric charge of an electrical system is simply the algebraic sum of individual charges. Meanwhile, the total color charge of a QCD system must be obtained by combining the individual color charges of the constituents in an analogous way, which is done for combining angular momenta in quantum mechanics.

There are three types of the color charge, arbitrarily labeled as red (R), green (G) and blue (B). The three color states form a basis in a three-dimensional complex vector space (color space), and an arbitrary color state of a quark is then a vector in this space. Any color state can be rotated by 3×3 unitary matrices. All such unitary transformations, with unit determinant, form a Lie group $SU(3)$ (commonly abbreviated to $SU(3)_c$). The defining symmetry for QCD is then the gauge symmetry $SU(3)_c$ that relates the color charges in quarks. Each quark flavor ψ , with subtypes ψ_R, ψ_G, ψ_B corresponding to quark colors, forms a triplet of fields, which transforms under the fundamental representation (3) of $SU(3)_c$. The properties of strong interactions are determined by requiring that the transformations of $SU(3)_c$ be local, i.e., being varied with spacetime. In particular, it implies the existence of eight gluon types to act as its force carriers (see the next section). Each quark carries a color, while each antiquark carries an anticolor. An antiquark field belongs to the complex conjugate representation (3^*) and also contains a triplet of fields. Then for the quark and antiquark fields one can write

$$\psi = \begin{bmatrix} \psi_R \\ \psi_G \\ \psi_B \end{bmatrix} \quad \text{and} \quad \bar{\psi} = \begin{bmatrix} \bar{\psi}_R^* \\ \bar{\psi}_G^* \\ \bar{\psi}_B^* \end{bmatrix}$$

A quark having a single color value can form a bound system with an antiquark carrying the corresponding anticolor. It results in color neutrality (or “white” color) between the two attracting particles

forming a meson. Similarly, the combination of three quarks (antiquarks), each with its color charge (anticolor charge), will result in the same color neutrality, and the formation of a baryon (antibaryon).

1.1.2 Gluons, asymptotic freedom and confinement

- **Gluons:** The interactions between quarks occur through gluons, which in strong interactions play a similar role as the photons in QED. The gluons are massless, spin-1 particles with two polarization states (left-handed and right-handed), like photons. They are represented by a four-component vector potential, $A_\mu(x)$, with a Lorentz index, $\mu = 0, 1, 2, 3$, called *gauge potential*. The free quark Lagrangian density $\mathcal{L}(x)$ in Eq. (1) is invariant under a global SU(3) transformation

$$\psi'(x) = U\psi(x), \quad (4)$$

where U is a 3×3 unitary matrix acting on color index. The meaning of global is that the field at different spacetime points is transformed in exactly the same way. There are eight types of gluons mediating the strong interactions. A generic SU(3)_c matrix requires eight real parameters, usually written in the form

$$U = \exp\left(i \sum_a \frac{\theta^a \lambda^a}{2}\right), \quad (5)$$

where $\lambda^a/2$ ($a = 1, \dots, 8$) are 3×3 hermitian matrices, called as *generators* of SU(3)_c rotations.

One can introduce eight gauge potentials, A_a^μ , for which the associated covariant derivative will be $D^\mu \equiv \partial^\mu + igA_a^\mu\lambda^a/2$. In this case the Lagrangian in Eq. (1) can be modified to the following form:

$$\mathcal{L}_q = \bar{\psi}(x)(i\gamma^\mu D_\mu - m_q)\psi(x). \quad (6)$$

If the gauge potential transforms according to

$$A^\mu \rightarrow U \left(A^\mu + \frac{i}{g} \partial^\mu \right) U^\dagger, \quad \text{with} \quad A^\mu = A_a^\mu \lambda^a / 2 \quad (7)$$

(where A^μ describes the 3×3 gluonic potential matrix), then the Lagrangian in Eq. (6) is invariant under SU(3)_c rotation of the quark fields.

By requiring a local color (gauge) symmetry, the quarks will not be free particles, however, they will interact with each other through the gauge potentials. The eight gluons are simply related to the eight parameters of the general SU(3)_c transformation, and the outcome is a well-defined dynamics of the color charges, which are generated from the gauge symmetry. The Lagrangian has an interaction term given by

$$\mathcal{L}_{int} = -g\bar{\psi}_j A_a^\mu \frac{\lambda_{ji}^a}{2} \gamma_\mu \psi_i, \quad (8)$$

where g is the coupling constant. The interaction of quarks and gluons takes place sort of in a way similar to electrons interacting with photons. The difference is that a quark can change its color from i to j by emitting or absorbing a gluon of color a , coupled through $SU(3)_c$ generator $t_{ij}^a \equiv \lambda_{ij}^a$, as shown in Fig. (1).

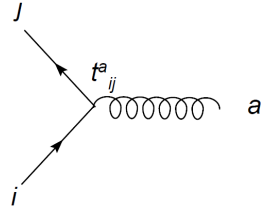


Figure 1: A diagram showing a quark changing its color from i to j by emitting or absorbing a gluon of color a .

The Lagrangian has also additional terms, which describe some physical features of gluons since they are physical degrees of freedom and carry energy and momentum themselves. The gluon kinetic energy term is described by

$$\mathcal{L}_g = -\frac{1}{4} F_{\mu\nu}^a F_{\mu\nu}^a, \quad (9)$$

where $F_{\mu\nu}^a$ is the antisymmetric field strength tensor, and in Eq. (9) summation over the color indices is implied². This new term will be gauge-invariant if the strength tensor is transformed by $F^{\mu\nu} \rightarrow UF^{\mu\nu}U^\dagger$. It can be obtained by choosing

$$F^{\mu\nu} = \partial^\mu A^\nu - \partial^\nu A^\mu - g[A^\mu, A^\nu]. \quad (10)$$

The last commutator term in the r.h.s of Eq. (10) is non-linear in terms of the gauge potential, which gives rise to three- and four-gluon self-interactions, as shown in Fig. (2).



Figure 2: Diagrams showing three and four self-interactions of gluons.

The gluon self-interactions are a source of the key differences between QCD and QED. For example, these interactions are responsible for asymptotic freedom and color confinement discussed in the following.

²The full QCD Lagrangian density will be the sum of the quark and gluon terms.

- **Asymptotic Freedom:** One of the very interesting properties of QCD is the *asymptotic freedom*. According to the asymptotic freedom the interaction strength between quarks becomes smaller if the distance between them gets shorter. In the quantum field theory, the vacuum is the lowest energy state of a field system, and it is filled with electrons of negative energies. When a photon passes through the vacuum, it can induce transitions of an electron from negative to positive energy states, virtually creating a pair of e^+e^- , known as vacuum fluctuation (see Fig. (3)). From this process, it follows that there can be a charge screening effect due to the quantum vacuum. If we look at a QED example of an electron, the electron polarizing the vacuum will be surrounded by a cloud of positive charges. This cloud screens the electron, so that the charge one measures is dependent on the distance from that charge. In QED, the measured charge increases as the distance to that charge decreases (close enough to penetrate the positron cloud). This effect is known as the running of the coupling constant.

In the vacuum, the interaction between two electrons is equal to $\alpha_{em}(r)/r^2$, where α_{em} is an effective structure constant, which is the coupling measuring the interaction strength that depends on the distance r (or momentum transfer $q \sim 1/r$). At $r \rightarrow \infty$, $\alpha_{em} = 1/137.015$. In QED, the dependence of α_{em} on r can be determined from renormalization group equations, such as

$$q \frac{d\alpha(q)}{dq} = \beta(\alpha(q)). \quad (11)$$

Since α_{em} is small, the β function can be calculated in perturbation theory. And since the interaction strength of the two electrons becomes stronger as the distance between them gets smaller, it results in QED becoming a strongly-coupled theory at very short distance scale.

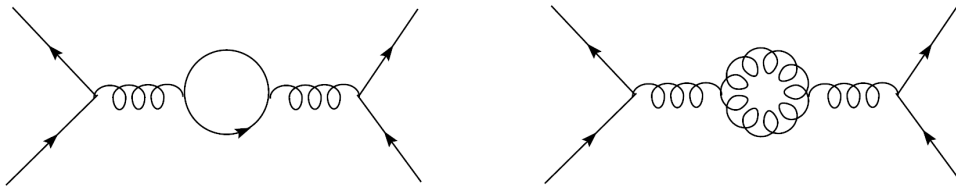


Figure 3: In the left panel diagram, the coupling becomes stronger at shorter distance (screening). In the right panel diagram, the coupling becomes weaker at short distance, arising from the nonlinear interaction between gluons in QCD (which has an antiscreening effect).

There is a similar screening in QCD with the color charges. But since the gluons have color charges and are self-interacting, this screening gives rise to a completely different running of the coupling constant than in QED. In QCD, the same Eq. (11) holds for the strong coupling constant, however, the β function is now different:

$$\beta(\alpha(q)) = -\frac{\beta_0}{2\pi}\alpha^2 + \dots, \quad (12)$$

where $\beta_0 = 11 - (2/3)n_f$, with n_f being the number of quark flavors. The first term in β_0 comes from the non-linear gluon contribution shown in the second diagram of Fig. (3), where the gluon self-coupling has an antiscreening effect. The second term in β_0 comes from quark-antiquark pair effect in the first diagram of Fig. (3), which scales like the number of quark flavors and is negative. From the renormalization group equation, the running of the coupling constant in QCD has been shown to have the following scale-dependence:

$$\alpha_s(Q^2) = \frac{12\pi}{(33 - 2n_f) \ln(Q^2/\Lambda_{QCD}^2)}, \quad (13)$$

where Λ_{QCD} is an intrinsic QCD scale (a dimensional parameter), and $Q^2 = -q^2$. Λ_{QCD} sets the scale at which the QCD coupling constant becomes large, and the physics becomes nonperturbative. In the $\overline{\text{MS}}$ -scheme with three quark flavors $\Lambda_{QCD} \sim 200 - 250$ MeV. In Eq. (13), $\alpha_s(Q^2) \rightarrow 0$ at $Q^2 \rightarrow \infty$ or $r \rightarrow 0$. This behavior of the QCD strong coupling has been verified in high-energy experiments to very high precision, as shown in Fig. (4). Thus in QCD, if one is closer to a charge, the smaller that measured charge will be. This is known as asymptotic freedom.

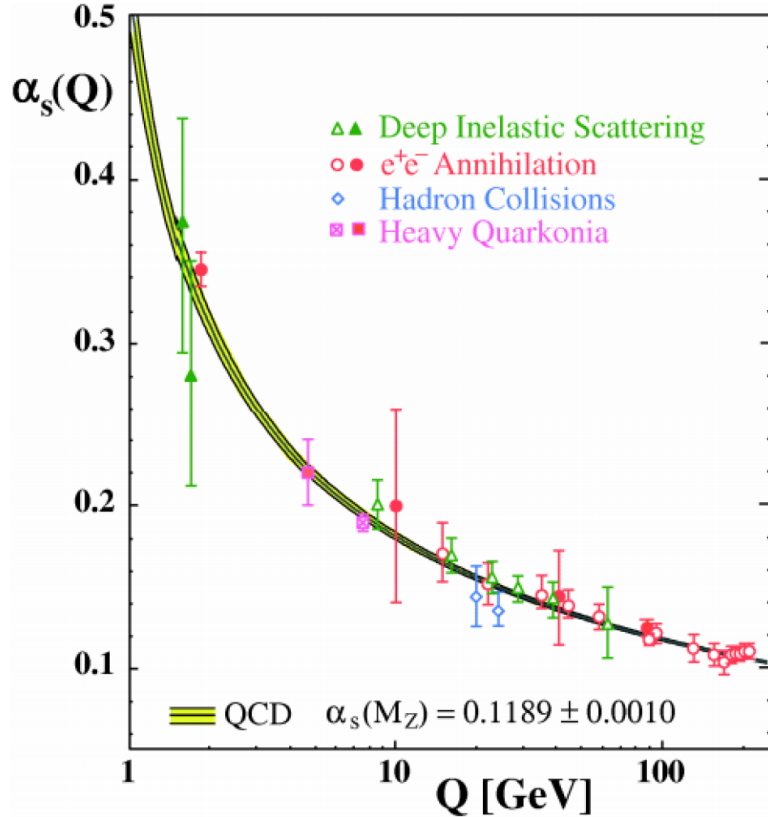


Figure 4: The theoretically calculated $\alpha_s(Q)$ in QCD as a function of momentum transfer compared to measurements shown as data points [6].

Due to the asymptotic freedom, the strong interaction physics can be calculated in perturbation theory, where the momentum transfer is large (perturbative regime). But for the lower energies (non-perturbative regime), one must use different techniques for calculations. Relating this notion to Eq. (13), a perturbative approach makes sense at small coupling when $Q^2 \gg \Lambda_{QCD}^2$. In this case, the one-gluon exchange diagram becomes a good approximation for quark interactions. When $Q^2 \sim \Lambda_{QCD}^2$, the coupling is no longer small at which quarks and gluons form tightly bound hadrons. Thereby, Λ_{QCD} sort of marks the boundary of the world of quarks and gluons, and that of hadrons. This scale is largely responsible for the proton and neutron mass scale, and correspondingly for the mass scale of the baryonic mass in the Universe. At present, the most accomplished results of QCD research field are obtained in the perturbative region, where many experimental data have been explained well by perturbative QCD (pQCD) physics.

- **Color Confinement:** Another quite interesting property of QCD at low energy region is the *color confinement*. The color confinement of QCD is a theoretical conjecture consistent with experimental facts, however, its proof is still a challenge that has not been overcome. Its consequence is that color charged particles (such as quarks and gluons) cannot be isolated, and therefore cannot be directly observed in normal conditions below the Hagedorn temperature. The nature keeps colored objects confined within color neutral objects. Indeed, the bare quarks (or gluons) have never been directly observed, meanwhile we measure hadrons that come out from the fragmentation of quarks.

The quarks and gluons cannot be separated from their parent hadron without producing new hadrons. This process can be rationalized if one considers two color charges ($q\bar{q}$ pair) moving apart from one another, as shown in the top row of Fig. (5). As they move apart, the flux tube connecting them gets longer, and the potential energy increases up to the point where there is enough energy to form another $q\bar{q}$ pair. The tube roughly has a constant cross section with constant energy density.

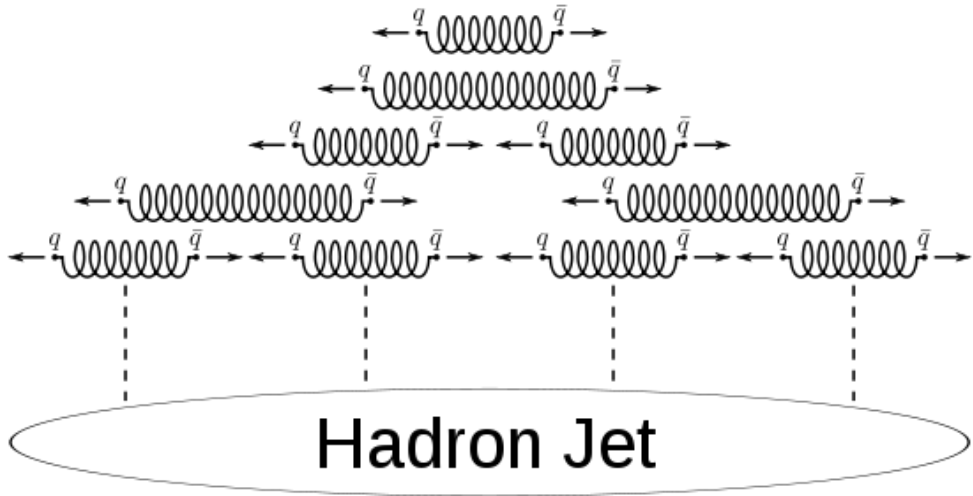


Figure 5: A cartoon illustrating the quark confinement.

Then the energy stored in the flux increases linearly with the length of the flux. In this case (the third row of Fig. (5)) the flux tube connecting the $q\bar{q}$ pair will split into two lower energy tubes, since it becomes energetically more favorable for the tube to break forming a new pair, which will close the open end of the broken flux tubes. Thus, this process continues until it is no longer energetically favorable for the tubes to break in order to form other pairs.

At high baryon densities and/or high temperatures, the quarks are deconfined and become relevant degrees of freedom of a system. This regime can be probed in relativistic heavy ion collisions. The temperature and density dependence of the nuclear matter produced in heavy ion collisions can be mapped out in a phase diagram. Mapping out this phase diagram and finding a *critical point* between the hadronic matter and quark matter is one of the major goals of high energy physics programs. One of the representations of the basic QCD phase diagram is shown in Fig. (6). The state of matter in which the quarks and gluons become deconfined from hadrons is named *Quark Gluon Plasma (QGP)*, and it is one of the subjects of the next section.

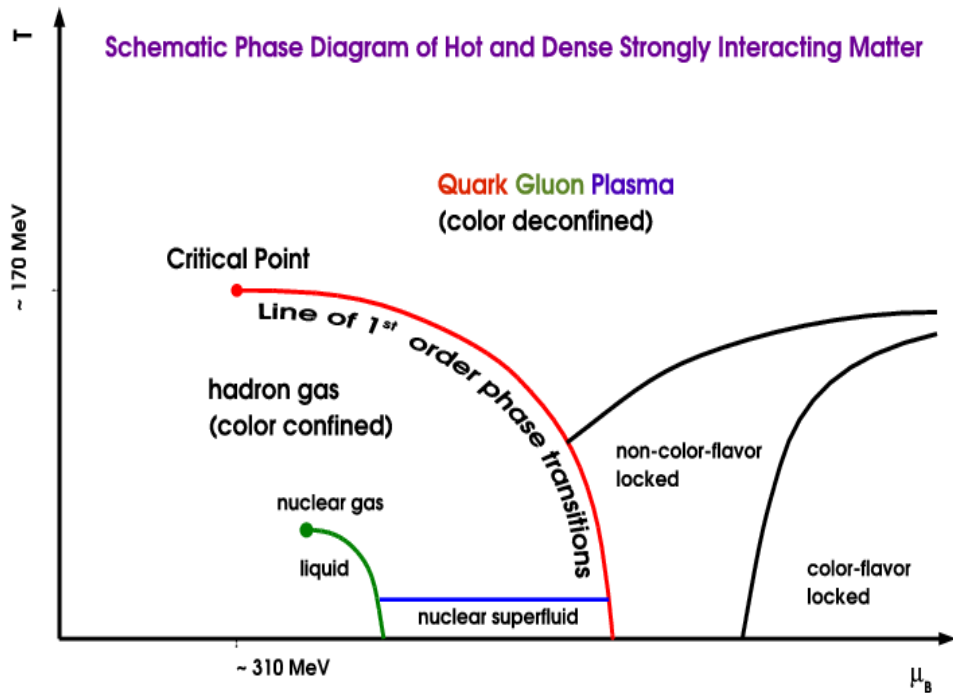


Figure 6: Schematic phase diagram of QCD based on [7, 8], as a function of temperature and baryochemical potential.

1.2 Heavy ion collisions

In this section we discuss the evolutionary phases of the matter produced in relativistic heavy ion collisions. But first we will look into the pre-collision phase of two colliding nuclei, the phase which

is called *Color Glass Condensate (CGC)*.

1.2.1 Pre-collision phase: Color Glass Condensate (CGC)

We do have some knowledge about the very early time dynamics of the heavy ion collisions, and one such very possible scenario involves the concept of the CGC [9, 10, 11, 12, 13, 14, 15, 16, 17]. The CGC gives a description of two colliding nuclei before they collide, by considering a highly coherent, high energy density ensemble of gluon states. As the Lorentz contracted nuclei pass through each other, their fields interact and form the phase called *Glasma*. Then the Glasma evolves to the thermalized strongly-coupled QGP after which the matter undergoes the *hadronization* phase. Such a generic view of a heavy ion collision is shown Fig. (7). Another view is depicted in Fig. (8), where the collision-produced system expands rapidly along the collision axis and time. Let us now focus on the CGC but the other phases will be discussed subsequently.

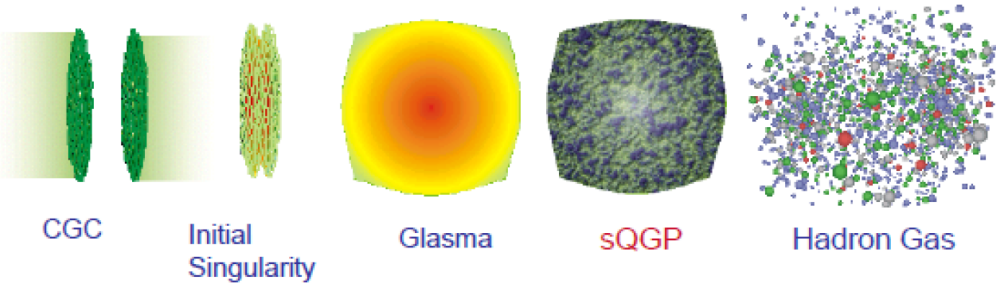


Figure 7: A visualization of successive phases of a heavy ion collision.

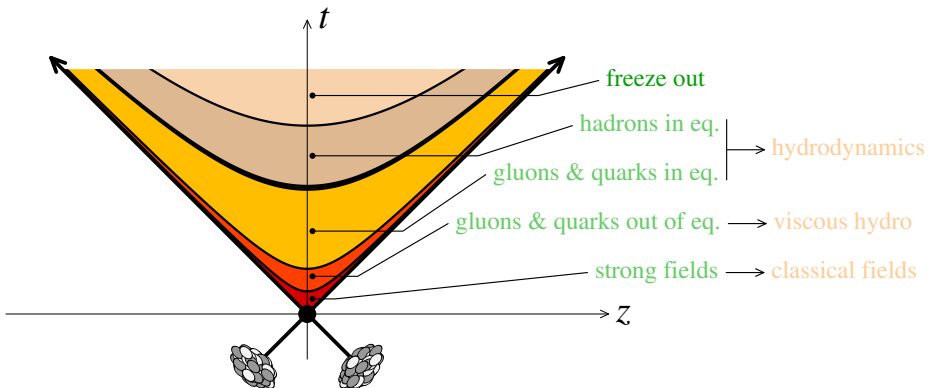


Figure 8: Another view of a heavy ion collision, along with the most widely used approaches to describe each phase.

In low energy hadronic collisions, the three valence quarks of a nucleon, bound by gluons, can temporarily fluctuate into states that have additional gluons and $q\bar{q}$ pairs. These fluctuations are short

lived, with a lifetime being inversely proportional to their energy. The largest possible lifetime of these fluctuations is comparable to the nucleon size. However, in a given reaction that probes a nucleon, there is always a characteristic time scale set by the resolution power of the probe. Only the fluctuations that are longer lived as compared to this characteristic time scale can actually be seen in the process. The shorter lived fluctuations are present but do not affect the reaction. Therefore, in collisions involving a low energy nucleon, only its valence quarks and a few of these fluctuations are visible. Furthermore, for a low energy nucleon, during the collision process there will typically be interactions between its constituents with the probe, thus making the low energy reactions very complicated.

Nonetheless, this picture is being dramatically modified when the reaction involves a high energy nucleon, since in this case the relativistic kinematics comes into action. First, due to Lorentz contraction the nucleon (nucleus) appears almost a two-dimensional sheet in the laboratory frame, like a pancake. Simultaneously, all the internal timescales of the nucleon, in particular the lifetimes of the fluctuations and the duration of interactions among the constituents, are multiplied by the same Lorentz factor. As a consequence of this time dilation, the partons are now unlikely to interact precisely during the time interval probed in the reaction. This results in a picture where the constituents of a high energy nucleon appear to be free during the collision. Second, since the lifetimes of the fluctuations are also dilated, more fluctuations are now visible by the probe. The number of gluons (partons) seen in a reaction increases with the collision energy. This increase has been observed experimentally in Deep Inelastic Scattering (DIS), like at HERA for protons [18] (see Fig. (9)). In the figure, the horizontal axis corresponds to small values of the longitudinal momentum fraction, x , carried by a parton: $x \equiv p_z/\sqrt{s}$, which is a measure of high energy. The other important feature of the parton distributions at small- x (high energy) is that the gluons outnumber all the other parton species³.

When the parton distributions are small, and when a fairly small number of graphs contribute at each order, one can use the tools of perturbation theory. But when the parton distributions increase, processes involving many partons become more and more important, and the computations of these processes in this regime become difficult. And when the gluon occupation number is of order $1/\alpha_s$, an infinite number of graphs contribute at each order. This regime of high parton densities is non-perturbative, even if the coupling constant is weak. The non-perturbative features arise from the fact that the large parton density compensates the smallness of the coupling constant. One needs to accomplish not only the summation of an infinite set of Feynman diagrams but also this situation requires some knowledge about the probability of occurrence of multigluon states in the wavefunctions of two colliding objects, which is not provided by the usual parton distributions (they give information only

³The valence quarks are completely negligible in this kinematical region, and the sea quarks are suppressed by one power of the coupling α_s , since they are produced from the gluons by the splitting process $g \rightarrow q\bar{q}$.

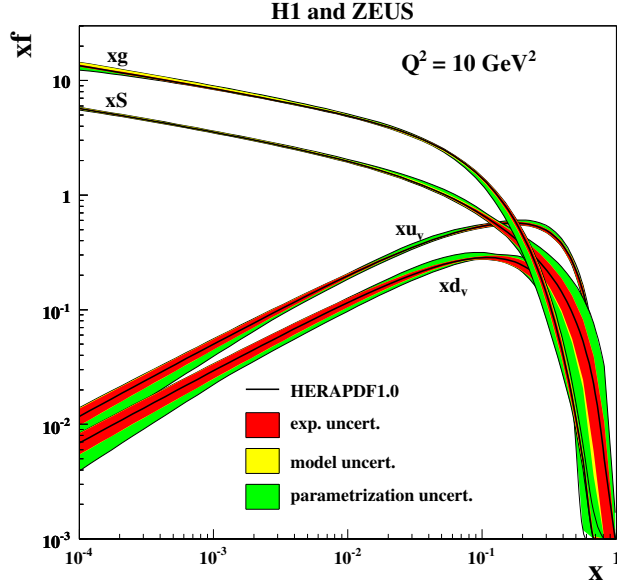


Figure 9: Parton distributions in a proton, measured in Deep Inelastic Scattering at HERA. The figure is from [18].

about the single parton density).

However, the weak coupling methods can be used in this picture too, due to the dynamical generation of a scale that is much larger than the non-perturbative scale Λ_{QCD} . This scale, known as saturation momentum and denoted as Q_s , is due to non-linear interactions among gluons. Roughly speaking, the saturation scale is defined as the coupling constant α_s times the gluon density per unit area (because now we have sheets of gluons in the laboratory frame). Fig. (10) illustrates how the packing of gluons in a proton increases as a function of collision energy. Since the density is very high, the gluons are packed very tightly and thus intrinsically have a small interaction strength via asymptotic freedom in QCD.

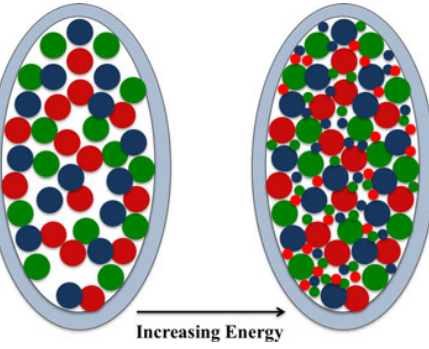


Figure 10: Increasing gluon density within a proton with increasing energy. Quarks are not displayed.

The visualization of the gluon-associated color fields inside a sheet is shown in Fig.(11), where the vectors represent the color electric, \vec{E} , and color magnetic fields, \vec{B} . The vector \hat{z} points along the beam direction (perpendicular to the page) so that all the vectors are orthogonal to one another. The fields have random polarizations and colors.

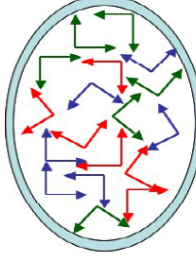


Figure 11: An illustration of the classical color fields inside a color glass sheet.

So if we go from nucleons to nuclei and define gluon density per unit area in a nucleus of mass A to be $xG_A(x, Q^2)/\pi R_A^2$ (where $G_A(x, Q^2) \sim A \cdot G_N(x, Q^2)$), then the saturation momentum will be described by

$$Q_s^2 \sim \frac{\alpha_s \cdot xG_A(x, Q_s^2)}{\pi R_A^2} \sim A^{1/3} \frac{1}{x^{0.3}}, \quad (14)$$

where $A^{1/3}$ is the nuclear enhancement of Q_s . One can think of Q_s as a measure of the strength of gluon recombination processes that may occur when the gluon density becomes large. Any process involving momenta smaller than Q_s may be affected by gluon saturation.

The CGC theory has been developed in order to organize the calculations of processes in the saturation regime. In the expression *Color Glass Condensate*, the meaning of each word is the following:

Color: The gluons are colored objects.

Glass: It corresponds to a disordered state of gluons, where the gluons pile on each other in an amorphous manner. The disorder arises, in part, because of a gluon sheet that is being built as a result of the Lorentz length contraction due to high relative velocity seen by the colliding particles.

Condensate: It refers to the large density of gluons as they pile up due to length contraction, and to a resulting coherence in the wave function of the gluons. The gluon phase space density is high and self-generated.

So the CGC is an effective theory that approximates the description of the fast partons in the wavefunction of a nucleon (nucleus) by exploiting the fact that their dynamics is slowed down by Lorentz time dilation, and provides a way to track the evolution with energy of the multigluon states that are

relevant in the dense parton regime. This ansatz has been applied to a range of reactions at high energies: DIS, proton-nucleus (p+A) collisions and nucleus-nucleus (A+A) collisions.

The evidence for the CGC is based on highly correlated directions of some of the released particles from two million p+Pb collisions observed in the Compact Muon Solenoid (CMS) experiment at the Large Hadron Collider facility [19]. The same behavior between generated particle pairs has been observed in CMS experiments in p+p collisions [20].

1.2.2 Pre-thermal phase: Glasma and bottom-up thermalization scenarios

- **Glasma:** Here we discuss the phase called *Glasma* [17, 21, 22, 23], which is theorized to exist based on the gluon saturation physics. Let us now imagine a case of a relativistic heavy ion collision (or hardronic collision), where two CGC sheets are heading toward each other. In Fig. (12) the classical color electric and color magnetic fields are shown on two color glass sheets before the collision. These fields are frozen in time. The total classical field of one sheet propagating along the light cone $z = \tau$ is superimposed with the total classical field of the other sheet propagating along the light cone $z = -\tau$ to obtain the initial superimposed classical field. This is the description until the collision, in which case one must solve the classical Yang-Mills equations in the forward light cone.

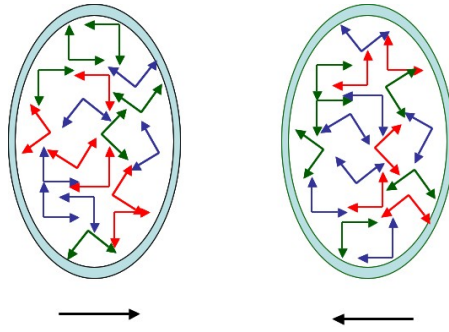


Figure 12: The collision of two color glass sheets.

In Fig. (13) one can see what happens when the color glass sheets pass through one another. An infinitesimal time after the collision, in addition to the transverse fields present in each of the sheets, longitudinal color electric and color magnetic fields will form between them. They form on a very short time scale, and their production is associated with the initial singularity in the high energy limit of the collision. The typical scale of the transverse variation of these fields is the inverse of the saturation momentum, $r \sim 1/Q_s$. These longitudinal fields are produced by the surface color electric and magnetic charges as the color glass sheets pass. The induced charges are equal and opposite on each sheet, and the fields must be treated symmetrically where the Yang-Mills equations are self dual under $\vec{E} \leftrightarrow \vec{B}$. The fields become more disperse as the system expands, and they can be thought of as quanta of gluons when the field strength is sufficiently small. The matter produced in this phase

has different properties than the CGC, due to these longitudinal fields⁴. This phase of matter is in between of the CGC and QGP. This is the Glasma, which eventually evolves into a thermalized QGP. Initially it is very far from local equilibrium. It is in a coherent state rather than in a mixed thermal state, and in the system the initial field configuration has a large negative longitudinal pressure.

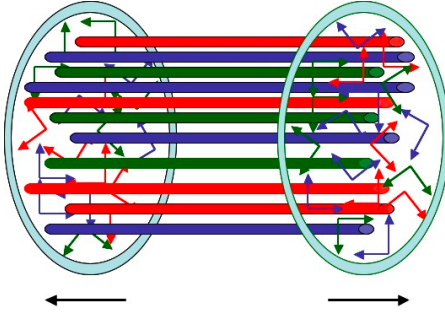


Figure 13: The longitudinal color electric and color magnetic fields making a longitudinal color flux tube in a high energy collision of two color glass sheets.

So in order to be described as quanta of gluons, the classical fields associated with these quanta must be weak. In the Glasma environment, the gluon emission approximately occurs during the time interval $1/Q_s \ll \tau \ll 1/(\alpha_s Q_s)$. The time scale will roughly be $1/Q_s$ since α_s varies logarithmically with Q_s . There is also an intermediate time scale, where the classical solutions to the evolution of a coupled system of fields and gluons may be a good approximation. For a complete treatment, one should have a floating scale, which depends on time. Modes above this floating scale are “hard” gluons, and those below are “soft” ones. The interaction of the hard gluons among themselves is probably not so important during the time interval $1/Q_s \ll \tau \ll 1/(\alpha_s Q_s)$ because the characteristic time scale for hard particles to thermalize by interactions among themselves is of the order of $\tau \sim 1/(\alpha_s^2 Q_s)$ (these interactions involve scattering cross sections). The interaction of the classical fields with themselves is important, and the interaction of the hard fields with the classical fields is also important since the effects of the coupling constant cancel out in the interaction of the hard fields with the coherent fields, which have the strength $\sim 1/\sqrt{\alpha_s}$. The ultimate picture is that the classical fields evaporate into soft gluons in a system of hard gluons, which interact with these classical fields. This system is composed of highly coherent soft gluon fields of very high energy density.

In the Glasma phenomenological framework, the decay of the longitudinal color electric and color magnetic fields may produce two-particle correlations in rapidity. In addition, there may also be angular correlations developed by a combination of effects such as hydrodynamic flow, opacity, or intrinsic angular correlation in the decay of a flux tube [24, 25]. The phenomenon related to such angular and rapidity correlations is referred to as “ridge” since it appears as a structure long ranged

⁴The longitudinal fields are unstable against small perturbations of their initial conditions.

in rapidity but collimated in azimuthal angle. The Glasma phenomenological framework can also be used for calculations of charged particle multiplicity dependence on energy and average transverse momentum. But we will discuss direct photon production in Sec. (1.3.2) within a thermalizing Glasma description.

- **Bottom-up thermalization ansatz:** We know that a very important question in physics of relativistic heavy ion collisions is to understand the thermalization/equilibration. One can investigate it in the framework of perturbative QCD. In order to do so, we can address the bottom-up thermalization scenario [26, 27], which based on recent classical-statistical numerical lattice simulations turns out to be the correct weak coupling effective theory for thermalization in ultrarelativistic heavy ion collisions [28, 29, 30, 31]. The common argument in favor of thermalization is that at larger collision energies, more gluons are liberated in the first moment after a collision, which then collide more frequently with each other. However, the distribution of these gluons is initially very far from thermal equilibrium. In addition, the strong coupling constant decreases at high collision energies, making it more difficult to achieve the thermalization. Whether the system has enough time to thermalize/equilibrate before falling apart is thus not a simple question requiring detailed consideration of different physical processes during this evolutionary phase. In the limit $Q_s \gg \Lambda_{QCD}$ corresponding to very large nuclei and/or very high collision energy, the thermalization occurs relatively fast while the system is still undergoing one-dimensional expansion.

Here are some details on the bottom-up pre-thermalization evolution, which is divided into three temporal stages:

- (i) $Q_s^{-1} \ll \tau \ll Q_s^{-1} \alpha_s^{-3/2}$
- (ii) $Q_s^{-1} \alpha_s^{-3/2} \ll \tau \ll Q_s^{-1} \alpha_s^{-5/2}$
- (iii) $Q_s^{-1} \alpha_s^{-5/2} \ll \tau \ll Q_s^{-1} \alpha_s^{-13/5}$.

In the stage (i), the gluons (i.e. collision-produced primary hard gluons) are highly occupied. The occupation number ranges from $f \sim 1/\alpha_s$ at the earliest time, $\tau \sim Q_s^{-1}$, to unity at $\tau \sim Q_s^{-1} \alpha_s^{-3/2}$. At $\tau \sim Q_s^{-1}$, because of the large occupation number these gluons interact so strongly that it is more appropriate to describe them as a nonlinear gluon field rather than a collection of particles. The density of the hard gluons, n_h , decreases with time due to the one-dimensional expansion. Later on gluons (soft gluons, n_s) with smaller momenta, but still larger than Λ_{QCD} , are being produced. These gluons interact by elastic scatterings at small angles, with exchange momentum $k_s \ll Q_s$. The typical occupation number is large until $Q_s \tau \sim \alpha_s^{-3/2}$, when it becomes of $O(1)$. The occupation number decreases in time as $(Q_s \tau)^{-2/3}$, which is a consequence of broadening of the longitudinal momentum distribution by elastic scatterings amongst the hard gluons. These elastic scatterings modify the typical longitudinal momentum from $p_z \sim 1/\tau$ to $p_z \sim \tau^{-1/3}$. The first bottom-up stage has a transition

boundary between the region occupied by the non-linear classical gluon field and the one at which a description by the Boltzmann equation becomes applicable. In this case the field becomes classical and almost linear, by which one can start describing the gluons as particles on mass shell with a well-defined distribution $(1/\alpha_s) \cdot f(p_T/Q_s)$.

The quantum kinetic dynamics of the bottom-up scenario underlies the dynamics of the stages **(ii)** and **(iii)**, where the occupancy of hard gluons is less than unity. In the stage **(ii)**, the soft gluons are being produced as a result of inelastic scatterings, via processes $hard + hard \rightarrow hard + hard + soft$. They dominate the screening by providing a larger contribution to the Debye mass relative to that of the hard gluons. The typical longitudinal momentum of the hard gluons is $p_z^2 \sim \alpha_s Q_s^2$, which does not depend on the time anymore. The momentum anisotropy saturates at the value of the ratio of longitudinal to transverse pressure $P_L/P_T \sim \alpha_s$. The soft gluons have characteristic momenta estimated to be of the order of $\alpha_s^{1/2} Q_s > \Lambda_{QCD}$ (see Fig. (14)). However, the multiplicity of the soft gluons is still significantly smaller than the multiplicity of the hard gluons. The number of these soft gluons becomes comparable to that of the hard ones at $Q_s \tau \sim \alpha_s^{-5/2}$: $n_s \sim n_h$.

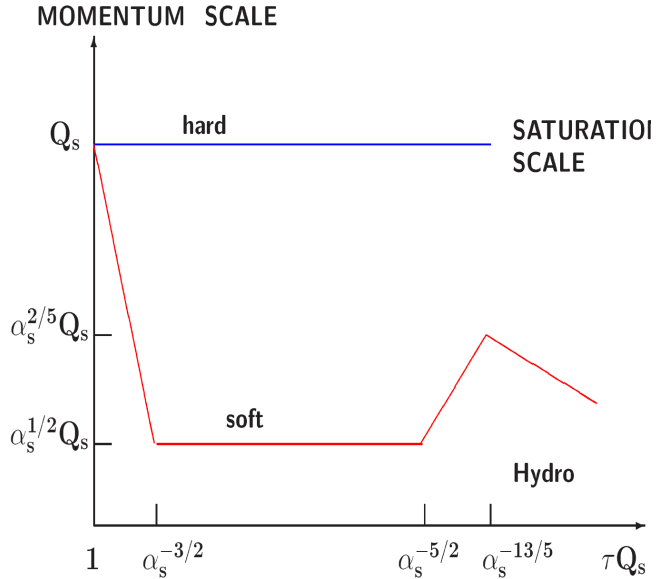


Figure 14: Characteristic momentum scales in the bottom-up thermalization scenario. The figure is from [27].

This is no longer the case by the beginning of the stage **(iii)**, with the soft gluons dominating the multiplicity at $\tau > Q_s^{-1} \alpha_s^{-5/2}$: $n_s \gg n_h$. They achieve thermal equilibration amongst themselves. Although the whole system is still not in thermal equilibrium, its soft modes are characterized by temperature T : $n_s \sim T^3$. The remaining hard gluons collide with the soft ones, and constantly loose energy to the soft gluon thermal heat bath. A hard gluon emits a softer energy gluon, which splits into gluons with comparable momenta. The products of this branching quickly cascade further,

giving all their energy to the thermal heat bath. The soft gluons become completely thermalized at their relaxation time, $\tau > \tau_{\text{rel}}$. Even though the system is expanding, the infusion of energy into the heat bath raises its temperature temporarily to saturate finally at thermalization temperature, $T_{\text{therm}} = c_T c_{\text{eq}} \alpha_s^{2/5} Q_s$, and at thermalization time, $\tau_{\text{therm}} = c_{\text{eq}} \alpha_s^{-13/5} Q_s^{-1}$, where c_T and c_{eq} are constants. Subsequently, the system undergoes hydrodynamical expansion with the temperature of the system cooling down as $T \sim \tau^{-1/3}$.

The bottom-up thermalization scenario has been applied for explanation of charged hadron multiplicities produced in Au+Au collisions at $\sqrt{s_{NN}} = 200 \text{ GeV}$ and in Pb+Pb collisions at $\sqrt{s_{NN}} = 2760 \text{ GeV}$ center of mass energies in [27]. It has also been applied to explanation of direct photon production, which we will discuss in Sec. (1.3.3) within the bottom-up description.

1.2.3 Thermal phase: Quark Gluon Plasma (QGP) and hadronic gas (HG)

- **Quark Gluon Plasma (QGP):** The *Quark Gluon Plasma (QGP)* is a state of QCD matter existing at extremely high temperatures and densities⁵. Some degree of thermalization in heavy ion collisions is already a prerequisite for the QGP formation. The QGP is one of the evolutionary phases of the matter produced in such collisions where it is in thermalized/equilibrated state. It consists of asymptotically free strong-interacting quarks and gluons. Due to the asymptotic freedom, at sufficiently high temperatures, the QGP can be well-described as a free relativistic parton gas that exists in the context of QCD, when the particles have energies much larger than their rest masses. In this case they can be described using relativistic kinematics, in which these energetic particles form a system of a hot relativistic free gas. The number densities of the partons (species i) are then described by the following quantum distribution functions:

$$n_i = \int \frac{d^3 p_i}{(2\pi)^3} \frac{1}{e^{\beta(E_i - \mu_b)} \pm 1}, \quad (15)$$

where $\beta = 1/kT$. The parton energy densities are also described by the same distribution functions:

$$\epsilon_i = \int \frac{d^3 p_i}{(2\pi)^3} \frac{E_i}{e^{\beta(E_i - \mu_b)} \pm 1}, \quad (16)$$

In such an environment, particles and antiparticles can be created and annihilated easily. As a consequence their densities are much larger than their density differences. Therefore the baryon chemical potential, μ_b , can be neglected in Eq. (15) and Eq. (16). In Eq. (15), the sign “−” is for the bosons, and the sign “+” is for the fermions. Integrating over the phase space, we find the following quantities:

⁵For more details on the QGP phase we refer to Refs. [32, 33].

$$\begin{aligned} n_i &= \frac{\zeta(3)}{\pi^2} T^3 && (\text{bosons}), \\ n_i &= \frac{3\zeta(3)}{4\pi^2} T^3 && (\text{fermions}), \end{aligned} \quad (17)$$

and

$$\begin{aligned} \epsilon_i &= \frac{\pi^2}{30} T^4 && (\text{bosons}), \\ \epsilon_i &= \frac{7\pi^2}{8\cdot 30} T^4 && (\text{fermions}), \end{aligned} \quad (18)$$

where $\zeta(3)$ is the Riemann zeta function, $\zeta(3) = 1.2021$, and the fermion energy density is $7/8$ of that of the boson. These expressions are valid for the spin/flavor/electric-charge/color-charge of each particle. However, one should also include separate degeneracy factors for various particles:

$$\epsilon = \sum_i g_i \epsilon_i = g \frac{\pi^2}{30} T^4, \quad (19)$$

where $g = g_B + (7/8)g_F$ with g_B and g_F being the factors for the bosons and fermions, respectively. Each of these degeneracy factors counts the total number of degrees of freedom, summed over the spins, flavors, electric charges (particle and antiparticle) and color charges. When some particle species are thermally decoupled from other species due to the absence of interactions, they no longer contribute to the degeneracy factor.

Thereby, by considering the QGP as a free relativistic parton gas, one can calculate its contribution to the energy density. For a gluon (which is a boson) there are 2 helicity states and 8 colors. Then the total degeneracy factor for the gluon will be $g_B = 2 \times 8 = 16$. For each quark flavor (which is a fermion) there are 3 colors, 2 charges and 2 spin states. At temperatures below $kT \sim 1$ GeV, there are 3 quark flavors, u, d, s . Then the total degeneracy factor for such a quark will be $g_B = 3 \times 2 \times 2 \times 3 = 36^6$. Consequently, the QGP energy density will be represented as

$$\epsilon_{QGP} = \left((2 \times 8) + \frac{7}{8} (3 \times 2 \times 2 \times 3) \right) \frac{\pi^2}{30} T^4 \simeq \frac{47.5\pi^2}{30} T^4. \quad (20)$$

The pressure of the free relativistic parton gas can be calculated just like in the case of black-body radiation:

$$P_{QGP} = \frac{1}{3} \epsilon_{QGP}, \quad (21)$$

which is the equation of state. Also, the entropy density for an isolated system of relativistic particles

⁶If we take into account all the particles of the Standard Model, then the total degeneracy factor is $g = 106.75$.

has the following form:

$$s_{QGP} = \frac{4}{3} \frac{\epsilon_{QGP}}{T}. \quad (22)$$

For this system, the total entropy is expected to be conserved. Ultimately, in the QGP scenario described here we have

number density, $n \propto T^3$; energy density, $\epsilon \propto T^4$; pressure, $P \propto T^4$; entropy density, $s \propto T^3$.

- **Hadronic gas (HG):** During its space-time expansion, the QGP fireball cools down, which then undergoes the phase transition and produces a large amount of hadrons in the *hadronization* phase. The hadronization is a process of formation of hadrons out of quarks and gluons. In the Standard Model they combine with quarks/antiquarks spontaneously produced from the vacuum to form hadrons. The hadronization process is not yet fully understood, but it is modeled and parameterized in a number of phenomenological studies, including various long-range QCD approximation schemes [34].

In this phase, the hadrons subsequently experience frequent inelastic and elastic collisions during the evolution of the hadronic gas (HG). In the HG, after the termination of the inelastic and elastic collisions, the evolving system reaches the states called chemical freeze-out and thermal freeze-out, respectively. The chemical freeze-out temperature, T_{ch} , and the baryon chemical potential, μ_b , can be extracted from the particle yields of various hadrons using statistical models [35, 36], which give uniform T_{ch} and μ_b for all hadrons species. Similarly, hydrodynamic simulations can implement a uniform thermal freeze-out temperature for constructing the freeze-out hyper-surface, which decouples various hadrons from the bulk matter [37]. Microscopically, the related inelastic and elastic scattering processes are different for each hadron species. As a result, the chemical and thermal freeze-out procedures are quite possibly hadron-species dependent.

One can estimate the transition (pseudo-critical) temperature, T_c , by comparing the QGP pressure with that of HG. At temperatures below $kT \sim 1$ GeV, the lightest hadrons are the pions (π^+, π^0, π^-), and we might expect a gas of relativistic pions to exist. This system has only 3 degrees of freedom, $g_\pi = 3$. Its energy density and pressure will be

$$\epsilon_\pi = g_\pi \frac{\pi^2}{30} T^4 = \frac{3\pi^2}{30} T^4, \quad (23)$$

$$P_\pi = \frac{1}{3} \epsilon_\pi = \frac{3\pi^2}{90} T^4. \quad (24)$$

However, the total pressure of the HG is somewhat different because the pions are collective excitations of the non-perturbative QCD vacuum, and this true ground state of the QCD vacuum has a lower energy (denoted as B) than the perturbative QCD vacuum. This low energy B is the origin of the quark confinement in the MIT bag model of hadrons. In the MIT model [38, 39], the hadrons are considered as bags embedded into a non-perturbative QCD vacuum, which is also called physi-

cal or normal QCD vacuum⁷. The energy B is the bag constant. All the non-perturbative physics is included in this universal quantity, which is defined as the energy density difference between the perturbative and physical vacua:

$$\epsilon_{bag} - \epsilon_{vac} \equiv B > 0. \quad (25)$$

The value of B is determined by fits to the masses of physical hadrons: $B_{MIT} = 0.56 \text{ GeV/fm}^3$. Now taking into account that the non-perturbative QCD vacuum has a positive pressure, Eq. (24) will be rewritten as

$$P_\pi = \frac{3\pi^2}{90} T^4 + B. \quad (26)$$

By considering only the three quark flavors for the QGP, one finds P_{QGP} as

$$P_{QGP} = \frac{47.5\pi^2}{90} T^4. \quad (27)$$

Equating the two pressures in Eq. (26) and Eq. (27), we can calculate the transition temperature:

$$T_c = \left(\frac{90B}{44.5\pi^2} \right)^{1/4} \approx 172 \text{ MeV}. \quad (28)$$

For the two quark flavors (u, d) $\rightarrow T_c \approx 184 \text{ MeV}$.

The energy difference (latent heat) between the QGP and HG for the three quark flavors at the transition temperature is

$$\Delta\epsilon = \frac{44.5\pi^2}{30} T^4 + B, \quad (29)$$

which is of the order of 2 GeV/fm^3 . For the two quark flavors $\rightarrow \Delta\epsilon = (34\pi^2/30)T^4 + B$.

1.3 Some mechanisms of direct photon production in heavy ion collisions

1.3.1 Thermal photon puzzle and recent direct photon measurements in A+A collisions

Direct photons, produced during all stages of relativistic heavy ion collisions, are a unique observable to study the fundamental properties and probe the entire space-time evolution of the hot and dense medium produced in these collisions. These photons are defined to be all the produced photons except those not originating from hadronic decays, which occur during the last phase of the evolution. Being produced from almost all known or conjectured phases after a collision, they have long mean free path and escape the collision region basically unmodified with almost no final state interaction. Thereby, the direct photons carry information on the conditions of their production environment at the time when they are produced. In particular, hard (prompt) direct photons, produced in the pre-

⁷One can also think of hadrons as drops of the perturbative phase of QCD immersed into the normal QCD vacuum.

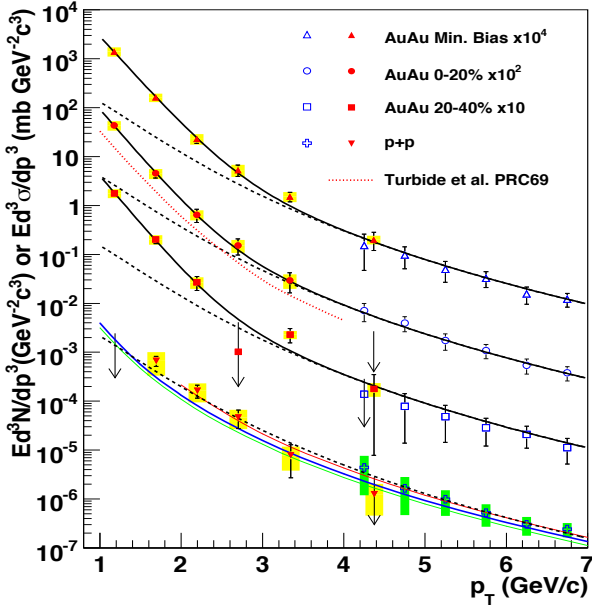


Figure 15: (Color online) The invariant cross section ($p+p$) and the invariant yield ($Au+Au$) of direct photons as a function of p_T . The three curves on the $p+p$ data represent NLO pQCD calculations, and the dashed curves show the power-law fit to the $p+p$ data scaled by the Glauber nuclear overlap function, T_{AA} , for $Au+Au$. The black solid curves are an exponential plus the T_{AA} -scaled $p+p$ fit. The dotted (red) curve near the 0-20 % centrality data is a theory calculation [46]. This figure is from Refs. [40, 41].

equilibrium phase at high- p_T from initial hard scatterings of incoming partons, carry information on parton distributions in colliding nuclei. Thermal direct photons, produced in and after the equilibrium phase at low- p_T from the QGP and HG, provide information about the energy density, temperature and collective motion (azimuthal anisotropy) of the matter. There are also direct photons originating from jet-plasma interactions, and those from jet fragmentation processes.

Although the direct photon measurements are quite challenging especially in the low- p_T region, the PHENIX, STAR and ALICE experimental collaborations have observed thermal yield from $Au+Au$ [40, 41, 42, 43], $Cu+Cu$ [44] at RHIC $\sqrt{s_{NN}} = 200$ GeV and from $Pb+Pb$ collisions [45] at LHC $\sqrt{s_{NN}} = 2760$ GeV center-of-mass energies⁸. The PHENIX 200 GeV and ALICE 2760 GeV direct photon results are shown in Figs. (15) and (16) as well as in Fig. (17).

Generally there are three methods for measuring direct photons. These measurement techniques include measuring i) photons that directly deposit energy into electromagnetic calorimeters; ii) virtual photons that internally convert into e^+e^- pairs, and which allow a clean low- or high- p_T measurement; iii) real photons that externally convert into e^+e^- pairs in a well-selected detector material, which also allow a clean low- or high- p_T measurement. The main challenge is usually related to the measurements with the electromagnetic calorimeters, based on the presence of minimal ionizing particles, a large background of photons from final state hadronic decays, and worsening calorimeter resolution.

In the low- and intermediate- p_T range it has been predicted that the photon yield is enhanced by thermal radiation from the QGP and HG [46]. The yield at $p_T > 4$ GeV/c is found to be consistent with the next-to-leading order perturbative QCD (NLO pQCD) calculations scaled by the number of

⁸We will give details about the PHENIX detector and RHIC facility in Sec. 2.

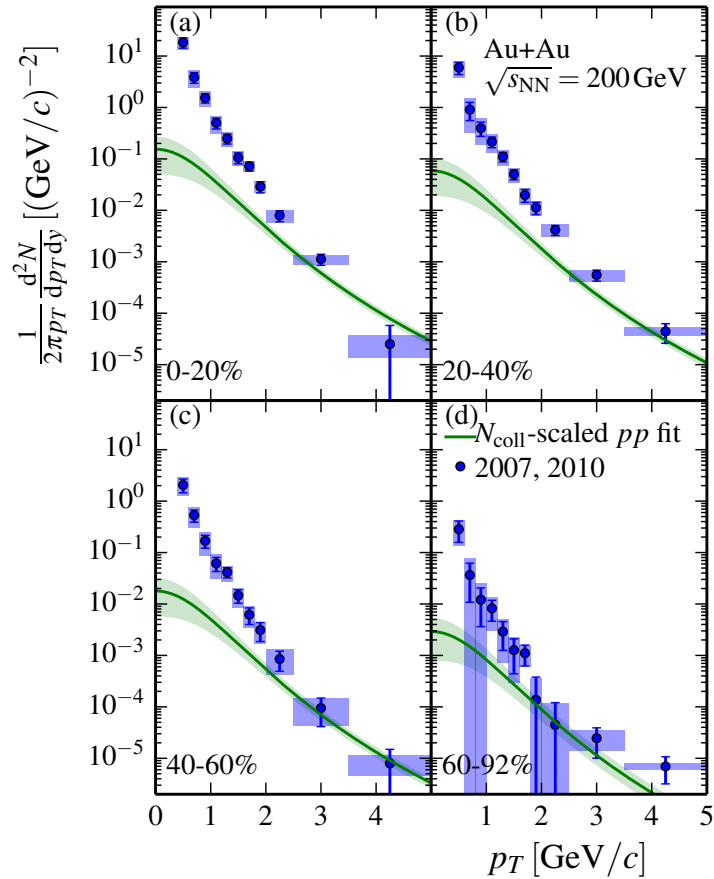


Figure 16: Direct photon p_T spectra in centrality bins 0-20%, 20-40%, 40-60% and 60-92% in Au+Au collisions at $\sqrt{s_{NN}} = 200$ GeV. The error bars (boxes) of the data points are statistical (systematic) uncertainties. Widths of filled boxes indicate the p_T bin widths. The green bands show a N_{coll} scaled modified power-law fit to the PHENIX p+p data and its extrapolation below 1 GeV/c. The figure is from [42].

binary collisions (or by the Glauber nuclear overlap function) at different centralities. Besides, the direct photon yield in p+p collisions [47] is consistent with the NLO pQCD calculations as well. The results in the baseline p+p serve as a crucial reference for results in Au+Au.

Another interesting observable is the azimuthal anisotropy (or elliptic flow) with respect to the collision reaction plane, quantified as v_2 , measured by PHENIX [48] and ALICE [49] recently. The PHENIX and ALICE flow results are shown in Fig. (18) and Fig. (19)⁹. The observed flow is surprisingly large being comparable to that measured for hadrons. In the earliest stages of evolution the yield of thermal photons is expected to be the largest when the temperature of the system is the highest but the flow is the smallest. Then the collective motion builds up over time, and when the photon production occurs at very late stages of the evolution, the collective flow of the system is already fully

⁹In Fig. (18) it is also shown the triangular flow, v_3 , which characterizes the triangular anisotropy of the initial nuclear overlap geometry.

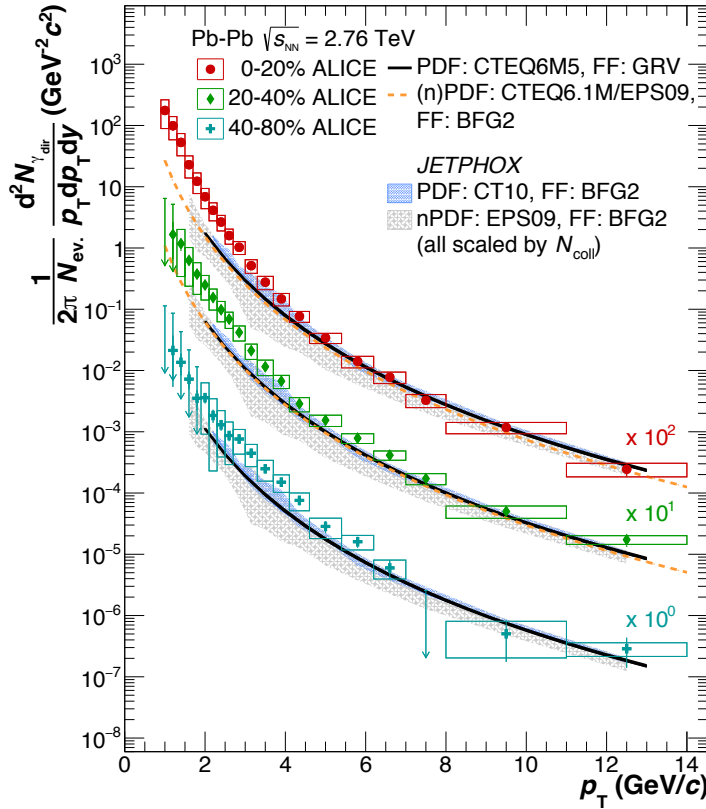


Figure 17: Direct photon p_T spectra in centrality bins 0-20% (scaled by a factor 100), 20-40% (scaled by a factor 10) and 40-80% in Pb+Pb collisions at $\sqrt{s_{NN}} = 2760$ GeV, compared to NLO pQCD predictions for the direct photon yield in p+p collisions at the same energy, scaled by the number of binary nucleon collisions for each centrality bin. The figure is from [45].

developed there, while the temperature is the lowest.

For example, if one compares the measured p_T spectra to theoretical model calculations, the yield based on the hydrodynamic evolution of a system gives a reasonable agreement at initial temperatures: $T_0 \geq 300$ MeV. However, the theoretical models and interpretations encounter difficulties in order to simultaneously describe the observed large yields and large anisotropies by PHENIX and ALICE, which has brought a problem conventionally called as “thermal photon puzzle”. Thus, our current understanding is that the yield results from early times at high temperatures of matter, while the elliptic flow builds up during the hadronic phase when the collective motion of the matter is large but the temperatures are lower.

Various photon production mechanisms, developed in a large amount of theoretical work, exist in the literature for calculating the yields and anisotropies as well as for solving the “thermal photon puzzle”. In particular, there are yield calculations for the preequilibrium and equilibrium phases based on the gluon saturation in the Glasma [50, 51, 52, 53] (see Sec. 1.3.2) and in the bottom-up thermalization scenario [54] (see Sec. 1.3.3) as well as calculations in the late HG [55, 56, 57] (see

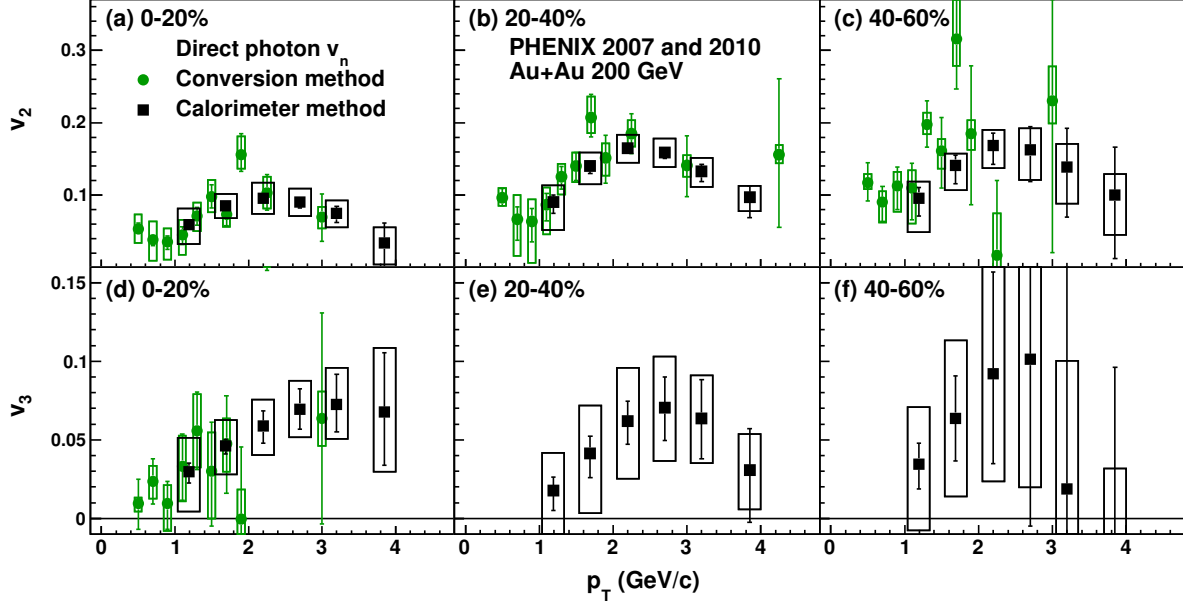


Figure 18: Direct photon v_2 and v_3 in centrality bins 0-20%, 20-40% and 40-60% in Au+Au collisions at $\sqrt{s_{NN}} = 200$ GeV, measured with the conversion method (solid circles, green) and calorimeter method (solid squares, black). The error bars (boxes) of the data points are statistical (systematic) uncertainties. The figure is from [48].

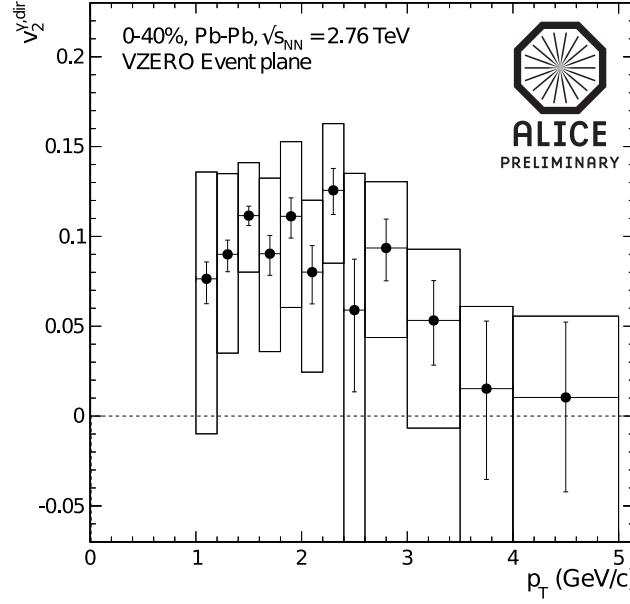


Figure 19: Direct photon v_2 in centrality bins 0-40% in Pb+Pb collisions at $\sqrt{s_{NN}} = 2760$ GeV. The figure is from [49].

Sec. 1.3.4). Some of the yield calculations are based on the elliptic-fireball expansion [58, 59, 60] and hydrodynamic simulations of the fireball evolution [61, 62, 63, 64] (see Sec. 1.3.5). Other results obtained from studies with similar and various other photon production mechanisms can be found in [65, 66, 67, 68, 69, 70, 71, 72, 73, 74, 75, 76, 77, 78, 79, 80, 81, 82].

1.3.2 Pre-thermal and thermal photon production in the thermalizing Glasma phase

In this section we follow the discussion of [50] and show some of its main results (keeping most of its nomenclature), where the first step is made for a parametric estimate of photon production in the thermalizing Glasma (see also [51, 52, 53]), and which is then compared to direct photon data measured in Au+Au collisions at $\sqrt{s_{NN}} = 200$ GeV center-of-mass energy [40, 42].

- The Glasma hypothesis yields a simple and robust estimate for the dependence of photon production on collision centrality as a consequence of geometric scaling of the radiation amplitudes. The direct photon data satisfy such geometric scaling.
- This hypothesis can generate the correct shape of the transverse momentum spectrum.
- The photon elliptic flow [48, 49], while not computable in this current approach, may arise naturally from preequilibrium flow patterns that can be generated in the Glasma, earlier than it is usually assumed with initial conditions for the thermalized QGP. In the Glasma, the quark contribution becomes substantial only until relatively late times of the evolution, thus allowing flow to establish.
- **Some properties of the thermalizing Glasma:** We will concentrate on the time interval $1/Q_{sat} \ll \tau \ll \tau_{therm}$. During this time interval, the quark density increases to a value of the order of the gluon density, and is no longer suppressed. Since electromagnetic particle production ultimately arises from the electric charges of quarks, it is plausible that the production at $\tau_0 \sim 1/Q_s$ might not be important. Further, we will concentrate on transverse momentum and mass scales, where we expect that the effects of the evolution to a thermalized distribution are enhanced. It is assumed that the gluon distribution function is of the form

$$f_g = \frac{\Lambda_s}{\alpha_s p} F_g(p/\Lambda), \quad (30)$$

where p is the gluon momentum. Λ_s is a momentum scale at which the gluons are maximally coherent and is time dependent. At the earliest times $\Lambda_s(\tau_0) \sim Q_s$. Λ is a time dependent ultraviolet cutoff, which at the earliest time coincides with Λ_s , i.e., $\Lambda(\tau_0) = \Lambda_s(\tau_0)$. The scale Λ , however, continuously separates from Λ_s during the course of thermalization, and upon equilibration becomes the initial temperature for the QGP, $\Lambda(t_{therm}) \sim T_{in}$. The soft scale Λ_s , on the other hand, becomes the non-perturbative “magnetic scale” [83, 84] in the thermalized plasma, $\Lambda_s(\tau_{therm}) \sim \alpha_s T_{in}$. The

thermalization is therefore accomplished by splitting parametrically apart these initially overlapping momentum scales by α_s , and the corresponding time is being determined by the following requirement:

$$\Lambda_s(\tau_{therm}) \sim \alpha_s \Lambda(\tau_{therm}). \quad (31)$$

To achieve such a separation, it takes parametrically a long time in the very high energy limit, even at larger RHIC energies.

It was shown in [85, 86] that the time evolution is dominated by the gluon density, and that there may be some fixed asymmetry between the typical transverse and longitudinal momentum scales characterized by a parameter δ' . This parameter δ' is defined in terms of the longitudinal pressure

$$P_L = \delta' \epsilon, \quad (32)$$

where $0 \leq \delta' \leq 1/3$, with $\delta' = 0$ and $\delta' = 1/3$ corresponding to the free-streaming (thus maximal anisotropy between the longitudinal and transverse pressure) and the isotropic expansion, respectively. The time evolution of the scales Λ_s and Λ is found to be

$$\Lambda_s \sim Q_s \left(\frac{\tau_0}{\tau} \right)^{(4+\delta')/7}, \quad (33)$$

and

$$\Lambda \sim Q_s \left(\frac{\tau_0}{\tau} \right)^{(1+2\delta')/7}. \quad (34)$$

This can be translated into the gluon density and the Debye mass such as

$$n_g \sim \frac{Q_s^3}{\alpha_s} \left(\frac{\tau_0}{\tau} \right)^{(6+5\delta')/7}, \quad (35)$$

and

$$M_D^2 \sim Q_s^2 \left(\frac{\tau_0}{\tau} \right)^{(5+3\delta')/7}. \quad (36)$$

The thermalization time is given by

$$\tau_{therm} \sim \tau_0 \left(\frac{1}{\alpha_s} \right)^{7/(3-\delta')}. \quad (37)$$

Finally, to complete the description, we need to have the quark number density, that is

$$f_q = F_q(p/\Lambda), \quad (38)$$

so that the quark number density is

$$n_q \sim \Lambda^3 \quad (39)$$

At the earliest times, $n_q \sim \alpha_s n_g \ll n_g$, but at later times the two densities approach each other, i.e., $n_q \sim n_g$.

- **Photon production from the Glasma:** One can estimate the rate of photon production from the Glasma. Recall that the quark number density, up to an overall constant, is identical to the quark number density in the QGP with the replacement $\Lambda \rightarrow T$. The computations of the rate for photon production at finite temperature are reviewed in Refs. [87, 88]. For thermal emission from a QGP in a fixed box the result is

$$\frac{dN}{d^4x dy d^2p_T} = \frac{\alpha \alpha_s}{2\pi^2} T^2 e^{-E/T} h(E/T), \quad (40)$$

where h is a slowly varying function of E/T of the order of one. The factor of α_s arises from the interaction of quarks with the medium in the photon production process¹⁰. In the Glasma, this is compensated for by the high gluon density $\sim 1/\alpha_s$ associated with the coherence of the Glasma. For Glasma emission we shall use a simplified form of this equation,

$$\frac{dN}{d^4x dy d^2p_T} = \frac{\alpha}{\pi} \Lambda_s \Lambda g(E/\Lambda). \quad (41)$$

Here g is a function of the order of one that cuts off when the photon energy is of the order of the UV cutoff scale Λ . This form follows from dimensional reasoning, and from the fact that the overall rate must be proportional to the electromagnetic coupling. The factor of Λ is analogous to the temperature factor for thermal emission. The factor of Λ_s arises because one of the external legs of the diagram that induces photon emissions couples to a coherent Glasma gluon, and this has a distribution function proportional to Λ_s/α_s . The factor of $g(E/\Lambda)$ occurs because Λ is the largest momentum scale in the problem, and quarks always have a typical momentum scale of the order of Λ . Note that at thermalization when $T \sim \Lambda \sim \Lambda_s/\alpha_s$, Eq. (41) reduces to Eq. (40) for thermal emission.

To obtain the overall photon rate, we need to integrate over longitudinal coordinates. We assume that the early time expansion is purely longitudinal, and that in the integration the space-time rapidity is strongly correlated with the momentum-space rapidity. We then have that

$$\frac{dN}{d^2r_T dy d^2p_T} \sim \alpha \int \tau d\tau \Lambda_s \Lambda g(p_T/\Lambda). \quad (42)$$

Using the result of the previous section for the time dependence of the scales Λ_s and Λ (Eq. (33) and Eq. (34)), we will have

$$\tau d\tau = \kappa' \frac{d\Lambda}{\Lambda} \frac{1}{Q_s^2} \left(\frac{Q_s}{\Lambda} \right)^{14/(1+2\delta')}. \quad (43)$$

¹⁰This formula and the ones that follow are evaluated in the local rest frame of the fluid, and require generalization for use in a boosted frame.

The constant κ' is of the order of 1. Doing the integration over Λ in Eq. (42), we find that

$$\frac{dN}{d^2r_T dy d^2p_T} \sim \alpha \left(\frac{Q_s}{p_T} \right)^{\frac{9-3\delta'}{1+2\delta'}}. \quad (44)$$

Now integrating over d^2r_T , and identifying the overlap cross section as proportional to the number of participants, we finally obtain

$$\frac{dN_\gamma}{dy d^2p_T} = \alpha R_0^2 N_{part}^{2/3} \left(\frac{Q_s}{p_T} \right)^\eta, \quad (45)$$

where $\eta = (9 - 3\delta')/(1 + 2\delta')$. The factor of $N_{part}^{2/3}$ arises because the number of participants in a collision is proportional to the nuclear volume $R^3 \sim N_{part}$. Here R_0 is a constant with dimensions of length. It should be of the order of 1 fm but cannot be determined precisely due to the approximations made. The power of Q_s/p_T ranges from

$$9 \geq \eta \geq 24/5, \quad (46)$$

with two limits $\eta = 9$ and $\eta = 24/5$ corresponding to $\delta' = 0$ (maximal anisotropy) and $\delta' = 1/3$ (isotropic expansion), respectively. Note that in Eq. (45), once the power of p_T is determined from experiment, then given that $Q_s^2 \sim N_{part}^{1/3}$, we have the cross section scaling as $N_{part}^{2/3+\eta/6}$. This is a very rapid dependence on the number of participants.

It is important to note that in the derivation of this result, we have assumed that the largest part of the contribution, when integrating over Λ , does not come from the end points of the integration. If the end points become important, then the physics either from the earliest times (hard processes) or from the thermalized QGP will become important. For the QGP case, the dominant region of integration is $p_T \sim 6T$. The smallest possible value for Λ would be of the order of the QCD transition temperature T_c , and the highest possible value for Λ , for example at RHIC energies, shall be around 1 GeV. These considerations are therefore valid at best for photon production in the range of $1 \text{ GeV} \leq p_T \leq 10 \text{ GeV}$.

• Phenomenology and comparison with direct photon data: Now one can derive a phenomenological formula for estimate of photon production based on Eq. (45) for the photon yield. So the power of Q_s/p_T ranges from $9 \geq \eta \geq 24/5$ (corresponding to $0 < \delta' < 1/3$). For the saturation scale we use the following parameterization:

$$Q_s^2(p_T/\sqrt{s}) = Q_0^2 \left(\frac{\sqrt{s} \times 10^{-3}}{p_T} \right)^\lambda, \quad (47)$$

where λ is a parameter characterizing the growth of the saturation momentum with decreasing x . This parameterization is paralleling that from the analysis for p+p scattering in Ref. [89]. Thereby, Eq. (45)

will be rewritten as

$$\frac{dN_\gamma}{dy d^2p_T} \sim \alpha R_0^2 N_{part}^{2/3} \left(\frac{\sqrt{Q_0^2 (\sqrt{s} \times 10^{-3}/p_T)^\lambda}}{p_T} \right)^\eta \sim \alpha R_0^2 N_{part}^{2/3} \frac{\left(Q_0^2 (\sqrt{s} \times 10^{-3})^\lambda \right)^{\eta/2}}{p_T^{\eta(1+\lambda/2)}}. \quad (48)$$

We can examine the phenomenologically expected range of λ , being in the interval of $0.2 \leq \lambda \leq 0.35$, and find the best fitting results (with data) along with using the η range. Thus, we will use the following phenomenological formula for parameterizing the contribution from the Glasma evolution to the photon production:

$$F(\lambda, \eta) \equiv C_\gamma N_{part}^{2/3} \times \frac{\left[Q_0^2 (\sqrt{s} \times 10^{-3})^\lambda \right]^{\eta/2}}{p_T^{\eta(1+\lambda/2)}}. \quad (49)$$

where the constant coefficient $C_\gamma \propto \alpha R_0^2$ can be determined by fitting at one centrality bin, and then applied to all other centralities. For comparison with data, one also needs to include the photon production from the initial p+p collisions (without any medium effect). Such a production can be described by properly scaled-up contribution from p+p collisions. We use the following power-law function for parameterizing this “trivial” contribution:

$$G = T_{AA} \times \frac{A_{pp}}{(1 + p_T^2/b)^n}, \quad (50)$$

where T_{AA} is the Glauber nuclear overlap function depending on centrality. This part of the total yield has been studied with the parameters determined to be $A_{pp} = 0.0133264 \text{ mb GeV}^{-2}$, $b = 1.5251 \text{ GeV}^2$ and $n = 3.24692$. Then the phenomenological formula for the total photon production will therefore be a sum of the two contributions, $F + G$.

The data we aim to describe is the invariant yield of direct photons [40, 41] from Au+Au collisions for centralities 0-20%, 20-40%, and 0-92% (minimum bias) at $\sqrt{s_{NN}} = 200 \text{ GeV}$ as a function of p_T , measured by the PHENIX collaboration (Fig. 34 of Ref. [41]). The strategy is the following: for given values of λ and η in Eq. (49), we will fix the coefficient C_γ from the fitting for 0-20%, and test how well the formula describes the data at the other two centrality choices. This will provide a critical test of the geometrical scaling properties of the present model. Now we can discuss the various parameters involved in the comparison.

- (1) For the key parameters λ and η in Eq. (49), we test a wide range of choices for $0.2 \leq \lambda \leq 0.35$ and $24/5 \leq \eta \leq 9$. For each specification of λ and η values, we can do the fitting for photon data at the available centralities and evaluate the corresponding $\chi^2/\text{d.o.f.}$, which will allow us to find the regions of λ and η for the best fitting results ($\chi^2/\text{d.o.f}$ stands for chi square per degrees

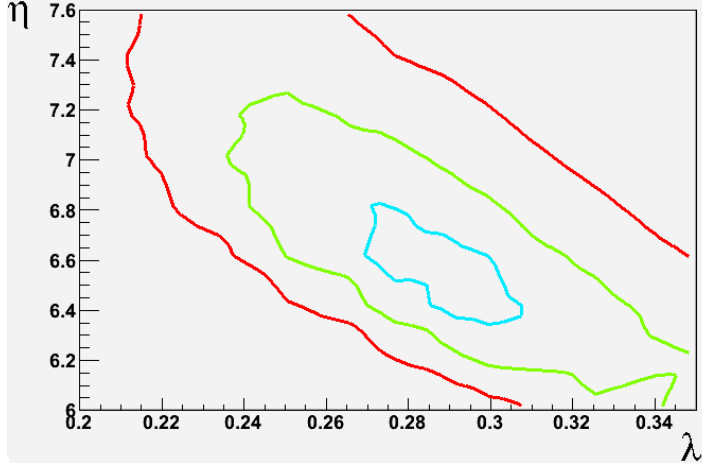


Figure 20: The result from $\chi^2/\text{d.o.f.}$ analysis in the λ - η parameter space for the discussed PHENIX direct photon data in three centrality classes by fitting with the present model, with the blue, green, and red contours indicating 1-, 2-, and 3- σ errors, respectively. The figure is from Ref. [50].

of freedom).

- (2) For N_{part} and T_{AA} , we use the Glauber model calculation from PHENIX for these centralities: $\langle N_{part} \rangle = 279.9$ and $T_{AA} = 18.55 \text{ mb}^{-1}$ at 0-20%; $\langle N_{part} \rangle = 140.4$ and $T_{AA} = 7.065 \text{ mb}^{-1}$ at 20-40%; $\langle N_{part} \rangle = 109.1$ and $T_{AA} = 6.14 \text{ mb}^{-1}$ at 0-92% (minimum bias).
- (3) For the scale Q_0 in Eq. (49), we determine its value at various centralities and beam energies by using the scaling properties $Q_0^2 \propto N_{part}^{1/3}$ and $Q_0^2 \propto (\sqrt{s})^{\lambda/(1+\lambda/2)}$ (see [90, 91] for details), which gives the following values $Q_0^2(0\text{-}20\%)=1.895 \text{ GeV}^2$, $Q_0^2(20\text{-}40\%)=1.490 \text{ GeV}^2$, and $Q_0^2(0\text{-}92\%)=1.384 \text{ GeV}^2$ to be used in our case.

Finally, the fitting results for the photon data are presented in the following. In Fig. 20, we show the result of $\chi^2/\text{d.o.f.}$ in the λ - η parameter space for the PHENIX direct photon data in the three centrality bins under consideration, by plotting the three contours corresponding to 1- σ (blue), 2- σ (green), and 3- σ (red) errors. Based on this analysis, one can identify the best-fitting zone (at about 2- σ level) to be $\lambda = 0.29 \pm 0.05$ and $\eta = 6.65 \pm 0.60$: the latter corresponding to the asymmetry parameter $\delta = 0.144 \pm 0.045$.

Having identified the optimal parameter regime, we now show in Fig. 21 the direct comparison between the data and our model fitted with $\lambda = 0.29$ and $\eta = 6.65 \pm 0.60$. For each centrality bin, the PHENIX data points are compared with: (a) the contribution from only the T_{AA} -scaled p+p yield, i.e. the power-law function in Eq. (50), represented by the black dashed curves; and (b) the full yield including both the T_{AA} -scaled p+p yield and the contribution from the Glasma in Eq. (49), represented by the colorful bands, where the upper and lower boundary curves for each band correspond to the

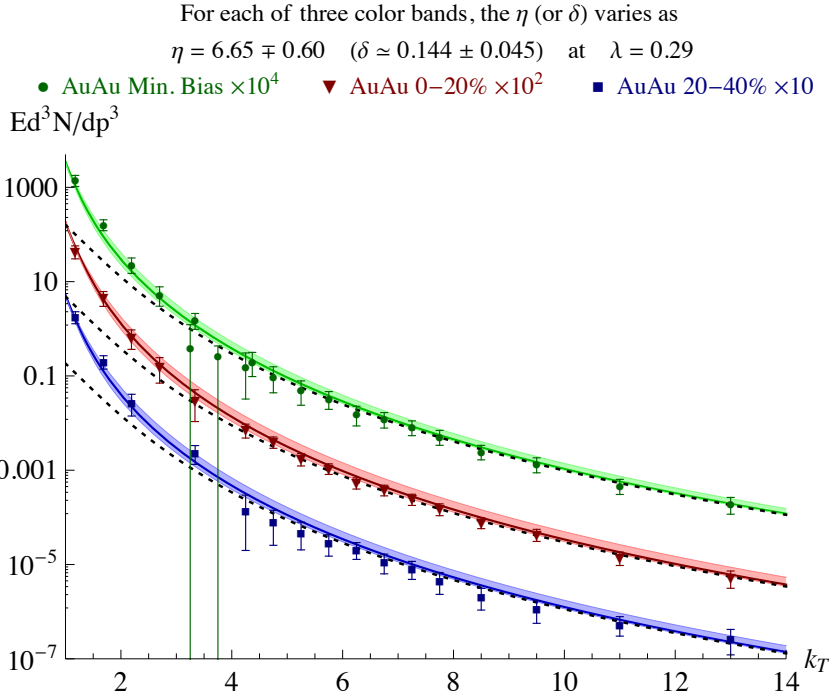


Figure 21: Comparison between the PHENIX direct photon data [40, 41] and the present model with $\lambda = 0.29$ and varied values of η for three centrality bins. The black dashed curves represent the T_{AA} -scaled p+p yield from Eq. (50), and the colorful bands represent the full yield including also the Glasma contribution from Eq. (49) with the upper and lower boundary curves for each band corresponding to the results with the parameter $\eta = 6.05$ and $\eta = 7.25$, respectively (see the text for more details). In the figure $\delta \equiv \delta'$. The figure is from Ref. [50].

results with $\eta = 6.65 - 0.60 = 6.05$ and $\eta = 6.65 + 0.60 = 7.25$, respectively. The plots show good agreement between the PHENIX data and our model fitting at all centralities. The only parameter directly determined from fitting is the overall normalization C_γ in Eq. (49): it has been fixed from the 0-20% case to be $C_\gamma \approx 0.0234 \text{ fm}^2$ and then used in all other centralities. We notice that this value is consistent with the expectation $C_\gamma \sim \alpha R_0^2$, provided $\alpha = 1/137$ and R_0 being of the order of a fm.

A few remarks are in order from the comparison. First, while the very high $p_T > 3 \text{ GeV}$ data are well described by the T_{AA} -scaled p+p yield only, the inclusion of the Glasma contribution is necessary and even dominant for describing the “excess” in the yield, and the p_T -dependence in the softer region at about $1 \text{ GeV} \sim 3 \text{ GeV}$. Second, the fact that the data for varied centralities can be well fitted by one parameter C_γ , fixed at one centrality, provides strong evidence that our model for Glasma photon production has captured the essential geometrical scaling in such data in the relatively lower- p_T region. Last, the comparison implies for the parameter η a preferred region $\eta = 6.65 \pm 0.60$, corresponding to a region $\delta' = 0.144 \pm 0.045$ for the asymmetric parameter δ' in Eq. (32), which appears to indicate a strong anisotropy between longitudinal and transverse scales in the Glasma

evolution.

1.3.3 Pre-thermal and thermal photon production in the bottom-up thermalization scenario

In this section we follow the discussion of [54] and show some of its main results (keeping most of its nomenclature), where a parametric estimate of photon production both in the preequilibrium phase and the thermal QGP phase is accomplished in the bottom-up thermalization ansatz. We will consider the photon production in the three evolutionary temporal stages (plus the thermal QGP phase) of the bottom-up thermalization scenario. These stages were discussed in Sec. (1.2.2).

First we discuss the photon production in the QGP thermal phase. The starting point for computations for the thermal phase is the well-known thermal photon production rate [87, 88], which leads to Eq. (40). In this connection, one can derive a more elaborated form of Eq. (40). The basis of this derivation is the kinetic expression for production of on-shell photons with four-momentum $p = (E, p_1, p_2, p_3)$ at a space-time point $x = (\tau, x^1, x^2, x^3)$ from $2 \leftrightarrow 2$ elastic scattering:

$$E \frac{dN}{d^4x d^3p} = \frac{1}{2(2\pi)^3} \int_{p_1, p_2, p_3} |\mathcal{M}|^2 (2\pi)^4 \delta^4(p_1 + p_2 - p_3 - p) f_1(p_1) f_2(p_2) [1 \pm f_3(p_3)] , \quad (51)$$

where

$$\int_p = \int \frac{d^3p}{(2\pi)^3 2E} , \quad \text{with } p = (E, \vec{p}) \quad (52)$$

The squared amplitude $|\mathcal{M}|^2$ is summed over spins, colors and flavors of all incoming and outgoing particles. For the massless u and d quarks, the amplitude is given in terms of the Mandelstam variables $s = (p_1 + p_2)^2 = (p_3 + p)^2$, $t = (p_1 - p_3)^2 = (p - p_2)^2$ and $u = (p_1 - p)^2 = (p_3 - p_2)^2$:

$$|\mathcal{M}_{\text{an}}|^2 = \frac{160}{9} 16\pi^2 \alpha \alpha_s \frac{u^2 + t^2}{ut} , \quad \text{for the annihilation process} \quad (53)$$

$$|\mathcal{M}_{\text{Comp}}|^2 = \frac{320}{9} 16\pi^2 \alpha \alpha_s \frac{u^2 + s^2}{-us} , \quad \text{for the Compton scattering} \quad (54)$$

where p_1 and p_2 are the four-momenta of the incoming particles, p_3 and p are the four-momenta of the outgoing particles. Because the photons are never in equilibrium in the QGP, Eq. (51) is valid for both equilibrium and non-equilibrium rates as long as the kinetic description is applicable.

For the photon production from a thermal medium, one can make the following approximation:

$$f_1(E_1) f_2(E_2) \simeq e^{-(E_1 + E_2)/T} , \quad (55)$$

which is a good approximation for high-energy photons with $E_1 + E_2 > E \gg T$. For $f_3(E_3)$, one has to keep the Bose-Einstein or the Fermi-Dirac distribution form because in this case E_3 is not necessarily large. Using this simplification, the final formula for the thermal photon production rate

from $2 \leftrightarrow 2$ elastic scattering will be

$$E \frac{dN^{\text{therm}}}{d^4x d^3p} = K \frac{5}{9} \frac{\alpha \alpha_s}{2\pi^2} T^2 e^{-E/T} \log \left(\frac{2.912}{g^2} \frac{E}{T} \right), \quad (56)$$

which as was noted is a more elaborated form of Eq.(40). In the derivation of this expression, the infrared divergence is regulated by the Hard Thermal Loop resummed quark propagator. This rate is leading order (LO) in α and α_s . However, the bremsstrahlung and inelastic pair annihilation processes, which are naively higher order, contribute at parametrically the same order as the $2 \leftrightarrow 2$ elastic scattering processes [92, 93, 94]. For $\alpha_s = 0.2$, the naive LO rate differs from the complete LO rate by a factor of two in the photon momentum range of $2.5 \leq p_T/T \leq 10$. The K factor is introduced in Eq. (56) to approximately take into account these effects ($K \simeq 2$).

Thereby, one can make a parametric estimate of the photon yield in the thermal QGP phase based on the bottom-up picture for the space-time evolution. For simplicity it is assumed that the medium expansion is boost-invariant, and the temperature is a function of proper time, $T \equiv T(\tau)$. Then Eq. (56) can be rewritten as

$$\begin{aligned} \frac{1}{S_T} \frac{dN^{\text{therm}}}{dy d^2p_T} &= K \frac{5}{9} \frac{\alpha \alpha_s}{2\pi^2} \int \tau d\tau \int d\eta T^2 e^{-E/T} \log \left(1 + \frac{2.912}{g^2} \frac{E}{T} \right) \\ &\simeq \frac{5}{9} C \frac{\alpha \alpha_s}{2\pi^2} \int \tau d\tau T^2 \int d\eta e^{-E/T}. \end{aligned} \quad (57)$$

Here S_T is the A+A collision overlap region. In the second line it is assumed that the τ - and η -dependence of the logarithmic factor is slower than other factors, and the logarithmic function $\log(1 + (2.912/g^2)(E/T))$ is replaced by a numerical factor $\log(1 + (2.912/g^2))$, which is denoted by C after being combined with the K -factor:

$$C = K \log \left(1 + \frac{2.912}{g^2} \right). \quad (58)$$

In the Lorentz covariant description, the photon energy should be replaced by $p^\mu u_\mu$, where p^μ is the energy-momentum four-vector and u_μ is the co-moving four-velocity,

$$u_\mu = (\cosh \eta, 0, 0, \sinh \eta). \quad (59)$$

The integration over η can be done analytically,

$$\int_{-\infty}^{\infty} d\eta e^{-p^\mu u_\mu / T} = \int_{-\infty}^{\infty} d\eta e^{-p_T \cosh(\eta - y)/T} = 2 K_0(p_T/T), \quad (60)$$

where $K_n(z)$ is the modified Bessel function of the second kind. Then integrating the yield in Eq. (57)

over the transverse momentum, we further find that

$$\frac{1}{S_T} \frac{dN^{\text{therm}}}{dy} = \frac{10}{9} C \frac{\alpha \alpha_s}{2\pi^2} \int_{\tau_{\text{therm}}}^{\tau_c} \tau d\tau T(\tau)^4, \quad (61)$$

where τ_c is the time when the temperature of the system reaches the pseudo-critical temperature, at which the QGP phase ends up. If we use the τ -dependence of the temperature according to the 1d-Bjorken expansion

$$T(\tau) = T_{\text{therm}} \left(\frac{\tau_{\text{therm}}}{\tau} \right)^{1/3}, \quad (62)$$

(with $T_{\text{therm}} \equiv T(\tau_{\text{therm}})$), and also the bottom-up thermalization time and thermalization temperature

$$\tau_{\text{therm}} \simeq c_{\text{eq}} \alpha_s^{-13/5} Q_s^{-1} \quad \text{and} \quad T_{\text{therm}} \simeq c_T c_{\text{eq}} \alpha_s^{2/5} Q_s, \quad (63)$$

then the final expression for the thermal yield will be the following:

$$\frac{1}{Q_s^2 S_T} \frac{dN^{\text{therm}}}{dy} \simeq \frac{5}{3} c_{\text{eq}}^6 c_T^4 C \frac{\alpha}{2\pi^2} \alpha_s^{-13/5} \left[c_{\text{eq}}^2 c_T^2 \alpha_s^{4/5} \left(\frac{Q_s}{T_c} \right)^2 - 1 \right]. \quad (64)$$

Now one can move on to parametric estimates of photon production in the bottom-up stages **(i)**, **(ii)** and **(iii)**. The stage **(i)** is characterized by the gluon overoccupation. Its typical occupation number is much larger than unity and typical transverse momentum is $\sim Q_s$ (see Sec. (1.2.2)). As it has been found in [28, 29], the gluon distribution function f_g shows a characteristic scaling behavior because of the competition between the effects of the longitudinal expansion and multiple $2 \leftrightarrow 2$ scatterings:

$$f_g(p_T, p_z, \tau) = (Q_s \tau)^{-2/3} f_S(p_T, (Q_s \tau)^{1/3} p_z), \quad (65)$$

where f_S is a scaling function. One can fix the overall normalization of f_S by making use of the results of classical Yang-Mills simulations with the CGC initial condition [95, 96]. As regards the quark distribution function f_q , it satisfies the same scaling law as the gluon distribution for typical momenta [97]. The reason is that the quark-gluon scatterings are Bose-enhanced in a similar way, which happens for the gluon-gluon scatterings.

By considering the Compton scatterings and annihilation processes as well as utilizing the small-angle approximation [98] (which dominates the $2 \leftrightarrow 2$ scattering of energetic partons), one can write down the photon production rate as

$$E \frac{dN}{d^4x d^3p} = \frac{40}{9\pi^2} \alpha \alpha_s \mathcal{L}_C f_q(\vec{p}) \int \frac{d^3p'}{(2\pi)^3} \frac{1}{p'} [f_g(\vec{p}') + f_q(\vec{p}')] . \quad (66)$$

The symbol \mathcal{L}_C is the Coulomb logarithm: $\mathcal{L}_C = \int dq/q$, which should be regularized by infrared and

ultraviolet cutoffs. It is set to be $\mathcal{L}_C = 0.5 \log(1 + (2.9/g^2))$ so that the small-angle approximation reproduces the known formula for the thermal photon yield.

By doing all necessary momentum integrations of the single particle distribution functions, the photon yield in the bottom-up stage **(i)** will be

$$\begin{aligned} \frac{1}{Q_s^2 S_T} \frac{dN^{(i)}}{dy} &= \frac{40}{9\pi} \frac{\alpha}{2\pi^2} \mathcal{L}_C \kappa_g \kappa_q \int_{\tau_0}^{\tau_1} d\tau \tau^{-1} \\ &= \frac{40}{9\pi} \frac{\alpha}{2\pi^2} \mathcal{L}_C \kappa_g \kappa_q \log \alpha_s^{-3/2}, \end{aligned} \quad (67)$$

where one should use $\tau_0 \sim Q_s^{-1}$ and $\tau_1 \sim Q_s^{-1} \alpha_s^{-3/2}$. The constants κ_g and κ_q are given as $\kappa_g = c/2N_c$ and $\kappa_q = c/2N_c$, where c is the gluon liberation coefficient¹¹. One can take it as $c = 1.1$ from solutions of the boost-invariant classical Yang-Mills equations [96]. Thus, Eq. (67) gives a good estimate of the non-equilibrium photon yield in the very early phase of the bottom-up evolution, described by the stage **(i)** of this scenario.

In the stage **(ii)**, the hard gluon typical occupancy is less than unity, which decreases as $f \sim \alpha_s^{-3/2}/(Q_s \tau)$. The Debye screening mass is dominated by the soft gluons, though the total particle number is still dominated by the hard gluons. The behavior of the Debye mass is like $m_D \sim \alpha_s^{3/8} Q_s (Q_s \tau)^{-1/4}$. Nonetheless, the photon yield from the stage **(ii)** can be estimated in the same way as from the stage **(i)**. But the momentum integral of the gluon distribution will be dominated by the soft gluons from number-changing inelastic processes. The final formula for the photon yield in this non-equilibrium phase, described by the stage **(ii)** of the bottom-up scenario is

$$\frac{1}{Q_s^2 S_T} \frac{dN^{(ii)}}{dy} \simeq \frac{80}{9\pi} \frac{\alpha}{2\pi^2} \mathcal{L} \kappa_q \kappa_q (\alpha_s^{-1/2} - 1). \quad (68)$$

In the weak coupling limit this yield is much larger than the photon yield coming out from the bottom-up stage **(i)** given in Eq. (67).

In the stage **(iii)** the matter is in equilibrium. The soft gluons create a thermal bath because they have a short relaxation time compared with the typical time scale of the system. The remaining hard gluons subsequently lose their energy to this thermal bath by a turbulent bremsstrahlung process, and the thermal bath in turn is being heated up. The yield of photons radiated from the soft gluon thermal bath can be estimated from the thermal rate in Eq. (61), by replacing τ_{therm} by $\tau_2 = c_2 Q_s^{-1} \alpha_s^{-5/2}$ and τ_c by $\tau_{\text{therm}} = c_{\text{eq}} Q_s^{-1} \alpha_s^{-13/5}$:

¹¹The gluon liberation coefficient is a constant that links the number of gluons in the nucleus wave function to the number of gluons freed during a heavy ion collision.

$$\begin{aligned} \frac{1}{Q_s^2 S_T} \frac{dN^{(iii)}}{dy} &= \frac{10 \alpha \alpha_s}{9 2\pi^2} C Q_s^{-2} \int_{\tau_2}^{\tau_{\text{therm}}} \tau T(\tau)^4 d\tau \\ &\simeq \frac{5}{27} \frac{\alpha}{2\pi^2} c_{\text{eq}}^6 c_T^4 C \left[\alpha_s^{-13/5} - \left(\frac{c_2}{c_{\text{eq}}} \right)^6 \alpha_s^{-2} \right]. \end{aligned} \quad (69)$$

Since the temperature of the thermal bath increases in time [26, 27] as

$$T(\tau) = c_T \alpha_s^3 Q_s^2 \tau, \quad (70)$$

the photon yield will be dominated by $\tau \sim \tau_{\text{therm}}$. The ratio c_2/c_{eq} is of the order of unity. In the limit of weak coupling the second term in Eq. (69) is negligible compared to the first term.

Thus, the bottom-up photon yield from the thermal QGP phase is given by Eq. (57), while the bottom-up photon yields from the stages **(i)**, **(ii)** and **(iii)** are given in Eqs. (67), (68) and (69), respectively. Fig. 22 shows the comparison between the summed up photon yields (**(i)+(ii)+(iii)**) in the bottom-up thermalization scenario, and the yield in a “hydro” scenario plus the thermal QGP yield, where by “hydro” it is understood the thermal yield from Eq. (57) extended to early times τ_0 (basically integrated from τ_0 to τ_c).

1.3.4 Thermal photon production from the hadronic phase based upon a spectral function approach within a hydrodynamical description

In this section let us follow the discussion of [57] and show some of its main results (keeping its nomenclature), where the invariant yield of direct photons and the elliptic flow v_2 are obtained based on the photon rates derived from the spectral function and density expansion approach. The photon rates are calculated in the hardonic phase. The partonic photon rates from the QGP phase are used from other studies as well. If the hadrons thermalize with pions and nucleons as the only strongly stable constituents, then one can consider the photon production processes by expanding them not in terms of processes but rather in terms of final hadronic states. The hadronic photon rates are worked out in terms of chiral reduction formulas, where the rates are related to vacuum correlation functions [55, 56].

For a HG (hadronic gas) in thermal equilibrium the number of photons, produced per unit four-volume and unit three-momentum, is tied to the electromagnetic current-current correlation function:

$$\frac{q^0 dN_\gamma}{d^4 x d^3 q} = -\frac{\alpha}{4\pi^2} \frac{2}{1 + e^{q_0/T}} \text{Im}\mathbf{W}(q), \quad (71)$$

with $q^2 = 0$ and

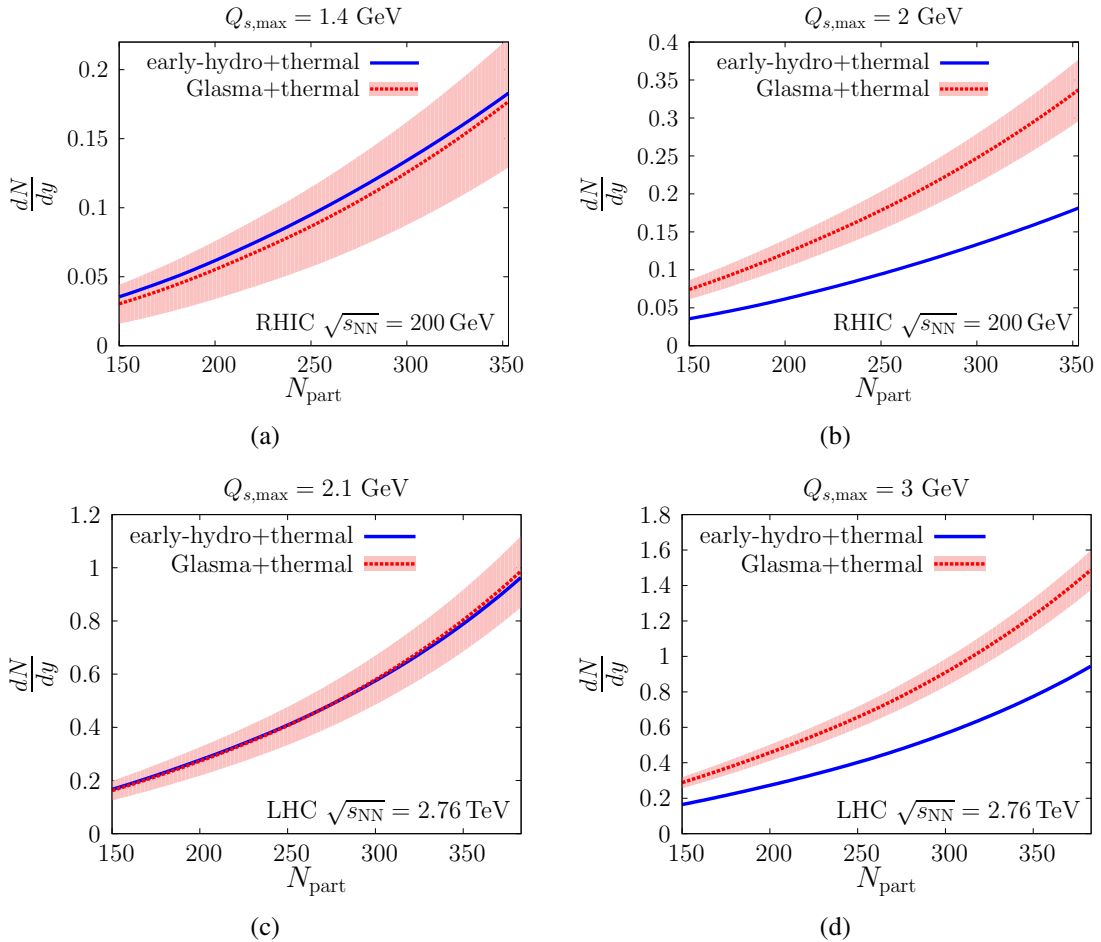


Figure 22: The comparison between the total photon yield ((i)+(ii)+(iii)) in the bottom-up thermalization scenario (named as Glasma), and the yield in a “hydro” scenario (that assumes early thermalization) plus the thermal QGP yield. Top: The normalization of the saturation scale Q_s is chosen such that its values in Au+Au 0-5% collisions at RHIC $\sqrt{s_{NN}}=200$ GeV are 1.4 GeV and 2 GeV. Bottom: The normalization of Q_s is chosen such that its values in Pb+Pb 0-5% collisions at LHC $\sqrt{s_{NN}}=2760$ GeV is 2.1 GeV and 3 GeV. The red color bands denote the uncertainty for the bottom-up total photon yield corresponding to the variation of $c_{eq} = 0.1\text{--}0.4$ (bottom edge of band to top edge). The red dashed lines correspond to $c_T = 0.18$. This figure is from Ref. [54].

$$\mathbf{W}(q) = \int d^4x e^{-iq\cdot x} \text{Tr}\left(e^{-(\mathbf{H}-F)/T} \mathbf{J}^\mu(x) \mathbf{J}_\mu(0)\right). \quad (72)$$

Here \mathbf{J}_μ is the hadronic part of the electromagnetic current, \mathbf{H} is the hadronic Hamiltonian and F is the free energy. The trace $\text{Tr}(\dots)$ is over a complete set of stable hadronic states, e.g., pions and nucleons, for temperatures below the pseudocritical T_c . The correlator in Eq. (72) can be expanded in terms of final pion states at finite temperature and zero baryon chemical potential:

$$\mathbf{W}^F(q) = \mathbf{W}_{0\pi} + \int d\pi_1 \mathbf{W}_{1\pi} + \frac{1}{2!} \int d\pi_1 d\pi_2 \mathbf{W}_{2\pi} + \dots, \quad (73)$$

along with the pion thermal phase space factors included:

$$d\pi_i = \frac{d^3 k_i}{(2\pi)^3} \frac{n(E_i)}{2E_i}. \quad (74)$$

The general expression for $\mathbf{W}_{n\pi}$ is

$$\mathbf{W}_{n\pi} = i \int d^4x e^{iq \cdot x} \langle \pi^{a_1}(k_1) \dots \pi^{a_n}(k_n) | T^* \mathbf{J}^\mu(x) \mathbf{J}_\mu(0) | \pi^{a_1}(k_1) \dots \pi^{a_n}(k_n) \rangle, \quad (75)$$

with the sum over isospin subsumed.

The first contribution in Eq. (73) is dominated by the transverse part of the isovector correlator, and is entirely fixed experimentally by the measured electroproduction data. It vanishes for real photons, i.e., $\mathbf{W}_{0\pi} = 0$ since the heat bath is stable against spontaneous photon radiation. The other two terms, $\mathbf{W}_{1\pi}$ and $\mathbf{W}_{2\pi}$, can be reduced to measurable vacuum correlators [55, 56]:

$$\begin{aligned} \mathbf{W}_{1\pi}^F(q, k) &= \frac{12}{f_\pi^2} q^2 \text{Im}\Pi_V(q^2) \\ &- \frac{6}{f_\pi^2} (k+q)^2 \text{Im}\Pi_A((k+q)^2) + (q \rightarrow -q) \\ &+ \frac{8}{f_\pi^2} ((k \cdot q)^2 - m_\pi^2 q^2) \text{Im}\Pi_V(q^2) \times \text{Re}\Delta_R(k+q) + (q \rightarrow -q), \end{aligned} \quad (76)$$

where $\text{Re}\Delta_R$ is the real part of the retarded pion propagator, and Π_V and Π_A are the transverse parts of the VV and AA correlators. Their spectral functions are related to both e^+e^- annihilation and τ -decay data. The two-pion reduced contribution $\mathbf{W}_{2\pi}$ is more involved, which can be found in the above references.

Thus, all these one- and two-pion contributions give the photon rates from the pion HG, without pion chemical potential and with zero baryon chemical potential. The two-pion contribution $W_{2\pi}$, which includes $\pi\pi \rightarrow \rho\gamma$ and $\rho \rightarrow \pi\pi\gamma$ processes, dominates at low q_0 . As regards the partonic photon rates from the QGP phase, the focus here is on using the QGP photon rates in QCD both at leading [99] and next-to-leading order [100]. A complete leading order photon emission requires the inclusion of two-loop diagrams corresponding to the annihilation $q + \bar{q} \rightarrow \gamma$ and Compton $g + q(\bar{q}) \rightarrow q(\bar{q}) + \gamma$ processes as well as the inclusion of collinear bremsstrahlung and inelastic pair annihilations with their subsequent suppression through the LPM (Landau-Migdal-Pomeranchuk) effect. The photon rates with these NLO QCD calculations are referred to as the resummed QGP (AMY) rates.

Ultimately, the hadronic and partonic rates are convoluted with the time-evolution history of the fireball from inception at about 1/2 fm/c to thermal freezeout at about 10 fm/c to 15 fm/c, depending on the collision energy of heavy ions. The final evolved rates are then folded with the PHENIX and ALICE detector acceptances to compare with the corresponding experimental direct photon data by

means of hydrodynamic simulations of the evolution of the QGP and hadronic phases. The results and comparisons with the direct photon data from the PHENIX [40, 42] and ALICE [45] collaborations are shown in Fig. (23).

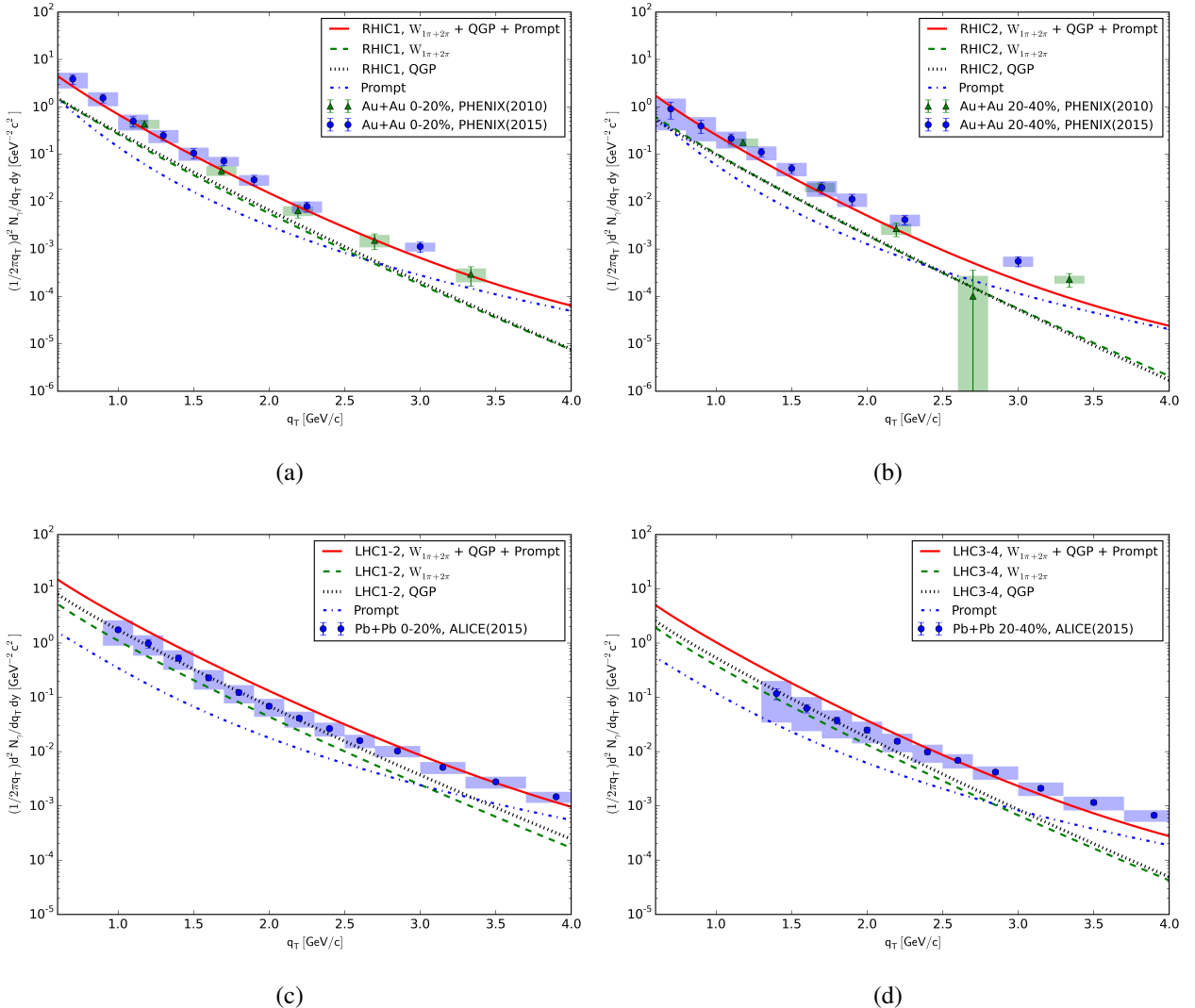


Figure 23: Direct photon spectra for PHENIX [40, 42] at $\sqrt{s_{NN}} = 200 \text{ GeV}$ in Au+Au centrality bins 0-20% (23(a)) and 20-40% (23(b)) as well as for ALICE [45] at $\sqrt{s_{NN}} = 2.76 \text{ TeV}$ in Pb+Pb centrality bins 0-20% (23(c)) and 20-40% (23(d)). One can see the sum of one- and two-pion contributions from the hadronic phase plus also the contributions from the prompt photons and from the QGP phase. The curves are obtained with different hydrodynamical parameters, which depend on the center-of-mass energy and centrality of the colliding systems. These plots are from [57].

We also wish to show the results on direct photon elliptic flow. Here the anisotropy calculations are fulfilled by using the distribution of the emitted photons, which follow from the integrated space-

time hydrodynamically evolved emission rates within the freeze-out volume:

$$\frac{d^3 N_\gamma}{q_T dq_T dy d\phi}(q_T, y, \phi) = \int_{\tau_0}^{\tau_{f,o}} \tau d\tau \int_{-\infty}^{\infty} d\eta \int_0^{r_{\max}} r dr \int_0^{2\pi} d\theta \left[q^0 \frac{dR_\gamma}{d^3 q}(q = \vec{q} \cdot \vec{u}; T, \mu_B, \mu_\pi) \right] \Theta(T > T_f), \quad (77)$$

where $R_\gamma \equiv dN_\gamma/d^4x$ is the photon production rate, i.e., the number of direct photons per unit four-volume in the local rest frame of the fireball. The elliptic flow and higher harmonics $v_n(q_T, y)$ in each event follow by expanding Eq. (77) in Fourier components. In general the Fourier series require amplitudes and phases (or sines and cosines), such as

$$\frac{d^3 N_\gamma}{q_T dq_T dy d\phi} = \frac{1}{2\pi} \frac{d^2 N_\gamma}{q_T dq_T dy} \left(1 + \sum_{n=1}^{\infty} v_{n\gamma}(q_T, y) e^{in(\phi - \Psi_{n\gamma}(q_T, y))} \right) + \text{c.c.}, \quad (78)$$

where c.c. denotes complex conjugation. The amplitude $v_{n\gamma}(q_T, y)$ is real and positive semi-definite, and the phase is real. The “photon elliptic flow” is the event-averaged correlation between the photon yield and integrated charged hadron yields, which define the n -th order reaction plane (see Sec. 2.3.4 for the definition of the reaction plane). Without going into more details we wish to show the simulation results and comparison with the elliptic flow data from PHENIX [48] and ALICE [49], shown in Fig. (24). The “thermal photon puzzle” is well visualized when we look at Fig. (23) and Fig. (24). The simultaneous description of the data becomes challenging since the shown photon elliptic flows are overall lower than the ones reported by both the PHENIX and ALICE collaborations.

1.3.5 Photon production based upon thermal fireball and hydrodynamical models

In this section we show some of the principal results from [60] and [63]. We will see other results on calculations of direct photons spectra, and elliptic flow and their comparisons with the data.

- **Direct photon spectra and elliptic flow based upon the expanding fireball and ideal hydrodynamics [60]:** The starting point is the differential emission rate of photons per unit phase space from a strongly interacting medium of temperature T and baryon-chemical potential μ_B :

$$q_0 \frac{dN_\gamma}{d^4 x d^3 q} = -\frac{\alpha}{\pi^2} f^B(q_0; T) \times \text{Im}\Pi_{\text{EM}}^T(q_0 = q; \mu_B, T), \quad (79)$$

where f^B is the thermal Bose distribution function, Π_{EM}^T is the electromagnetic current correlator, and $q_0 = q$ denotes the energy and three-momentum of the photon in the local rest frame of the medium. In order to get the thermal photon spectrum, this rate should be integrated over the entire four-volume of the reaction, $V_4 = \int d^4x$, accounting for the local temperature and collective expansion velocity of the emission point. It is done in two different models: i) in a schematic blast-wave type fireball and ii) in ideal hydrodynamics. Both models are based on the same equation of state and fit to the

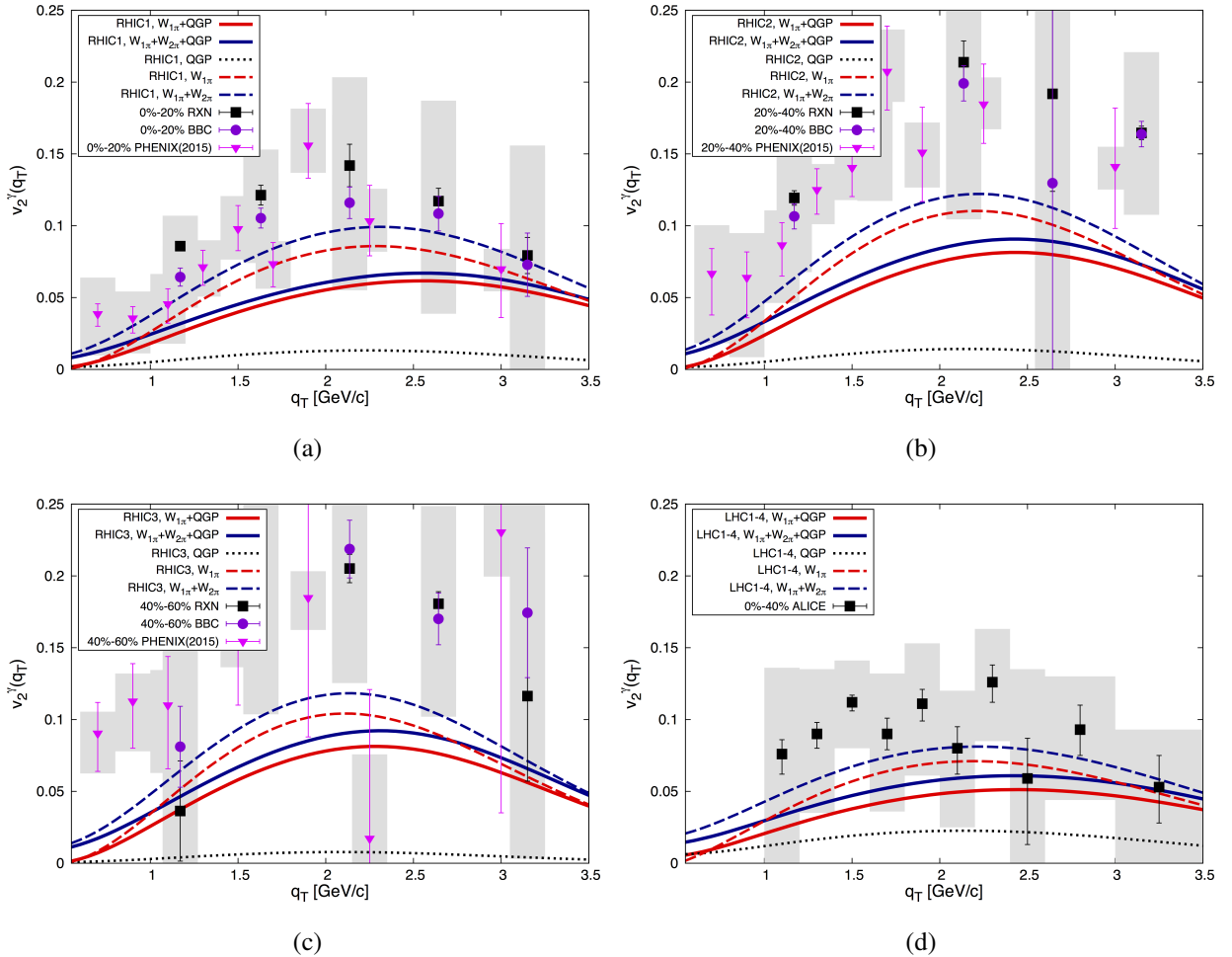


Figure 24: Direct photon elliptic flow v_2 for PHENIX [48] at $\sqrt{s_{NN}} = 200$ GeV in Au+Au centrality bins 0-20% (24(a)), 20-40% (24(b)) and 40-60% (24(c)) as well as for ALICE [49] at $\sqrt{s_{NN}} = 2.76$ TeV in Pb+Pb centrality bin 0-40% (24(d)). These plots are from [57].

same set of bulk-hadron observables. The QGP and hadronic thermal emission rates are taken from the literature.

The thermal fireball model is based on an isotropically expanding cylinder. Initially, as it was used by Ralf Rapp and his collaborators, the volume expansion could be approximated by a cylindrical geometry, by employing two fire-cylinders expanding in $\pm z$ direction. Depending on parameters, this geometry can interpolate between 1d and 3d expansions. Then the description of the space-time evolution of central and semi-central A+A collisions can be approximated by an expanding thermal fireball characterized by a time-dependent cylindrical volume. In the case of relativistic expansion the cylindrical volume is

$$V_{FB}(\tau) = \pi \left(r_{T,0} + \left(\frac{(1 + a_T^2 \tau^2)^{1/2} - 1}{a_T} \right) \right)^2 \left(z_0 + v_{L,0} \tau + \frac{1}{2} a_L \tau^2 \right), \quad (80)$$

where the effects due to finite ellipticity are neglected. In [58, 59, 60] (and references therein) one can find the values of the transverse size, $r_{T,0}$, initial longitudinal size, z_0 , initial longitudinal velocity $v_{L,0}$, longitudinal a_L and transverse a_T accelerations. z_0 controls the formation time of the thermal medium. In this case if we assume a constant total entropy, S_{tot} , of the fireball at a given collision centrality (fixed by the observed number of charged particles), then the time evolution of the entropy density is given by $s(t) = S_{\text{tot}}/V_{\text{FB}}(t)$. In the calculations the values for the pseudo-critical temperature, $T_c = 170 \text{ MeV}$, and for the chemical freezeout, $T_{\text{ch}} = 160 \text{ MeV}$, are used at both RHIC and LHC energies. Also, along with the fireball model, ideal hydrodynamical calculations are accomplished from a hydrodynamical model described in detail in Ref. [101], which is based on the 2+1-dimensional ideal hydro code of Ref. [102]. Both fireball and ideal hydro evolution models identify the transition region around T_c as a key domain for the thermal photon emission. The results and

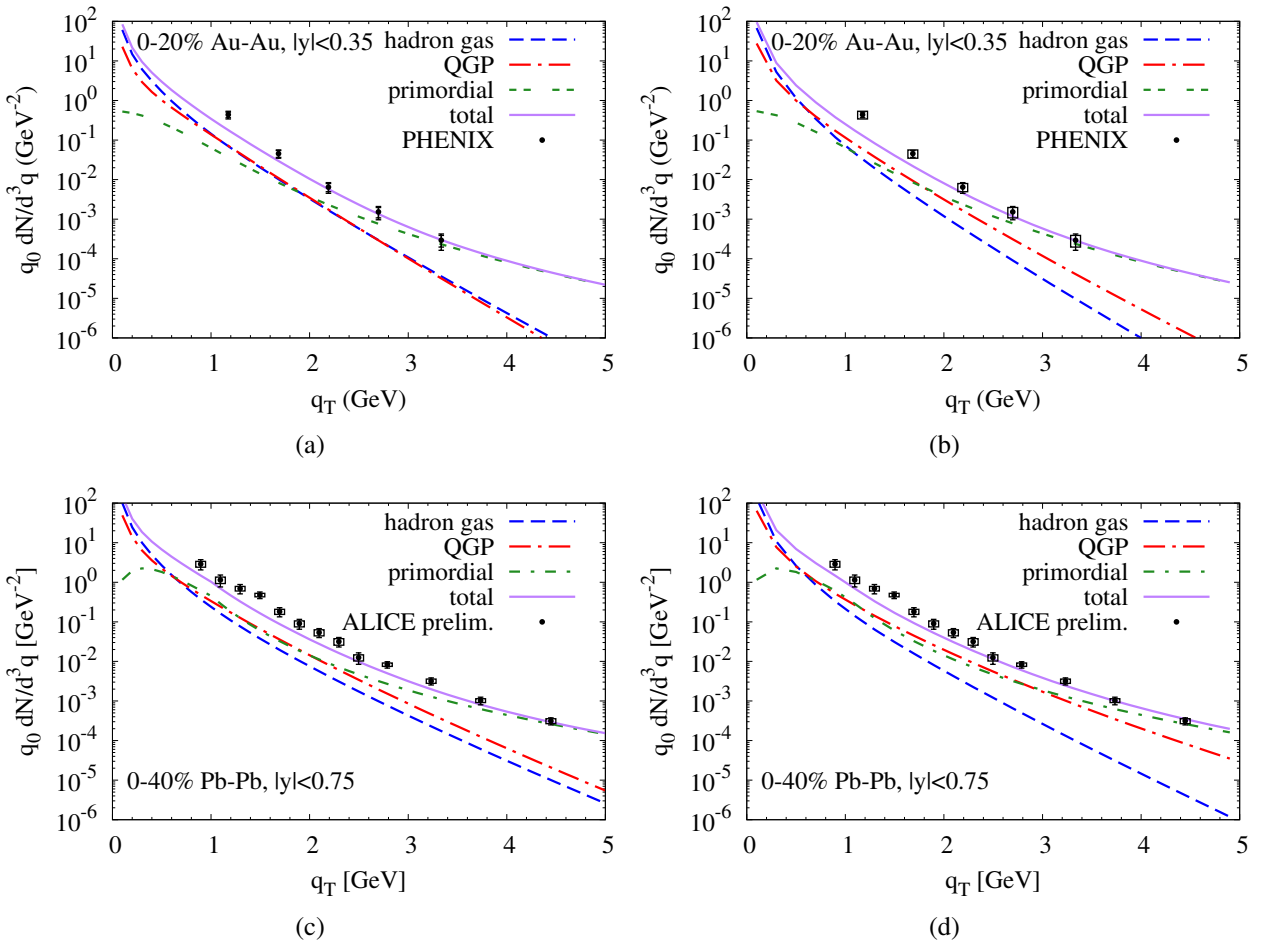


Figure 25: Direct photon spectra for PHENIX [40] at $\sqrt{s_{NN}} = 200 \text{ GeV}$ in Au+Au centrality bin 0-20% (25(a)) using the expanding fireball and 0-20% (25(b)) using the ideal hydrodynamics as well as for ALICE [45] at $\sqrt{s_{NN}} = 2.76 \text{ TeV}$ in Pb+Pb centrality bin 0-40% (25(c)) using the expanding fireball and 0-40% (25(d)) using the ideal hydrodynamics. The plots are from [60].

comparisons with the direct photon data from PHENIX [40] and ALICE [45] are shown in Fig. (25). Besides, the results and comparisons with the elliptic flow data from PHENIX [48] and ALICE [49] are shown in Fig. (26).

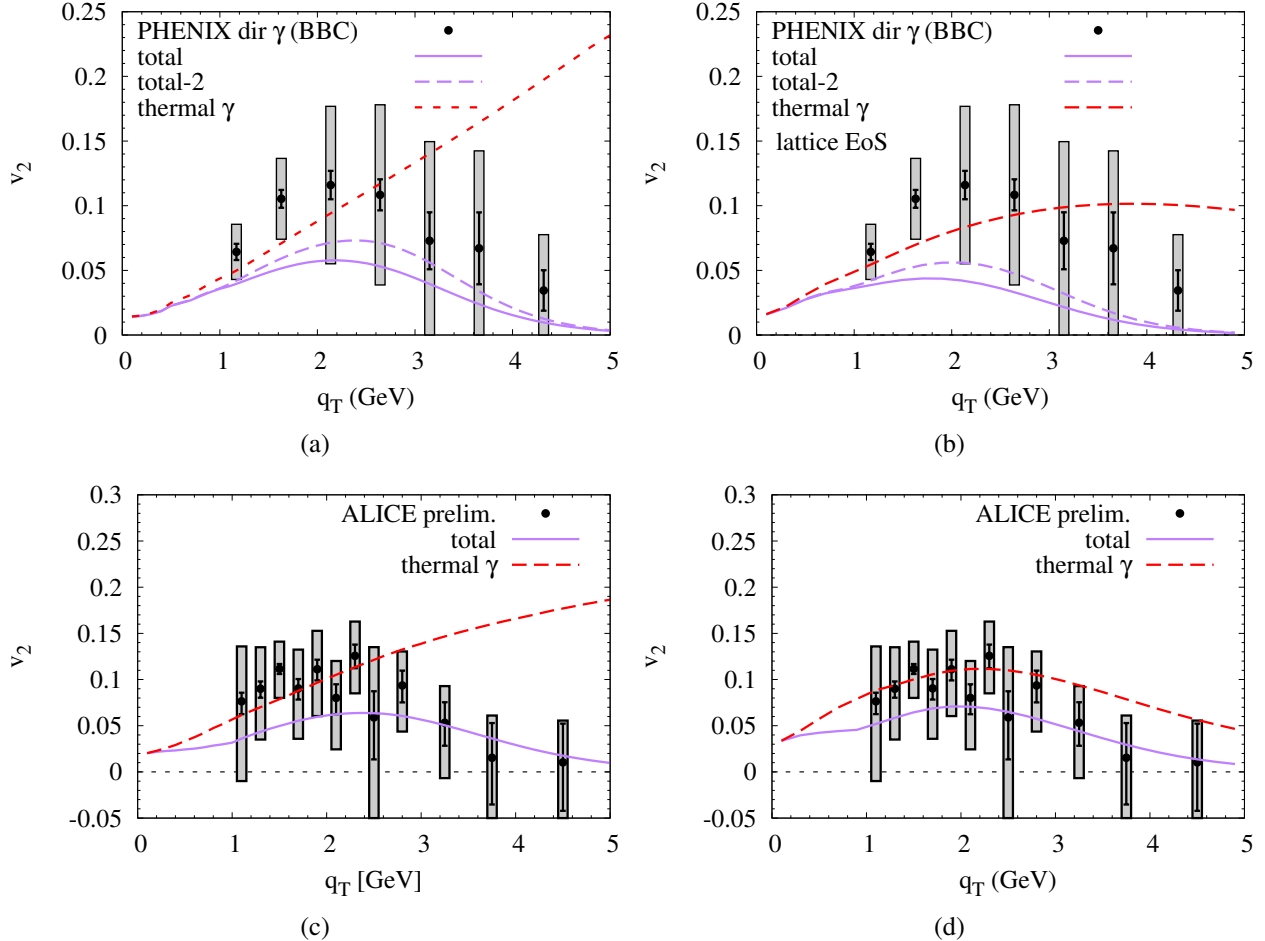


Figure 26: Direct photon elliptic flow v_2 for PHENIX [48] at $\sqrt{s_{NN}} = 200$ GeV in Au+Au centrality bin 0-20% (26(a)) using the expanding fireball and 0-20% (26(b)) using the ideal hydrodynamics as well as for ALICE [49] at $\sqrt{s_{NN}} = 2.76$ TeV in Pb+Pb centrality bin 0-40% (26(c)) using the expanding fireball and 0-40% (26(d)) using the ideal hydrodynamics. The plots are from [60].

- **Direct photon spectra and elliptic flow based upon an event-by-event hydrodynamical model [63]:** In this paper, an event-by-event hydrodynamical model of direct photon production is presented. It is an up-to-date hydro model of heavy ion collisions [103], which also incorporates the latest photon emission rates [46, 80]. The initial state of nuclear collisions is modeled by using the IP-Glasma initial conditions [104]. The IP-Glasma is an approach that builds on the “impact parameter dependent saturation model” (IP-Sat[Q_s]) that constrains the distribution of initial colour sources based on electron-proton and electron-nucleus collision data. The color fields are then evolved in the space-time according to the classical Yang-Mills equations: $[D_\mu, F^{\mu\nu}] = 0$, up to a proper time τ_0 of

the order of $\sim 1/Q_s$. In order to initialize the hydrodynamical evolution one should use the energy density, ϵ , and the flow velocity, u^μ , from the Yang-Mills evolution. This is accomplished by solving $u_\mu(\tau_0)T^{\mu\nu}(\tau_0) = \epsilon(\tau_0)u^\nu(\tau_0)$, where $T^{\mu\nu}$ is the classical Yang-Mills energy-momentum tensor. The IP-Glasma initial conditions are boost-invariant, and the subsequent hydrodynamical evolution is $2+1$ -dimensional. We will not go into the details of the calculations but will represent the results and

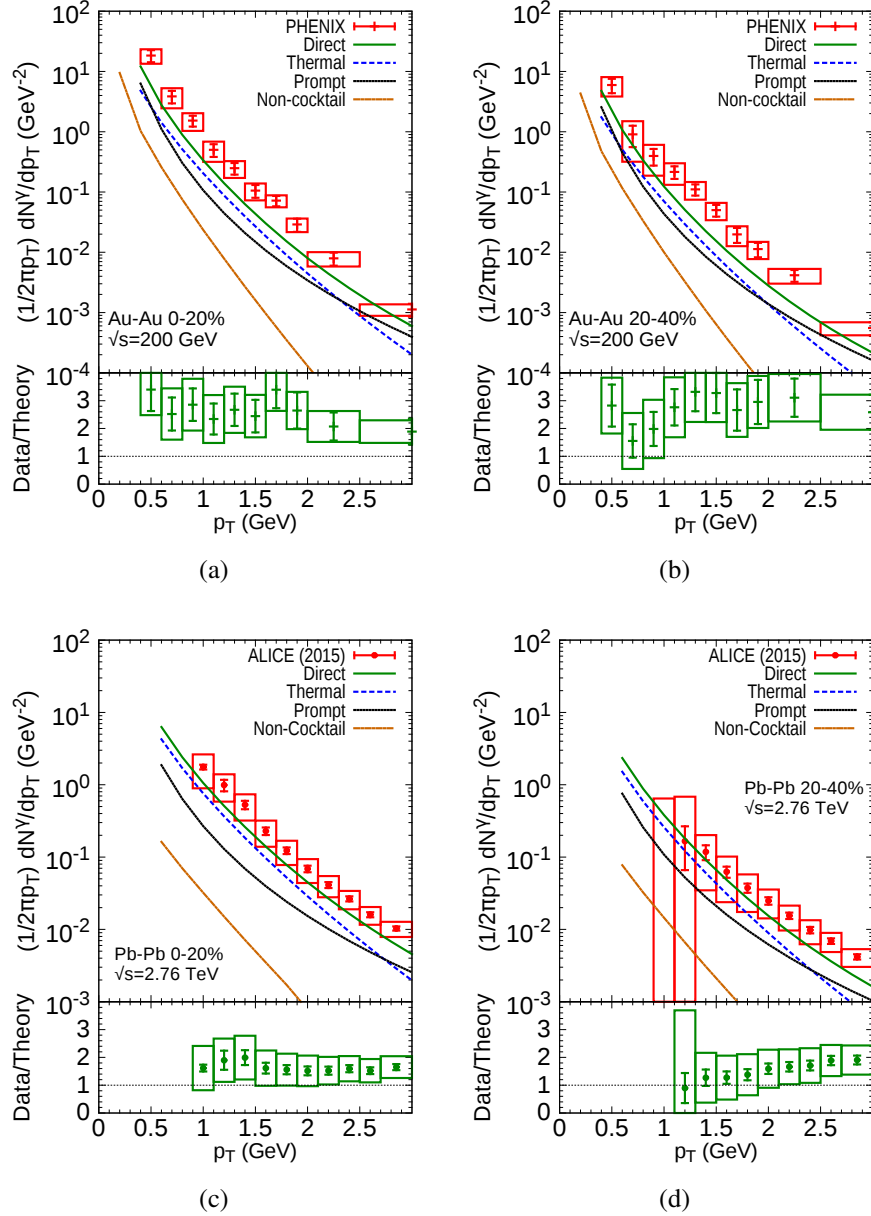


Figure 27: Direct photon spectra for PHENIX [42] at $\sqrt{s_{NN}} = 200 \text{ GeV}$ in Au+Au centrality bins 0-20% (27(a)) and 20-40% (27(b)) as well as for ALICE [45] at $\sqrt{s_{NN}} = 2.76 \text{ TeV}$ in Pb+Pb centrality bins 0-20% (27(c)) and 20-40% (27(d)). The plots are from [63].

comparisons with the direct photon data from PHENIX [42] and ALICE [45], shown in Fig. (27). The

results and comparisons with the elliptic flow data from PHENIX [48] and ALICE [45] are shown in Fig. (28). We refer to Ref. [63] for the other plots obtained by taking into account effects from both shear and bulk viscosities on the photon rates.

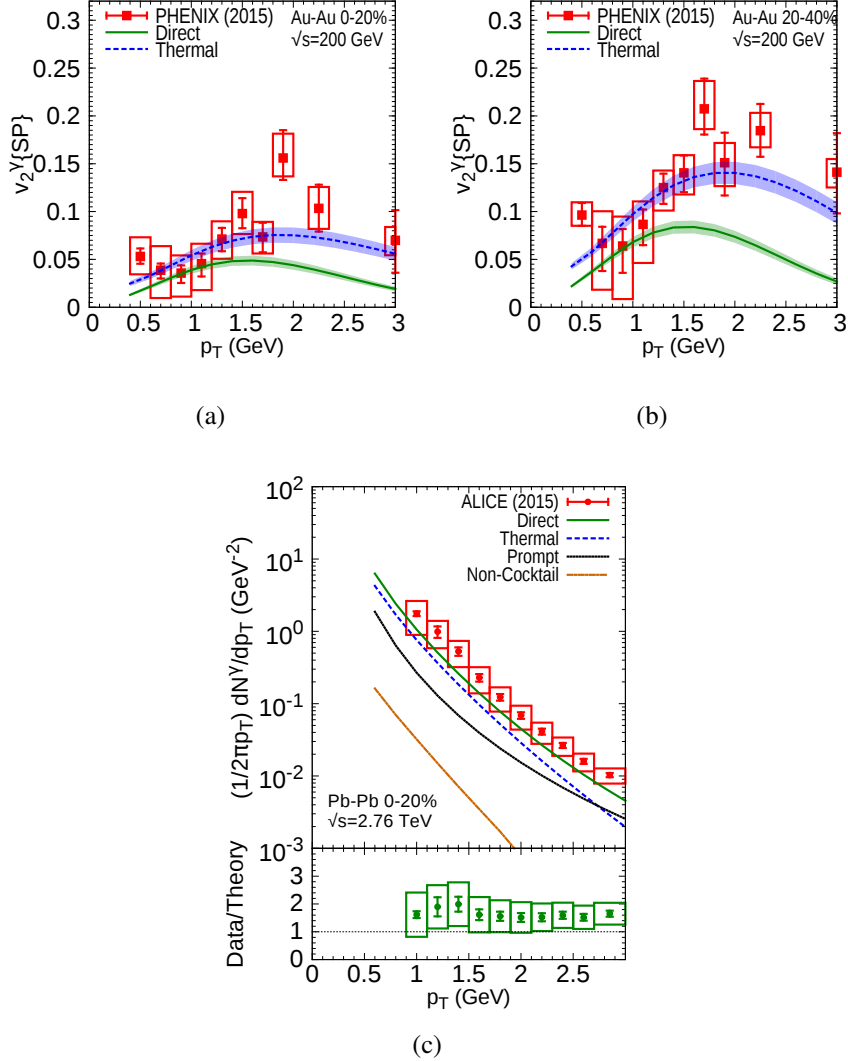


Figure 28: Direct photon elliptic flow v_2 for PHENIX [48] at $\sqrt{s_{NN}} = 200$ GeV in Au+Au centrality bins 0-20% (28(a)) and 20-40% (28(b)) as well as for ALICE [49] at $\sqrt{s_{NN}} = 2.76$ TeV in Pb+Pb centrality bin 0-40% (28(c)). The plots are from [63].

Chapter 2

2 The PHENIX Experiment

In this chapter we describe the PHENIX detector and several of its subsystems. Some of these subsystems have been used for our low momentum direct photon measurements.

2.1 The PHENIX detector at RHIC Facility

The PHENIX experiment (Pioneering High Energy Nuclear Interaction eXperiment) was the largest amongst the four experiments¹² that have taken data at Relativistic Heavy Ion Collider (RHIC) facility at Brookhaven National Laboratory (BNL). The primary goal of the PHENIX experiment was to discover and study the QGP, since detecting and understanding the QGP might give us better understanding of the universe in the moments after the Big Bang. The focus of the experiment was on investigations of high energy collisions of heavy ions and protons, and it was designed specifically to measure direct probes of collisions such as electrons, photons, muons, charged hadrons, etc. One can think of the PHENIX experimental collaboration looking “inside” the hot and dense matter formed in heavy ion collisions, much like medical doctors looking “inside” of the human body using x-rays. The PHENIX data suggest that the QGP has indeed been discovered, and its behavior is of a perfect fluid. Also, by colliding spin-polarized protons, the spin structure of the proton has been explored in order to measure the gluon contribution to the proton spin. Some other important projects involving PHENIX were to study the matter produced in heavy ion collisions in conditions of extreme temperatures and high densities as well as the map of the QCD phase diagram.

The experiment was based on the PHENIX detector, which was capable of recording many different species of particles emerging from RHIC collisions. The weight of the whole detector was 4000 tons, and it consisted of a collection of detector subsystems, each of which performed a specific role in a given measurement. The detector subsystems were grouped into two central arms, which were capable of measuring a variety of particles including photons, electrons, pions, kaons, protons, deuterons, and two muon arms with the focus on measurements of muon particles. There were also additional event characterization detectors that provided additional information about a collision, and a set of three huge magnets that bent the charged particle trajectories. These detectors operated to-

¹²The other experiments are STAR (Solenoidal Tracker at RHIC), PHOBOS and BRAHMS.

gether in an advanced high-speed data acquisition system to collect information about the events and investigate properties of the QGP subsequently.

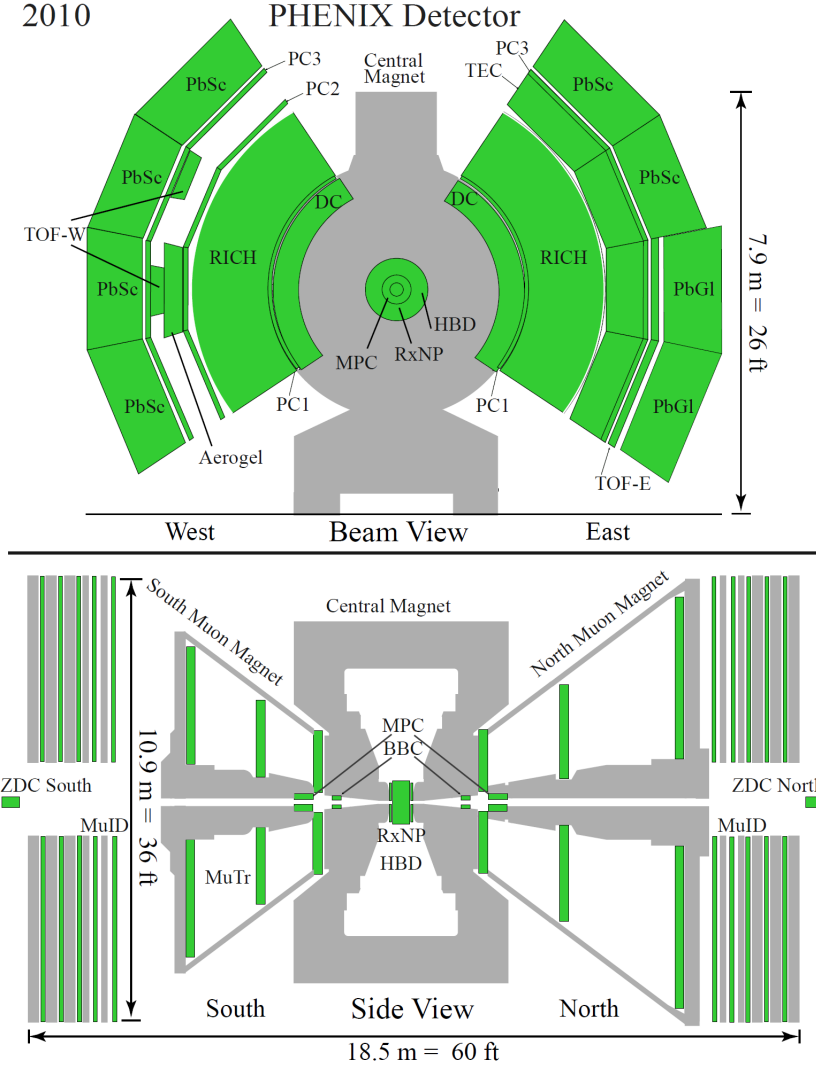


Figure 29: The top figure shows a cross-sectional view of the PHENIX detector for the 2010 setup (in the x-y plane), displaying the PHENIX central arms. The bottom figure shows a side view, showing the forward muon arms.

Some detector subsystems will be discussed in the following sections. A cartoon view of the PHENIX detector's configuration as of 2010 can be seen in Fig. (29). The central arms of the PHENIX detector cover a pseudorapidity range of $|\eta| < 0.35$. As it can be seen from Fig. (29), the central arms consist of two arm spectrometers. Each arm covers 90° in azimuthal angle ϕ and is separated by about 90° . One can find more details on the PHENIX detector in [105, 106, 107] and some of the PHENIX results with an emphasis on implications for the formation of a new state of dense matter in [108].



Figure 30: Members of the PHENIX collaboration standing and sitting in front of the detector. The photo is taken in 2008.

The analysis results in this thesis are based on measurements at midrapidity in the PHENIX central arms.

The PHENIX detector recorded collisions, which were produced due to the operation of RHIC. RHIC is a collider facility with the ability to collide heavy nuclei as well as proton beams. As of 2017, RHIC is the second-highest-energy heavy ion collider in the world, after the Large Hadron Collider at European Organization for Nuclear Research (CERN). RHIC has been built as an upgrade to the previous Alternate Gradient Synchrotron (AGS) rings, which are still being used in the process of accelerating the beams to full energy, and was essentially born out of the canceled ISABELLE project. The main RHIC rings are 2.4 miles (3.9 km) in circumference. The two rings (arbitrarily denoted as “Blue” and “Yellow” rings, shown in Fig. (31)) circulate heavy ions and/or protons in opposite directions and allow a virtually free choice of colliding positively charged particles. In particular, the machine is able to collide various species of symmetric systems such as Cu+Cu, Au+Au, U+U as well as asymmetric systems such as p+Al, p+Au, d+Au, $^3\text{He}+\text{Au}$, Cu+Au plus also baseline p+p collisions at various beam energies. The collision energy range varies between 7.7 GeV and 510 GeV depending on a colliding system.

The atoms start moving to the RHIC rings in the Tandem Van de Graaff accelerators. Here these atoms are being ionized and initially accelerated. Their next stop is in the booster synchrotron, shown in light blue in Fig. (31). The ions are moving at about 37% the speed of light at the end of their time

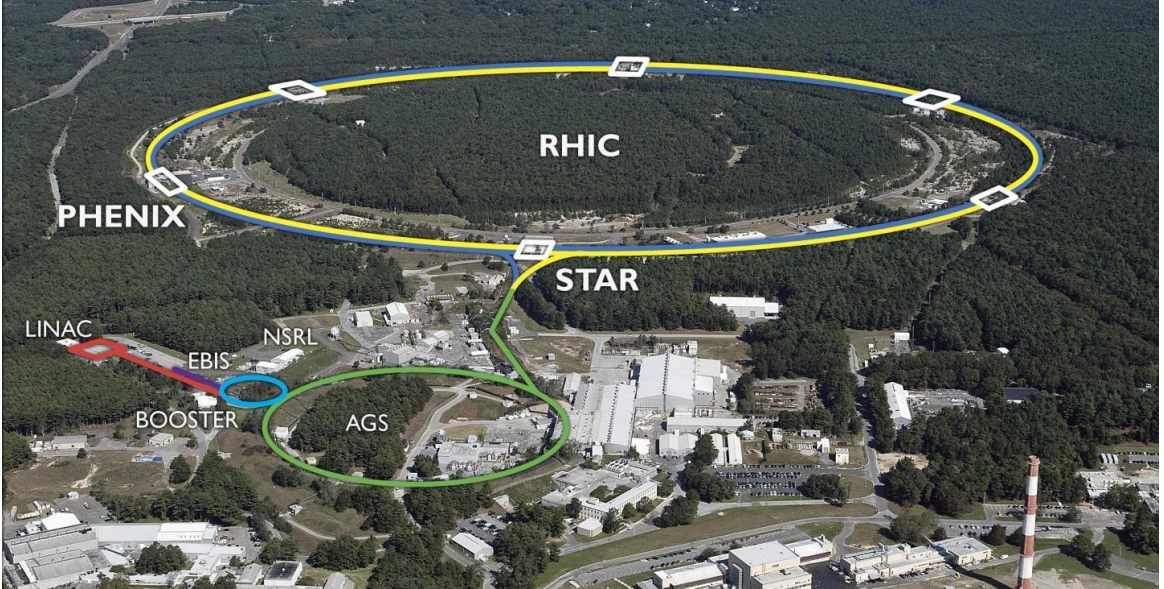


Figure 31: An aerial photograph of the RHIC facility. The various colors show different sub-facilities that produce ion beams in (ultra)relativistic heavy ion collisions, and bring them up to full energy.

in the boosters. In order to accelerate the ions further, they are being sent into the AGS rings, shown as green rings in Fig. (31). Here they are accelerated up to 99.7% the speed of light. Ultimately, the ions are being fed into the two main RHIC rings, where they are brought up to full energy. The beams of these ions are delivered in bunches, and they are traveling in opposite directions in each ring. The beams can circulate inside the RHIC rings for a number of hours depending on the energy of the beams. In the case of p+p collisions, the protons start their journey at the LINAC (Linear Accelerator) and then are being fed into the boosters.

There are six interaction regions around the RHIC rings, where the beams can cross, four of which have been occupied by the RHIC experiments. The interaction points are enumerated by clock positions. There is one detector continuing to operate at RHIC, which is the STAR detector (6 o'clock). PHENIX (8 o'clock) finished its operations in June of 2016, PHOBOS (10 o'clock) completed its operation in 2005, and BRAHMS (2 o'clock) in 2006. More details on the RHIC collider and related physics can be found in [109, 110, 111, 112, 113, 114].

2.2 The PHENIX coordinate system

We can briefly discuss the coordinate system used in PHENIX before going to detailed description of the detector subsystems. That coordinate system used in Cartesian coordinates is displayed in Fig. (32). The axis z points along the beam line with positive z values pointing north. The axis x

points horizontal to the detector with positive x values pointing west. The axis y runs vertically. The angle ϕ is defined as the azimuthal angle in the x-y plane. The angle θ is defined as the polar angle in the y-z plane. The origin of the coordinate system coincides with the center of the PHENIX detector.

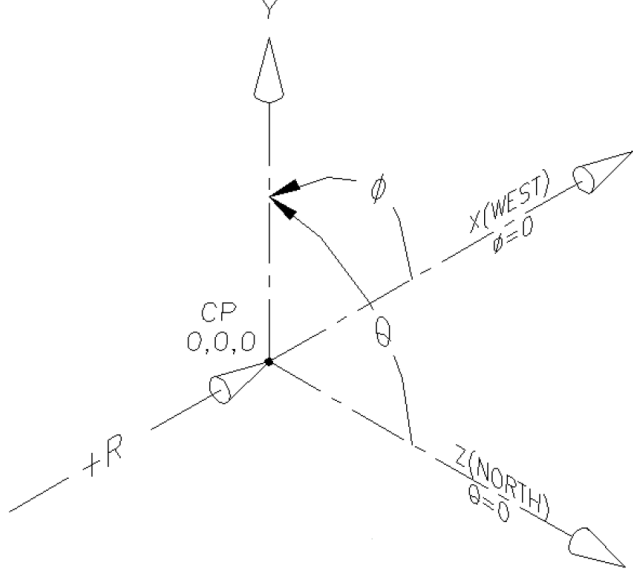


Figure 32: A cartoon illustrating the coordinate system used in the PHENIX detector. The cartoon is from [115].

In connection to this coordinate system, other commonly used quantities are the pseudorapidity, η , and rapidity y . The pseudorapidity describes the angle of a particle relative to the beam axis. It is related to θ and is defined as

$$\eta \equiv -\ln\left[\tan\left(\frac{\theta}{2}\right)\right]. \quad (81)$$

Fig. (33) shows the relation between η and θ in graphical form. One can rewrite η as a function of the three-momentum \vec{p} :

$$\eta = \frac{1}{2} \ln\left(\frac{|\vec{p}| + p_L}{|\vec{p}| - p_L}\right), \quad (82)$$

where p_L is the longitudinal momentum. It is slightly different from the definition of rapidity (which is commonly used as a measure for relativistic velocity), with substitution of $|\vec{p}|$ by energy E :

$$y = \frac{1}{2} \ln\left(\frac{E + p_L}{E - p_L}\right). \quad (83)$$

Thus, the pseudorapidity depends on the polar angle of a particle's trajectory, the rapidity depends on the particle's energy. The rapidity difference, Δy , between two particles is Lorentz invariant under

boosts along the longitudinal z axis¹³. The other useful relations are

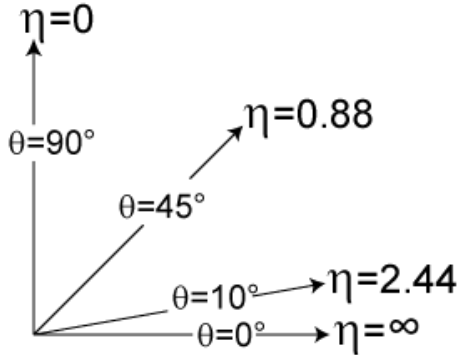


Figure 33: The illustration of the relation between η and θ relative to the beam line z.

$$E = m_T \cosh y, \quad p_L = m_T \sinh y : \quad \text{with} \quad m_T = \sqrt{p_T^2 + m^2}, \quad (84)$$

where m_T is the transverse mass. In the limit of $m \rightarrow 0$ and $y \rightarrow \eta$

$$t = \tau \cosh \eta, \quad z = \tau \sinh \eta : \quad \text{with} \quad \tau = \sqrt{t^2 - z^2}, \quad (85)$$

where τ is the proper time, which was widely used in the sections of introduction.

2.3 The PHENIX global detectors

All the PHENIX global detectors are in its north and south arms, at forward and backward rapidity (Fig. (29)). We will discuss three of them in this section.

2.3.1 Beam–Beam Counters, BBCs

In PHENIX, one of the detector subsystems for determining the timing, location and particle multiplicity from heavy ion collisions is the Beam–Beam Counters (BBCs) [116]. The BBCs provide information about the position of a collision and time of interaction from the flight time of prompt particles. The BBCs consist of two identical sets of counters installed on both sides of the interaction point along the beam line, one on the north side and the other one on the south side of the PHENIX collision region, where each counter is named as BBCN and BBCS, respectively.

These counters are located down the beam line at 144 cm in both directions, in the pseudorapidity range of $3.0 < |\eta| < 3.9$. Each of BBCs consists of 64 photomultiplier tubes (PMTs) arranged around

¹³The same is also true for the pseudorapidity difference, $\Delta\eta$, if the particles involved are massless.

the beam pipe, for 2π coverage in the transverse plane to the beam axis. In front of each PMT there is a quartz radiator. Particles passing through this radiator emit Cherenkov light, which is captured by the PMTs. Fig. (34) shows the BBC construction. The BBCs have excellent timing resolution equal to 54 ± 4 ps, setting the starting time, t_0 , for the whole PHENIX detector.



Figure 34: a) The assembly of one side of the BBCs. b) One BBC element.

There are some requirements for the BBC operation. The number of charged particles produced in Au+Au collisions at $\sqrt{s_{NN}} = 200$ GeV within the BBC acceptance should be as much as a few thousands for central collisions. Since the BBCs are placed in a very high-level radiation area around the beam pipe near the collision point, it is required to be radiation hard. The BBCs are installed just behind the PHENIX central spectrometer magnet, and the magnetic field along the beam axis around this location is ~ 3 kG. Therefore the BBC counters need to work in a high magnetic field environment.

2.3.2 Zero Degree Calorimeters, ZDCs

Another detector subsystem for determining the timing, location and particle multiplicity from a heavy ion collision is the Zero Degree Calorimeters (ZDCs) [117]. The ZDCs are hadronic calorimeters installed far down the beam axis in both the north and south direction, at a distance of 18 meters (the pseudorapidity is about 6). The purpose of the ZDCs is to detect neutrons emitted within a cone region of $\theta \leq 4$ mrad, along both beam directions and measure their total energy (from which we calculate the multiplicity).

The ZDC detectors consist of tungsten modules interlaid with optical fibers, connected to PMTs. A schematic of the tungsten modules is shown in Fig. (35). Only neutrons are detected since the ZDCs are past the forward dipole magnets, where charge beam remnants are swept away. By measuring the spectator neutrons, the ZDCs thereby assist in the centrality determination of events. These hadronic calorimeters see only neutral, forward going particles, and they are affected by any processes that produce or remove free neutrons. After a heavy ion collision, the produced free neutrons and protons can coalesce, removing the neutron deposition in the ZDCs. Meanwhile, other fragments can boil off

neutrons, increasing the neutron deposition in the ZDCs. In Fig. (36) one can see the plan view of the interaction region and particle trajectories, including also the BBC and ZDC locations.

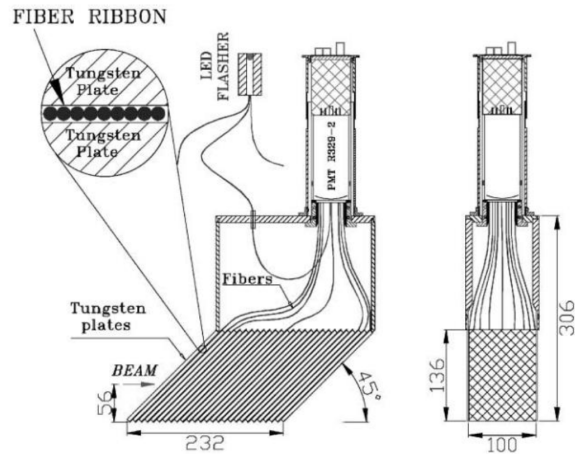


Figure 35: A schematic of the ZDC tungsten modules. All dimensions are in mm.

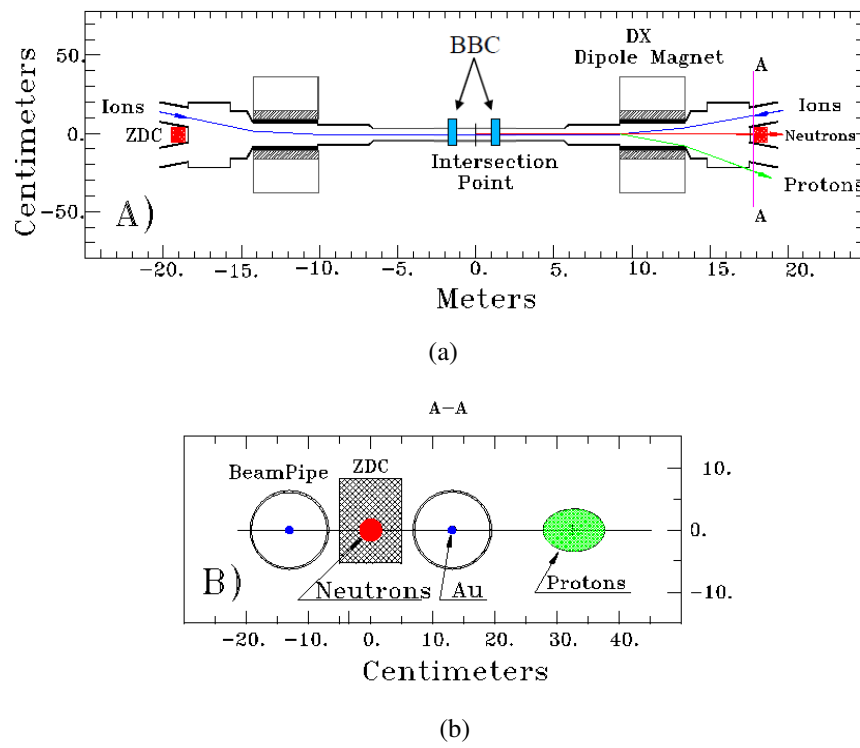


Figure 36: a) The plan view of the collision region and particle trajectories, with the BBC and ZDC locations along the beam axis (by indicating also deflections of protons and charged fragments). b) The “beam’s eye” view (section A-A) of the ZDC location.

2.3.3 Reaction Plane Detectors, RXPs

The reaction plane of an event is determined by utilizing the Reaction Plane Detectors (RXPs) [118]. The RXP detectors consist of two sets of plastic scintillators positioned on either side of the collision vertex, $38 < |z| < 40$ cm, and they have a pseudorapidity coverage range of $1.0 < \eta < 2.8$. Each detector consists of 24 scintillators, which detect traversing charged particles, and is arranged in two concentric circles around the beam axis, as shown in Fig. (37(a)). These scintillators are located in 12 segments in azimuth ϕ , and in 2 segments in pseudorapidity η . The scintillators closer to the beam pipe make the inner RXP, which covers $1.0 < |\eta| < 1.5$ in pseudorapidity. The scintillators farther to the beam pipe make the outer RXP, which covers $1.5 < |\eta| < 2.8$ in pseudorapidity. When charged particles pass through a scintillator they deposit energy. As a consequence of it photons are produced, which are then collected and amplified by PMTs. The resulting signal is proportional to the original energy deposition in each individual segment. To additionally increase the measurable charged particle multiplicity, the collision-facing sides of the RXPs are covered with lead converters of 2 cm thickness, which cause conversion electron production from otherwise undetected photons. The RXP detectors are mounted to the face of the central arm detector (see Fig. (37(b))).

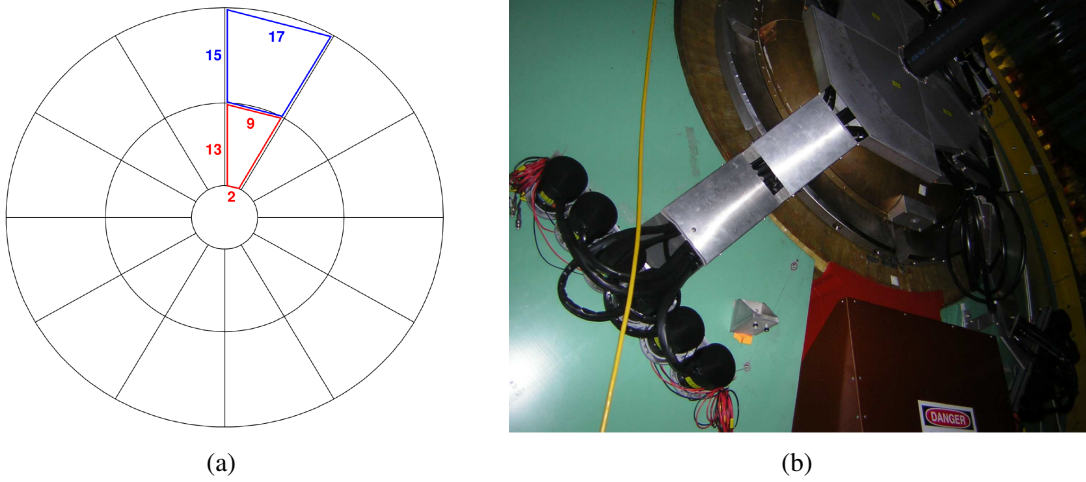


Figure 37: a) The schematic diagram of one RXP detector. The beam pipe goes through a hole in the center of the detector (perpendicular to the plane), and around it the scintillator paddles of the detector are arranged in concentric circles. The inner RXP detector is shown in red color, the outer one in blue color. The numbers give the scintillator dimensions in cm. b) One of the RXP detectors installed on the face of the central arm magnet, where the black pipe near the top right is the beam pipe.

2.3.4 Determination of the reaction plane, centrality and collision vertex

- **Reaction plane:** From the anisotropy of particle distribution, one can experimentally measure the reaction plane of an event, which is defined by the impact parameter of colliding nuclei and the beam

direction, as shown in Fig. (38). In this picture the reaction plane of a collision is shown, in which the overlap region has an almond-like shape. In particular, there is growth toward this shape in non-central collisions. The overlap region depending on the shape has different pressure gradients. The pressure gradients in the reaction plane are larger than those out of plane. This anisotropy results in the flow of particles in the reaction plane. The direction of the beam goes along with the z-direction, and the impact parameter, being a 2d vector connecting the centers of the colliding nuclei, points in the x-direction.

The particle distribution can be Fourier decomposed where each harmonic of the distribution has its own plane in which it is oriented. These planes may or may not be correlated with each other depending on the order. In general, for the n^{th} harmonic, the event plane is defined as

$$\Psi_n = \frac{1}{n} \tan^{-1} \left(\frac{Y_n}{X_n} \right), \quad \text{where } Y_n = \sum_i \sin(n\phi_i) \quad \text{and} \quad X_n = \sum_i \cos(n\phi_i), \quad (86)$$

where the sum is carried out over i particles. The number n in Eq. (86) refers to the n^{th} order harmonic, and ϕ is the angle of emission of a particle in the plane transverse to the beam.

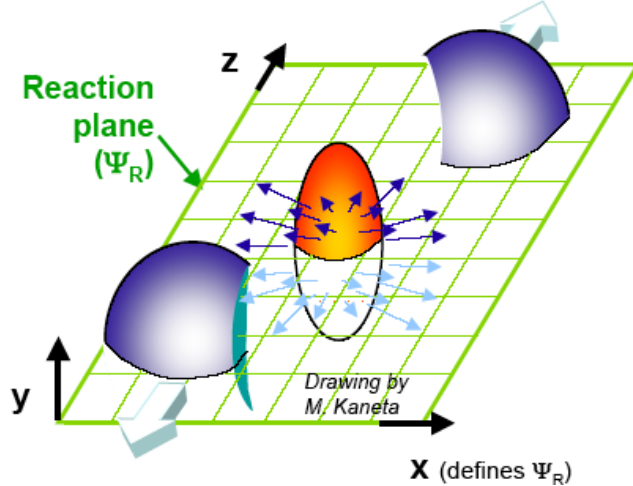


Figure 38: The reaction plane, Ψ_R , defined by the impact parameter of colliding nuclei and the beam direction.

- **Centrality:** The centrality of a collision is defined as a percentage of the total inelastic cross-section. The percentage is defined such that it roughly corresponds to the impact parameter of the collision. If the colliding nuclei are viewed as hard spheres with radius R , a 0%-centrality collision is a direct, head on collision with an impact parameter of $b = 0$ fm; peripheral collisions will be in the range of $0 < b < 2R$; ultraperipheral collisions will be in the range of $b > 2R$. Thereby, a larger centrality is related to a larger impact parameter. The number of participants, N_{part} , depends on the impact parameter and the radius of the colliding nuclei. A very peripheral event will have nuclei barely

touching each other, and in this case there will be only a few participating nucleons. The measurable total multiplicity of particles also depends on N_{part} . It can be used to characterize the centrality of an event. The centrality is determined experimentally by measuring the charge sum deposited in the BBCs. The measurement method is based on the assumption that the total charge deposited in each BBC is linearly proportional to the number of participants. Under this linearity condition, the charge sum follows a negative binomial distribution as does the measured charged-particle multiplicity.

- **Collision vertex:** The BBCs are also used to determine the event vertex of a collision in the z-direction (along the beam axis). The timing difference between particles hitting the BBC south and north detectors determines the z-vertex:

$$z_{vertex} = c \cdot (t_S - t_N) / 2. \quad (87)$$

Here c is the speed of light, and t_S/t_N is the time at which the BBCS/BBCN is fired. With the excellent timing resolution of the BBCs, the z-vertex resolution of a few centimeters is achieved. The z-vertex of a collision is an important piece of information. Ideally we would like to have collisions occurring in the very center of the PHENIX detector, but it is not the case because of the spread of collisions. For the analysis discussed in this thesis, a z-vertex cut of ± 10 cm is made (see Sec. (3.3.1)).

2.4 Central arm detectors

The central arm contains detectors for identifying and measuring charged particles, and photons at midrapidity $|\eta| < 0.35$. It is subdivided into the west and east arms, where the west arm roughly covers the azimuthal range of $(-\pi/4) < \phi < (\pi/2)$, while the east arm covers the range of $\pi < \phi < (3\pi/2)$.

2.4.1 Central arm magnets

In PHENIX, a strong axial magnetic field [119] is used to bend trajectories of particles emitted in the transverse plane at midrapidity, since the momenta of charged particles produced in p+p, p+A, A+A collisions are typically measured via the curvature of their trajectories in a strong magnetic field. The curved trajectories originate from charged particles undergoing the Lorentz force exerted by the magnetic field. This is achieved for the central arm tracking by the central arm magnets. These magnets are huge, standing 9 meters tall and weigh almost 500 tons (Fig. (39)).

The magnets consist of two pairs of concentric coils (inner and outer) located outside of the central region along the beam axis. These inner and outer coils can be operated separately. They can run together in the same direction such that their fields add up (++ field), or they can run in an opposite configuration such that their fields partially cancel each other (+- field). Straight tracks going

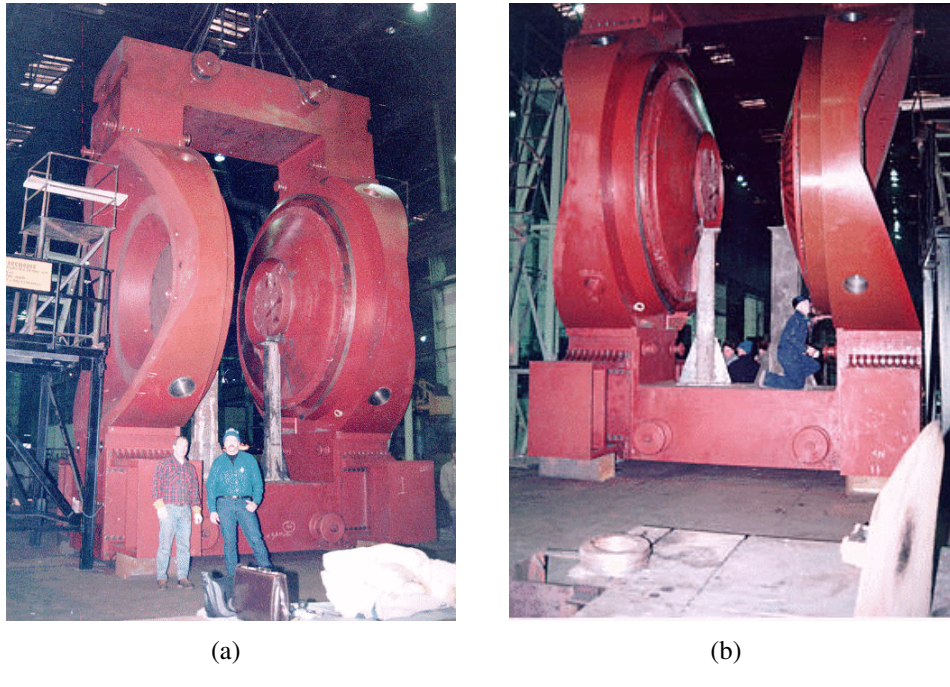


Figure 39: The PHENIX central magnets shown from different sides.

through the detectors are the easiest to observe and to track in a high multiplicity environment. That is why the magnets are designed in such a way that the field strength is minimal, where the tracking detectors reside. At a radius of $R \approx 1$ m, the field reaches its maximal value of approximately 3.5 kG, and then decreases until it becomes quite small at $R \approx 2.5$ m. The total field integral at full strength is 0.78 Tm. In Fig. (40) one can see the magnetic field lines for both $++$ and $+-$ field configurations from a Garfield simulation.

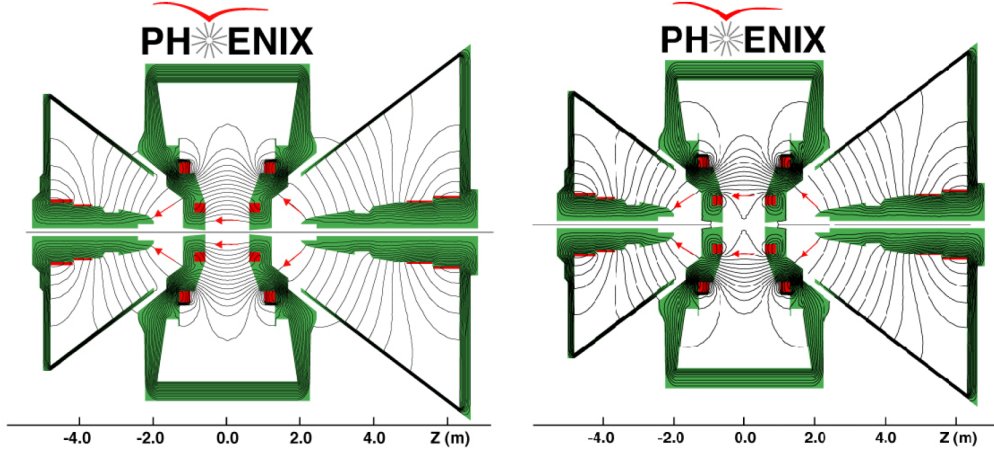


Figure 40: Calculations of the magnetic fields from a Garfield simulation: for the $(++)$ -configuration (left panel) and for the $(+-)$ -configuration (right panel).

2.4.2 Drift Chambers, DCs

The Drift Chambers (DCs), consisting of two identical detectors located in the east and west halves of the central arm, are the main tracking detectors for PHENIX [120]. The DCs sit at a radial distance from 2.02 m to 2.46 m from the interaction point (where the residual magnetic field is less than 0.6 kG), and extend in 1.8 m in the z-direction. Each DC arm covers $\pi/2$ in azimuth ϕ . Fig. (41) shows one of the DC arms in the process of its delivery.

The DC detector is a multiwire chamber filled with almost equal amount of argon and ethane gases (plus also 1% of C_2H_5OH), specifically chosen for stability of the ionization drift velocity over small variations of the electric field strength in a region of the detector's operation. The electric field strength is approximately 1 kV/cm, which results in a drift velocity of the order of $50\ \mu\text{m/ns}$. The purpose of this detector is to help determine the transverse momentum, azimuthal angle, charge sign of particles as well as the quality of track candidates. It is also used for pointing of a charged track to various subsystems.

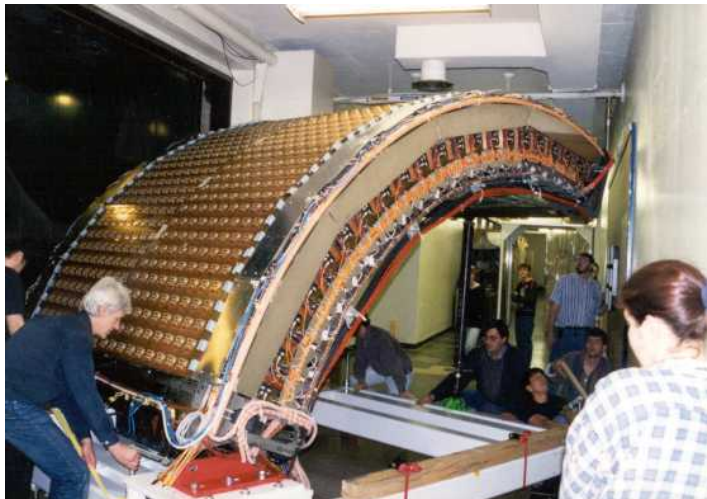


Figure 41: The process of the DC delivery.

Each of the DC detectors is segmented into north and south halves, composed of twenty identical sectors called *keystones*, as shown in Fig. (42(a)). These keystones cover 4.5° in ϕ , where combinations of adjacent keystones in the north and south halves are read out by the same electronics, which is referred to as *board*. Each keystone has six radial layers of wire nets at constant azimuth ϕ , labeled as X1, X2, U1, U2, V1, V2. The purpose of these wire nets is to create and shape an electric field causing the drift of ionization to dedicated sense wires. The layout of a layered wire net of a keystone is shown in Fig. (42(b)). The side view of a keystone is depicted on the left side of Fig. (43).

The DCs track charged particles by measuring the ionization from tracks passing through the gas inside the detector. Because of a static electric field applied in the detector, two ionized clouds

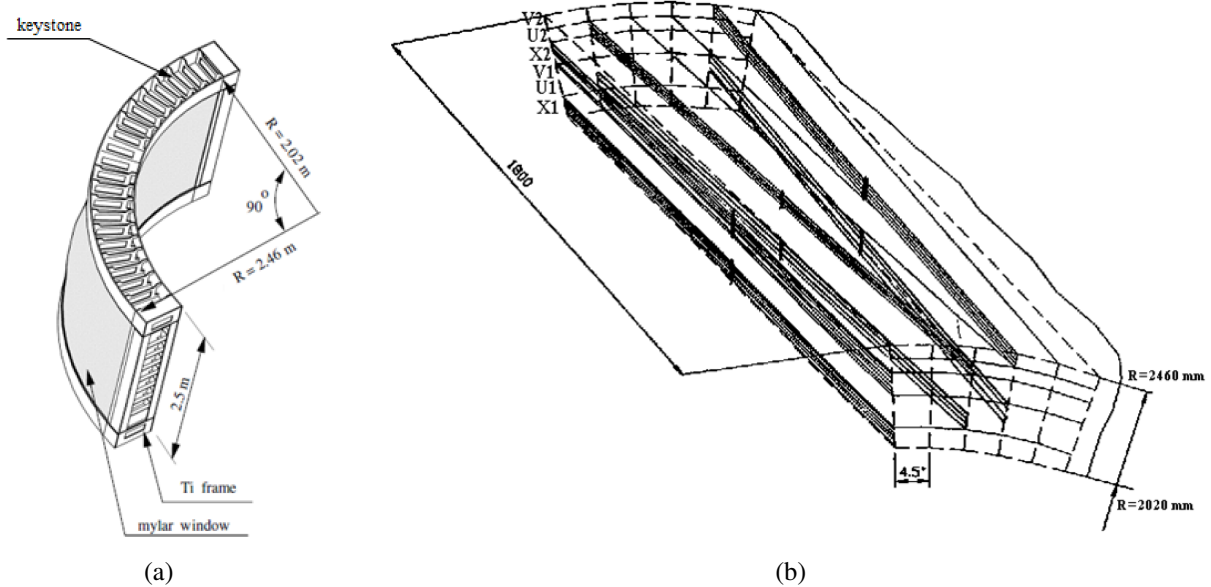


Figure 42: a) A schematic of the frame of one DC arm. The dimensions are given in meters. b) The layered wire net layout of a keystone. The dimensions are given in mm.

of positively charged ions and negatively charged electrons are produced, which drift in opposite directions from the field. The DCs use the charge of fast moving electrons from ionization as a signal since the electrons have a larger drift velocity. And due to higher mobility, the electrons move much faster than the heavier ions and create an avalanche as they approach the anode wire, thus leading to an amplification of the signal. A gain of the order of 10^4 is obtained, given the gas mixture and field set inside the chambers. Thereby, one can measure the time it takes for ionizing particles to produce a signal. The distance between the ionization signal's origin and the sense wire can then be calculated from this time and from the known drift velocity. By this way the hits in a position space are measured, and eventually the charged tracks can be reconstructed from these hits.

Let us now look at some details in Fig. (43), where it is shown the layout of a single wire net inside a keystone. The wire nets are made up of many different wires having different functions. Any of the keystones can be split up into planes, which is shown on the left side of Fig. (43). These planes alternate as anode (dashed lines) and cathode (dotted lines) planes. The cathode planes are composed of cathode wires, which create the electric field with the anode wires. The anode plane have five different types of wires (shown in the middle of the figure). First, those are *termination wires* at the edge of the net, which reduce boundary effects and keep the field uniform. There are *gate wires*, which limit the drift region width (the drift region between wires is 3 mm). There are also *potential wires* that help separate the region between the wires and control gas gain. The *back wires* block the signal from one side of the wire, eliminating the left-right ambiguity of the track reconstruction. Then the signal drifts to the *sense (anode) wires*.

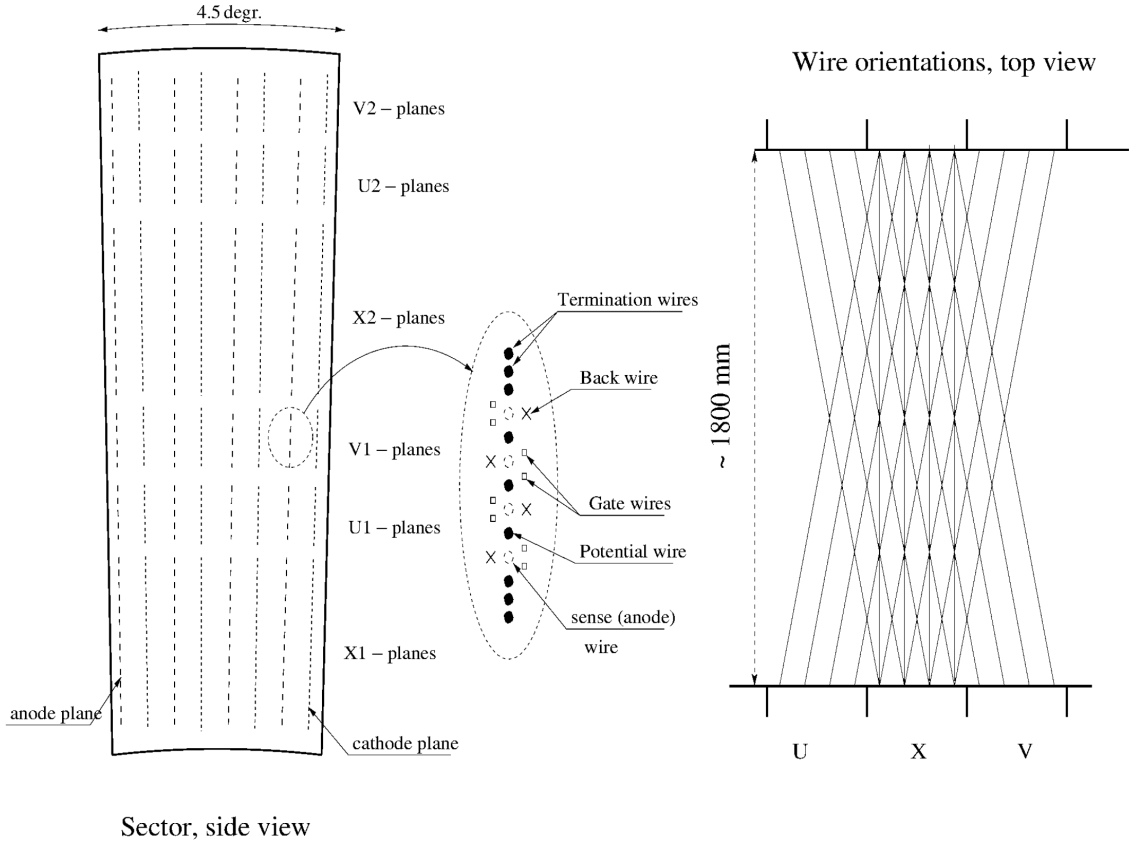


Figure 43: The wire layout of the DC sector (keystone). **The left panel** shows the positions of different wire planes along the beam axis: namely X1, X2, U1, U2, V1, V2 planes are indicated in the side view of a keystone. The dashed lines represent the anode plane, and the dotted lines represent the cathode plane. **The right panel** of the figure shows the orientation of the wire layers from the top view. **In the middle**, a zoom-in of single anode plane wire net is shown with different wire types. Filled circles and open squares denote the position of wires used to create or shape the electric field, open circles denote wires that are used to collect and measure the ionization.

2.4.3 Pad Chambers, PCs

The Pad Chambers (PCs), multiwire proportional chambers, determine the z-position of a track [120, 121]. They also allow for additional track quality constraints, and charged hadron rejection. There are three PC layers (PC1, PC2, PC3) arranged in increasing radius outside of the DCs, in both east and west arms. In Fig. (29) one can see the PC1¹⁴ right after the DCs, the PC2 after the RICH but only in the west arm, and the PC3 located in front of the EMCals (see also Fig. (44)).

Each PC contains single layer of anode wires in a volume of gas, sandwiched between two cathode planes from above and below, as shown in Fig. (45). As a charged particle passes through the gas volume, it creates ionization drifting to the anode or cathodes. The bottom cathode plane is made

¹⁴The hit information from the PC1 is used to constrain the quality of tracks reconstructed in the DCs.

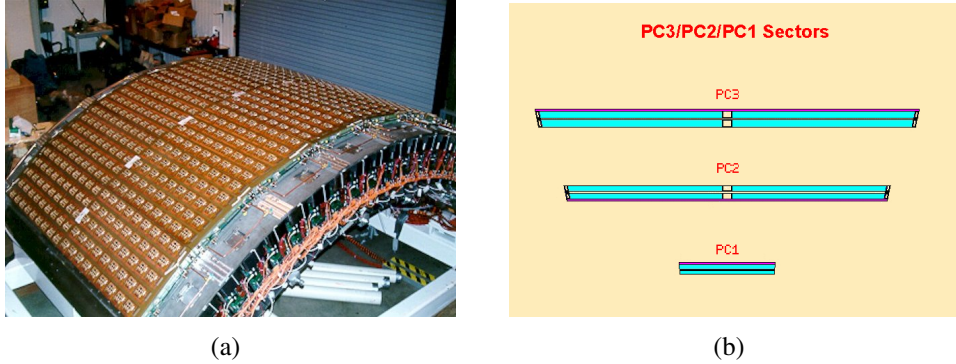


Figure 44: a) The view of one of the PC1 arms. b) The relative sizes of PC1, PC2 and PC3 sectors.

of solid copper, while the top cathode plane is segmented into pixels (in z - and ϕ -direction) for the pad readout. The signals from the pixels are transmitted, amplified and discriminated outside of the gas volume by utilizing the Read Out Cards (ROCs). Finally, the collected charge will be read out providing position measurements.

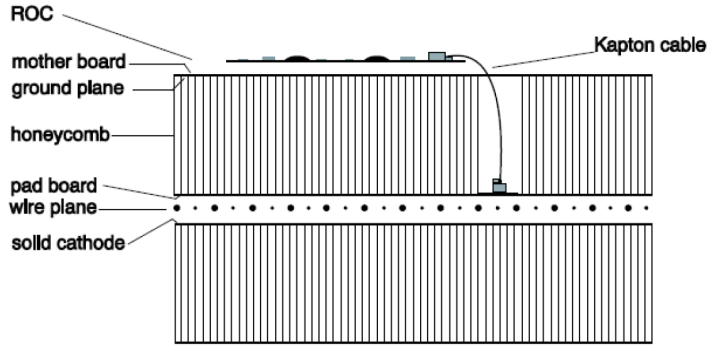


Figure 45: A view of a vertical cut through the PC.

2.4.4 Ring Imaging Cherenkov Detector, RICH

The Ring Imaging Cherenkov detector (RICH) [122, 123] is the primary device for electron identification in the PHENIX central arms (see Fig. (29)). It is a threshold gas Cherenkov detector with a high angular segmentation to identify electron tracks in a very high particle density environment.

Each arm of the RICH detector consists of a large chamber (filled with CO_2 used as a radiator), and two thin spherical mirrors (Fig. (46)). Each chamber has a gas volume of 40 m^3 . The entrance window of the chamber has an area of 8.9 m^2 , and the exit window of it has an area of 21.6 m^2 . Each RICH arm detector consists of 48 composite mirror panels. The panels form two intersecting spherical planes, resulting in a total reflecting area of 20 m^2 .



Figure 46: One arm of the RICH detector after the mirror alignment is accomplished.

Fig. (47(a)) shows a side view of the RICH detector, and Fig. (47(b)) shows a cutaway view of one arm of the RICH detector. When an electron passes through the RICH gas volume, Cherenkov photons emitted from the electron are reflected by the spherical mirrors and are focused onto two arrays of 1280 Hamamatsu H3171S UV PMTs, forming a ring shaped pattern¹⁵. The direction of the electron track is then measured from the position of the Cherenkov ring. A charged particle track, measured by the tracking system of the central arm, is identified as an electron if its direction matches the direction measured from the ring.

The charged tracks, which are found using the tracking system, are associated with hit PMTs in the RICH during the reconstruction process. The quality of the information found in the RICH is quantified as the number of hit PMTs in rings of different sizes. The track is projected to the RICH PMT plane. Then hit PMTs are found that are around the track projection. The number of found hits is quantified by a variable called n_0 , which is defined as the number of hit PMTs within a ring around the track projection with an inner radius of 3.4 cm and an outer radius of 8.4 cm. This ring is chosen based on the known ring diameter, and the position resolution of the PMTs defined by a PMT size (about 2.5 cm).

The gas is chosen in such a way that the electrons emit Cherenkov radiation at all relevant momenta while the main background, which consists of charged pions, starts to radiate at $p_T > 4.65 \text{ GeV}/c$. This is the Cherenkov threshold for pions, and below it the pions and heavier particles produce no signal in the RICH. An electron emits on average 12 photons per ring with a ring diameter

¹⁵Particles passing through the detector see a minimum thickness of gas of 87 cm, and a maximum of it at about 150 cm.

of about 11.8 cm, for a 120 cm path length. The Cherenkov angle, θ_c , is given by $\cos(1/(n\beta))$, where n is the index of the gas refraction, and β is the fraction of the speed of light that the passing particle has.

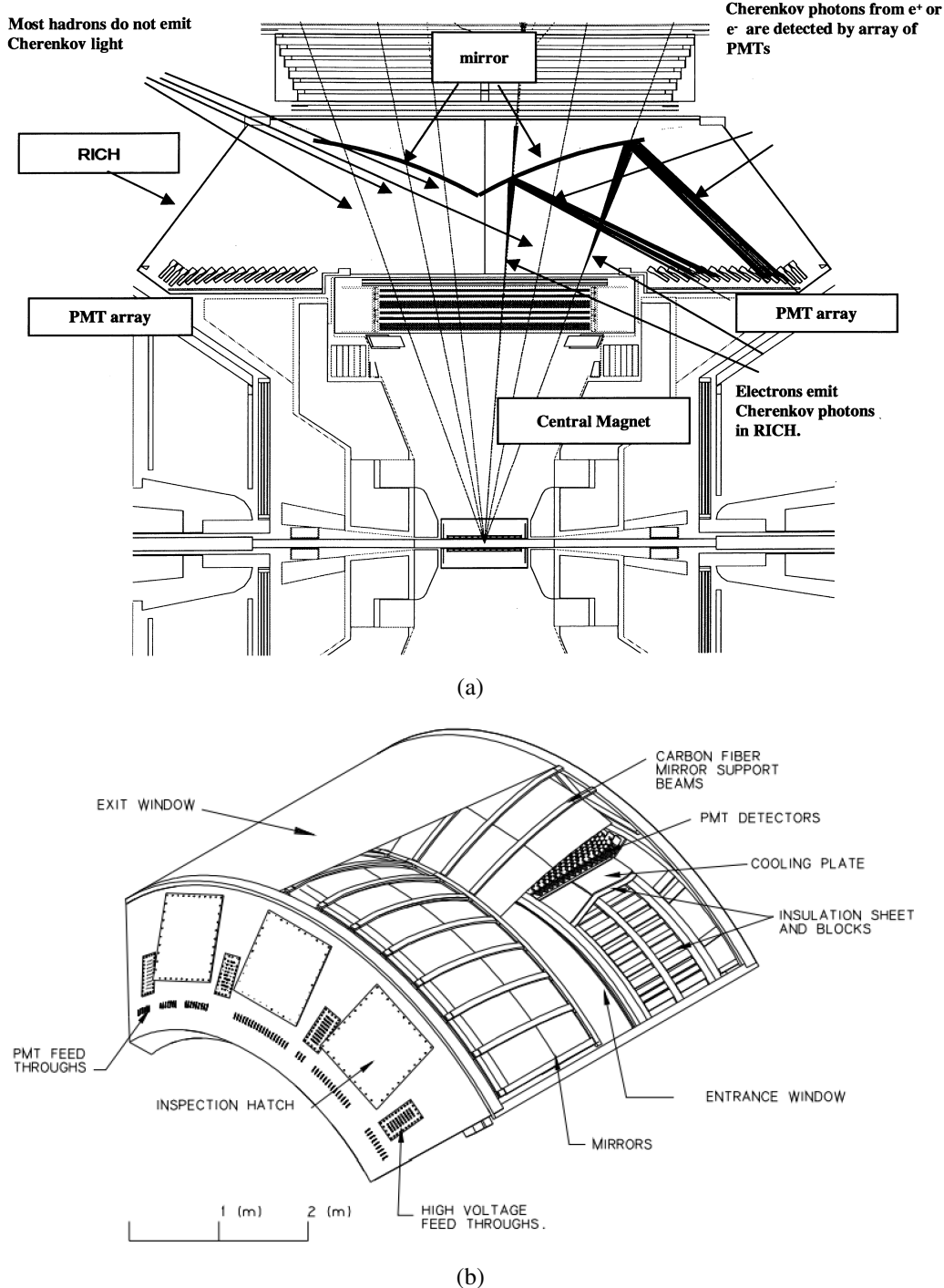


Figure 47: a) A cut through view of the RICH detector. b) Cutaway view of one arm of the RICH detector.

2.4.5 Hadron Blind Detector, HBD

The Hadron-Blind Detector (HBD) [124] (see Fig. (29) and Fig. (48)) is a Cherenkov detector installed around the beam pipe, which sits in the central arms of PHENIX. It is installed just after the beam pipe at radius of about 5 cm, and extends up to a radius of about 60 cm. The detector has a pseudorapidity coverage of $|\eta| < 0.45$, and an acceptance of 135° in ϕ . The HBD consists of a cylindrical volume of radius $R = 50$ cm filled with CF_4 gas acting as a radiator, followed by a series of gas electron multipliers (GEMs) that amplify the photon signal. The readout electronics has a relative radiation length of $X/X_0 = 2 \div 3\%$, and consists of a triple GEM stack with a CsI photocathode on the top layer and a pad readout on the bottom layer. The construction of one side of the HBD is shown Fig. (49(a)).

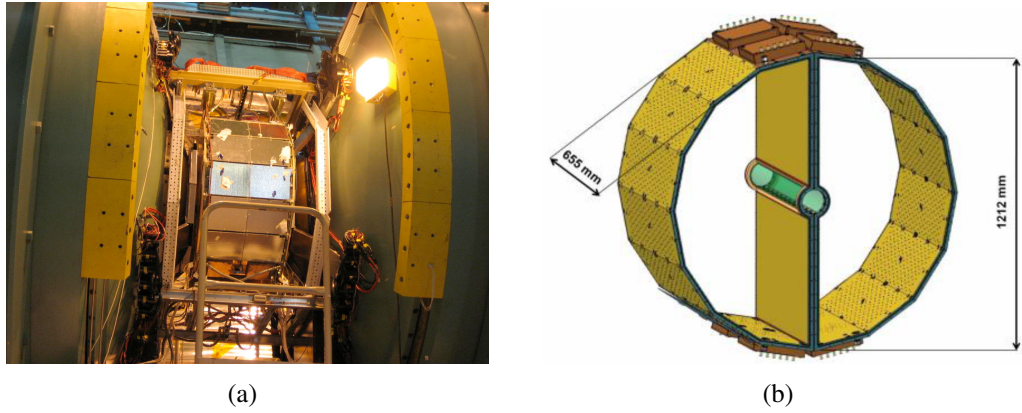


Figure 48: a) The front view of one half of the HBD. b) The schematic view of both HBD halves.

The principal design goal of the HBD was to identify photon conversion pairs, $\gamma \rightarrow e^+e^-$, originating in the beam pipe (Fig. (49(b))), and electron pairs from π^0 Dalitz decays, $\pi^0 \rightarrow \gamma e^+e^-$, which are the main sources of the background in dielectron measurements. These pairs would be observed in the HBD with minimal opening angle because the inner space of the HBD was practically field-free. However, in 2007 when the detector was installed, it did not function as planned. In our analysis we use the HBD strictly as a photon converter, and the focus is on conversions that occur in the HBD backplane (readout boards and electronics) at the radius ≈ 60 cm.

2.4.6 Electromagnetic Calorimeters, EMCals

The Electromagnetic Calorimeter (EMCal) [125] is located in the central arm at about 5 meters away from the interaction point. It is designed to measure the position and energy/momentum of photons and electrons by absorbing the energy of electromagnetic showers. The EMCal consists of two different types of subdetectors (calorimeters). They are split up into eight sectors, with four sectors in the east arm and four sectors in the west arm (Fig. (29)).

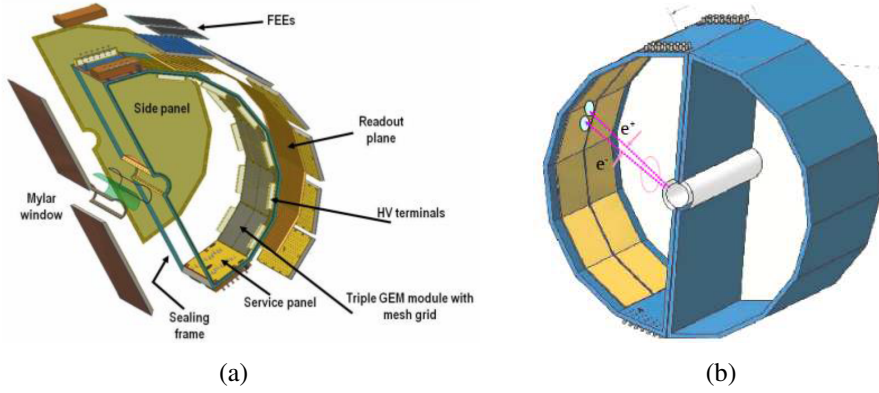


Figure 49: a) The construction of one of the HBD sides. b) Visualization of a photon conversion originating in the beam pipe.

The east arm has two different types of calorimeters: lead-glass Cherenkov calorimeters (PbGl) and shashlik type lead-scintillator calorimeters (PbSc). The west arm has only four PbSc. Both PbGl and PbSc types have slightly different efficiencies and tower segmentation. Both types have good energy and position resolution but each of them has its own strengths and weaknesses in the design. The main strength of the PbSc sectors is the timing and linearity of response to charged particles [126]. The main strength of the PbGl sectors is the energy resolution and a finer granularity. This allows for a comparison of EMCAL measurements with these two distinct types of calorimeters. The basic properties of the EMCals are described in Table (1).

The PbSc and PbGl are required to have a wide dynamic range for measurements, from few hundred MeV up to 80 GeV. The energy scale uncertainty is the major contribution to the systematic error of a steeply falling cross section spectrum, thus the calorimeters are required to have less than 2% uncertainty in the absolute energy scale. The high multiplicity of heavy ion collisions demands very fine granularity about $\Delta\eta \times \Delta\phi \approx 0.01 \times 0.01$ to achieve less than 20% occupancy in a central Au+Au collision at $\sqrt{s_{NN}} = 200$ GeV. In the following two sections, both subdetectors are described with a bit more details.

- **Lead-Scintillator Calorimeter:** The PbSc electromagnetic calorimeter is a shashlik type [127, 128] sampling calorimeter (made of lead and scintillator), which can be see in Figs. (50) and (51).

The basic construction of this sampling calorimeter starts with one tower. Each tower contains 66 sampling layers of alternating tiles of lead and scintillator with a thickness of 1.5 mm and 4 mm, respectively. These 66 layers are optically connected by 36 wavelength shifting fibers, read out to 30mm FEU115M phototubes attached to the back of the towers for light collection [129]. These fibers penetrate longitudinally into the tower. There are 15,552 of these individual towers in the detector covering about 48 m^2 in area. Four towers are mechanically combined, which creates the PbSc module. The scintillator is made of Polystyrene. The edges of the tiles are plated with

Electromagnetic Calorimeters	PbSc	PbGl
Type	Shashlik	Cherenkov
Radiation length (X_0) [mm]	21	29
Moliere radius [mm]	43	37
Cross section of a tower [mm 2]	52.5 \times 52.5	40 \times 40
Depth [mm] (X_0)	375 (18)	400 (14)
$\Delta\eta \times \Delta\phi$ of a tower	0.011 \times 0.011	0.008 \times 0.008
Number of sectors	6	2
Number of towers	15552	9216

Table 1: The summary of the parameters of the PHENIX EMCals. There are two types of EMCAL detectors: lead-scintillator (PbSc) and lead-glass (PbGl).



Figure 50: Some of the PbSc modules.

Aluminum. Fig. (51) shows a diagram of a single module. 36 of such modules are then bound together to form a rigid structure called a supermodule. 18 supermodules form a single sector, held together in its own rigid $2 \times 4 \text{ m}^2$ steel frame.

A monitoring system is implemented for calibration of each tower [130], based on a UV laser that deposits energy into the calorimeter towers through a series of optical splitters and fibers. The laser light is split in three steps and delivered into 3888 modules in total. The laser amplitude is monitored by a phototube at emission and photodiodes in all light splitters. By utilizing cosmic rays for all towers during construction, the laser calibration system has been established to normalize the initial energy calibration. The calorimeter performance has been tested at CERN and BNL test beam facilities [131, 132] with a well calibrated electron-positron beam. The energy and position resolutions of the PbSc calorimeter have the following forms [133]:

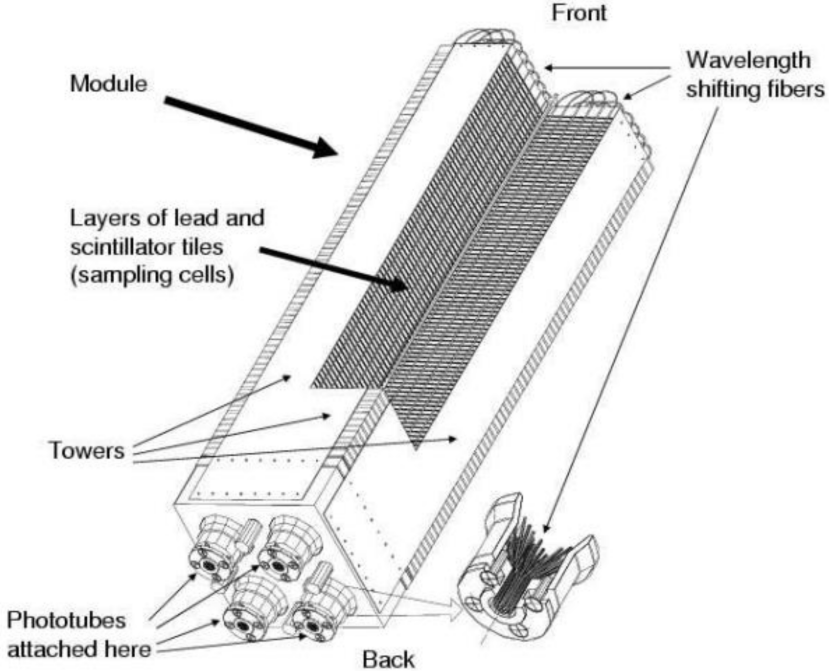


Figure 51: A diagram showing the interior view of the lead-scintillator calorimeter (PbSc) module.

i) energy resolution

$$\frac{\sigma(E[\text{GeV}])}{E[\text{GeV}]} = 1.2\% + \frac{6.2\%}{\sqrt{E[\text{GeV}]}} , \quad (\text{linear dependence}) \quad (88)$$

$$\frac{\sigma(E[\text{GeV}])}{E[\text{GeV}]} = 2.1\% \oplus \frac{8.1\%}{\sqrt{E[\text{GeV}]}} , \quad (\text{quadratic dependence}) \quad (89)$$

where the sign \oplus is defined to be the square root of the quadratic sum: $a \oplus b = \sqrt{a^2 + b^2}$.

ii) position resolution

$$\frac{\sigma_x(E[\text{GeV}])}{E[\text{GeV}]}|_{\theta'=0} = 1.4 \text{ mm} + \frac{5.9 \text{ mm}}{\sqrt{E[\text{GeV}]}} , \quad (90)$$

$$\sigma_x(\theta') = (20.0 \cdot \sin \theta') \oplus \sigma_x(\theta' = 0) , \quad (91)$$

where θ' is the angle of an incoming particle with respect to the perpendicular axis from the surface of the calorimeter.

- **Lead-Glass Calorimeter:** In contrast the PbSc detector, the lead glass calorimeter (PbGl) is a Cherenkov type detector (see Figs. (52) and (53)). Like the PbSc calorimeters, the PbGl sectors are also built up into the module/supermodule structure. Each PbGl sector is made from 192 supermod-

ules, in a formation of 16×24 . In turn, each PbGl supermodule is built from 24 modules and has 6×4 length and width, respectively. In the PbGl calorimeter there are 9216 modules. Single PbGl modules, with dimensions $4 \times 4 \times 40 \text{ cm}^3$, are wrapped into a reflecting mylar foil and connected together into a full sector.



Figure 52: Some of the lead-glass calorimeter (PbGl) modules.

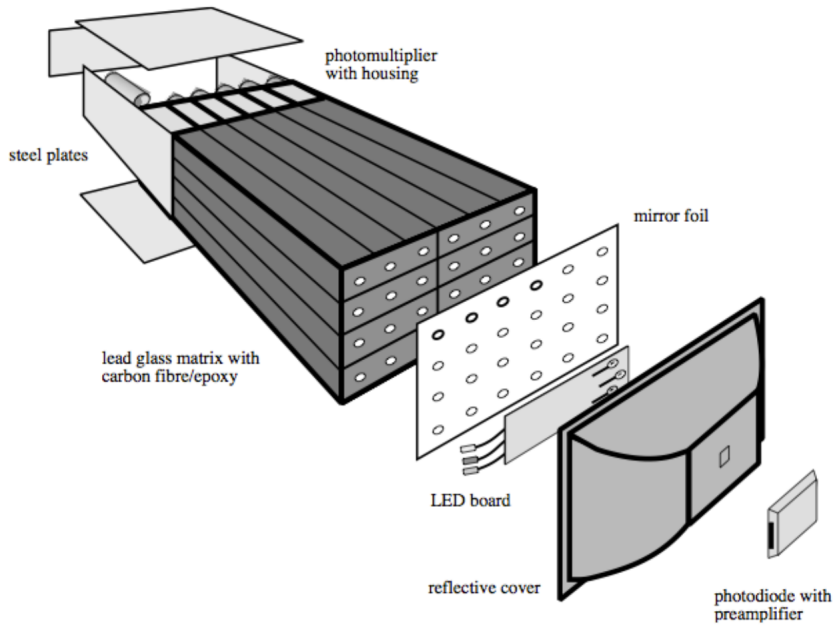


Figure 53: A diagram illustrating the construction of a PbGl supermodule.

A calibration and monitoring system consisted of light-emitting diodes (LEDs) is utilized. A LED

in front of each 24 towers creates a reference light measured by the FEU-84 PMTs in the back of the towers. Each supermodule is equipped with its own set of LEDs. All 24 modules in the supermodule see the light from the LEDs. The e^+e^- pairs in the electromagnetic shower produce a constant number of Cherenkov photons per unit length. The full length of all electron and positron tracks in the shower is linearly dependent on the total energy of the incoming particle, by which the total light produced is proportional to this energy. The energy and position resolutions of the PbGl calorimeter have the following forms [133]:

- i) energy resolution

$$\frac{\sigma(E[\text{GeV}])}{E[\text{GeV}]} = \frac{5.9\%}{\sqrt{E[\text{GeV}]}} \oplus 0.8\%, \quad (92)$$

- ii) position resolution

$$\frac{\sigma_x(E[\text{GeV}])}{E[\text{GeV}]} = \frac{5.9 \text{ mm}}{\sqrt{E[\text{GeV}]}} \oplus 0.2\%. \quad (93)$$

The PbGl performance has been tested at both CERN and BNL test beam facilities.

Part II

Analysis

Chapter 3

3 Data analysis for the relative direct photon yield, R_γ

3.1 The motivation and goal of the measurements and analysis of low-momentum direct photons in Au+Au collisions at $\sqrt{s_{NN}} = 62.4 \text{ GeV}$ and $\sqrt{s_{NN}} = 39 \text{ GeV}$

In Sec. 1.3.1 we already noted that the large yield and large anisotropy of low momentum direct photons, observed by PHENIX and ALICE collaborations pose a significant challenge to theoretical models commonly referred to as “thermal photon puzzle”. Measurements at lower collision energies may provide new insight on the origin and properties of the low momentum direct photons, which might be an additional piece of information in understanding and solving this puzzle. These lower collision energies are $\sqrt{s_{NN}} = 62.4 \text{ GeV}$ and $\sqrt{s_{NN}} = 39 \text{ GeV}$, and we have measured photons from data samples obtained from Au+Au collisions at these RHIC energies.

We have also discussed that the measurements of direct photons are possible making use of EMCals. Nevertheless, such measurements become contaminated with misidentified hadrons, minimal-ionizing particles (MIPs) or even fake clusters, leaving some irreducible background consisting of a large part of MIPs, and making a challenge to low p_T measurements with the EMCals. However, another strategy of measuring low-momentum direct photons has been developed in [42, 115, 134], where the direct photons are not measured directly in the PHENIX EMCals but are detected via external photon conversions to e^+e^- pairs in a well-chosen detector material. This strategy virtually eliminates the hadron contamination due to a very clean photon identification based on e^+e^- pairs. Also, a novel technique is applied that minimizes the combined statistical and systematic uncertainties, which usually limit direct photon measurements, in particular at low p_T . In PHENIX, the e^+e^- pairs are primarily reconstructed from curved tracks in the PHENIX DCs, in which the lower the momentum of a track the better its momentum can be reconstructed, giving a good resolution toward lower p_T . Besides, in this momentum range the fake tracks are orders of magnitude rarer than those from EMCal measurements. In the analyses of [42, 115, 134] the HBD backplane is used, which provides a well-defined location for conversion photons. By having the knowledge of the conversion location allows us to reconstruct the real conversion photon momentum. We have used the aforementioned strategy and method in our analysis of low-momentum direct photons in Au+Au collisions at

$\sqrt{s_{NN}} = 62.4 \text{ GeV}$ and $\sqrt{s_{NN}} = 39 \text{ GeV}$.

The goals of the analysis are explained as follows. The experimentally measured inclusive yield of converted photons, N_{ee}^{incl} (being a function of the converted photon momentum), is related to the inclusive yield of real photons γ^{incl} such as

$$N_{ee}^{\text{incl}}(p_{Tee}) = a_{ee} \varepsilon_{ee} p_{conv} \gamma^{\text{incl}}(p_{Tee}), \quad (94)$$

where a_{ee} is the conversion pair geometrical acceptance, ε_{ee} is the conversion pair reconstruction efficiency, and p_{conv} is the probability for a photon to actually undergo a conversion in the HBD backplane. These factors are p_T -dependent, where p_{conv} has much weaker dependence of it.

A subset of the inclusive conversion photon sample is tagged as photons from $\pi^0 \rightarrow 2\gamma$ decays if they reconstruct the π^0 mass with a photon-like shower from the EMCAL. The experimentally measured π^0 -tagged photon yield, $N_{ee}^{\pi^0,\text{tag}}$ (being a function of the converted photon momentum), is related to the yield of real photons coming out from π^0 decays such as

$$N_{ee}^{\pi^0,\text{tag}}(p_{Tee}) = a_{ee} \varepsilon_{ee} p_{conv} \langle \varepsilon_\gamma f \rangle \gamma^{\pi^0}(p_{Tee}) = \langle \varepsilon_\gamma f \rangle N_{ee}^{\pi^0}(p_{Tee}), \quad (95)$$

with the same acceptance, efficiency and probability factors along with another factor, $\langle \varepsilon_\gamma f \rangle$, called for *pion tagging efficiency correction* (Sec. 4.1), which quantifies the efficiency with which the conversion pair is successfully tagged as coming from a π^0 decay given that we have already reconstructed that conversion pair. In the ratio $\gamma^{\text{incl}}/\gamma^{\pi^0}$ the p_T -dependent factors cancel explicitly at each p_{Tee} , except for $\langle \varepsilon_\gamma f \rangle$, which is also a function of the converted photon momentum. Then one can address to this ratio with a more straightforward interpretation in terms of R_γ , which is the ratio of γ^{incl} to photons from hadronic decays. Given this ratio, let us perform the following transformation taking also into account that the ratio $\gamma^{\text{incl}}/\gamma^{\pi^0}$ does not change from a 4π -detector to PHENIX acceptance:

$$R_\gamma = \frac{\gamma^{\text{incl}}}{\gamma^{\text{hadron}}} = \frac{\left(\gamma^{\text{incl}}/\gamma^{\pi^0}\right)}{\left(\gamma^{\text{hadron}}/\gamma^{\pi^0}\right)} = \frac{\left(N_{ee}^{\text{incl}}/N_{ee}^{\pi^0}\right)}{\left(\gamma^{\text{hadron}}/\gamma^{\pi^0}\right)}. \quad (96)$$

Doing some more math with Eq. (96) we derive R_γ to be

$$R_\gamma = \frac{\left(N_{ee}^{\pi^0,\text{tag}}/N_{ee}^{\pi^0}\right) \left(N_{ee}^{\text{incl}}/N_{ee}^{\pi^0,\text{tag}}\right)}{\left(\gamma^{\text{hadron}}/\gamma^{\pi^0}\right)} = \frac{\langle \varepsilon_\gamma f \rangle \left(N_{ee}^{\text{incl}}/N_{ee}^{\pi^0,\text{tag}}\right)}{\left(\gamma^{\text{hadron}}/\gamma^{\pi^0}\right)}. \quad (97)$$

Thereby, the first goal of this analysis is to obtain the ratio R_γ (Sec. 6)

$$R_\gamma = \frac{\langle \varepsilon_\gamma f \rangle \left(N_{ee}^{\text{incl}}/N_{ee}^{\pi^0,\text{tag}}\right)_{\text{data}}}{\left(\gamma^{\text{hadron}}/\gamma^{\pi^0}\right)_{\text{sim}}}. \quad (98)$$

In the double ratio of Eq. (98), the first ratio in the numerator shall be extracted from the data; the second ratio in the denominator, called *cocktail ratio* (Sec. 4.2), plus the factor $\langle \varepsilon_\gamma f \rangle$ shall be extracted from Monte-Carlo simulations.

If we observe more photons than what is expected from hadronic decays we will find that $R_\gamma > 1$. Any such excess photon yield is called *direct photon* yield. Thus, by definition

- Direct photons = Inclusive photons – Hadronic decay photons ,

where the inclusive photons are all the photons, which are measured experimentally. The second goal of the analysis is to obtain the invariant yield of direct photons using the formula

$$\gamma^{\text{direct}} = (R_\gamma - 1) \gamma^{\text{hadron}} \quad (\text{Sec. 7.1}) . \quad (99)$$

In addition to achieving the above-mentioned goals, an important question to answer is the following. If the QGP is produced in Au+Au collisions at 62.4 GeV and 39 GeV center-of-mass energies, whether it can be probed by low-momentum direct photons ?

3.2 Run quality analysis (QA)

The efficiency of charged tracks over the DC can be homogenized if one rejects tracks from the detector edges or depending on a specific run group, from badly performing parts of the DC. We find the run group dependent cuts using the same method, which has been developed for a dielectron analysis, for the PHENIX run10 data set at $\sqrt{s_{NN}} = 200$ GeV [135] (see Sec. 3.2.1 for some more details). The useful runs are grouped into four run groups at 62.4 GeV, and into three run groups at 39 GeV. We show the run group details in Fig. (54), along with the entire run list used in the analysis at both collision energies.

$\sqrt{s_{NN}} = 62.4$ GeV, Run Group 1:

310698, 310699, 310714, 310715, 310718, 310820, 310842, 310843, 310844,
 310845, 310846, 310847, 310933, 310935, 310967, 310968, 310969, 310970,
 310972, 310973, 310974, 310980, 310982, 310983, 310988, 310989, 310990,
 310993, 310996, 310998, 310999, 311000, 311057, 311059, 311092, 311094,
 311095, 311102, 311140, 311142, 311147, 311227, 311228, 311229, 311231,
 311232, 311301, 311302, 311303, 311304, 311307, 311308, 311309, 311311,
 311313, 311314, 311316, 311548, 311550, 311552, 311553, 311561, 311563,
 311564, 311598, 311599, 311623, 311624, 311625, 311626, 311655, 311656,
 311657, 311658, 311659, 311676, 311677, 311678, 311679, 311717, 311718,
 311721, 311722, 311728, 311730, 311731, 311732, 311735, 311736, 311738,

After QA			
Total Number of Events at 62.4 GeV		Total Number of Events at 39 GeV	
RG1+RG2+RG3+RG4 +RG5	$2.24407 \cdot 10^8$ (322 Runs)	RG1+RG2+RG3 +RG4	$8.08667 \cdot 10^7$ (223 runs)
All the Runs Aggregated	100 %	All the Runs Aggregated	100 %
RG1+RG2+RG3+RG4	$2.12011 \cdot 10^8$ (302 Runs)	RG1+RG2+RG3	$7.78933 \cdot 10^7$ (214 runs)
Only the Good Runs Aggregated	94.4762 % (of All)	Only the Good Runs Aggregated	96.3230 % (of All)
Run Group1	$1.72605 \cdot 10^8$	Run Group1	$3.10682 \cdot 10^7$
(250 Runs)	76.9164 % (of All)	(93 Runs)	38.4191 % (of All)
Run Group2	$2.07279 \cdot 10^7$	Run Group2	$4.1638 \cdot 10^7$
(28 Runs)	9.23675 % (of All)	(111 Runs)	51.4896 % (of All)
Run Group3	$1.06814 \cdot 10^7$	Run Group3	$5.18708 \cdot 10^6$
(13 Runs)	4.75983 % (of All)	(10 Runs)	6.41435% (of All)
Run Group4	$7.99604 \cdot 10^6$	Run Group4 (bad runs)	$2.97343 \cdot 10^6$
(11 Runs)	3.56319 % (of All)	(9 Runs)	3.67695 % (of All)
Run Group5 (bad runs)	$1.23959 \cdot 10^7$		
(20 Runs)	5.52384 % (of All)		

Figure 54: The run group details for data samples at $\sqrt{s_{NN}} = 62.4 \text{ GeV}$ and $\sqrt{s_{NN}} = 39 \text{ GeV}$. It is shown the total number of events and the number of runs in all run groups, in both used (“good”) and thrown out (“bad”) run groups.

311739, 311740, 311741, 311744, 311745, 311748, 311749, 311750, 311753, 311795, 311796, 311797, 311800, 311801, 311803, 311804, 311841, 311848, 311849, 311857, 311858, 311859, 311860, 311866, 311867, 311868, 311869, 311870, 311873, 311874, 311937, 311938, 311939, 311940, 311991, 311994, 311995, 311998, 311999, 312001, 312002, 312003, 312004, 312025, 312026, 312029, 312031, 312032, 312036, 312055, 312057, 312061, 312063, 312067, 312095, 312096, 312097, 312098, 312101, 312167, 312168, 312172, 312174, 312195, 312196, 312197, 312200, 312201, 312207, 312208, 312209, 312210, 312212, 312213, 312214, 312215, 312216, 312222, 312223, 312224, 312225, 312226, 312326, 312327, 312328, 312329, 312330, 312332, 312357, 312361, 312363, 312364, 312449, 312450, 312451, 312453, 312470, 312471, 312472, 312473, 312474, 312475, 312476, 312477, 312479, 312597, 312599, 312608,

312615, 312617, 312618, 312633, 312635, 312638, 312640, 312642, 312643, 312759, 312739, 312764, 312770, 312771, 312772, 312773, 312787, 312789, 312791, 312793, 312794, 312818, 312828, 312891, 312937, 312938, 312939, 312940, 312990, 312992, 312994, 312995, 312998, 312999, 313004, 313005, 313006, 313011, 313012, 313013, 313087, 313088, 313089, 313278, 313279, 313282, 313284, 313290, 313298, 313301, 313305, 313322, 310716, 310717, 312371, 312825, 312645, 312650, 312651, 312190, 312192, 312193, 312194, 312467, 312468, 312483, 312648, 313010, 313014, 313147, 313149, 313302.

$\sqrt{s_{NN}} = 62.4 \text{ GeV}$, Run Group 2:

310723, 311032, 311033, 311034, 311037, 311053, 311054, 311055, 311056, 311487, 311488, 311489, 311979, 311983, 311984, 311986, 311990, 312646, 312810, 312814, 312815, 312817, 312824, 312826, 313093, 313094, 313095, 313096.

$\sqrt{s_{NN}} = 62.4 \text{ GeV}$, Run Group 3:

312686, 312687, 312691, 312746, 312747, 312749, 312750, 312751, 312753, 312754, 312755, 312756, 312769.

$\sqrt{s_{NN}} = 62.4 \text{ GeV}$, Run Group 4:

311889, 311890, 311905, 311906, 311907, 311908, 312171, 313128, 313129, 313130, 313131.

$\sqrt{s_{NN}} = 62.4 \text{ GeV}$, Run Group 5 (bad runs):

310716, 310717, 312371, 312825, 312645, 312650, 312651, 312190, 312192, 312193, 312194, 312467, 312468, 312483, 312648, 313010, 313014, 313147, 313149, 313302.

Total number of events in 62.4 GeV data sample:

nevents = 4.9298e+07 in the centrality bin 0-20%;

nevents = 4.9296e+07 in the centrality bin 20-40%;

nevents = 4.9307e+07 in the centrality bin 40-60%;

nevents = 6.4110e+07 in the centrality bin 60-86%;

nevents = 2.1201e+08 in the minimum bias 0-86%.

The charge measured in the BBCs is used to categorize the event centrality.

$\sqrt{s_{NN}} = 39 \text{ GeV}$, Run Group 1:

313591, 313592, 313595, 313596, 313619, 313620, 313625, 313628, 313629, 313641, 313725, 313726, 313727, 313728, 313729, 313731, 313736, 313737,

313739, 313740, 313743, 313744, 313745, 313746, 313748, 313749, 313751, 313752, 313757, 313758, 313790, 313791, 313792, 313793, 313849, 313850, 313851, 313852, 313883, 313884, 313885, 313887, 313897, 313901, 313904, 313908, 313909, 313910, 313911, 313969, 313971, 313972, 313980, 313981, 314011, 314012, 314013, 314015, 314016, 314018, 314019, 314025, 314026, 314027, 314028, 314029, 314031, 314039, 314041, 314042, 314061, 314071, 314072, 314075, 314076, 314077, 314078, 314080, 314261, 314264, 314265, 314268, 314270, 314271, 314273, 314281, 314283, 314284, 314285, 314299, 314300, 314301, 314303.

$\sqrt{s_{NN}} = 39 \text{ GeV}$, Run Group 2:

314309, 314311, 314313, 314447, 314448, 314453, 314455, 314458, 314459, 314463, 314464, 314465, 314469, 314470, 314543, 314580, 314581, 314582, 314583, 314587, 314589, 314590, 314591, 314593, 314594, 314596, 314597, 314598, 314599, 314600, 314601, 314603, 314604, 314606, 314607, 314608, 314609, 314624, 314625, 314626, 314627, 314628, 314693, 314695, 314696, 314697, 314698, 314699, 314700, 314702, 314703, 314704, 314707, 314708, 314709, 314735, 314736, 314753, 314754, 314756, 314757, 314758, 314795, 314796, 314797, 314799, 314829, 314831, 314832, 314833, 314834, 314835, 314836, 314837, 314840, 314841, 314842, 314843, 314858, 314859, 314861, 314862, 314863, 314865, 314866, 314867, 314868, 314935, 314936, 314937, 314941, 314942, 314944, 314945, 314947, 314948, 314949, 314950, 314951, 314955, 314956, 314957, 314973, 314974, 314975, 314976, 314990, 314991, 314992, 314993, 314994.

$\sqrt{s_{NN}} = 39 \text{ GeV}$, Run Group 3:

313606, 313609, 313614, 313618, 313754, 313755, 313896, 313907, 313967, 313968, 313978, 314033, 314034, 314058, 314059, 314314, 314315, 314316, 314318.

$\sqrt{s_{NN}} = 39 \text{ GeV}$, Run Group 4 (bad runs):

313614, 313618, 313978, 314033, 314034, 314314, 314315, 314316, 314318.

Total number of events in 39 GeV data sample:

nevents = 1.8113e+07 in the centrality bin 0-20%;

nevents = 1.8116e+07 in the centrality bin 20-40%;

nevents = 1.8116e+07 in the centrality bin 40-60%;

nevents = 2.3548e+07 in the centrality bin 60-86%;

`nevents = 7.7893e+07 in the minimum bias 0-86%.`

The charge measured in the BBCs is used to categorize the event centrality.

Also, we show the total number of events vs. centrality (in bins of 10%) from the data sets at both energies, which can be seen in Figs. (55) and (56). All further analysis is done in slices of converted photon p_{Tee} bins, which we show for each centrality class in Table (2) and Table (3).

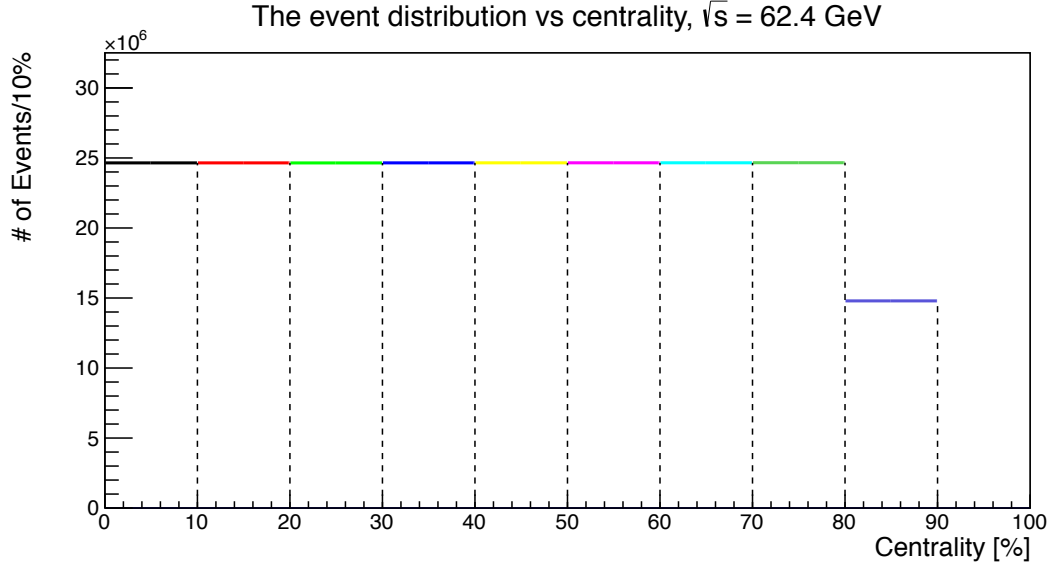


Figure 55: The total number of events in 62.4 GeV data set for centrality bins in 10%.

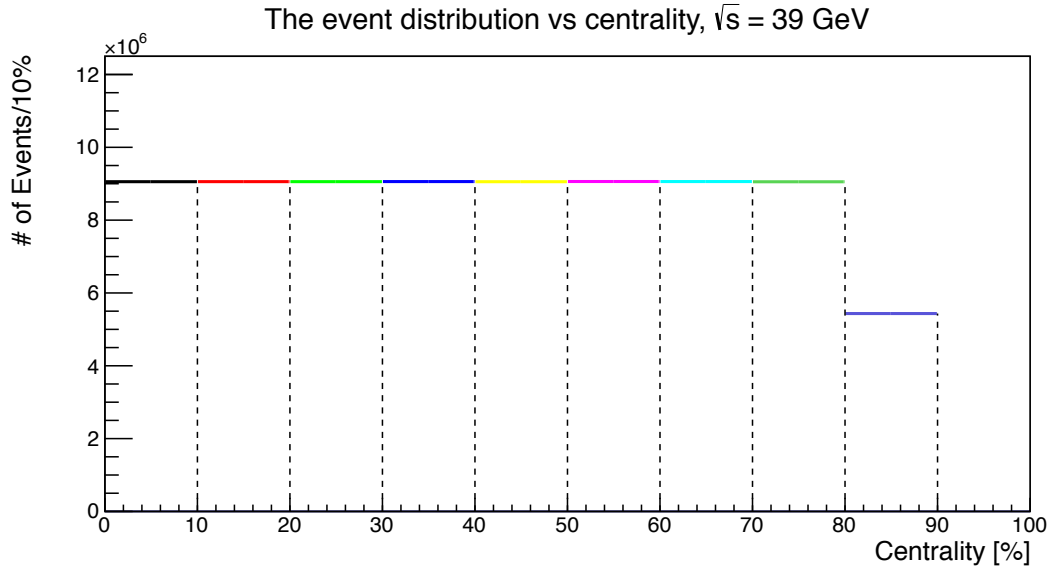


Figure 56: The total number of events in 39 GeV data set for centrality bins in 10%.

0-20%	20-40%	40-60%	60-86%	0-86%
0.5 - 0.7	0.5 - 0.7	0.5 - 0.7	0.5 - 0.7	0.5 - 0.7
0.7 - 0.9	0.7 - 0.9	0.7 - 0.9	0.7 - 0.9	0.7 - 0.9
0.9 - 1.1	0.9 - 1.1	0.9 - 1.1	0.9 - 1.1	0.9 - 1.1
1.1 - 1.3	1.1 - 1.3	1.1 - 1.3	1.1 - 1.3	1.1 - 1.3
1.3 - 1.5	1.3 - 1.5	1.3 - 1.5	1.3 - 1.5	1.3 - 1.5
1.5 - 1.7	1.5 - 1.7	1.5 - 1.7	1.5 - 1.7	1.5 - 1.7
1.7 - 1.9	1.7 - 1.9	1.7 - 1.9		1.7 - 1.9
1.9 - 2.1	1.9 - 2.1	1.9 - 2.1		1.9 - 2.1
2.1 - 2.5	2.1 - 2.5	2.1 - 2.5		2.1 - 2.5
2.5 - 3.0	2.5 - 3.0			2.5 - 3.0

Table 2: The segmented p_{Tee} bins of converted photons (in GeV/c) in four centrality bins plus the minimum bias at $\sqrt{s_{NN}} = 62.4$ GeV.

0-20%	20-40%	40-60%	60-86%	0-86%
0.4 - 0.6	0.4 - 0.6	0.4 - 0.6	0.4 - 0.6	0.4 - 0.6
0.6 - 0.8	0.6 - 0.8	0.6 - 0.8	0.6 - 0.8	0.6 - 0.8
0.8 - 1.0	0.8 - 1.0	0.8 - 1.0	0.8 - 1.0	0.8 - 1.0
1.0 - 1.2	1.0 - 1.2	1.0 - 1.2	1.0 - 1.2	1.0 - 1.2
1.2 - 1.4	1.2 - 1.4	1.2 - 1.4	1.2 - 1.4	1.2 - 1.4
1.4 - 1.6	1.4 - 1.6	1.4 - 1.6	1.4 - 1.6	1.4 - 1.6
1.6 - 1.8	1.6 - 1.8	1.6 - 1.8		1.6 - 1.8
1.8 - 2.0	1.8 - 2.0			1.8 - 2.0
2.0 - 3.0	2.0 - 3.0			2.0 - 3.0

Table 3: The segmented p_{Tee} bins of converted photons (in GeV/c) in four centrality bins plus the minimum bias at $\sqrt{s_{NN}} = 39$ GeV.

3.2.1 DC hitmaps/deadmaps, electron multiplicities and cluster multiplicities

The DC (and also PC) is designed to determine the trajectories and momenta of e^+e^- pairs. We use run group dependent cuts, called fiducial cuts, which are parametrized as a function of the track variables, α (in mrad), ϕ_{DC} (in mrad), z_{DC} (in cm) and the hit board in the DC:

- The variable α is the difference between the direction of a track at the reference radius and the radial direction. It can also be interpreted as a bend angle, which is proportional to the transverse momentum of a track, and which can be calculated from the charge q (assigned to each track) and p_T :

$$\alpha = -(3.28688 \cdot 10^{-5} + 0.0753907 \frac{q}{p_T}) . \quad (100)$$

- The variable ϕ_{DC} is the azimuth of a track at the reference radius of $R = 220$ cm.

- The variable z_{DC} is the z-location of a track along the beam axis at the reference radius.
- The hit board is a function of ϕ_{DC} parameterized as

$$\begin{aligned} \text{board} &= \frac{1}{0.01963496} (3.72402 - \phi_{DC} + 0.008047 \cos(\phi_{DC} + 0.87851)) \quad \text{if } \phi_{DC} > \frac{\pi}{2}, \\ \text{board} &= \frac{1}{0.01963496} (0.573231 - \phi_{DC} + 0.0046 \cos(\phi_{DC} + 0.05721)) \quad \text{else}. \end{aligned} \quad (101)$$

Since the DC board extends either in the positive or negative z-direction, the tracks are uniformly distributed in both directions with equal probabilities. The DC can have some badly performing parts like some cold regions (inefficient regions). We identify these regions because of broken wires or high voltage problems. The fiducial cuts then cut and exclude these regions, making the DC deadmaps on top of hitmaps.

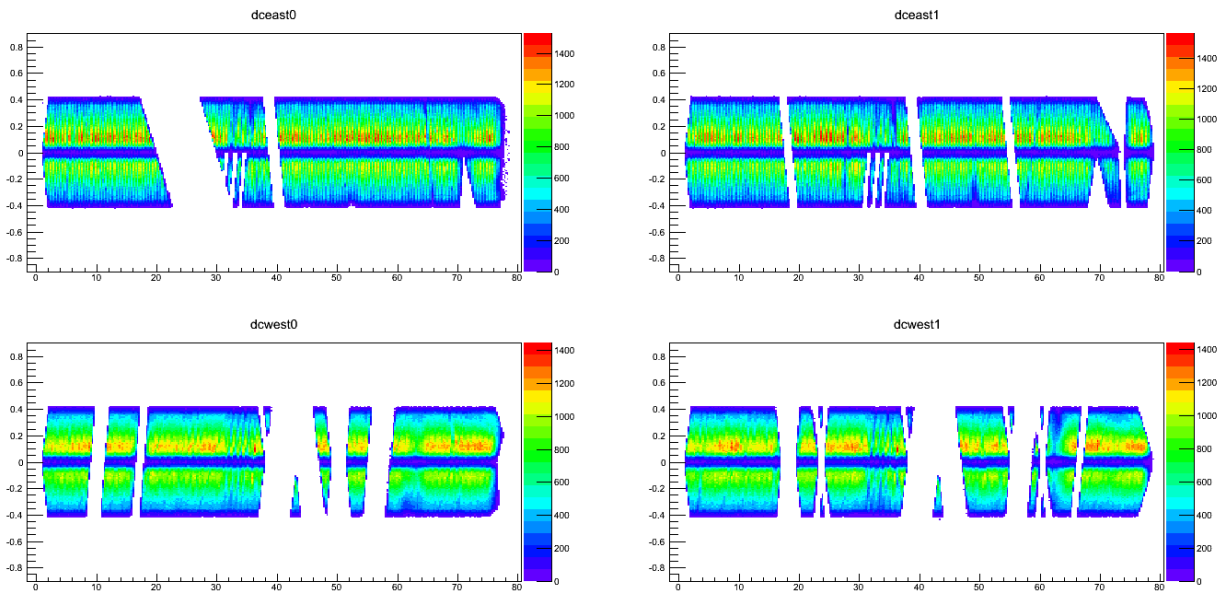


Figure 57: A randomly chosen DC hitmaps/deadmaps from the “good” Run Group 1 corresponding to the run number 310714 at $\sqrt{s_{NN}} = 62.4$ GeV. The vertical is α , the horizontal is the board number.

For the purpose of visualization it is relevant to show Figs. (57), (58), (59),(60), (61), which have the hitmaps/deadmaps at $\sqrt{s_{NN}} = 62.4$ GeV, and Figs. (62), (63), (64), (65), which have the hitmaps/deadmaps at $\sqrt{s_{NN}} = 39$ GeV. From each run group we randomly select one run, and each figure corresponds to one run selection (see run groups in Sec. 3.2). Each figure has four plots: the upper left corresponds to the DC northeast (dceast0), the upper right corresponds to the DC southeast (dceast1), the bottom left corresponds to the DC northwest (dcwest0), the bottom right corresponds to the DC southwest (dcwest1).

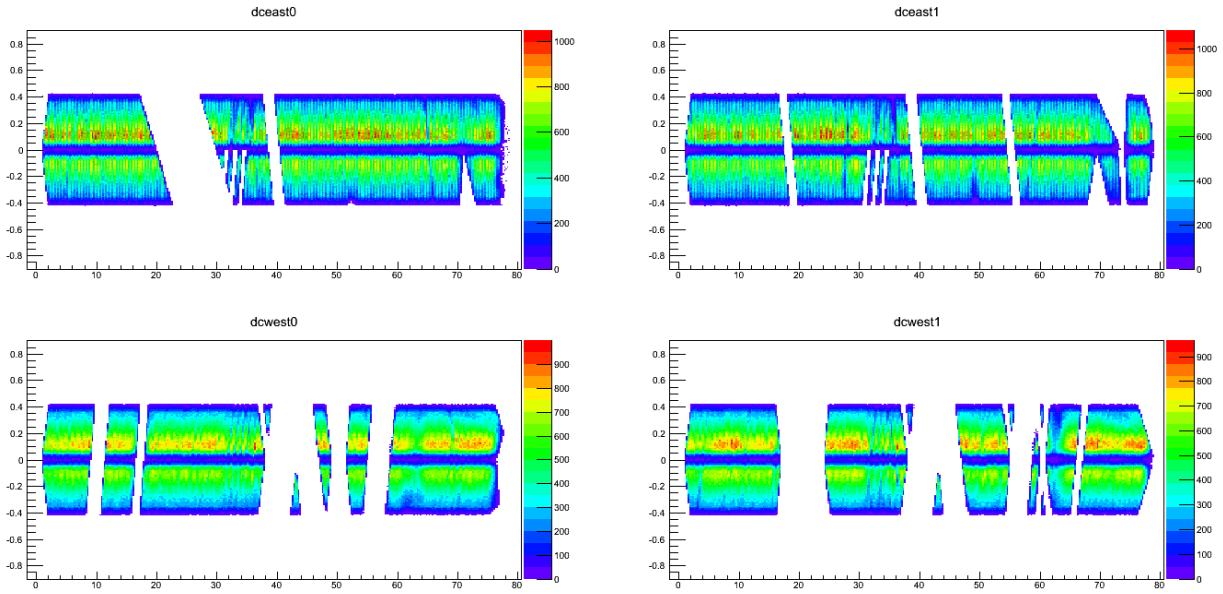


Figure 58: A randomly chosen DC hitmaps/deadmaps from the “good” Run Group 2 corresponding to the run number 311032 at $\sqrt{s_{NN}} = 62.4$ GeV. The vertical is α , the horizontal is the board number.

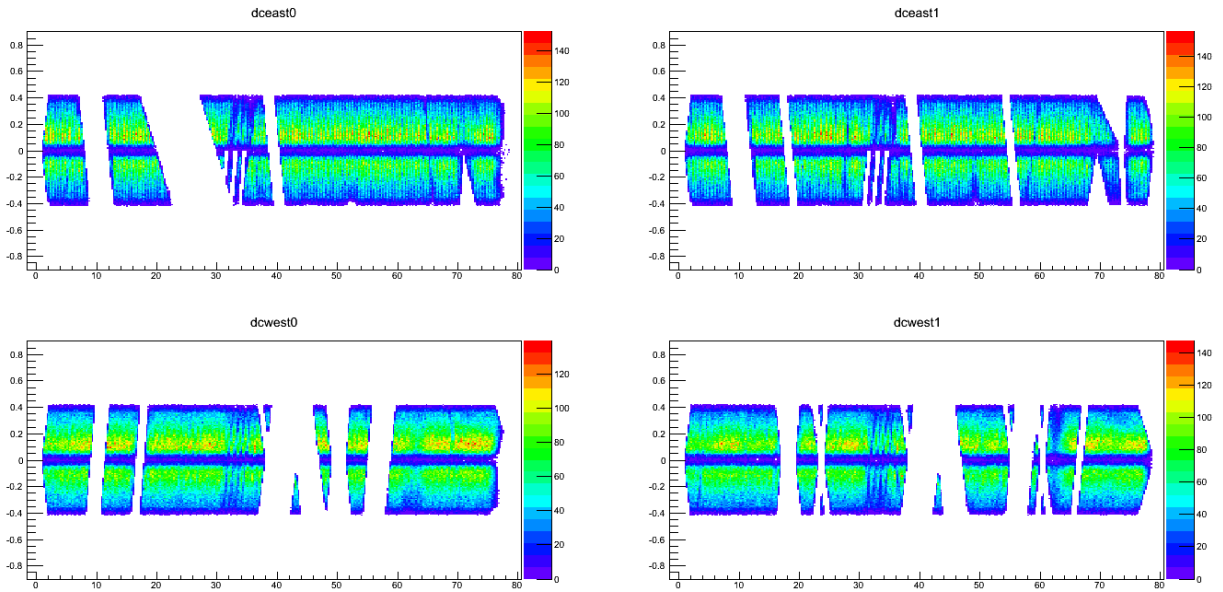


Figure 59: A randomly chosen DC hitmaps/deadmaps from the “good” Run Group 3 corresponding to the run number 312691 at $\sqrt{s_{NN}} = 62.4$ GeV. The vertical is α , the horizontal is the board number.

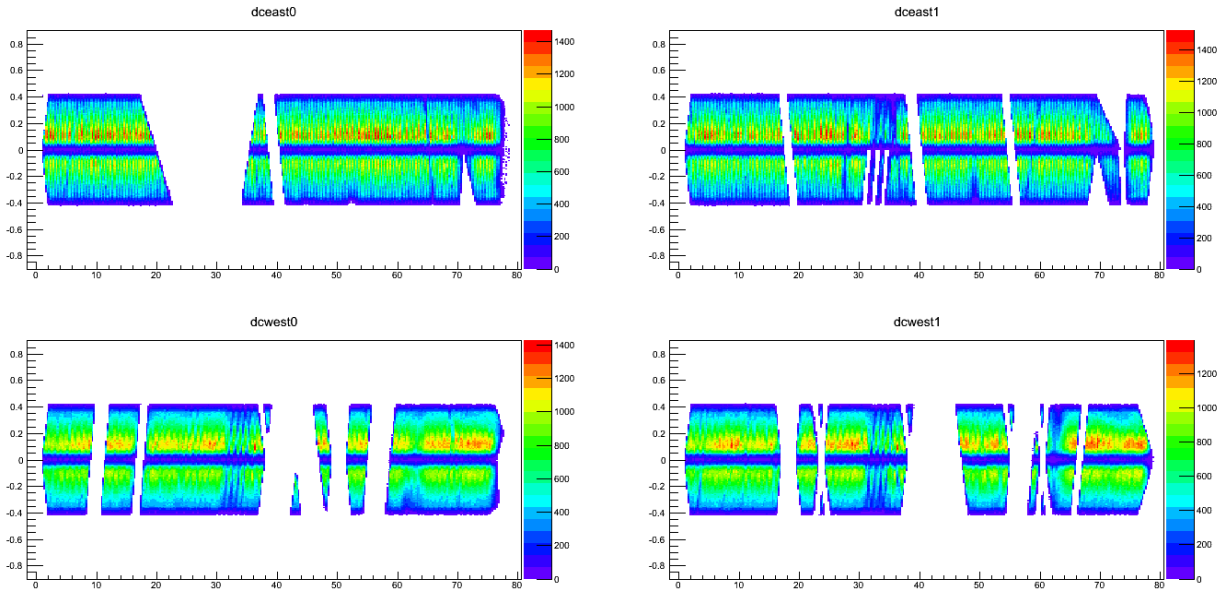


Figure 60: A randomly chosen DC hitmaps/deadmaps from the “good” Run Group 4 corresponding to the run number 311905 at $\sqrt{s_{NN}} = 62.4$ GeV. The vertical is α , the horizontal is the board number.

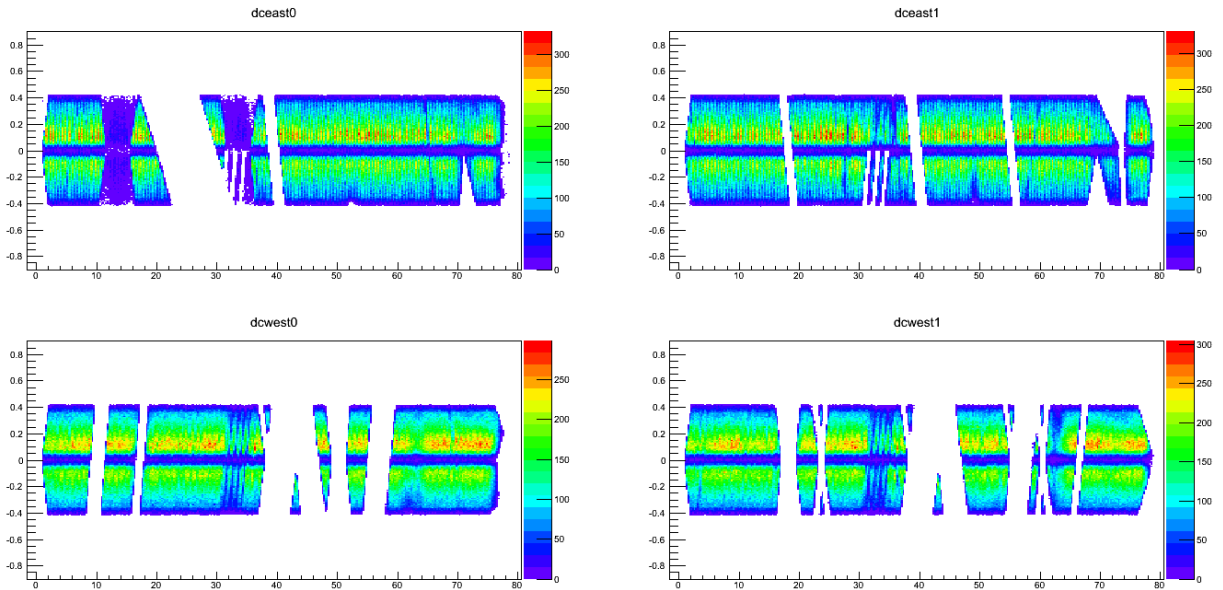


Figure 61: A randomly chosen DC hitmaps/deadmaps from the “bad” Run Group 5 corresponding to the run number 312467 at $\sqrt{s_{NN}} = 62.4$ GeV. The vertical is α , the horizontal is the board number.

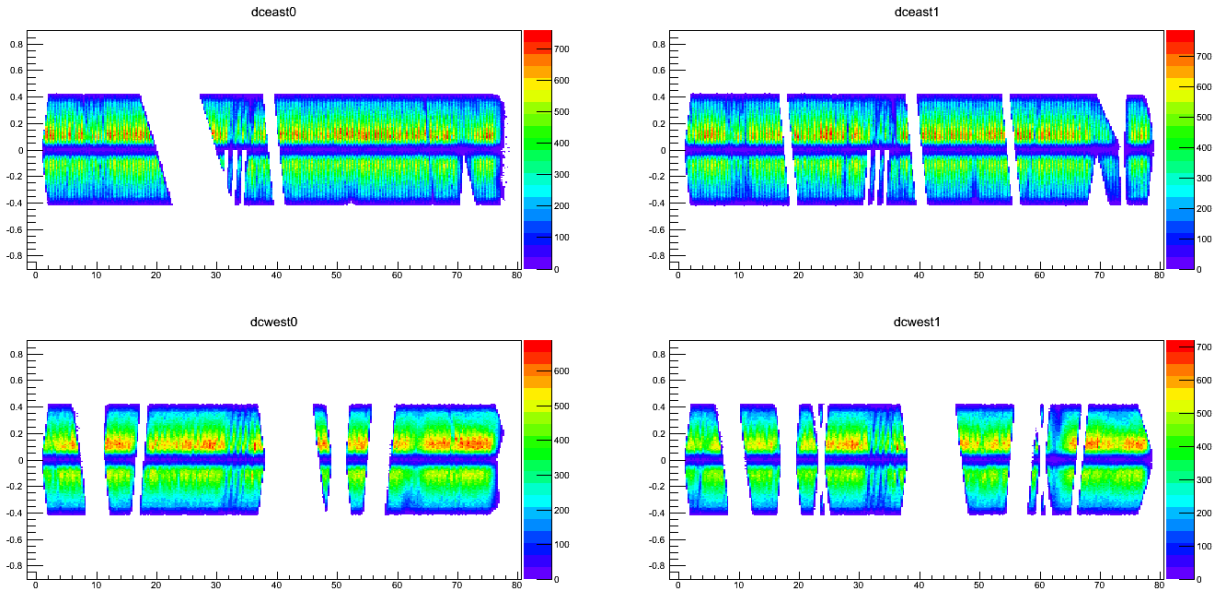


Figure 62: A randomly chosen DC hitmaps/deadmaps from the “good” Run Group 1 corresponding to the run number 313725 at $\sqrt{s_{NN}} = 39$ GeV. The vertical is α , the horizontal is the board number.

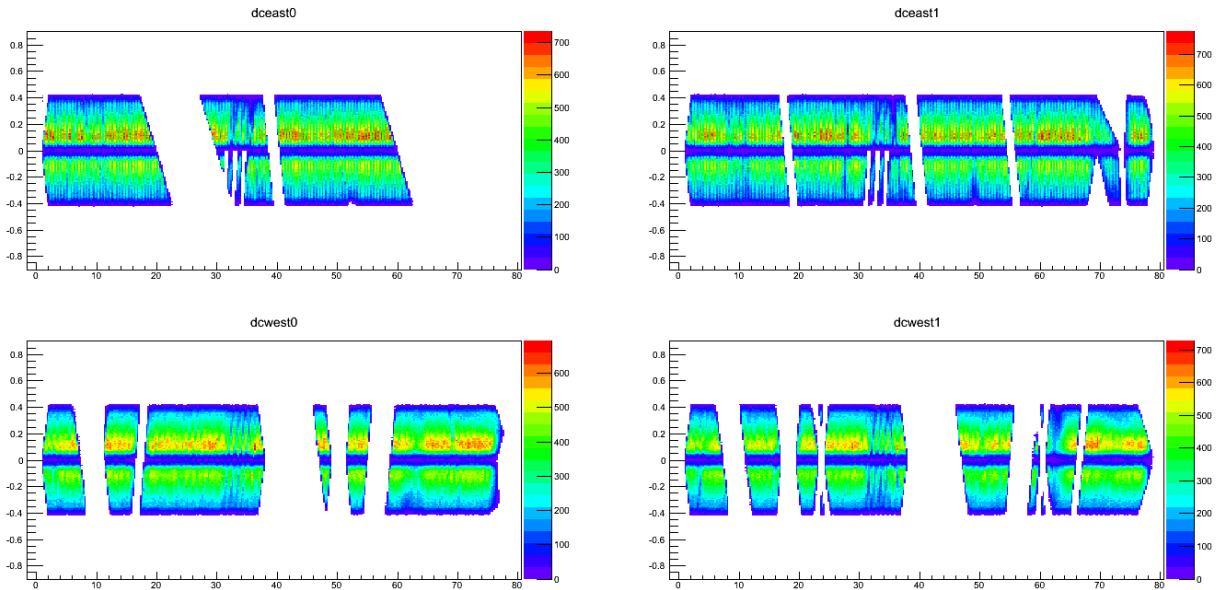


Figure 63: A randomly chosen DC hitmaps/deadmaps from the “good” Run Group 2 corresponding to the run number 314459 at $\sqrt{s_{NN}} = 39$ GeV. The vertical is α , the horizontal is the board number.

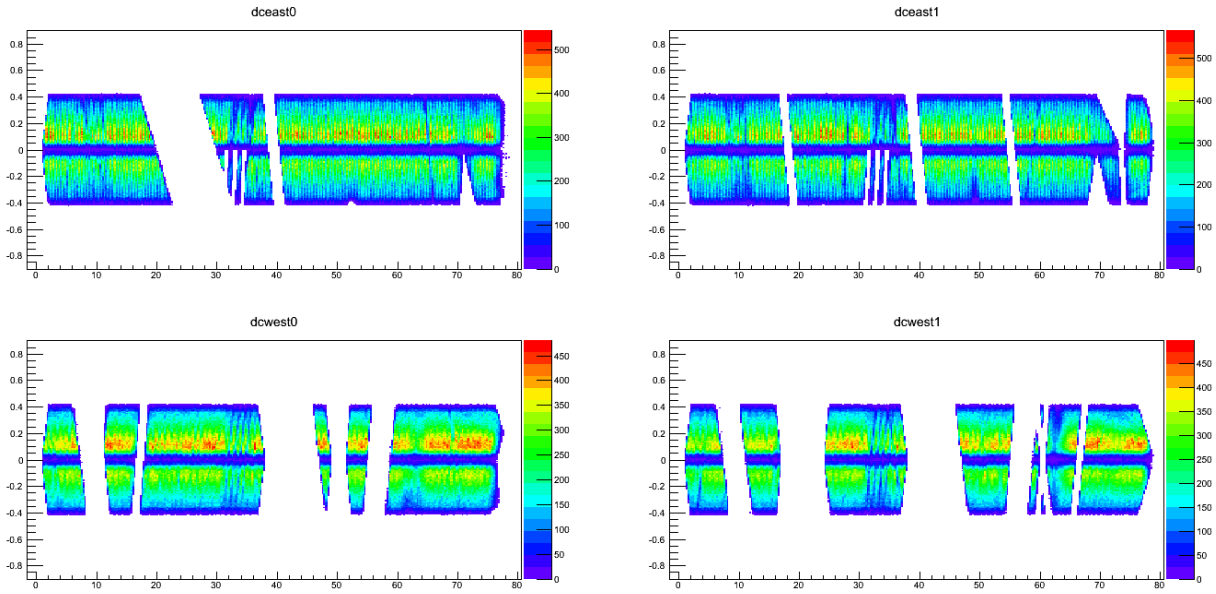


Figure 64: A randomly chosen DC hitmaps/deadmaps from the “good” Run Group 3 corresponding to the run number 313755 at $\sqrt{s_{NN}} = 39$ GeV. The vertical is α , the horizontal is the board number.

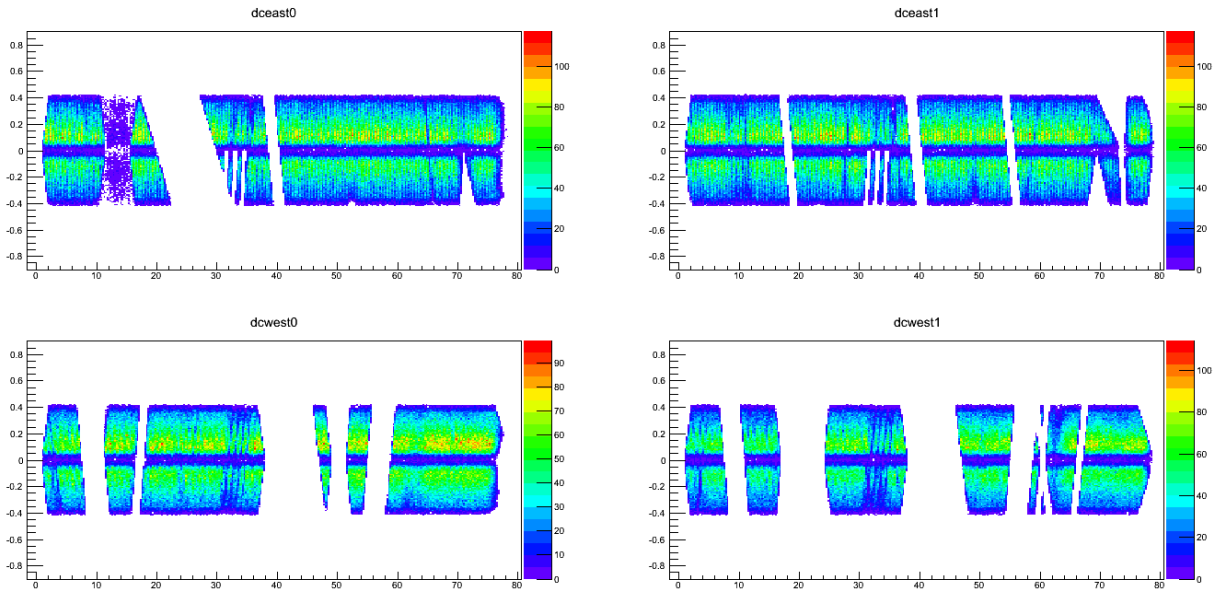


Figure 65: A randomly chosen DC hitmaps/deadmaps from the “bad” Run Group 4 corresponding to the run number 313614 at $\sqrt{s_{NN}} = 39$ GeV. The vertical is α , the horizontal is the board number.

In Figs. (66) and (67) one can see the integrated electron multiplicity (per number of events) vs run number for the first four run groups at 62.4 GeV, and for the first three run groups at 39 GeV. The same is also shown for the mean value of the EMCAL cluster multiplicity in Figs. (68) and (69).

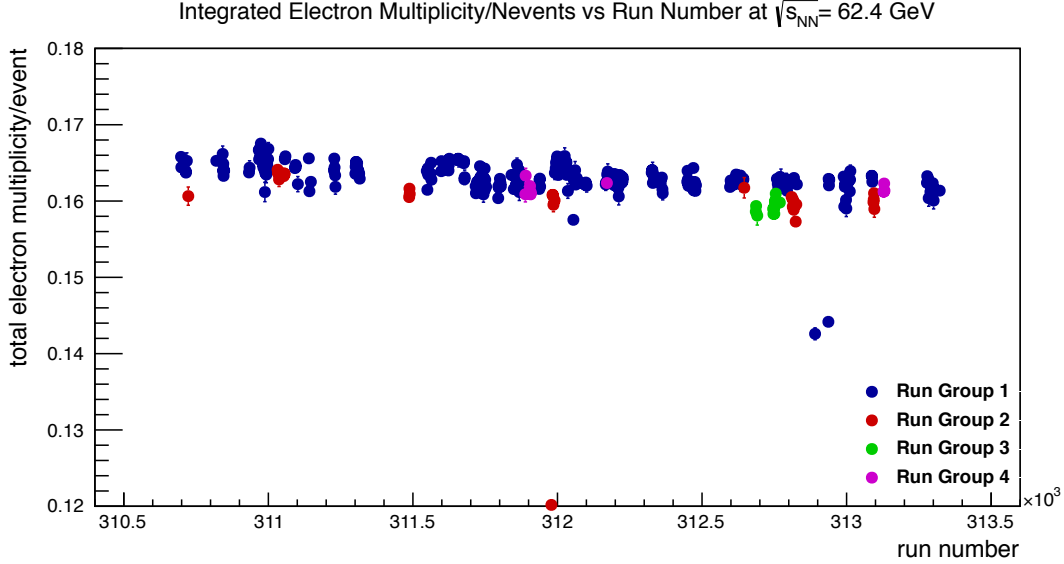


Figure 66: The integrated electron multiplicity (per number of events) vs run number for the first four run groups at $\sqrt{s_{NN}} = 62.4$ GeV.

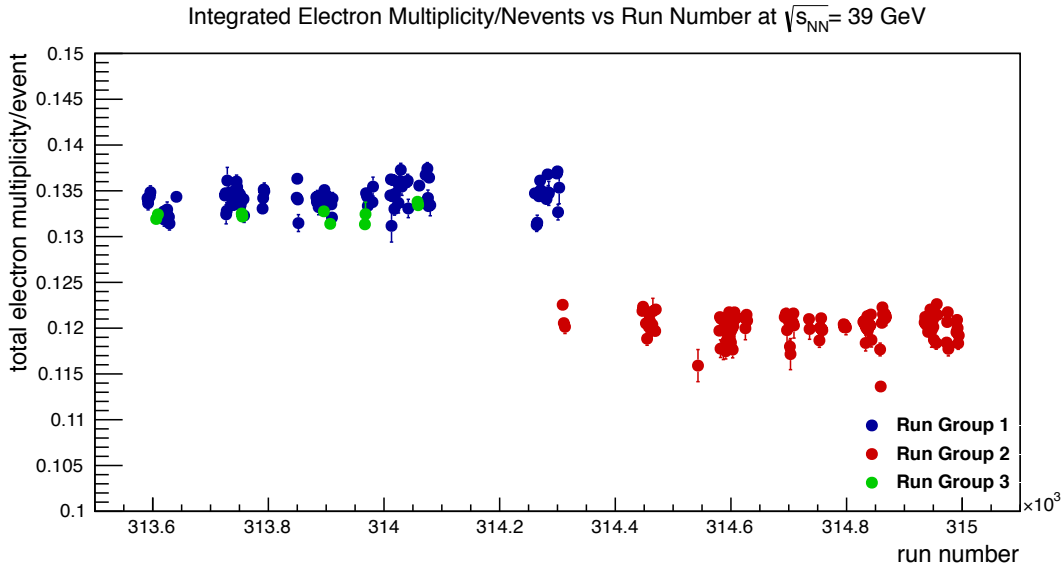


Figure 67: The integrated electron multiplicity (per number of events) vs run number for the first three run groups at $\sqrt{s_{NN}} = 39$ GeV. This difference between Run Group 1 and Run Group 2, for example, can be traced to Fig. (62) and Fig. (63). The dceast0 in Fig. (63) has a cold region cut out, which is not the case in Fig. (62). That is why the red points here are below the blue ones.

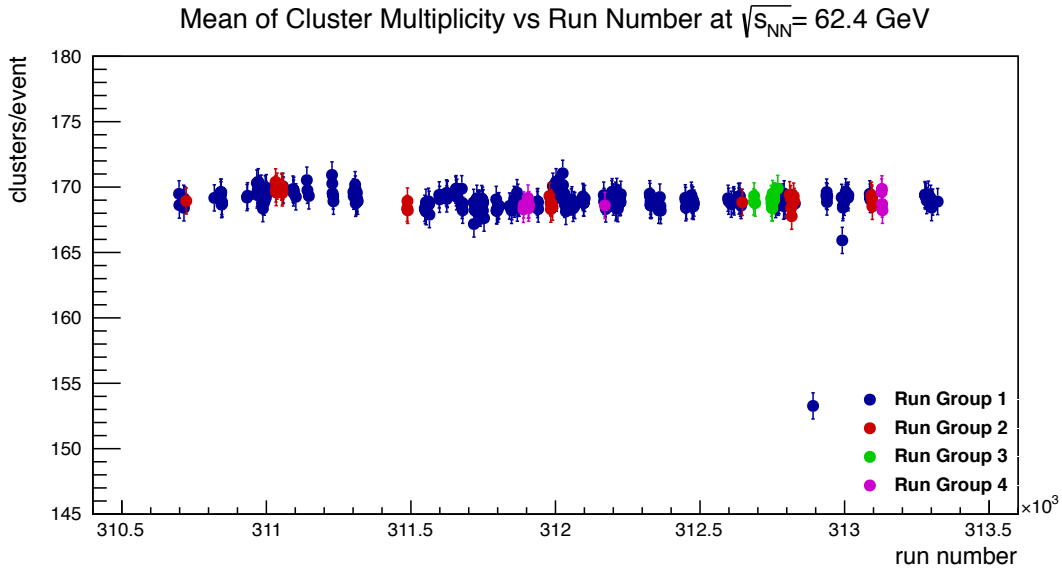


Figure 68: The mean value of the EMCal cluster multiplicity (per number of events) vs run number for the first four run groups at $\sqrt{s_{NN}} = 62.4$ GeV.

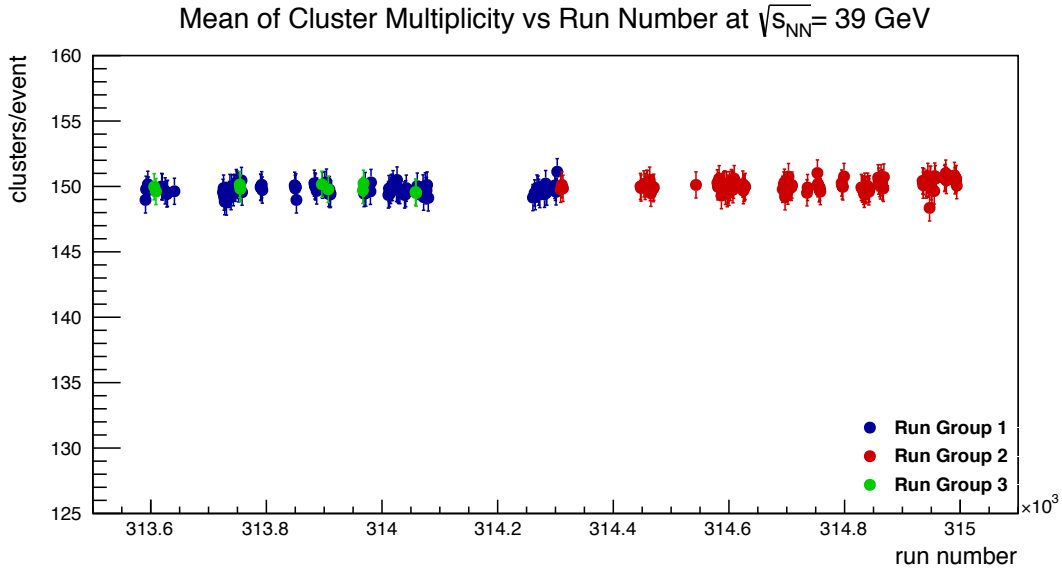


Figure 69: The mean value of the EMCal cluster multiplicity (per number of events) vs run number for the first three run groups at $\sqrt{s_{NN}} = 39$ GeV.

3.2.2 EMCal hitmaps/deadmaps

For the EMCal photon measurements we use a clustering algorithm, utilized for example in [115, 133]. The algorithm is based upon reconstruction of the full energy of an incoming particle as clusters in a calorimeter [136]. A minimum threshold of 10 MeV on each EMCal tower is applied in order to reduce noise effects. Adjacent towers, which share the same edges are combined into some clusters

called “isolated” clusters. These isolated clusters contain hits from one or more particles thus requiring further checks. Next a local maximum is identified within each isolated cluster, which suggests that multiple particles participate in the energy deposition. The requirements for the local maximum is

- a) There should be maximum energy in 3×3 tower area¹⁶.
- b) The energy in the central tower has to be more than 80 MeV.

If a tower is shared according to the amplitude and position of one or more local maxima, then the tower energy is split according to the shower profile determined from simulations and beam tests.

One can use an empirical formula describing a parametrization of the energy deposits in the towers [133, 137]:

$$\frac{E_i^{\text{pred}}}{E_{\text{all}}^{\text{meas}}} = p_1(E_{\text{all}}^{\text{meas}}, \theta) \times \exp\left(-\frac{(r_i/r_0)^3}{p_2(E_{\text{all}}^{\text{meas}}, \theta)}\right) + p_3(E_{\text{all}}^{\text{meas}}, \theta) \times \exp\left(-\frac{(r_i/r_0)}{p_4(E_{\text{all}}^{\text{meas}}, \theta)}\right), \quad (102)$$

where E_i^{pred} is the predicted energy deposit in the i^{th} tower from the shower shape profile, $E_{\text{all}}^{\text{meas}}$ is the measured energy of an incoming particle (equivalent to the total energy in the peak area). The angle θ is the impact angle between the perpendicular axis from the surface of the detector and the incoming particle. The distance r_i is the distance of the i^{th} tower center from the center-of-mass of the cluster, and r_0 is the single tower size. The parameters $p_i(E, \theta)$ are shown below:

$$\begin{aligned} p_1(E, \theta) &= 0.59 - (1.45 + 0.13 \ln E) \sin^2 \theta, \\ p_2(E, \theta) &= 0.26 + (0.80 + 0.32 \ln E) \sin^2 \theta, \\ p_3(E, \theta) &= 0.25 + (1.45 - 0.36 \ln E) \sin^2 \theta, \\ p_4(E, \theta) &= 0.42. \end{aligned} \quad (103)$$

In Eq. (102) the first term describes the shower profile, which is dominant at small distances from the impact point ($\ll 5$ cm), while the second term describes the exponential behavior dominating over the large distances.

The beam tests have also been used for energy fluctuation studies. If the particle impact angle is non-zero, then the result is the shifting of larger energy deposits from the impact point. Also, the width and depth of the shower depends on the energy of an incoming particle. The fluctuations of the energy deposits in the showers are described by

$$\sigma_i^2 = q(E_{\text{all}}^{\text{meas}}) + C E_i^{\text{pred}} \times \left(1 - \frac{E_i^{\text{pred}}}{E_{\text{all}}^{\text{meas}}} + f(E_{\text{all}}^{\text{meas}}, \theta) \left(1 - \frac{E_i^{\text{pred}}}{E_{\text{all}}^{\text{meas}}}\right)\right), \quad (104)$$

¹⁶Electromagnetic showers are typically contained in a 3×3 tower area.

where $C = 0.03 \text{ GeV}$ is the scale of the energy fluctuations obtained during the beam tests. Due to the threshold used in the clustering algorithm, the total energy of the cluster is biased as $q(E) = 0.005^2 + 0.0014^2 E^2 [\text{GeV}^2]$. The shape of the shower is distorted due to its energy and impact angle. This distortion is parametrized as $f(E, \theta) = (4.00/0.03)\sqrt{E} \sin^4\theta$.

It is also necessary to have information about the hit position of the clusters. The hit position of a cluster is determined from the center of gravity of the amplitudes of each tower in the cluster. Having just the tower center with the most deposited energy in the cluster is not sufficient for a good analysis, taking into account that the position measurement is also limited by the granularity. A precise position can be calculated from [133, 138]

$$(x, y)_{\text{cent}} = \frac{\sum_{\text{cluster}} [(x_i, y_i) \omega_i]}{\sum_{\text{cluster}} [\omega_i]}, \quad \text{with } \omega_i = \max\left(0, \omega_0 + \ln\left(\frac{E_i}{\sum E_i}\right)\right). \quad (105)$$

In the weight factor, ω_i , the logarithm enhances the contribution of the shower periphery to the coordinate measurement. At larger distances from the center, the logarithmic dependence of the deposited energy is more linear as a function of the distance. The linear behavior stems from the second term of Eq. (102), which dominates at larger distances. The free parameter, ω_0 , puts a threshold on the fraction of the total shower energy deposited in the tower, excluding some channels with noise level. The optimal value of ω_0 is from 3.0 (at $E = 0.5 \text{ GeV}$) to 4.0 (at $E = 8.0 \text{ GeV}$).

The true position of the impact is actually not the same as the center of gravity, because of the fact that the electromagnetic shower profile can be deformed depending on the incident angle. Therefore, the acquired position is further corrected by the incoming particle's angle, if one assumes that it is a photon. The parametrization of the shower center-of-gravity in terms of the tower coordinates, taking into account the position correction, is the following:

$$(x, y)_{\text{cent}}^{\text{corr}} = \frac{\sinh[(x, y)_{\text{imp}} + \Delta - \delta] / b}{2 \sinh[1/2b]} + \delta, \quad \text{with } |(x, y)_{\text{imp}} + \Delta + \delta| \leq \frac{1}{2}, \quad (106)$$

where $(x, y)_{\text{imp}}$ is the impact point of the particle from Eq. (105), Δ is the mean displacement of the calculated shower center-of-gravity from $(x, y)_{\text{imp}}$, δ is the phase shift related to the shape of the shower projection, b is the cross-sectional width of the shower. Fig. (70) shows an example of a symmetrically developed shower in terms of the tower energy deposits, with $\theta = 90^\circ$ impact at the center of a tower.

Now going back to the PHENIX EMCal we note that each of the six PbSc sectors has 36 towers in the y-direction and 72 towers in the z-direction. Also, each of the two PbGl sectors has 48 towers in the y-direction and 96 towers in the z-direction. Thereby, the total number of the towers in the EMCal will be

$$\text{Number of Towers} = 6 \cdot 36 \cdot 72 + 2 \cdot 48 \cdot 96 = 24768.$$

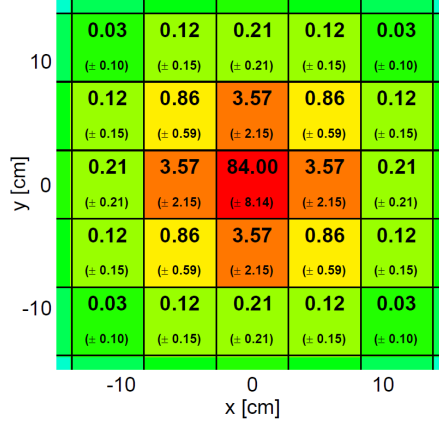


Figure 70: The fraction of the deposited energy in each tower of the PbSc by the electromagnetic shower at the impact point in (0, 0) cm, and with no impact angle ($\theta = 0$). Each cell corresponds to one tower. The upper number in each cell represents the fraction of the total deposited energy (from Eq. (102)), and the lower numbers represent the energy fluctuations (from Eq. (104)) with $E_{total} = 10$ GeV. The figure is from [133].

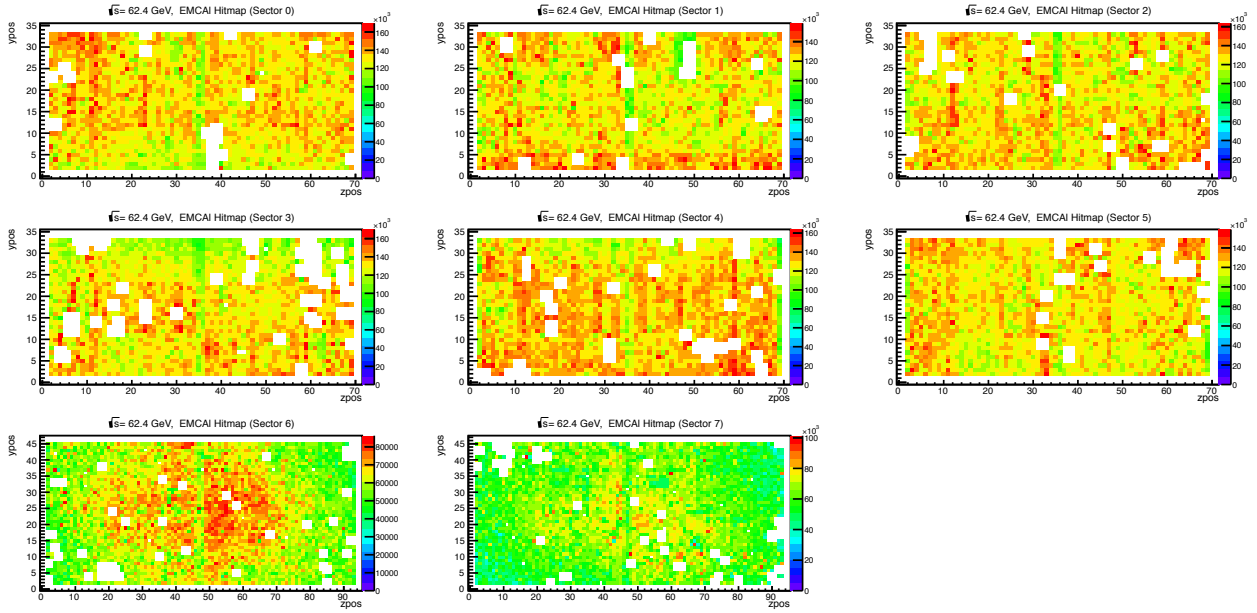


Figure 71: The EMCal hitmaps/deadmaps for the eight sectors at $\sqrt{s_{NN}} = 62.4$ GeV.

The EMCal deadmaps on top of hitmaps include masks on dead and hot towers as well as additional masking on an area of 3×3 towers around the dead/hot channels to avoid the signal loss and distortion from a photon depositing part of its energy into a dead tower. The clusters with centers on

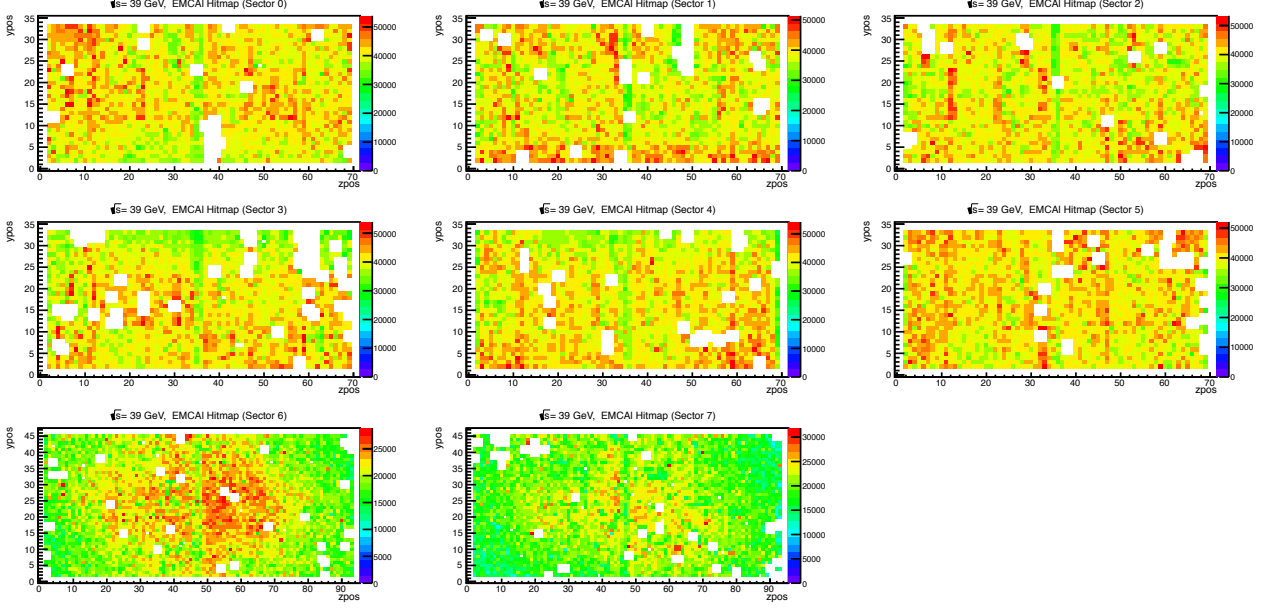


Figure 72: The EMCal hitmaps/deadmaps for the eight sectors at $\sqrt{s_{NN}} = 39 \text{ GeV}$.

these edge towers are rejected. In Figs. (71) and (72) one can see the EMCal hitmaps/deadmaps for the six PbSc (upper) and two PbGl (bottom) sectors at both collision energies. These deadmaps are obtained by excluding the hot and dead regions in the data, and later the deadmaps are put into the simulation.

3.3 The cuts of the inclusive photon sample

3.3.1 The event cut and electron cuts

- Event cut. In order to reconstruct and recalibrate the conversion pair tracks originating from the HBD backplane, we select only those events that are within a narrow z_{vertex} range, where the magnetic field is relatively uniform.

$$\text{Event cut: } |z_{vertex}| < 10 \text{ cm} . \quad (107)$$

We use the following standard Au+Au electron selection cuts.

- Momentum cut.

$$\text{Momentum cut: } 0.2 \text{ GeV/c} < p_T < 20 \text{ GeV/c} . \quad (108)$$

The lower limit $p_T > 0.2 \text{ GeV/c}$ is used to avoid edge effects. The upper limit $p_T < 20 \text{ GeV/c}$ is used to remove misreconstructed or fake tracks. By using these cuts we ensure that a good sample of well-reconstructed tracks is selected.

- Track quality cut. By correlating hits in the DCs and PCs outside of the magnetic field, we reconstruct the tracks of charged particles. We use a quality cut that encodes the hits used to form tracks in the DCs and PCs.

$$\text{Track quality cut: } \text{quality} \in \{31, 51, 63\} . \quad (109)$$

- 31: In this case a track has hits in the DC X_1 and X_2 layers, also a unique hit in the DC UV layer and a non-unique hit in the PC1;
- 51: In this case a track has hits in the DC X_1 and X_2 layers, also a unique hit in the PC1;
- 63: In this case a track has hits in the DC X_1 and X_2 layers, also unique hits in the DC UV layer and in the PC1.

- Ring Imaging Cherenkov Detector (RICH) electron ID cuts. These cuts are made for electron identification. One can quantify the information quality from the RICH in terms of the number of hit phototubes in rings of different sizes. We use the number n_0 , which is the number of phototubes that are hit in a ring with the radius $3.4 \text{ cm} < r < 8.4 \text{ cm}$, around a track's projection to the RICH.

$$\text{RICH } n_0 \text{ cut: } n_0 \geq 3 . \quad (110)$$

There is a variable called *disp*, which measures the distance between the track's projection and the center of the ring reconstructed in the RICH.

$$\text{RICH disp cut: } \text{disp} < 5 . \quad (111)$$

Another variable, χ^2 , measures the match of the fired phototubes to a ring shape, and the number of phototubes used in the ring is designated as *npe*. Then their ratio, χ^2/npe , quantifies the quality of the reconstructed ring:

$$\text{RICH } \chi^2/npe \text{ cut: } \chi^2/npe < 10 . \quad (112)$$

- EMCal electron ID cuts. These cuts are made to have additional rejection of hadrons passing the RICH cuts. We put a lower limit on the energy reconstructed in the EMCals:

$$\text{EMCal energy cut: } E > 0.15 \text{ GeV/c}^2 . \quad (113)$$

Besides, we also use an additional cut by which at least half of the energy expected from tracks should be recovered in the EMCals:

$$\text{EMCal energy-momentum ratio cut: } E/p > 0.5 . \quad (114)$$

3.3.2 The conversion pair cuts

In PHENIX we reconstruct the e^+e^- pair mass i) with the standard PHENIX momentum reconstruction algorithm assuming that the charged tracks originate from the true event vertex (interaction point); ii) with the alternate tracking model (ATM) [42, 115] assuming that the photon conversions take place at the HBD backplane along with the momenta of the conversion candidates being recalculated.

In the standard PHENIX momentum reconstruction algorithm the conversion pairs acquire a fake large invariant mass (designated as M_{vtx}). The electrons and positrons originating from ≈ 60 cm will be misreconstructed under an incorrect assumption of the origin at the true event vertex. This results in a misreconstruction of their momenta by which they acquire an artificial opening angle (see Fig. (73) for a cartoon). Although a photon conversion should have zero opening angle (the real photon is massless after all). Stated otherwise, at points $R \neq 0$ the off-vertex, the conversion pairs produced with zero opening angle and no mass, obtain an artificially enlarged opening angle if extrapolated to the true event vertex. This is because the extrapolation to this vertex gives an overestimate of the field integral experienced by particles, and causes their momenta to be overestimated by the reconstruction. This artificial opening angle translates to the above-mentioned fake invariant mass of the e^+e^- pair. The greater the amount of misreconstruction, the larger the fake mass.

Nonetheless, this does not happen with the conversion candidates in the HBD backplane, where the ATM faithfully reconstructs the tracks originating from it with very small opening angles (the corresponding mass is respectively small). The choice of the HBD backplane for the pair conversion location is due to the fact that its large distance from the true event vertex and its radiation thickness¹⁷, without any other comparable radiating material nearby, makes the converted photons' identification very accurate in our data samples obtained in Au+Au collisions at $\sqrt{s_{NN}} = 62.4$ GeV and $\sqrt{s_{NN}} = 39$ GeV (which was also the case for 200 GeV analysis).

The ATM is a re-parametrization of the reconstructed momenta with an alternate vertex assumption rather than with the true event vertex. It is based on a conversion recalibrator, which has been developed to increase the ability for selection of the conversion pairs from the HBD backplane [115]. This selection increases the photon sample purity, which is essential for a direct photon analysis. By implementing the ATM, the conversion recalibrator reconstructs the conversion pairs originating from the HBD backplane correctly. The recalibrator is applied to all tracks and provides more information to separate the conversion pairs from those originating from other sources. By using the recalibrated angles and p_T , one can recalculate the momentum vector components and the ATM invariant mass (designated as M_{HBD}).

In Figs. (74) and (75) one can see 2d reconstructions of the pair mass with the ATM and with the standard PHENIX momentum reconstruction algorithm. The red blob around $(M_{vtx}, M_{HBD}) = (0.012, 0.002)$ GeV/c² corresponds to conversion pairs selected by mass cuts, which are put on the

¹⁷In terms of the radiation length, X_0 , the relative thickness of HBD is $X/X_0 \approx 2\% \div 3\%$.

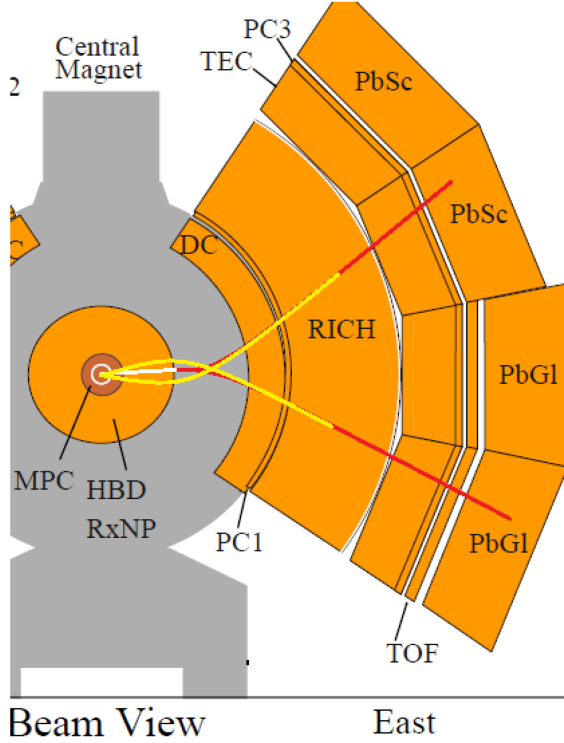


Figure 73: The illustration of the effect from the assumption of a track origin. For the purpose of visualization the effect is exaggerated. The true path of the e^+e^- pair through different subsystems is given by the red lines, which originate from the HBD backplane. The pair does not have an initial opening angle but the visible opening of the tracks happen further down due to the field. The yellow lines represent the wrong track projections, if we assume (incorrectly) that the particles come from the true event vertex. The cartoon is from [115].

vertical and horizontal masses to isolate the conversions in the HBD backplane. These cuts are the following:

$$\begin{aligned} \text{Conversion pair cuts: } & 10 \text{ MeV/c}^2 < M_{vtx} < 15 \text{ MeV/c}^2, \\ & M_{HBD} < 4.5 \text{ MeV/c}^2, \end{aligned} \quad (115)$$

and they select conversion pairs produced at distance $R \approx 60$ cm, away from the event vertex. The visible tail on the left corresponds to conversion pairs originating from π^0 Dalitz decays, and to other pairs coming before the HBD backplane.

The ATM can be represented as a parametrization, where its track variables are related to the track variables in the standard PHENIX algorithm. With the magnetic field being roughly homogeneous in azimuth, the parametrization is the following [115, 134]:

$$\phi_{ATM} = \phi_{DC} + 0.163 \alpha^3 + 0.03171 \alpha^2 + 0.7076 \alpha - 9 \cdot 10^{-5},$$

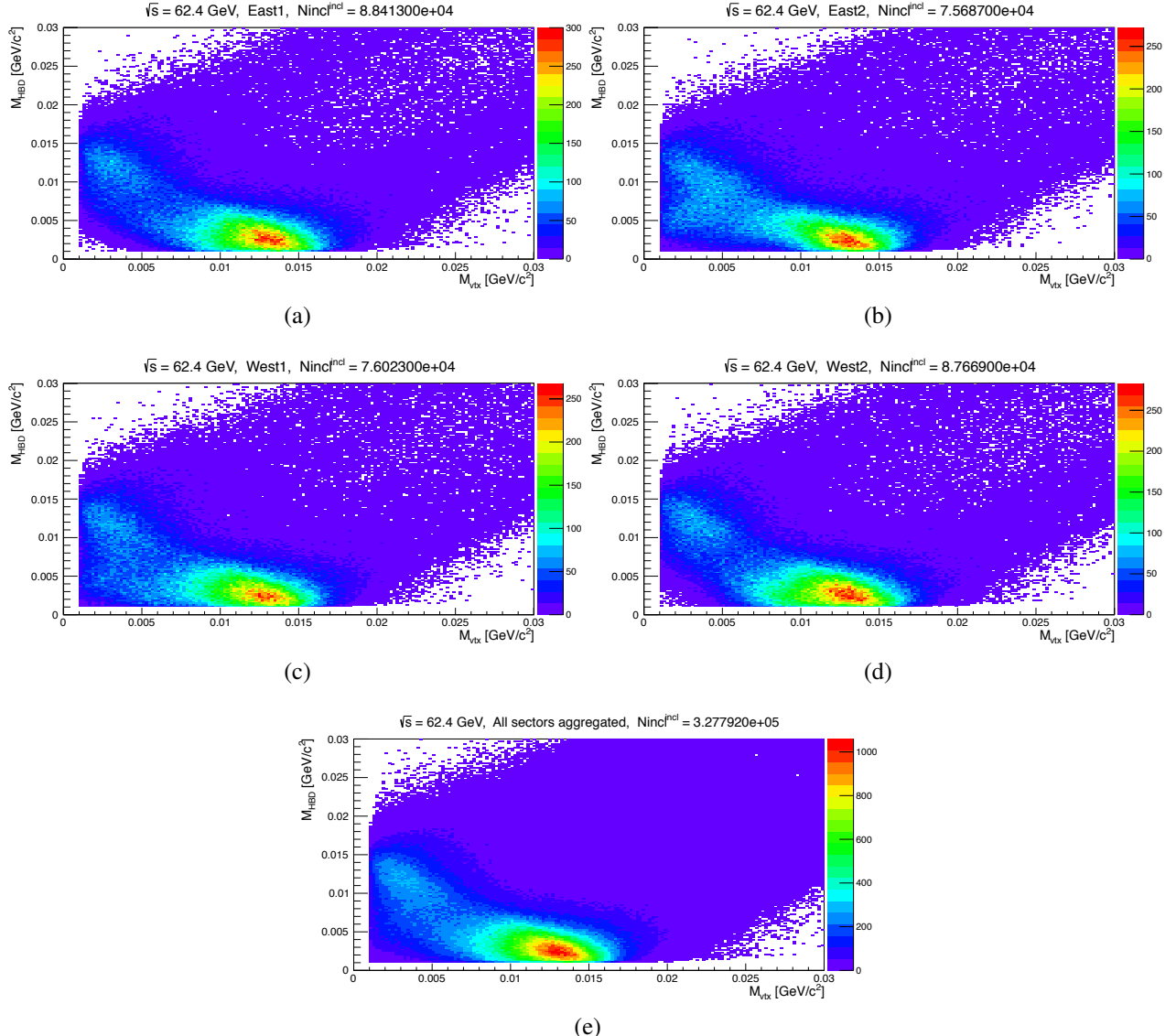


Figure 74: 2d mass plots for a view of the cut space used for the conversion photon identification at $\sqrt{s_{NN}} = 62.4 \text{ GeV}$. The upper four plots, Figs. (74(a)), (74(b)), (74(c)), (74(d)), correspond to the north-east, south-east, north-west, south-west, respectively. The bottom plot is the aggregation of all of them.

$$\begin{aligned} \theta_{ATM} &= \arccos(4.425 \cdot 10^{-3} (z_{DC} - z_{vertex}) - 5.15 \cdot 10^{-5}), \\ p_{T,ATM} &= |(m_p/\alpha) + b_p|, \end{aligned} \quad (116)$$

with

$$\begin{aligned} m_p &= 2.72 \cdot 10^{-6} |z_{vertex}|^2 - 7.11 \cdot 10^{-6} |z_{vertex}| + 0.0679, \\ b_p &= 9.422 \cdot 10^{-6} |z_{vertex}| + 4.2 \cdot 10^{-3}. \end{aligned} \quad (117)$$

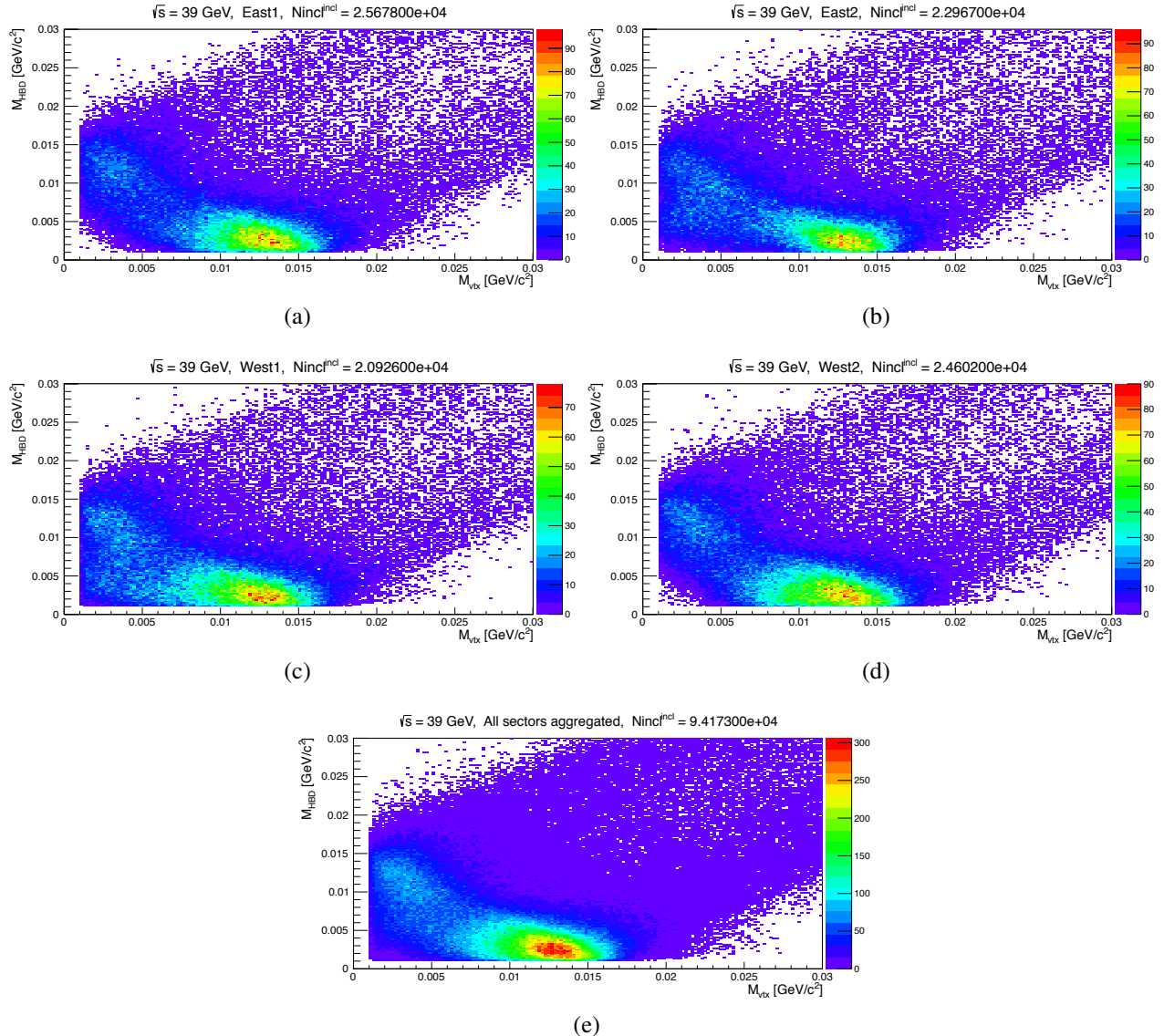


Figure 75: 2d mass plots for a view of the cut space used for the conversion photon identification at $\sqrt{s_{NN}} = 39 \text{ GeV}$. The differences between the plots is explained in the same way as in Fig. (74).

In these relations

- the variables ϕ_{ATM} (in mrad), θ_{ATM} (in mrad) and $p_{T,ATM}$ (in GeV/c) are reconstructed under the assumption of the track production originating from the HBD backplane,
 - the variables ϕ_{DC} (in mrad), α (in mrad), z_{DC} (in cm) and z_{vertex} (in cm) are reconstructed under the assumption of the track production originating at the true event vertex;
- ϕ_{DC} : the azimuth of a track at the reference radius of $R = 220 \text{ cm}$;
- α : the difference between the direction of a track at the reference radius and the radial direction;

z_{DC} : the z -location of a track along the beam axis at the reference radius;

z_{vertex} : the location of the true event vertex along the beam axis.

3.3.3 The EMCal photon cuts

In order to ensure a reasonable shape of the EMCal clusters we impose a cut

$$\text{EMCal cluster shape cut: } \chi^2 < 3. \quad (118)$$

This variable is similar to the χ^2 variable in the RICH. It quantifies how the measured shower profile in the EMCal towers is compared to the expected photon shower determined from test beam studies. This cut rejects some fraction of clusters with a strong mismatch between the cluster shape and reconstructed photon energy in the EMCals, however, the cut has a weak effect on the EMCal photon efficiency.

Also, we impose one more cut to make sure that the clusters have a minimal momentum limit. In our case we accept it to be

$$\text{EMCal } p_T \text{ cut: } p_{T,EMCal} > 500 \text{ MeV/c}. \quad (119)$$

$p_{T,EMCal} > 400 \text{ MeV/c}$ cut is used in [134], where it has also been shown that a cut in the range of $p_{T,EMCal} = 400 \div 600 \text{ MeV/c}$ optimizes the signal to background ratio in the π^0 yield extraction. Furthermore, this requirement on the EMCal photons puts strong kinematic restrictions on the measured yield from π^0 decays in the low- p_T region.

3.4 π^0 -tagged photon yield

For measuring the π^0 yield we pair the converted photons (i.e., inclusive photons reconstructed from conversions) with the EMCal photons (i.e., photons reconstructed in the EMCals) since for the EMCal photon identification only very weak cuts are needed, because of which the reconstruction efficiency of these photons is large and the systematic uncertainties from these cuts are small.

In order to estimate the shape of purely random combinations we mix photons from different events with similar characteristics. For example, we mix events from the same 10% bin in centrality with events within 1 cm of z_{vertex} . Since we cannot know if a pairing is genuine or just random and uncorrelated, we will estimate the combinatorial background under the π^0 peak with a mixed event technique: namely, we obtain the mixed event background of the converted and EMCal photons from events with similar characteristics by utilizing a generalized mixed event background generator called *CabanaBoy*. Pairings from the same event are the di-photon foreground, from different events

the mixed event background sample. Ultimately, the outcome are 2d-histograms in converted photon p_{Tee} and triplet mass $m_{ee\gamma}$.

The normalized background is determined by taking the ratio of histograms of the foreground and background distributions. Then we fit this ratio with a 2nd order polynomial in $m_{ee\gamma}$ by excluding the mass window $a_1 < m_{ee\gamma} < a_2$ around the π^0 peak, and by restricting all the fitting to another window $b_1 < m_{ee\gamma} < b_2$. By this way we obtain a normalization function, and in each p_{Tee} bin the combinatorial background distribution is then scaled with this normalization function and subtracted from the foreground distribution. After this subtraction we get a signal distribution, which is fitted to a Gaussian function. However, we also correct this π^0 subtracted distribution with a contribution coming from a residual background that we divide into the right and left backgrounds, which describe the “overshooting” (above zero) or “undershooting” (below zero) of the distribution around the peak. The extracted π^0 yield will be the sum (integral) of the mass bins in another range $c_1 < m_{ee\gamma} < c_2$.

Now for the visualization and some more details we address to the following. First of all, below are the values of a_1 and a_2 for the π^0 peak exclusion range, the values of b_1 and b_2 for the fitting restriction range, the values of c_1 and c_2 for the π^0 peak integration range to get the yield, etc. Also, one can see Figs. (76), (77) and (78) for some examples in the p_{Tee} range of $1100 < p_T < 1300 \text{ MeV}/c$ for 20-40% centrality bin at $\sqrt{s_{NN}} = 62.4 \text{ GeV}$.

For both $\sqrt{s_{NN}} = 62.4 \text{ GeV}$ and $\sqrt{s_{NN}} = 39 \text{ GeV}$ data samples:

- The π^0 peak exclusion range: $80 \text{ MeV}/c^2 < m_{ee\gamma} < 190 \text{ MeV}/c^2$.
- The fitting restriction range: $25 \text{ MeV}/c^2 < m_{ee\gamma} < 425 \text{ MeV}/c^2$.
- The π^0 peak summation (integration) range, $\Delta(\text{FG_yield})$: $110 \text{ MeV}/c^2 < m_{ee\gamma} < 165 \text{ MeV}/c^2$, which is $\sim 3\sigma$ range.
- The left residual background range, $\Delta(\text{BG_left})$: $35 \text{ MeV}/c^2 < m_{ee\gamma} < 110 \text{ MeV}/c^2$.
- The right residual background range, $\Delta(\text{BG_right})$: $165 \text{ MeV}/c^2 < m_{ee\gamma} < 240 \text{ MeV}/c^2$.

The total residual background is assumed to be described by averaging the sum of the relative yields of the BG_left and BG_right . Then this sum is subtracted from the original histogram of the π^0 yield extraction, depicted in Fig. (78) by blue color. The result will be an up- or a down-shifted histogram, depicted in Fig. (78) by purple color. It is also shown the relative yields of the BG_left and BG_right in respect with the FG_yield (which is the π^0 signal). The formulas that give the relative yields are

$$\text{BG_left relative yield} = \frac{\text{BG_left}/\Delta(\text{BG_left})}{\text{FG_yield}/\Delta(\text{FG_yield})} \times 100\%, \quad (120)$$

$$\text{BG_right relative yield} = \frac{\text{BG_right}/\Delta(\text{BG_right})}{\text{FG_yield}/\Delta(\text{FG_yield})} \times 100\%. \quad (121)$$

Analogous plots for two selected converted p_T bins at each available centrality are shown in Appendices A₁ [9], B₁ [11], C₁ [13] for 62.4 GeV, and in Appendices A₂ [10], B₂ [12], C₂ [14] for 39 GeV.

$\sqrt{s} = 62.4 \text{ GeV}, 20\text{-}40\% \text{ cent.}, 1100 < p_T < 1300 \text{ MeV}/c$

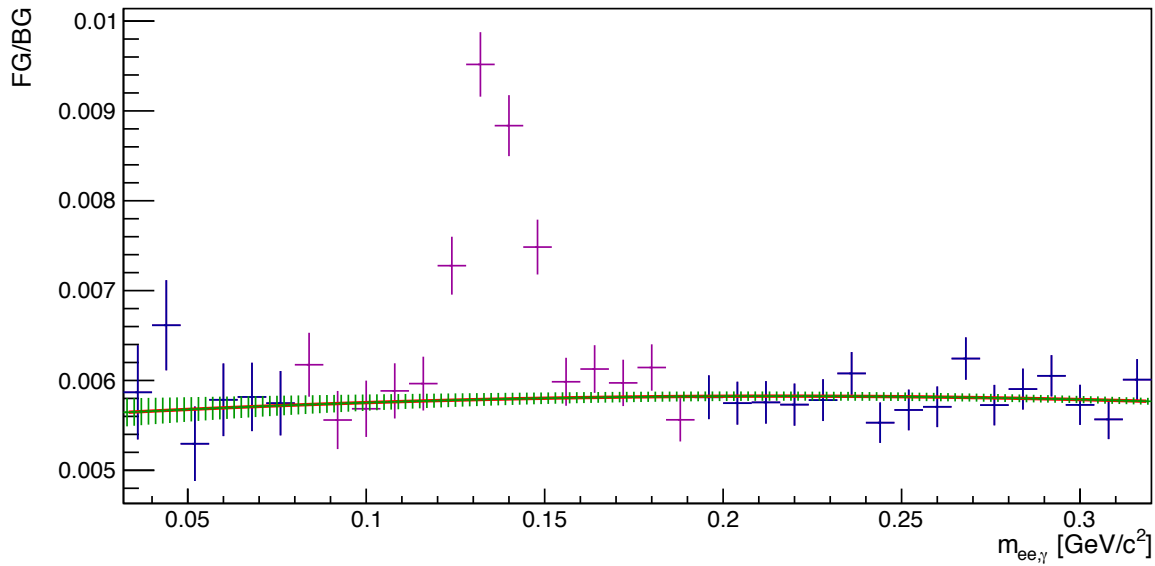


Figure 76: The converted di-photon foreground (FG) pair distribution in mass divided by the combinatorial mixed event background (BG) distribution for 20-40% centrality in the converted photon p_{Tee} bin of 1.1 - 1.3 GeV/c ($p_{Tee} \equiv p_T$) at $\sqrt{s_{NN}} = 62.4 \text{ GeV}$. The region of the purple colored pion peak is excluded. The ratio is fitted with a second order polynomial (shown in red).

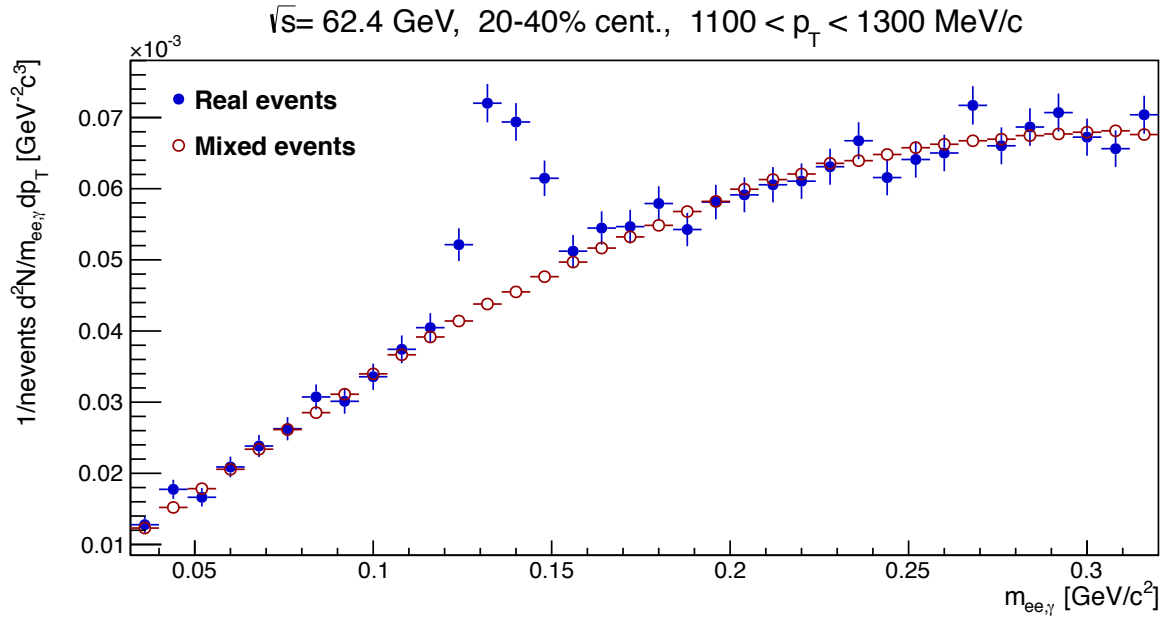


Figure 77: The di-photon foreground (blue) and normalized mixed event background (red) for 20-40% centrality in the converted photon p_{Tee} bin of 1.1 - 1.3 GeV/c ($p_{Tee} \equiv p_T$) at $\sqrt{s_{NN}} = 62.4 \text{ GeV}$. The uncertainty on the background includes both background's statistical uncertainty and the uncertainty in the normalization with CL=0.66.

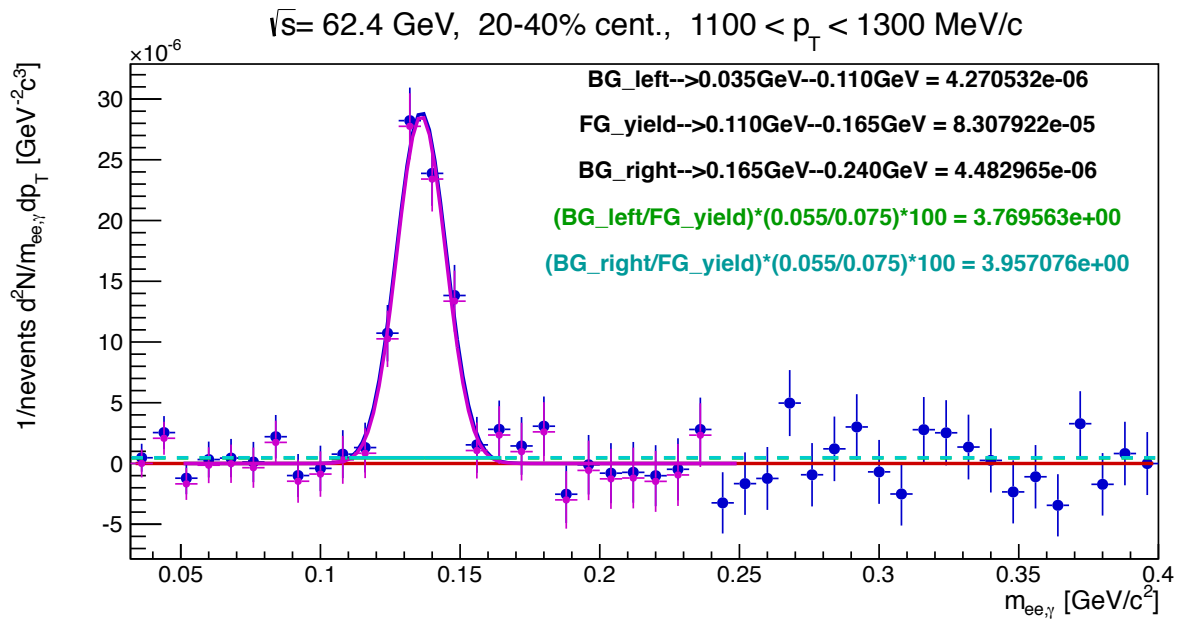


Figure 78: The π^0 yield extraction for 20-40% centrality in the converted photon p_{Tee} bin of 1.1 - 1.3 GeV/c ($p_{Tee} \equiv p_T$) at $\sqrt{s_{NN}} = 62.4$ GeV. The residual background is assumed to be described by averaging the sum of the green and cyan colored lines, which is subtracted from the original blue histogram of the π^0 yield extraction (fitted by the blue Gaussian). The result is the purple histogram (fitted by the purple Gaussian). In this plot the cyan color is on top of the green color.

4 Monte Carlo simulations

4.1 Pion tagging efficiency correction

As we noted in the last section, in order to measure the π^0 yield an inclusive photon reconstructed from a conversion should be paired with a second photon reconstructed in the EMCAL. The selections on the second photon will need to be accounted for when calculating the pion tagging efficiency. However, the tagging efficiency in turn should be corrected for. The reason is that only a fraction of the converted photons coming from $\pi^0 \rightarrow 2\gamma$ decays are successfully tagged because of limited EMCAL photon efficiency and acceptance.

The probability of reconstructing the converted and EMCAL photons are uncorrelated to the first order. The probability of the second photon's reconstruction from a π^0 decay in the EMCAL can be factorized into

- its probability to be emitted into the region covered by the EMCAL, along with the reconstruction of the converted photon (designated as f). The quantity f is called *conditional acceptance*.

and

- the photon reconstruction efficiency and probability to pass the cuts given that this photon falls into the acceptance of the EMCAL (designated as ε_γ). In short, we call ε_γ as the photon *efficiency*.

Afterwards, the product $\langle \varepsilon_\gamma f \rangle$ is averaged over all possible p_T values of the second photon from the EMCAL.

4.1.1 Photon efficiency, ε_γ

We use the code for a photon embedding simulation, which can be found in

```
https://www.phenix.bnl.gov/WWW/p/draft/bbannier/  
vg10_suppl/epsilon.tar.bz2.
```

This code has been used in the analysis of [134]. By using it, one can determine the centrality- and p_T -dependent efficiency of photons in a fully live EMCAL, doing a full simulation with the *PHENIX*

Geant3-based simulation Embed4All framework by utilizing the PISA (PHENIX Integrated Simulation Application). We embed the simulated photons into real data in order to account for the occupancy (multiplicity) effects.

In the first step, one should generate the input photons uniformly in the ranges of

$$-0.7 < \cos \theta < 0.7, \quad 0 < \phi < 2\pi, \quad \frac{1}{30} \text{ GeV/c} < \frac{1}{p_T} < \frac{1}{0.15} \text{ GeV/c}.$$

They are then processed through the PISA and embedded into the minimum bias run10 data sets from randomly chosen output files from 100 CNTs (CentralTrack base class) at $\sqrt{s_{NN}} = 62.4 \text{ GeV}$ and from 100 CNTs at $\sqrt{s_{NN}} = 39 \text{ GeV}$ on disk. It results in merging of the simulated detector response with clusters reconstructed in real events, by which the effects from the underlying event on the photon reconstruction are accounted for. So the clusters in the EMCal are reconstructed by making use of the combined simulated and real detector response. One should consider photons pointing to the EMCal detector regions with fully live towers, where the same deadmaps used in the analysis of the real data at 62.4 GeV and 39 GeV are being used here.

A generated photon can contribute to a certain cluster in primarily one of two possible ways.

- I) A cluster is reconstructed by a photon, which can directly deposit energy in one or multiple towers;
- II) The photon converts close enough to the EMCal or outside the magnetic field by having both electron and positron from the conversion pointing to the same cluster. The reconstructed cluster would closely resemble the cluster that the photon could have produced. Also, the e^+e^- tracks from the conversion can be bent too much such that each of them will be reconstructed in mutually distinct clusters. In this case the energy in each cluster will be different from the energy of the original photon.

In each case the photon is associated with a reconstructed cluster, which contains the largest fraction of the photon energy deposited. If the photon converts at points before reaching the EMCal, then it will not directly contribute energy to any of the reconstructed clusters. In that case one should find a cluster, where the conversion electron and positron contributed most of their energy to. If we identify the same cluster for the electron and positron, then we associate it with the generated photon.

Thereby, by this way we can check if the generated photons leave a hit in the simulation and if they satisfy the photon cuts (the same as used in the real data analysis). Thus we shall have two photon sets: the *all* and *passing* photons, namely

- I) *all* the photons, Γ_{in} , are input photons that point to fully live detector regions;
- II) the *passing* photons, Γ_{out} , are photons that are reconstructed in clusters passing all the cuts and hitting fully live 3×3 areas of the EMCal. Here Γ_{out} is a subset of Γ_{in} .

The ratio of passing and all photons gives the efficiency, ε_γ , at each EMCal photon $p_T \equiv p_{T\gamma}$.

$$\varepsilon(p_{T\gamma}) = \frac{\Gamma_{out}(p_{T\gamma})}{\Gamma_{in}(p_{T\gamma})}. \quad (122)$$

Then we calculate the efficiency (in different centrality bins) determined from a real event embedded into the PbGl and PbSc calorimeter subdetectors separately, where the centrality dependence of ε_γ is introduced by recording the centrality of that real event used in the embedding. It is stored as a function of $1/p_{T\gamma}$ to ensure good resolution near the photon $p_{T\gamma}$ cut. Figs. (79) and (80) show the resulting single photon efficiencies at $\sqrt{s_{NN}} = 62.4$ GeV and $\sqrt{s_{NN}} = 39$ GeV in our selected four centrality bins.

By performing the above analysis in each subclass, we extract centrality-dependent energy resolution functions for photons hitting a fully live 3×3 area in the calorimeters, just like for the photon efficiency. For each generated photon with energy E , having also the initial polar θ and azimuthal ϕ angles, we record the reconstructed energy and angles: $\hat{E}, \hat{\theta}, \hat{\phi}$. The centrality-dependent resolution functions are represented as histograms, which are then used as reference tables in the simulation for the pion tagging efficiency correction $\langle \varepsilon_\gamma f \rangle$:

$$\begin{aligned} \Gamma_E \left(\frac{1}{E} \right) &= \frac{E - \hat{E}}{E}, \\ \Gamma_\theta \left(\frac{1}{E} \right) &= \theta - \hat{\theta}, \\ \Gamma_\phi \left(\frac{1}{E} \right) &= \phi - \hat{\phi}, \end{aligned} \quad (123)$$

They are also stored as functions of $1/p_{T\gamma}$ to ensure good resolution near the photon $p_{T\gamma}$ cut. Figs. (311), (312), (313), (314), (315), (316) (from Ref. [139]) show the resulting relative (Γ_E) and absolute resolution (Γ_θ and Γ_ϕ) functions at $\sqrt{s_{NN}} = 62.4$ GeV, and Figs. (317), (318), (319), (320), (321), (322) (from Ref. [139]) show those at $\sqrt{s_{NN}} = 39$ GeV.

4.1.2 Efficiency and conditional acceptance, $\langle \varepsilon_\gamma f \rangle$

We use a fast Monte Carlo code based on *libexodus* for the simulation of the conditional acceptance. It can be found in

```
https://www.phenix.bnl.gov/WWW/p/draft/bbannier/
vg10_suppl/ef_sim.tar.bz2.
```

Let us write down the steps for the fast Monte Carlo simulation, which result in determining of the whole $\langle \varepsilon_\gamma f \rangle$ for 0-20%, 20-40%, 40-60%, 60-86% and 0-86% centrality classes.

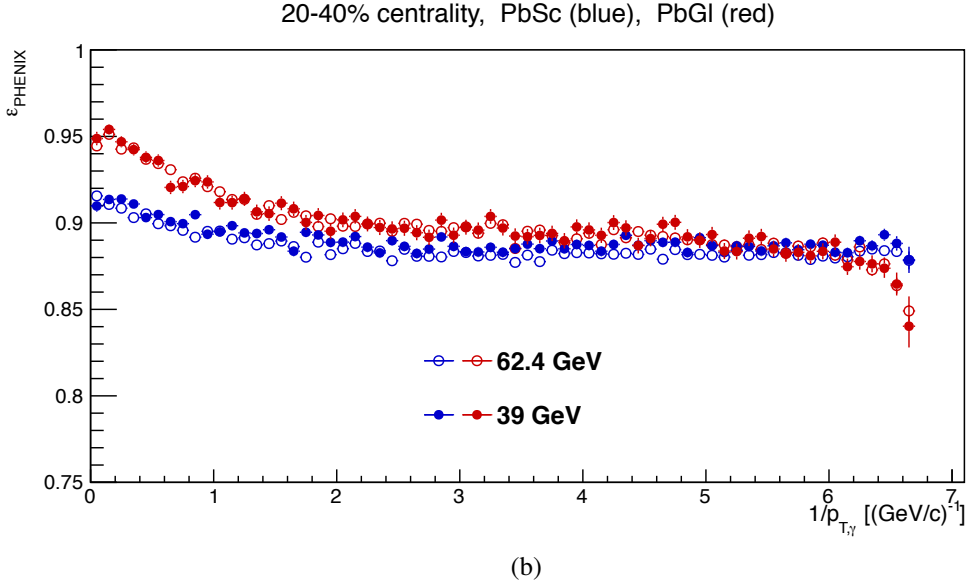
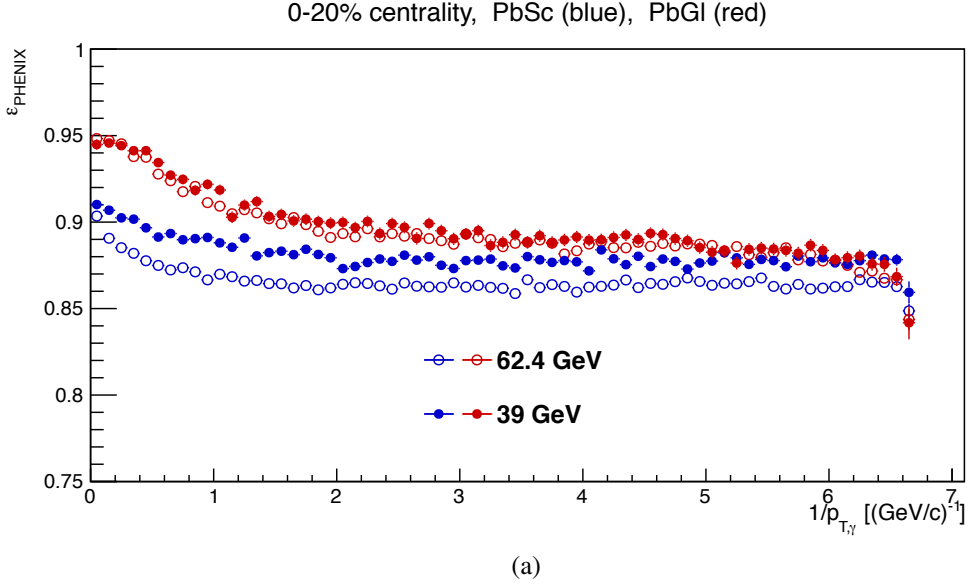


Figure 79: The single photon efficiency ε_γ (designated as $\varepsilon_{\text{PHENIX}}$) into the live detector as a function of the photon $1/p_{T,\gamma}$, in the first two centrality bins, for the PbSc (blue) and PbGl (red) at $\sqrt{s_{NN}} = 62.4 \text{ GeV}$ and $\sqrt{s_{NN}} = 39 \text{ GeV}$. Systematic uncertainties are not shown.

- 1) First of all we generate a parent π^0 particle from a centrality-dependent p_T distribution. The parametrization describing p_T spectra of this primary π^0 is a parametrization of real data with the modified Hagedorn function [41] given in what follows:

$$\frac{1}{2\pi p_T} \frac{d^2 N}{dy dp_T} = \frac{c}{(e^{-(a m'_T + b m'^2_T)} + (m'_T/p_0))^n}, \quad (124)$$

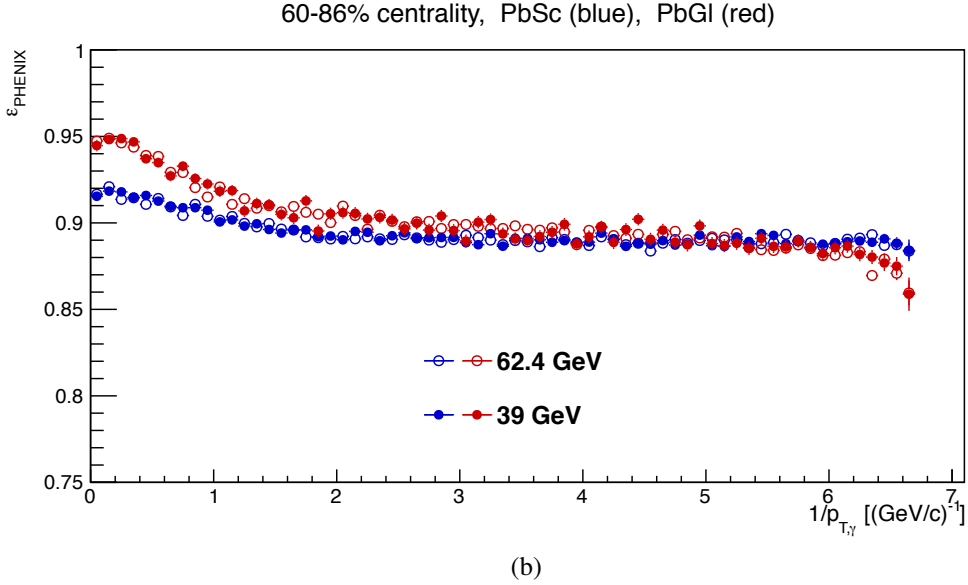
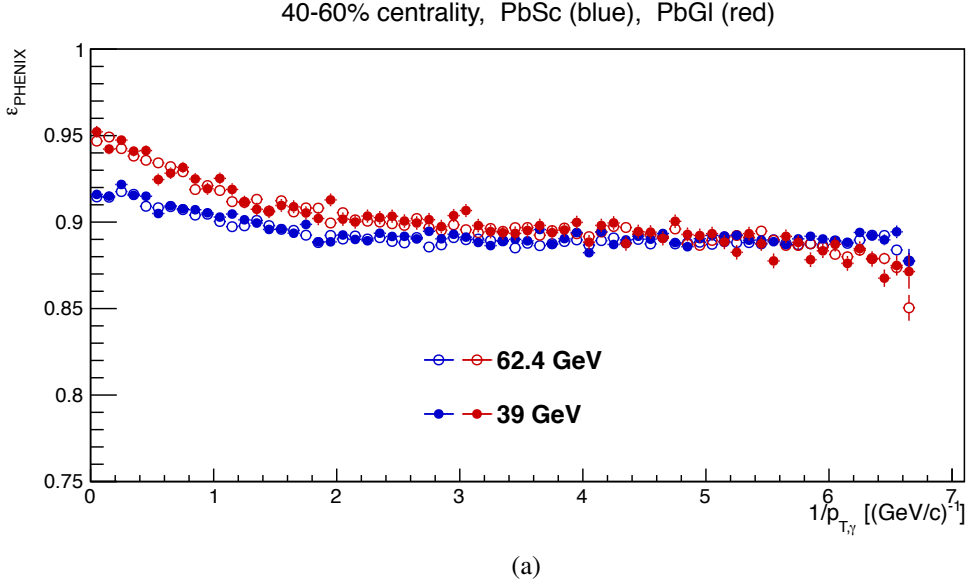


Figure 80: The single photon efficiency ε_{γ} (designated as $\varepsilon_{\text{PHENIX}}$) into the live detector as a function of the photon $1/p_{T,\gamma}$, in the second two centrality bins, for the PbSc (blue) and PbGl (red) at $\sqrt{s_{NN}} = 62.4 \text{ GeV}$ and $\sqrt{s_{NN}} = 39 \text{ GeV}$. Systematic uncertainties are not shown.

with

$$m'_T = \sqrt{m_T^2 - m_{\pi^0}^2} \quad \text{and} \quad m_T = \sqrt{m^2 + p_T^2}, \quad (125)$$

where m is the mass of a meson. All the parameters in Eq. (125) are determined by fitting the parametrization with the centrality-dependent neutral and charged meson data. Table (4) and Table (5) show the values of these parameters at $\sqrt{s_{NN}} = 62.4 \text{ GeV}$ and $\sqrt{s_{NN}} = 39 \text{ GeV}$. The p_T -integrated π^0 yield into one unit in rapidity, dN/dy , is given as well.

centrality	c	a	b	p_0	n	dN/dy
0 – 10%	1594.36	0.3251	0.1285	0.946	10.87	229.4
10 – 20%	700.0	0.3681	0.0620	1.047	11.10	134.5
20 – 40%	713.9	0.3104	0.0538	1.031	11.24	108.3
40 – 60%	25.9	0.3393	0.0669	0.959	10.68	39.0
60 – 86%	137.0	0.2669	0.1123	0.809	10.20	12.8

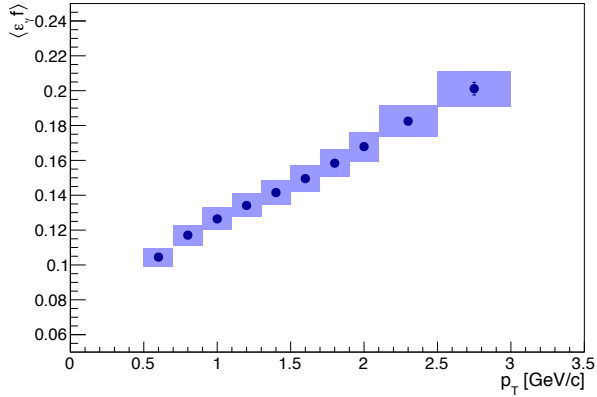
Table 4: The Hagedorn parameters of $\pi^0 p_T$ spectra obtained by fitting the modified Hagedorn function (Eq. (124)) with the PHENIX data [140] at $\sqrt{s_{NN}} = 62.4$ GeV.

centrality	c	a	b	p_0	n	dN/dy
0 – 10%	277.8	0.398	0.0	1.484	13.84	106.1
10 – 20%	172.5	0.387	0.0	1.549	13.98	67.04
20 – 40%	188.2	0.340	0.0	1.474	13.81	55.87
40 – 60%	95.34	0.233	0.0	1.684	14.90	23.47
60 – 86%	23.01	0.239	0.0	1.663	14.96	5.55

Table 5: The Hagedorn parameters of $\pi^0 p_T$ spectra obtained by fitting the modified Hagedorn function (Eq. (124) at $b = 0$) with the PHENIX data [143] at $\sqrt{s_{NN}} = 39$ GeV.

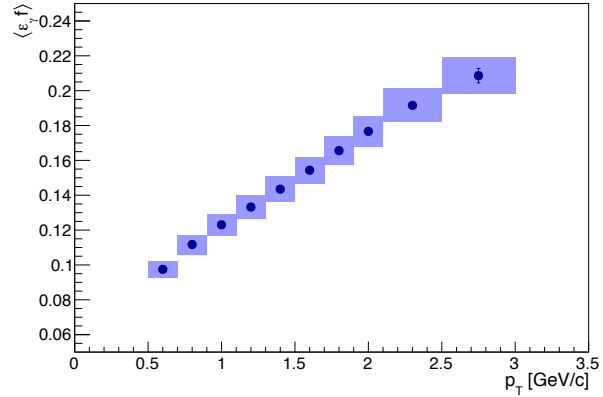
- 2) Then a generated π^0 is decayed into two photons (with a flat energy asymmetry in the decay).
- 3) One of these photons is converted to a e^+e^- pair (with a flat energy asymmetry). For the electron/positron of the conversion we check if they hit a live, run group-dependent region of the DC and a 3×3 area in the EMCAL with at least one live tower, before and after applying energy smearing by already having the reference tables from Eq. (123).
- 4) Making use of the same list of the EMCAL dead towers, which are used in the data analysis, we check if the second photon hits a fully live 3×3 area in the EMCAL before and after applying angular and energy smearing. If the second photon hits a live detector area and has a randomly sampled efficiency that is larger than the efficiency required for the photons of this $p_{T\gamma}$, and if it passes the $p_{T\gamma}$ cut, then one can consider the converted photon as being tagged.
- 5) Then the ratio of the accepted converted photons with the successfully reconstructed EMCAL photons to the full sample of the accepted converted photons will give us the quantity $\langle \varepsilon_\gamma f \rangle$, which we simply rename as conditional acceptance instead of the pion tagging efficiency correction. See the plots in Fig. (81) at $\sqrt{s_{NN}} = 62.4$ GeV and in Fig. (82) at $\sqrt{s_{NN}} = 39$ GeV.

$\sqrt{s} = 62.4 \text{ GeV}, 0\text{-}20\% \text{ cent., Conditional acceptance}$



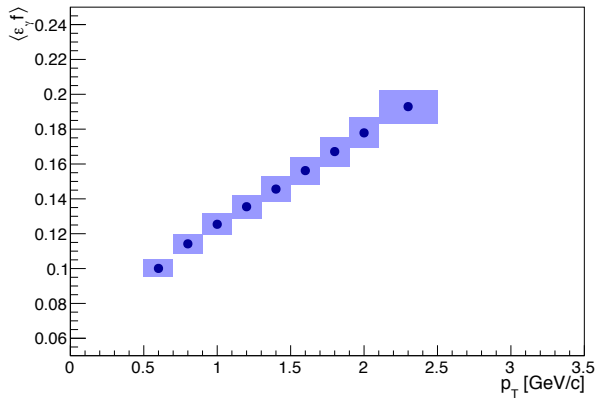
(a)

$\sqrt{s} = 62.4 \text{ GeV}, 20\text{-}40\% \text{ cent., Conditional acceptance}$



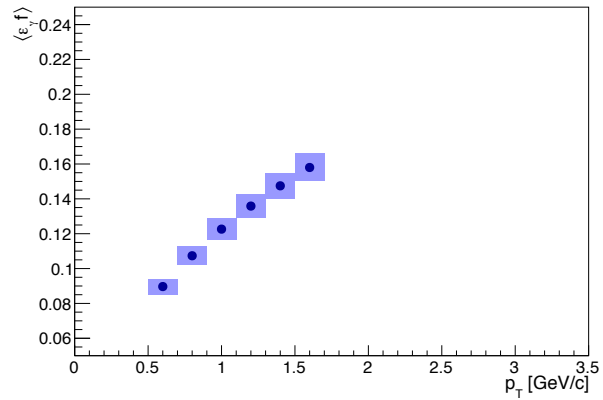
(b)

$\sqrt{s} = 62.4 \text{ GeV}, 40\text{-}60\% \text{ cent., Conditional acceptance}$



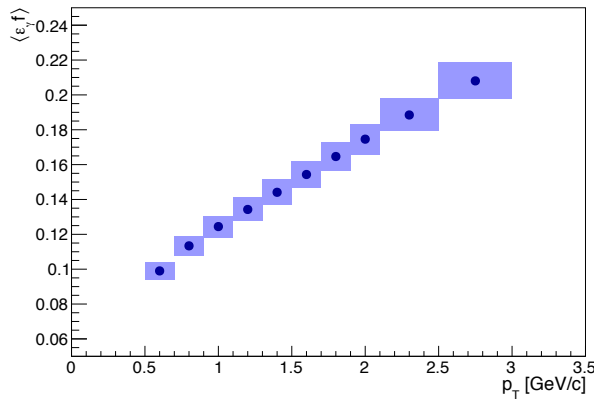
(c)

$\sqrt{s} = 62.4 \text{ GeV}, 60\text{-}86\% \text{ cent., Conditional acceptance}$



(d)

$\sqrt{s} = 62.4 \text{ GeV}, 0\text{-}86\% \text{ cent., Conditional acceptance}$



(e)

Figure 81: The conditional acceptance $\langle \varepsilon_\gamma f \rangle$ at $\sqrt{s_{NN}} = 62.4 \text{ GeV}$ in the centrality bins of 0-20% (81(a)), 20-40% (81(b)), 40-60% (81(c)), 60-86% (81(d)) and minimum bias 0-86% (81(e)).

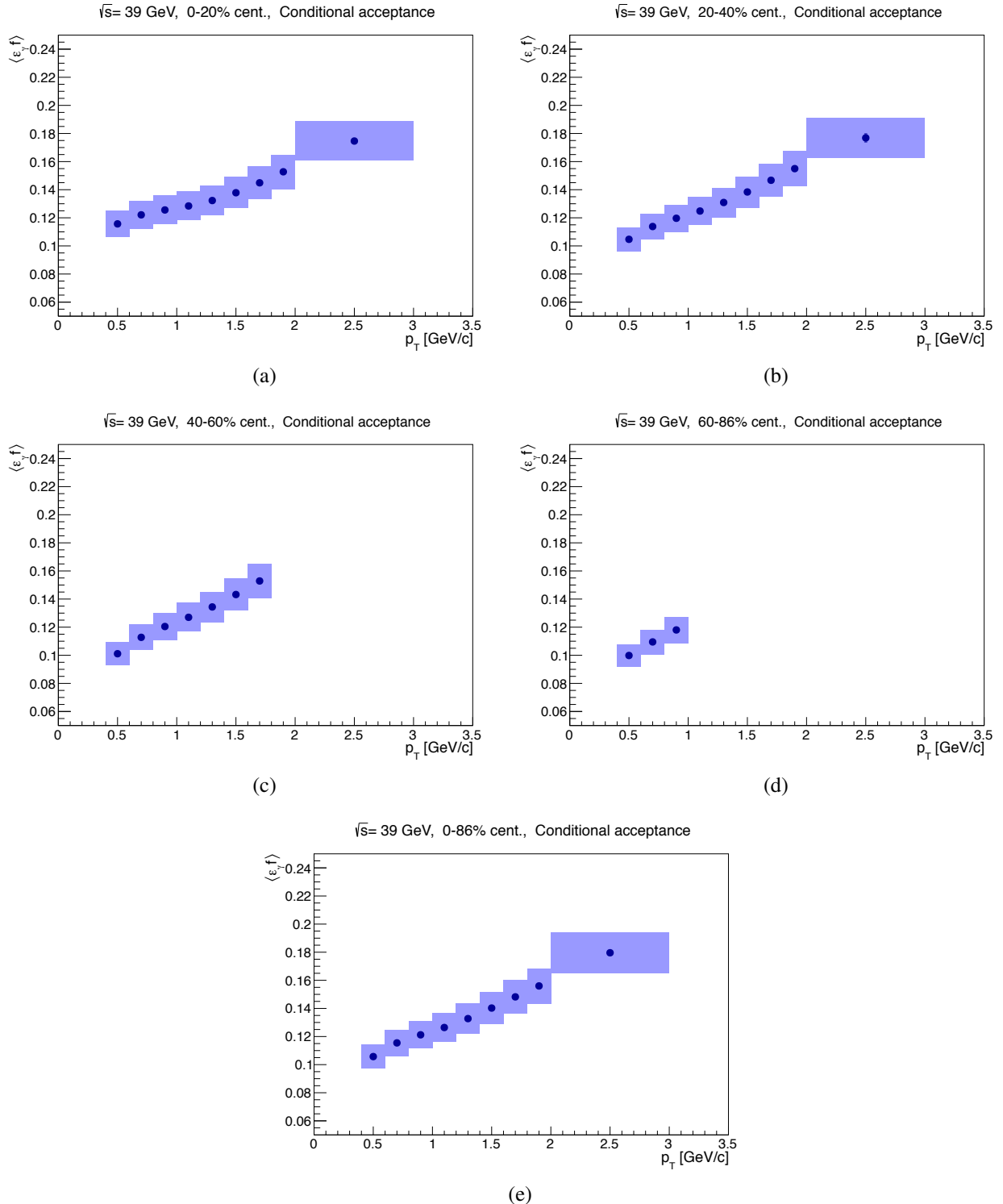


Figure 82: The conditional acceptance $\langle \varepsilon_\gamma f \rangle$ at $\sqrt{s_{NN}} = 39$ GeV in the centrality bins of 0-20% (82(a)), 20-40% (82(b)), 40-60% (82(c)), 60-86% (82(d)) and minimum bias 0-86% (82(e)).

4.2 Cocktail ratio from hadronic decays

Now one can look at the cocktail ratio in the denominator of Eq. (98), and let us designate it as

$$Y_{cocktail} = \left(\frac{\gamma^{hadron}}{\gamma^{\pi^0}} \right)_{sim}. \quad (126)$$

For the simulation we use a package based on *libexodus*, which can be found in:

```
https://www.phenix.bnl.gov/WWW/p/draft/bbannier/
vg10_suppl/cocktail.tar.bz2,
```

The experimentally measured ratio in the numerator of Eq. (98) is already corrected for detector and acceptance effects with the conditional acceptance $\langle \varepsilon_\gamma f \rangle$. Thereby, without taking into account these effects we can calculate the cocktail ratio at midrapidity.

The photon production channels used in the simulation are listed in Table (6).

primary particle	decay products	branching ratio
π^0	$\gamma\gamma$	98.8%
η	$\gamma\gamma$	39.3%
η	$\pi^+\pi^-\gamma$	4.6%
η'	$\gamma\gamma$	2.1%
η'	$\pi^+\pi^-\gamma$	23.0%
η'	$\omega\gamma$	2.8%
ω	$\pi^0\gamma$	8.3%

Table 6: The photon production channels used in our cocktail ratio simulation. The table is from [134].

These are channels, which directly produce at least a single photon. There are also channels, like $\eta \rightarrow \pi^0\pi^0\pi^0$ and $K_S^0 \rightarrow \pi^0\pi^0$, which produce π^0 but not directly photons because these photons are already included in the $\pi^0 \rightarrow \gamma\gamma$ decay channel. Therefore these η and K_S^0 decay channels are not included in our cocktail simulation. We also use the centrality-dependent modified Hagedorn parametrization of the $\pi^0 p_T$ spectra, the parameters of which are given in Table (4) and Table (5), i.e., the same parameters that are used in the simulation of the conditional acceptance.

We set the π^0 yield per event equal to 1. As regards the other hadrons, their p_T spectra are calculated from m_T -scaled π^0 spectra. The relative yields of all hadrons (with respect to π^0) in terms of the scale factors are listed in Table (7). These scale factors are determined at $p_T = 5 \text{ GeV}/c$, and we use the same hadron/ π^0 yield for all centrality bins. Under the m_T -scaling assumption, the spectra of different hadrons have the same shape, and their relative yields are determined from the flat, p_T -independent ratio of the m_T spectra. This assumption has been validated in the analysis of [134], where it was found that the particular choice of the parametrization does not affect the final R_γ results.

hadron	the yield relative to π^0
π^0	1
η	0.46 ± 0.06
η'	0.25 ± 0.075
ω	0.90 ± 0.06

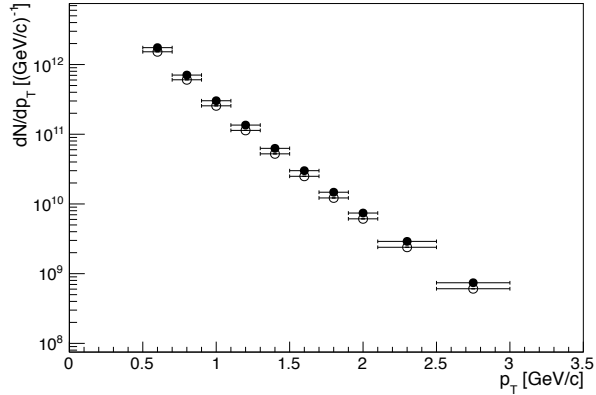
Table 7: The hadron yield relative to the π^0 yield. The table is from [134].

Ultimately, we fill two histograms:

- a) for γ^{hadron} - the yield of all photons coming from hadronic decays;
- b) for γ^{π^0} - the yield of photons coming from π^0 decays.

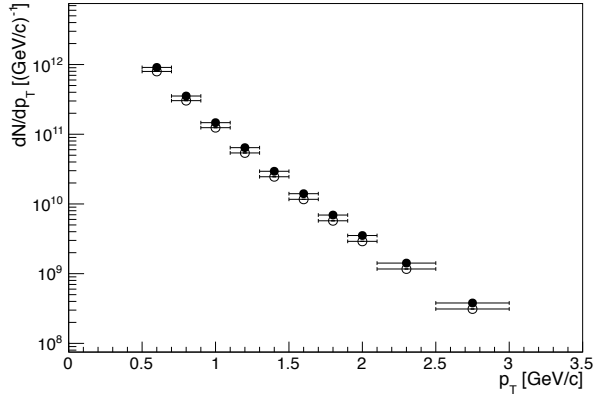
If the primary particle is not a π^0 , then the decay photon is counted to be in γ^{incl} . And if the primary particle is a π^0 , then the decay photon is counted to be in γ^{π^0} . Otherwise, if the photon is a product of secondary π^0 decays, then that photon gets thrown away since it is already produced from the primary π^0 decays. This procedure is necessary in order to avoid the double counting of the π^0 particles. Fig. (83) shows the simulated converted photon spectra and Fig. (84) shows the cocktail ratio $Y_{cocktail}$, both at $\sqrt{s_{NN}} = 62.4$ GeV. In addition, Fig. (85) shows the simulated converted photon spectra and Fig. (86) shows the $Y_{cocktail}$, both at $\sqrt{s_{NN}} = 39$ GeV.

$\sqrt{s} = 62.4 \text{ GeV}, 0\text{-}20\% \text{ cent.}$



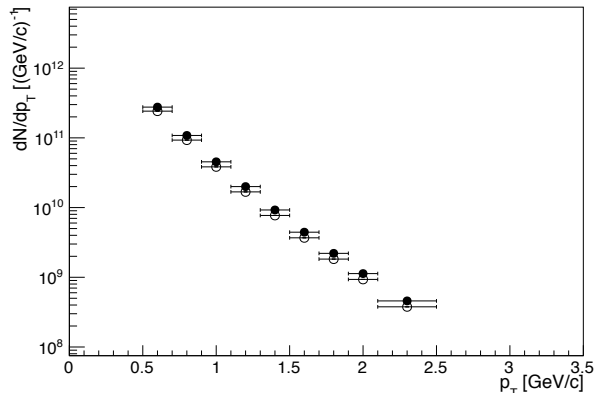
(a)

$\sqrt{s} = 62.4 \text{ GeV}, 20\text{-}40\% \text{ cent.}$



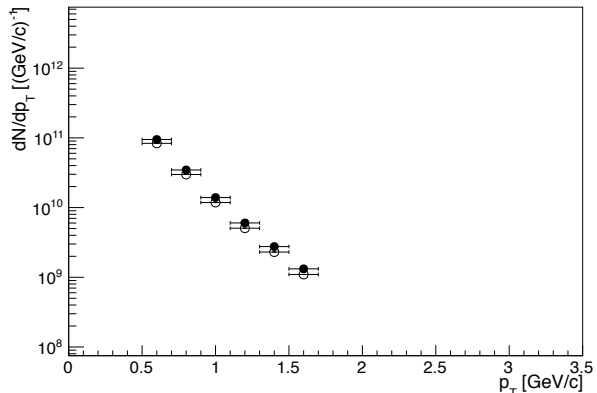
(b)

$\sqrt{s} = 62.4 \text{ GeV}, 40\text{-}60\% \text{ cent.}$



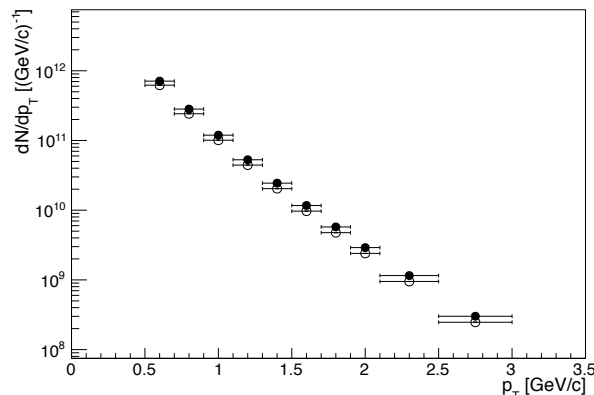
(c)

$\sqrt{s} = 62.4 \text{ GeV}, 60\text{-}86\% \text{ cent.}$



(d)

$\sqrt{s} = 62.4 \text{ GeV}, 0\text{-}86\% \text{ cent.}$



(e)

Figure 83: The simulated converted photon spectra of all photons from hadronic decays (filled circles) and of photons from π^0 decays (open circles) at $\sqrt{s_{NN}} = 62.4 \text{ GeV}$ in the centrality bins of 0-20% (83(a)), 20-40% (83(b)), 40-60% (83(c)), 60-86% (83(d)) and minimum bias 0-86% (83(e)).

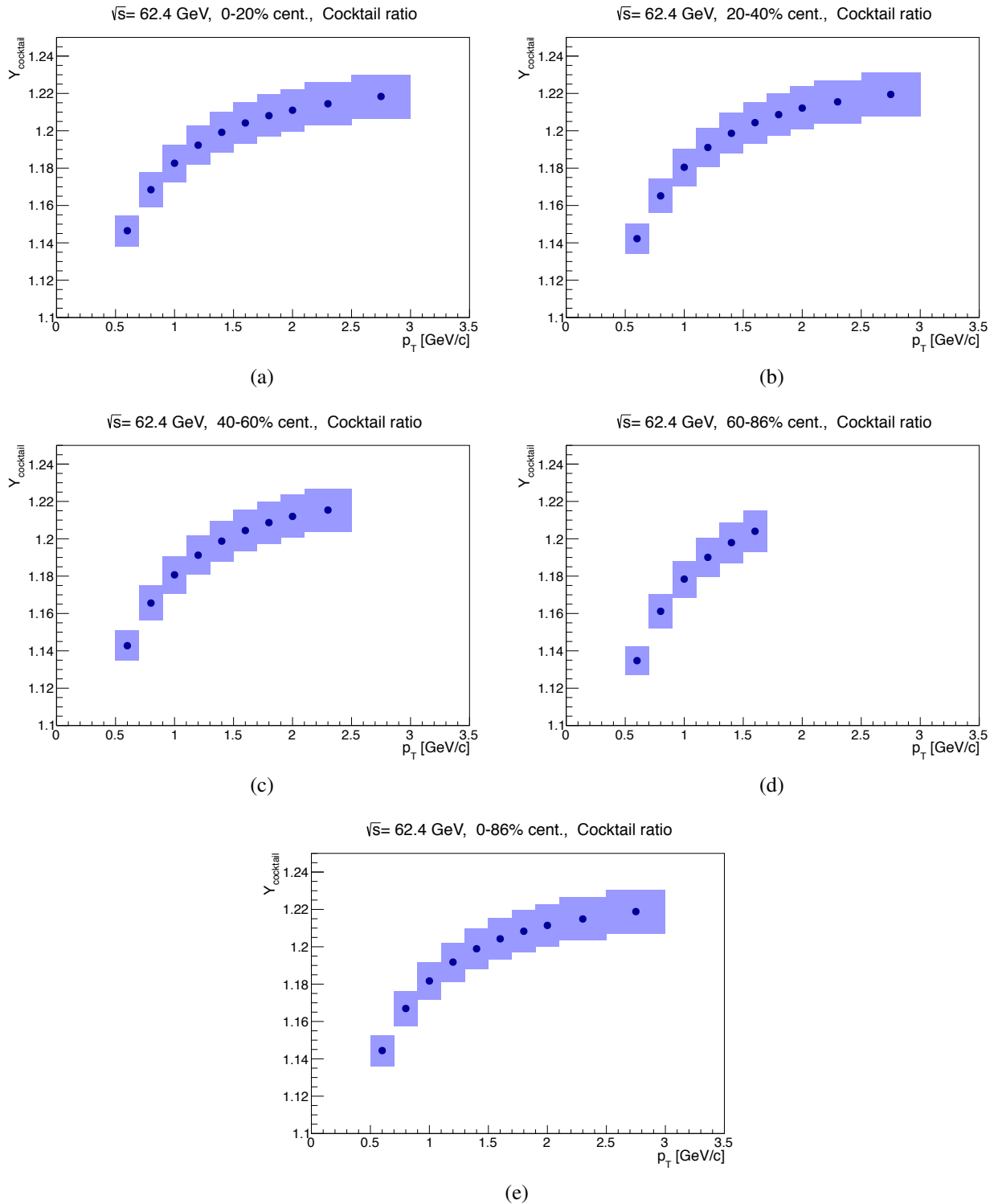


Figure 84: The simulated ratio (cocktail ratio) of all photons from hadronic decays to photons from π^0 decays at $\sqrt{s_{NN}} = 62.4 \text{ GeV}$ in the centrality bins of 0-20% (84(a)), 20-40% (84(b)), 40-60% (84(c)), 60-86% (84(d)) and minimum bias 0-86% (84(e)).

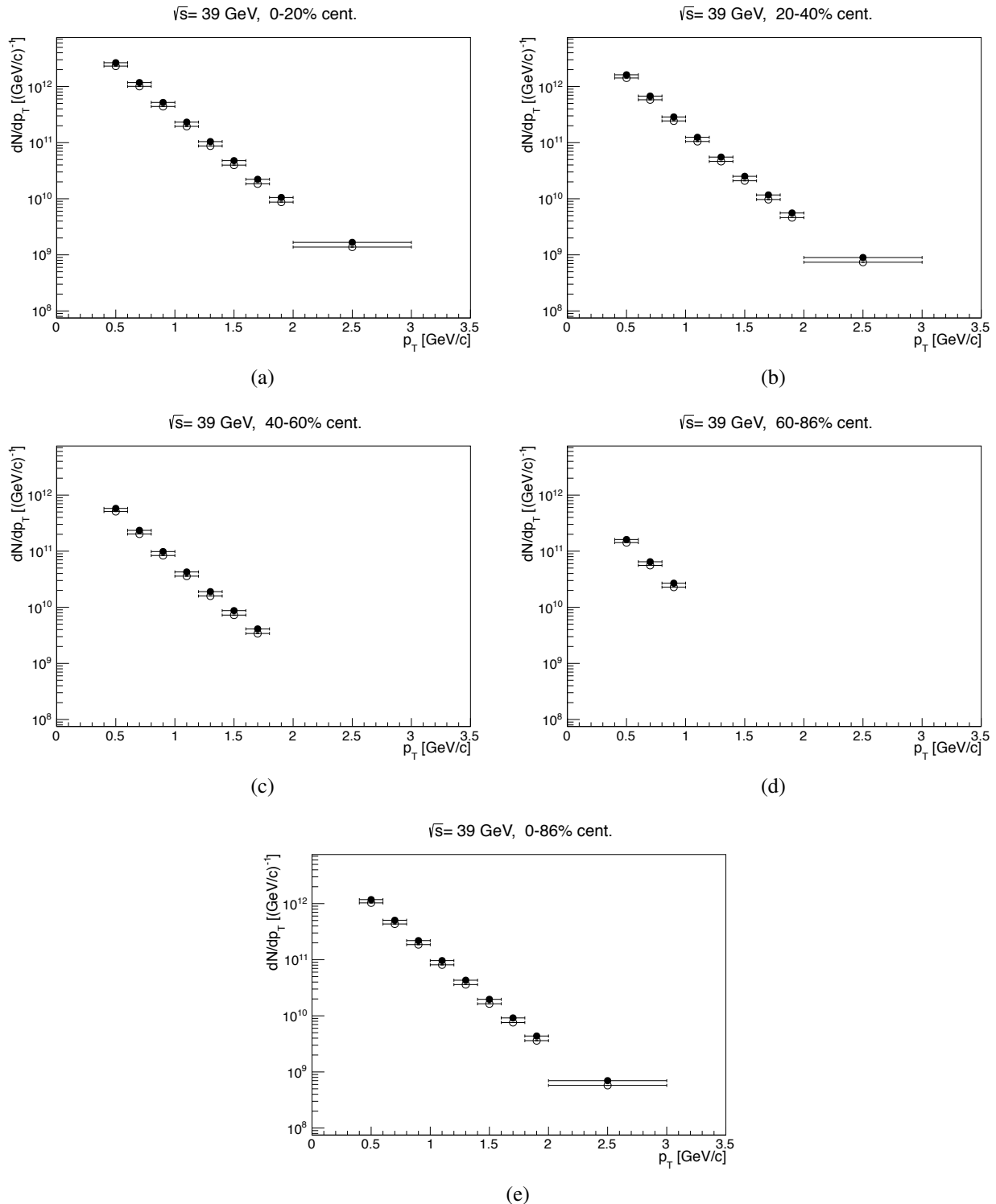


Figure 85: The simulated converted photon spectra of all photons from hadronic decays (filled circles) and of photons from π^0 decays (open circles) at $\sqrt{s_{NN}} = 39 \text{ GeV}$ in the centrality bins of 0-20% (85(a)), 20-40% (85(b)), 40-60% (85(c)), 60-86% (85(d)) and minimum bias 0-86% (85(e)).

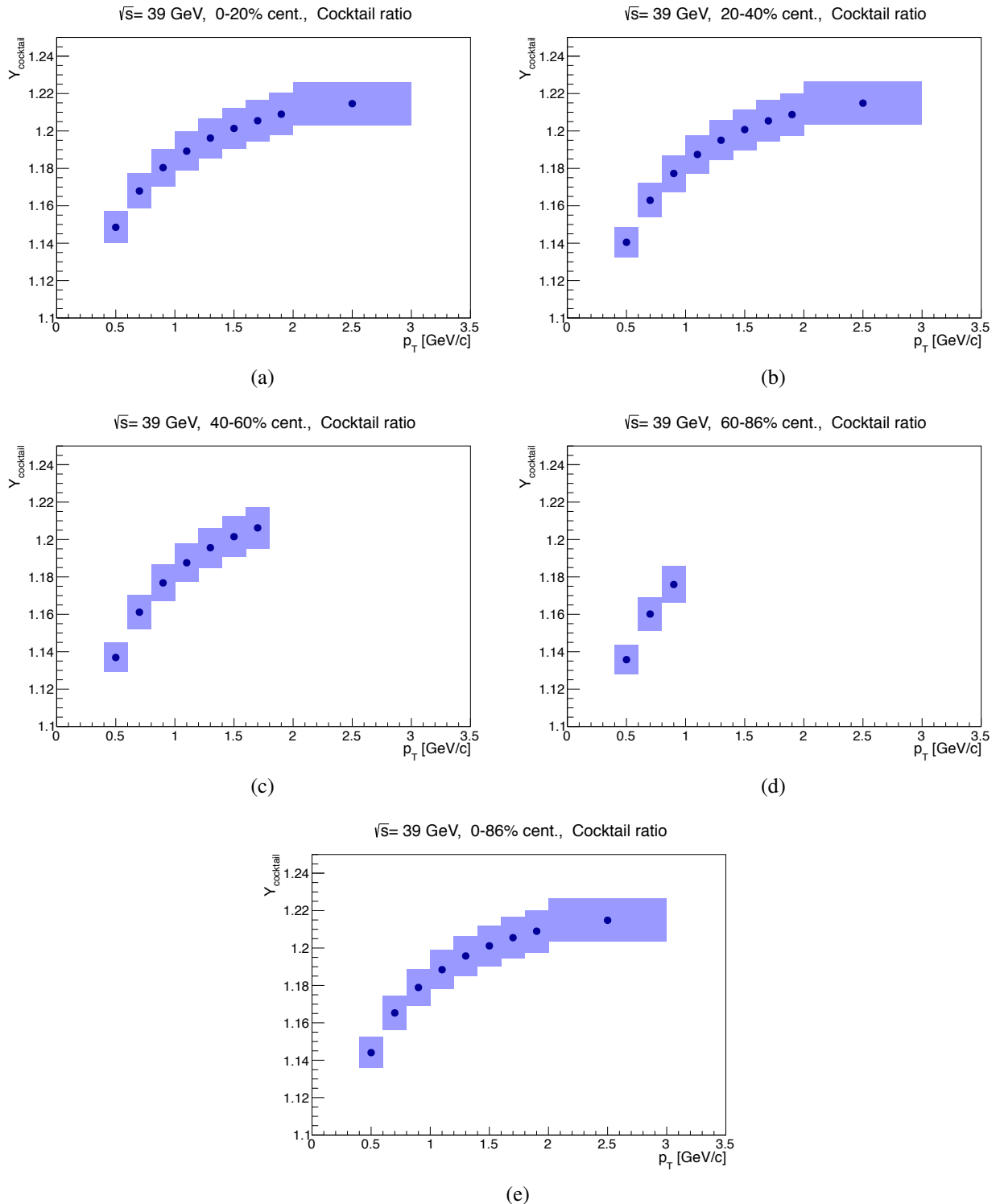


Figure 86: The simulated ratio (cocktail ratio) of all photons from hadronic decays to photons from π^0 decays at $\sqrt{s_{NN}} = 39 \text{ GeV}$ in the centrality bins of 0-20% (86(a)), 20-40% (86(b)), 40-60% (86(c)), 60-86% (86(d)) and minimum bias 0-86% (86(e)).

5 Systematic Uncertainties

In this section we discuss the systematic uncertainties of R_γ ingredients of Eq. (98). The summary is shown at the end of this section, in Table (10) and Table (11).

5.1 Conditional acceptance

The p_T spectra of π^0 particles are needed as input for direct photon measurements. Ref. [140] has studies of the reference spectra for π and η mesons in Au+Au collisions at $\sqrt{s_{NN}} = 62.4 \text{ GeV}$. In particular, the data of π^0 and π^\pm published by PHENIX [141] and STAR [142] are reviewed. Fig. (87)

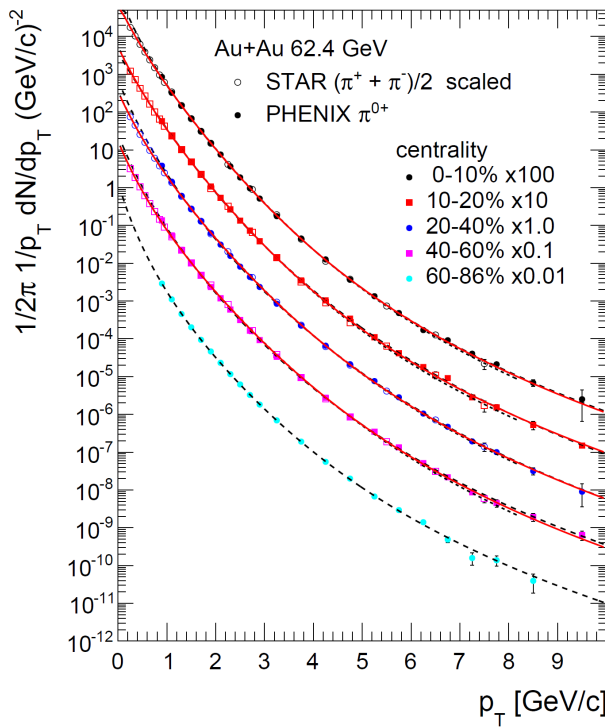


Figure 87: The neutral and charged pion invariant yield per event for PHENIX [141] and STAR [142]. The plot is from [140].

shows the data along with the fits obtained with the modified Hagedorn function. The parameters of the modified Hagedorn function fitted to the PHENIX data are shown in Table (4). The parameters

of the fits for the PHENIX plus STAR data and for the STAR data only can be found in [140]. One can see that within $\pm 10\%$ the PHENIX and STAR data agree quite well, indicated by the horizontal bands in Fig. (88). Each plot in this figure shows two ratios of the fits to the combined fit. These two

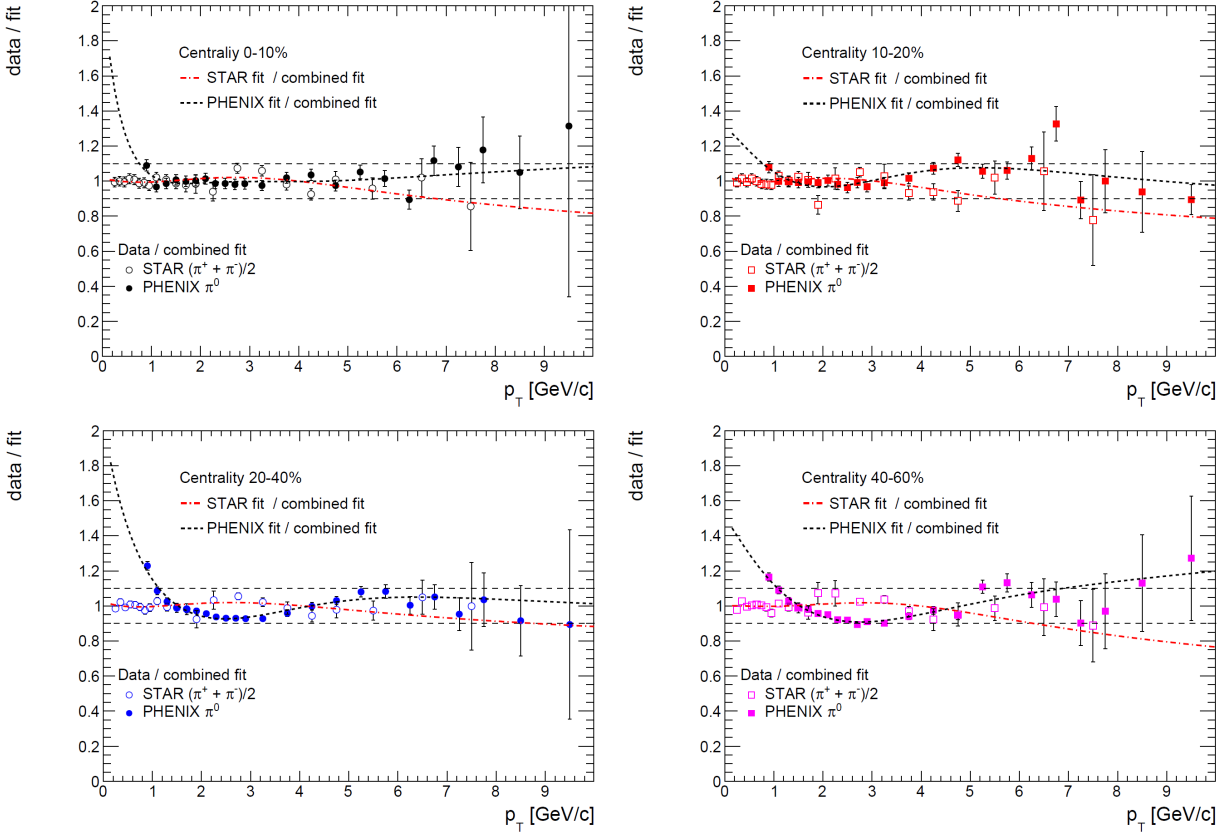


Figure 88: The ratios of the fits (to the data sets shown in Fig. (87)) to the combined fit. The plot is from [140].

ratios can be used as estimates for systematic uncertainties on the shape of the pion spectra, which translates to the systematic uncertainties for $\langle \varepsilon_\gamma f \rangle$. In our analysis we are interested in the region of $p_T < 3 \text{ GeV}/c$, and in this case the centrality-averaged shape differences between the PHENIX and STAR data will roughly be within the range of $\pm(4 \div 5)\%$, which we assign to $\langle \varepsilon_\gamma f \rangle^{18}$.

In the run10 analysis at 200 GeV [134], it was found that the minimal EMCAL photon momentum $p_{T,EMCAl} \geq 0.4 \text{ GeV}/c$ can play a dominant role for $\langle \varepsilon_\gamma f \rangle$. From the photon embedding simulation it was determined that the relative energy resolution¹⁹ in the EMCAL near the lower photon momentum cutoff is $\sigma_E \sim 10\%$. Then the behavior of the simulated photon efficiency²⁰ was examined near this

¹⁸The fit to the PHENIX data deviates significantly from that of the STAR data below $p_T \sim 1 \text{ GeV}/c$ because in this range no PHENIX data exist.

¹⁹The energy resolution plots in our case are shown in Figs. (311), (312), (317), (318) of [139].

²⁰The photon efficiency plots in our case are shown in Fig. (79) and Fig. (80).

momentum threshold over a $2\sigma_E$ window, by which one can see that the largest variations between the adjacent bins in this window are of the order of $(3 \div 4)\%$. Of this size of maximal relative Type B systematic uncertainty was assigned to the conditional acceptance: In our case at $\sqrt{s_{NN}} = 62.4 \text{ GeV}$,

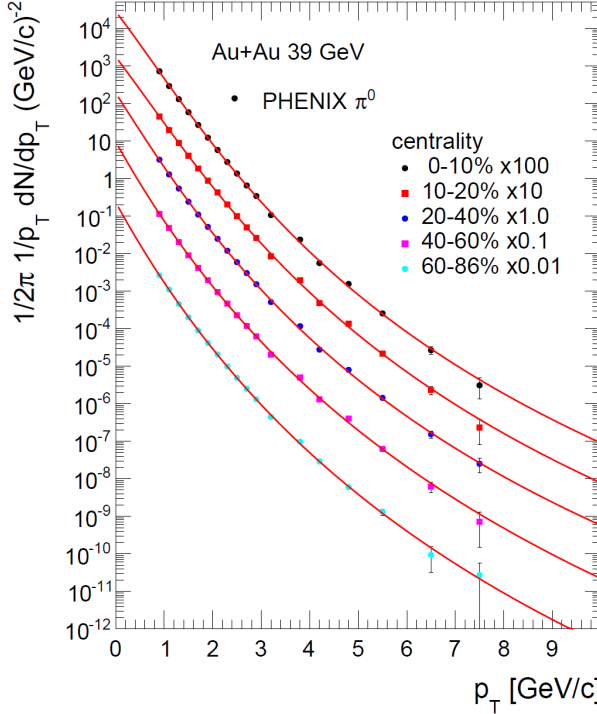


Figure 89: The neutral and charged pion invariant yield per event for PHENIX [141]. The plot is from [143].

if we follow the same procedure by looking at the relative energy resolution plots (Figs. (311) and (312) from [139]) near the p_T threshold (which again gives $\sigma_E \sim 10\%$) and investigate the behavior of the simulated efficiency (Figs. (79) and (80)), we can see that the variation between the adjacent bins there are of the order of $(1 \div 1.25)\%$. One reason this number comes out comparatively smaller than that at $\sqrt{s_{NN}} = 200 \text{ GeV}$ is because of less occupancy (multiplicity) effects at lower collision energies, which gives better photon reconstruction efficiency.

Thus as an input for the systematic uncertainty (of Type B) on the conditional acceptance we will use the dominant source driven by the p_T shape differences between the PHENIX and STAR data (taking also into account the smaller contribution of the systematic uncertainty from the energy scale):

$$\delta(\langle \varepsilon_\gamma f \rangle)_{sys} \sim 5\% \quad \text{at } \sqrt{s_{NN}} = 62.4 \text{ GeV}.$$

The same aforementioned arguments are also the case for 39 GeV. Similar to Figs. (87) and (88) we wish to show the π^0 data and the ratios of the fits to the combined fit at this collision energy in

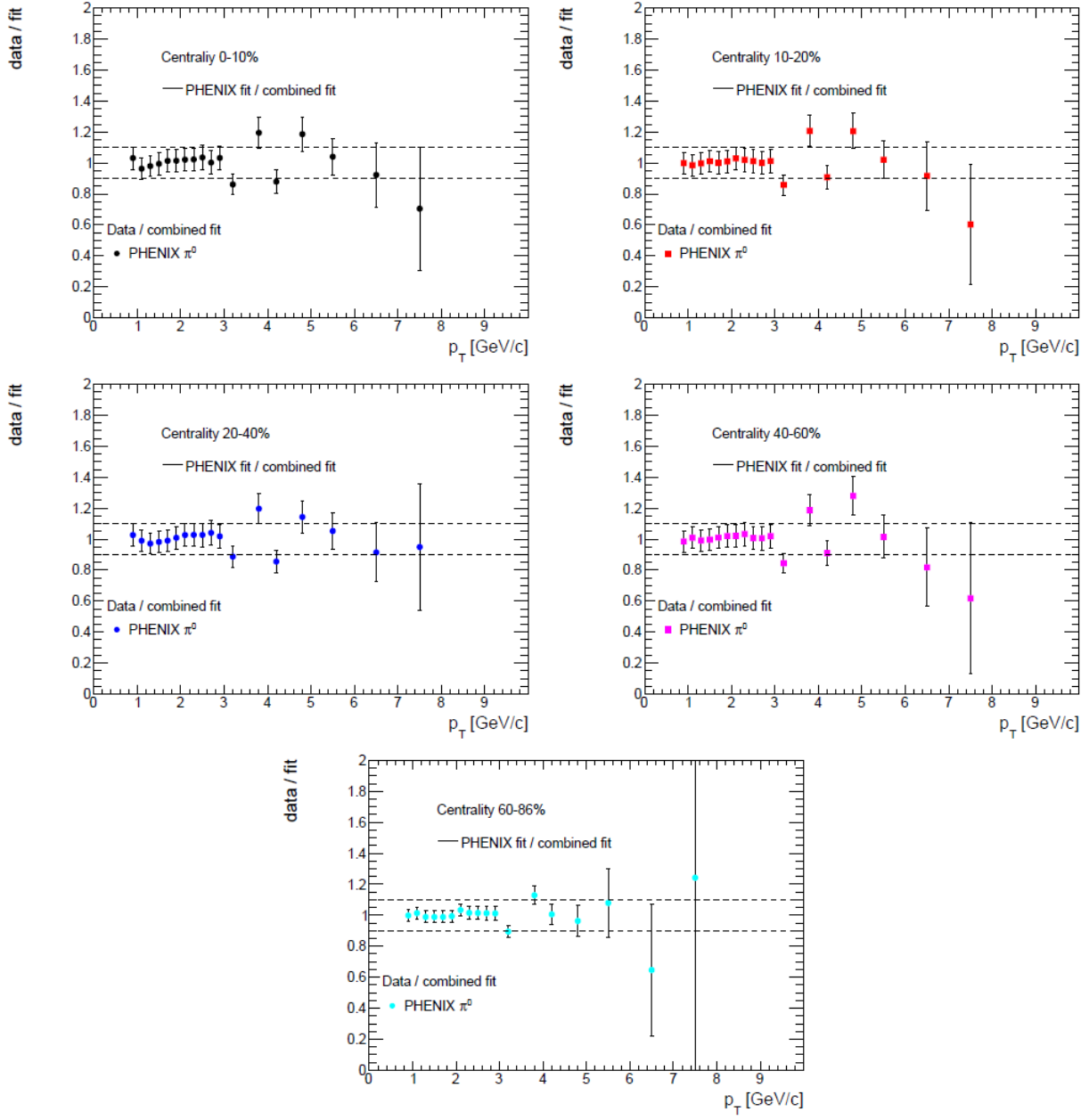


Figure 90: The ratios of the fits (to the data set shown in Fig. (89)) to the combined fit. The plot is from [143].

Figs. (89) and (90).

Thereby, in the region of $p_T < 3 \text{ GeV}/c$ one can use the following centrality-averaged systematic uncertainty (of Type B) on the conditional acceptance:

$$\delta(\langle \varepsilon_\gamma f \rangle)_{sys} \sim 8\% \quad \text{at } \sqrt{s_{NN}} = 39 \text{ GeV}.$$

5.2 Cocktail ratio

For the systematic uncertainty assessment on the cocktail ratio we take the uncertainty on an individual hadron to π^0 production rate ratio as a primary source. The ratios are determined in [134], shown in Fig. 91. The dashed line in the figure is described by the following analytical formula:

$$\delta Y_{cocktail} = \frac{0.06/0.46}{Y_{cocktail}} \frac{Y_{cocktail} - 1}{Y_{cocktail}}, \quad (127)$$

which is assumed to be derived when all uncertainties only come from the η production rate with the

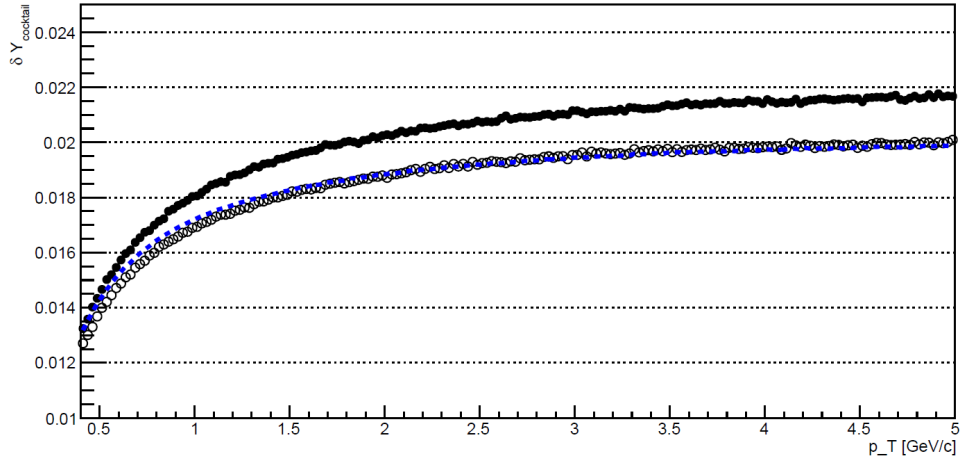


Figure 91: The relative uncertainty on the cocktail ratio taking into account all hadron to π^0 production rate uncertainties (closed points), and only the uncertainty from the η/π^0 production rate (open points). The [dashed line](#) is an analytical form shown in the text. This plot is from [134].

identical shape of the p_T distributions of η and π^0 . We see that the difference of $\delta Y_{cocktail}$ between the close and open points at large p_T values is only 10% at maximum. Therefore one can use Eq. (127) for an estimate of the relative Type B uncertainty on the cocktail ratio shown in Figs. (84) and (86) with an upper limit

$$\delta(Y_{cocktail})_{sys} \sim 2\% \text{ at } \sqrt{s_{NN}} = 62.4 \text{ GeV},$$

$$\delta(Y_{cocktail})_{sys} \sim 2\% \text{ at } \sqrt{s_{NN}} = 39 \text{ GeV}.$$

5.3 Background scale uncertainty in the π^0 yield extraction

A systematic uncertainty in the raw π^0 yield is calculated from varying models that determine the residual background: namely, varying the polynomials to which the ratio of the foreground and the combinatorial mixed event background is fitted. The variation includes 0th, 1st and 3rd order polynomials. Fig. (92), Fig. (95), Fig. (94) and Fig. (93) show the relative π^0 -tagged photon yields from

these different polynomial models at both collision energies. By looking at the plots, we assign p_T -independent uncorrelated uncertainties of 5% at 62.4 GeV and 8% at 39 GeV (treating them as Type A uncertainty), which are folded into the statistical errors of the π^0 -tagged photon yield.

$$\delta(\pi^0 \text{ yield})_{sys} \sim 5\% \text{ at } \sqrt{s_{NN}} = 62 \text{ GeV},$$

$$\delta(\pi^0 \text{ yield})_{sys} \sim 8\% \text{ at } \sqrt{s_{NN}} = 39 \text{ GeV}.$$

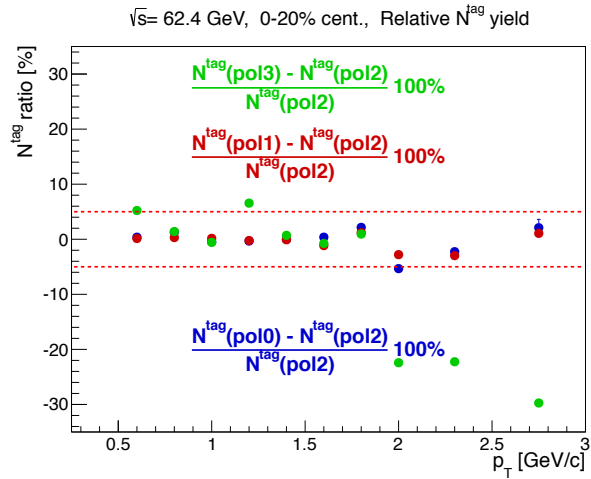
Fig. (92) and Fig. (95) are obtained with the p_{Tee} binning of this analysis, shown in Table (2) and Table (3). Meanwhile, Fig. (94) and Fig. (93) are obtained with different p_{Tee} binning, shown in Table (8) and Table (9).

0-20%	20-40%	40-60%	60-86%	0-86%
0.4 - 0.6	0.4 - 0.6	0.4 - 0.6	0.4 - 0.6	0.4 - 0.6
0.6 - 0.8	0.6 - 0.8	0.6 - 0.8	0.6 - 0.8	0.6 - 0.8
0.8 - 1.0	0.8 - 1.0	0.8 - 1.0	0.8 - 1.0	0.8 - 1.0
1.0 - 1.2	1.0 - 1.2	1.0 - 1.2	1.0 - 1.2	1.0 - 1.2
1.2 - 1.4	1.2 - 1.4	1.2 - 1.4	1.2 - 1.4	1.2 - 1.4
1.4 - 1.6	1.4 - 1.6	1.4 - 1.6	1.4 - 1.6	1.4 - 1.6
1.6 - 1.8	1.6 - 1.8	1.6 - 1.8		1.6 - 1.8
1.8 - 2.0	1.8 - 2.0	1.8 - 2.0		1.8 - 2.0
2.0 - 2.5	2.0 - 2.5	2.0 - 2.5		2.0 - 2.5
2.5 - 3.0	2.5 - 3.0			2.5 - 3.0

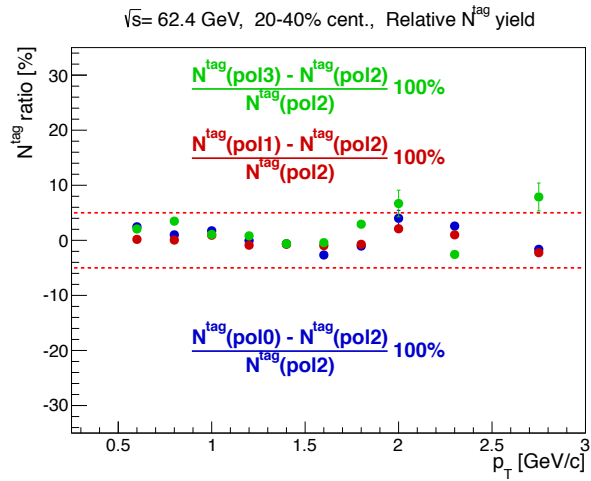
Table 8: The segmented p_{Tee} bins of converted photons (in GeV/c) in four centrality bins plus the minimum bias at $\sqrt{s_{NN}} = 62.4$ GeV. The p_{Tee} binning is different than what is used in this analysis.

0-20%	20-40%	40-60%	60-86%	0-86%
0.5 - 0.7	0.5 - 0.7	0.5 - 0.7	0.5 - 0.7	0.5 - 0.7
0.7 - 0.9	0.7 - 0.9	0.7 - 0.9	0.7 - 0.9	0.7 - 0.9
0.9 - 1.1	0.9 - 1.1	0.9 - 1.1	0.9 - 1.1	0.9 - 1.1
1.1 - 1.3	1.1 - 1.3	1.1 - 1.3	1.1 - 1.3	1.1 - 1.3
1.3 - 1.5	1.3 - 1.5	1.3 - 1.5	1.3 - 1.5	1.3 - 1.5
1.5 - 1.7	1.5 - 1.7	1.5 - 1.7	1.5 - 1.7	1.5 - 1.7
1.7 - 1.9	1.7 - 1.9	1.7 - 1.9		1.7 - 1.9
1.9 - 2.1	1.9 - 2.1			1.9 - 2.1
2.1 - 3.0	2.1 - 3.0			2.1 - 3.0

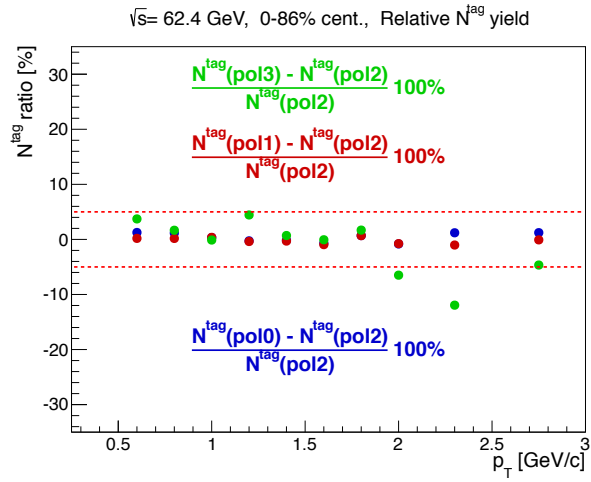
Table 9: The segmented p_{Tee} bins of converted photons (in GeV/c) in four centrality bins plus the minimum bias at $\sqrt{s_{NN}} = 39$ GeV. The p_{Tee} binning is different than what is used in this analysis.



(a)

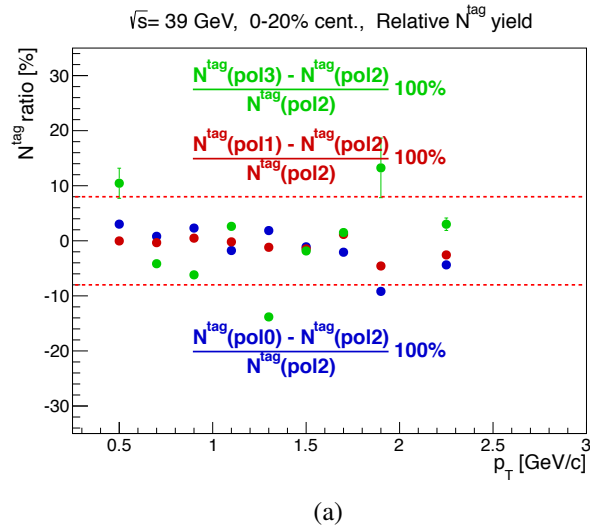


(b)

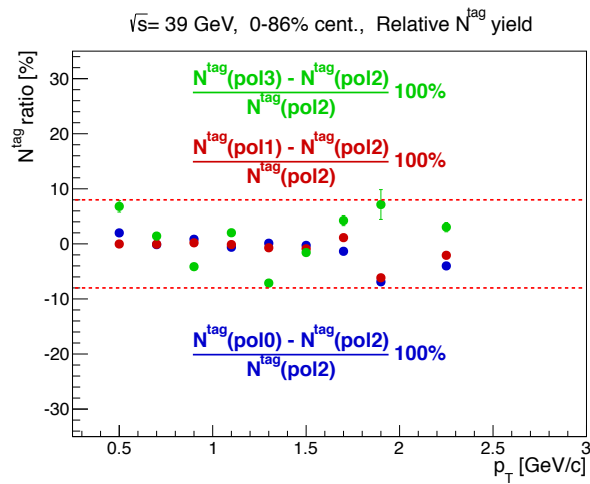


(c)

Figure 92: The relative π^0 -tagged photon yield determined from assumption of varying the residual background (which comes from various polynomial fits) at $\sqrt{s_{NN}} = 62.4 \text{ GeV}$ in the centrality bins of 0-20% (92(a)), 20-40% (92(b)) and minimum bias 0-86% (92(c)).

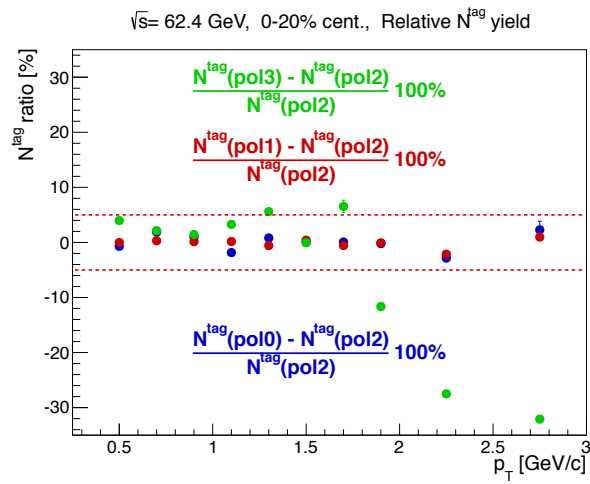


(a)

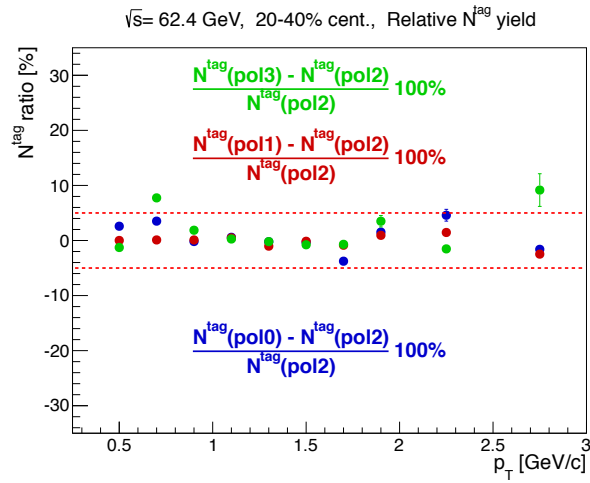


(b)

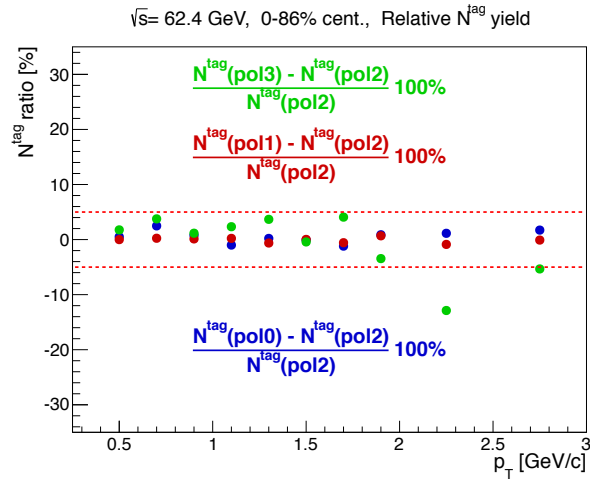
Figure 93: The relative π^0 -tagged photon yield determined from assumption of varying the residual background (which comes from various polynomial fits) at $\sqrt{s_{NN}} = 39 \text{ GeV}$ in the centrality bins of 0-20% (95(a)) and minimum bias 0-86% (95(b)).



(a)

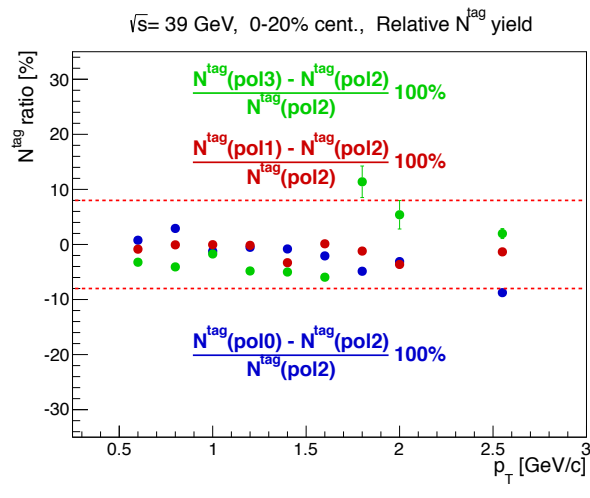


(b)

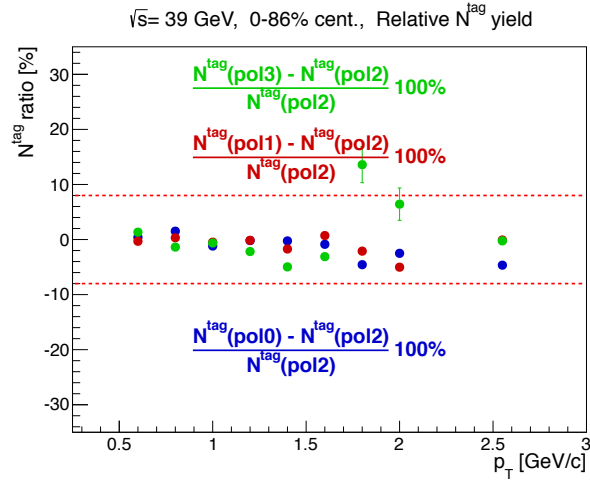


(c)

Figure 94: The nomenclature is the same as in Fig. (92), but the p_{Tee} binning is according to Table (8).



(a)



(b)

Figure 95: The nomenclature is the same as in Fig. (93), but the p_{Tee} binning is according to Table (9).

The summary of the systematic uncertainties of R_γ constituents, at the two center-of-mass energies of this analysis.

Systematic uncertainty source (62.4 GeV)	σ_{sys}/R_γ	Type
π^0 reconstruction		
tagged photon yield	5%	A
<i>Conditional acceptance</i>		
input Hagedorn p_T spectra and energy scale	5%	B
<i>Cocktail ratio</i>		
γ^{hadron}/π^0	2%	B

Table 10: The systematic uncertainties on R_γ constituents at $\sqrt{s_{NN}} = 62.4$ GeV. The type A is a source of uncertainty, which is uncorrelated between data points. The type B uncertainties are p_T -correlated.

Systematic uncertainty source (39 GeV)	σ_{sys}/R_γ	Type
π^0 reconstruction		
tagged photon yield	8%	A
<i>Conditional acceptance</i>		
input Hagedorn p_T spectra and energy scale	8%	B
<i>Cocktail ratio</i>		
γ^{hadron}/π^0	2%	B

Table 11: The systematic uncertainties on R_γ constituents at $\sqrt{s_{NN}} = 39$ GeV. The type A is a source of uncertainty, which is uncorrelated between data points. The type B uncertainties are p_T -correlated.

6 The R_γ results

The R_γ results are shown below in Fig. (96, which we can already construct by having its constituents from Eq. (98): namely, the conditional acceptance $\langle \varepsilon_\gamma f \rangle$, the cocktail ratio $Y_{cocktail}$, the raw inclusive photon yield N^{incl} , and the raw π^0 -tagged photon yield $N^{\pi^0,tag}$. $\langle \varepsilon_\gamma f \rangle$ is given in Figs. (81) and (82), $Y_{cocktail}$ is given in Figs. (84) and (86), N^{incl} is shown in Fig. (97), $N^{\pi^0,tag}$ is shown in Fig. (98), and the ratio $N^{incl}/N^{\pi^0,tag}$ is shown in Fig. (99). We show only those results of R_γ that have the

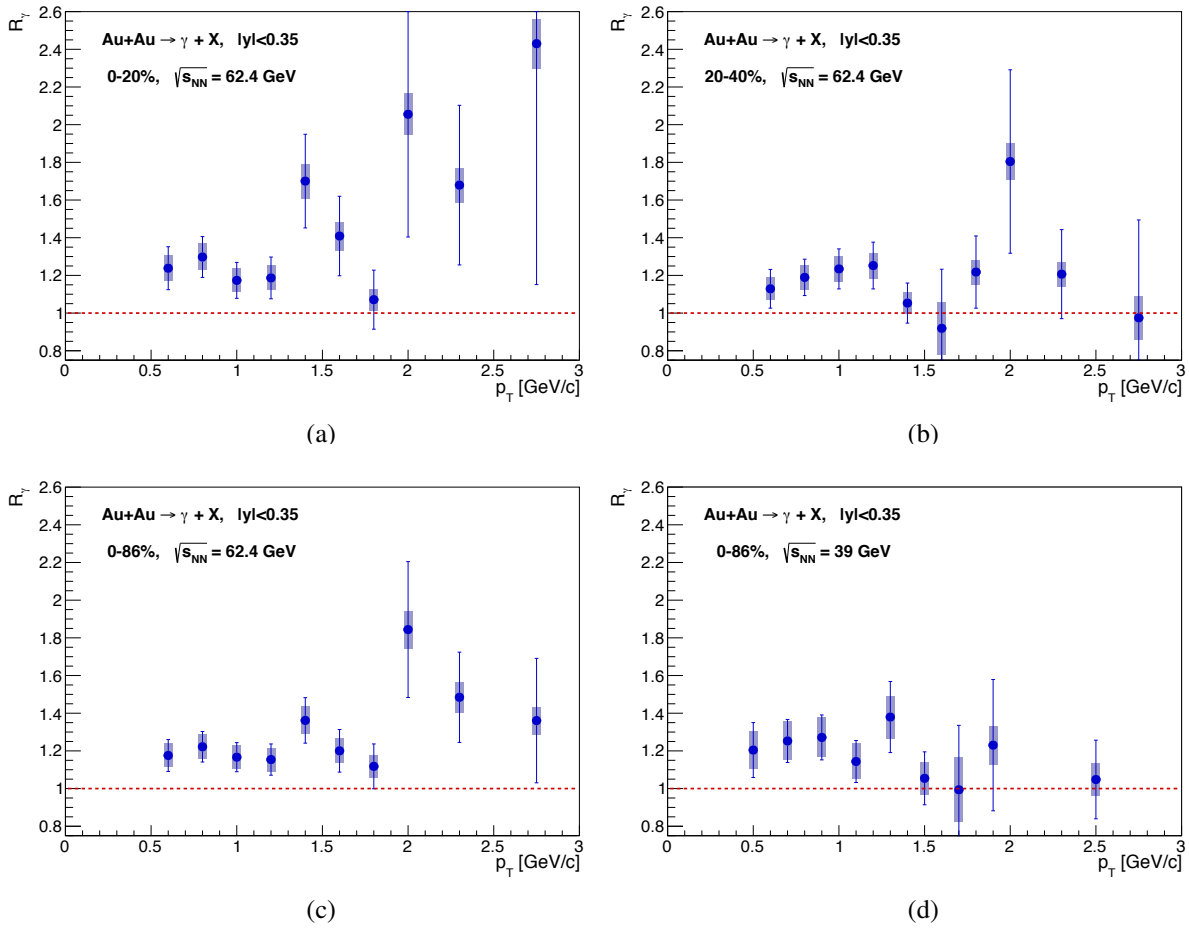


Figure 96: R_γ in the converted photon $p_{Tee} \equiv p_T$ bins at $\sqrt{s_{NN}} = 62.4$ GeV in the centrality bins of 0-20% (96(a)), 20-40% (96(b)) and minimum bias 0-86% (96(c)) as well as at $\sqrt{s_{NN}} = 39$ GeV in the minimum bias 0-86% (96(d)). The upper limits at $p_T = 1.6$ GeV/c and $p_T = 2.75$ GeV/c in Fig. (96(b)) are calculated with 95.4% confidence level (CL). The upper limit at $p_T = 1.7$ GeV/c in Fig. (96(d)) is also calculated with CL = 95.4%.

best statistics, obtained from 62.4 GeV data sample in the centralities 0-20%, 20-40% and minimum

bias 0-86%, and from 39 GeV data sample in the minimum bias 0-86%. The R_γ results in the other centralities at both collision energies are not shown because of poor statistics.

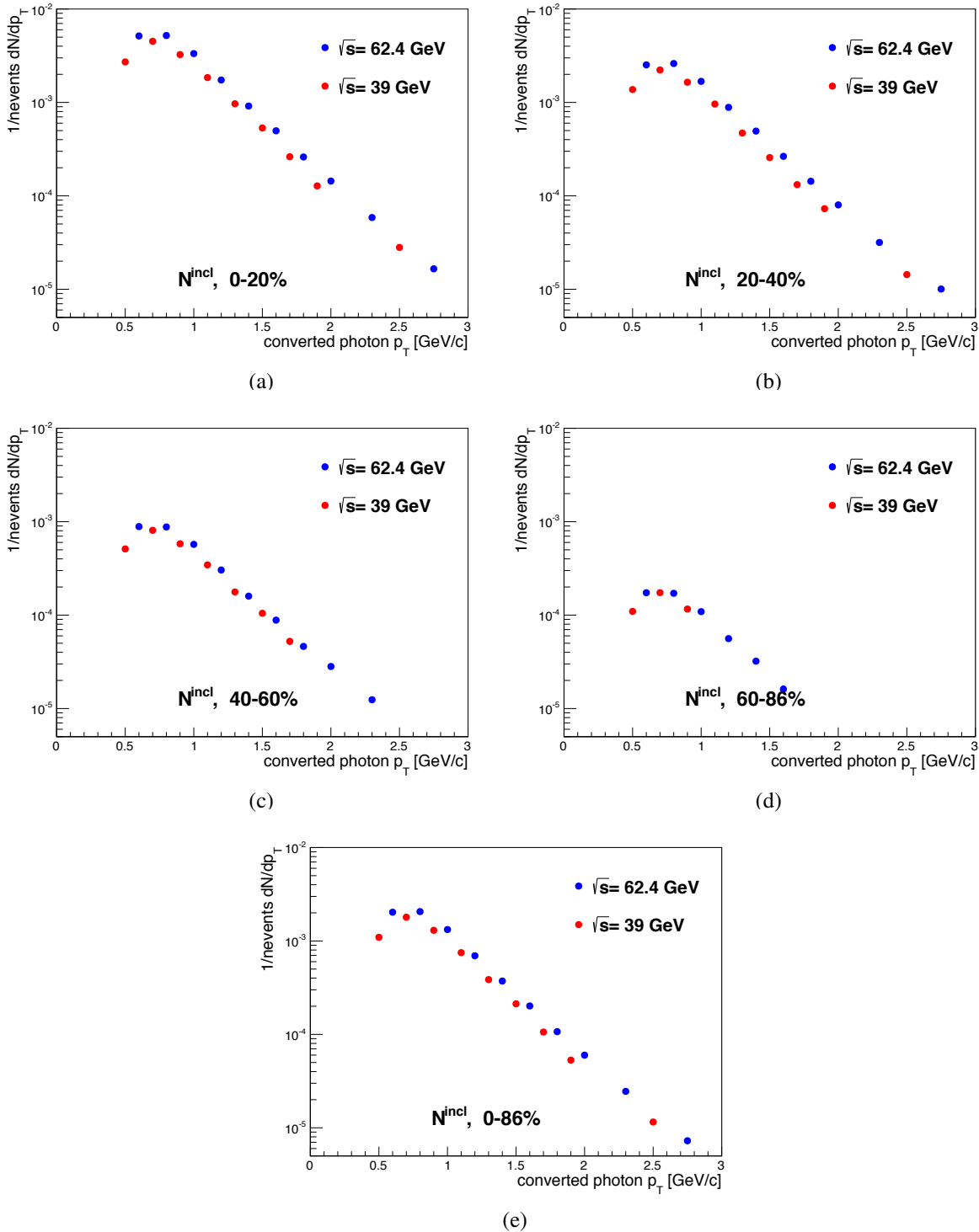


Figure 97: The raw inclusive photon yield at $\sqrt{s_{NN}} = 62.4 \text{ GeV}$ and 39 GeV in the centrality bins of 0-20% (97(a)), 20-40% (97(b)), 40-60% (97(c)), 60-86% (97(d)) and minimum bias 0-86% (97(e)).

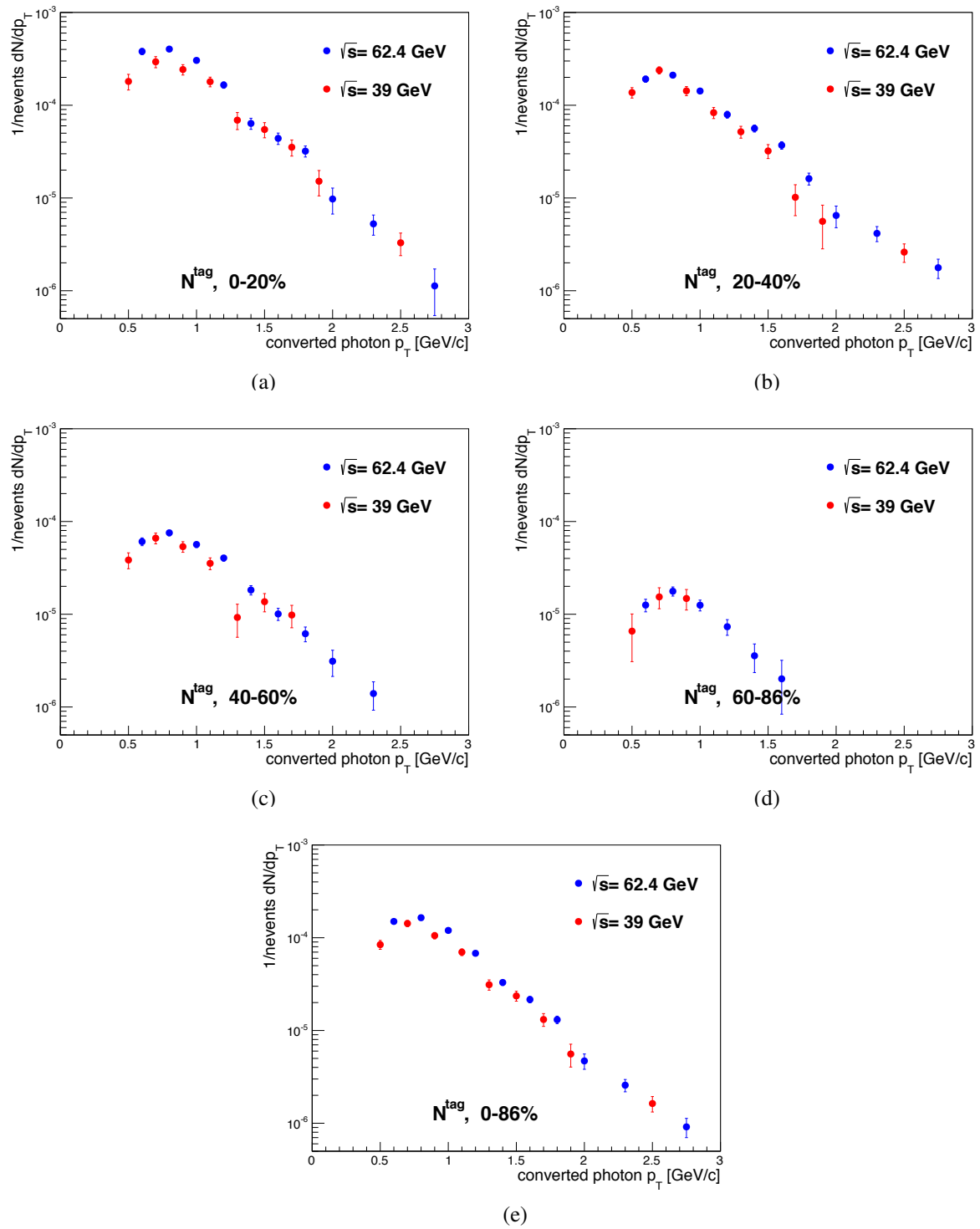


Figure 98: The raw π^0 -tagged photon yield at $\sqrt{s_{NN}} = 62.4 \text{ GeV}$ and 39 GeV in the centrality bins of 0-20% (98(a)), 20-40% (98(b)), 40-60% (98(c)), 60-86% (98(d)) and minimum bias 0-86% (98(e)).

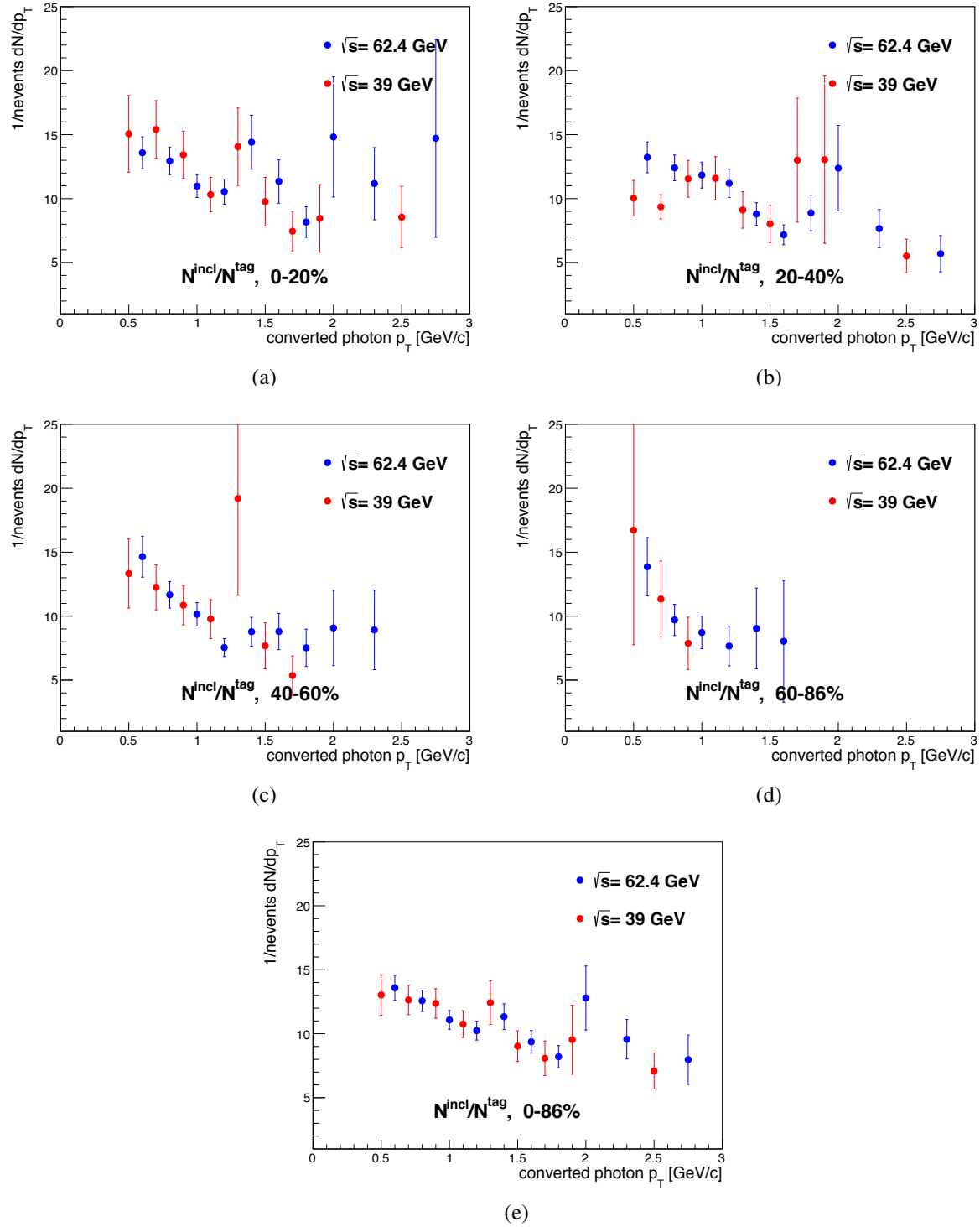


Figure 99: The ratio of the raw inclusive photon yield to the raw π^0 -tagged photon yield at $\sqrt{s_{NN}} = 62.4 \text{ GeV}$ and $\sqrt{s_{NN}} = 39 \text{ GeV}$ in the centrality bins of 0-20% (99(a)), 20-40% (99(b)), 40-60% (99(c)), 60-86% (99(d)) and minimum bias 0-86% (99(e)).

Part III

Discussion

Chapter 4

7 Discussion of the analysis results

7.1 Direct photon invariant yield at $\sqrt{s_{NN}} = 62.4 \text{ GeV}$ and $\sqrt{s_{NN}} = 39 \text{ GeV}$

In Fig. (96) we showed the results for R_γ in the transverse momentum range of $0.4 \text{ GeV}/c < p_T < 3.0 \text{ GeV}/c$, and in the centrality bins of 0-20%, 20-40% and minimum bias 0-86% at $\sqrt{s_{NN}} = 62.4 \text{ GeV}$ as well as in the minimum bias 0-86% at $\sqrt{s_{NN}} = 39 \text{ GeV}$. We observe that for most of the data points R_γ roughly shows a flat structure within our experimental uncertainties, and these points are around $R_\gamma \sim 1.2$. This means that in all given centrality classes at both energies, the magnitude of R_γ is roughly constant within the uncertainties for most of the covered momentum range, showing a signal of direct photons for most of 62.4 GeV points and at least for lowest p_T points at 39 GeV.

Thereby, we can transform these R_γ measurements to direct photon p_T spectra (invariant yield) in the same centrality classes at both collision energies using Eq. (99). One can write it down one more time

$$\gamma^{\text{direct}} = (R_\gamma - 1) \gamma^{\text{hadron}}. \quad (128)$$

Here we also use the decay photon spectra shown in Fig. (83) and Fig. (85), where the relative uncertainty ($\sim 10\%$) on the π^0 yield does not drop out as in the cocktail ratio but it should be taken into account. The calculated direct photon p_T spectra are shown in Fig. (100), Fig. (101), Fig. (102) and Fig. (103). In these plots one can also see the T_{AA} -scaled pQCD curves (from hard processes) based upon calculations from [63, 144], where one of them is extrapolated down to $p_T = 1 \text{ GeV}/c$ at the scale $\mu = 0.5 p_T$. Note that $T_{AA} = N_{\text{coll}}/\sigma_{\text{in}}$. We use $\sigma_{\text{in}} = 35.61 \text{ mb}$ at 62.4 GeV and $\sigma_{\text{in}} = 33.8 \text{ mb}$ at 39 GeV. The N_{coll} values are given in Table 70.

To characterize the shape of the excess photon spectra at low- p_T observed in these figures, we can parametrize the data with a falling exponential function

$$\frac{1}{2\pi} \frac{d^2N}{dp_T dy} \sim \exp\left(-\frac{p_T}{T_{\text{eff}}}\right), \quad (129)$$

where the inverse slope parameter, T_{eff} , quantifies the shape of the spectra, however, cannot describe

the medium temperature. We use Eq. (129) and extract the values of T_{eff} in the centrality classes under consideration. We fit the function in the range of $\sim 0.5 \text{ GeV}/c - 2.0 \text{ GeV}/c$. Table (12) shows the used T_{AA} numbers along with the extracted T_{eff} values.

Beam energy ($\sqrt{s_{NN}}$)	Centrality	$T_{AA} (\text{mb}^{-1})$	$T_{\text{eff}} (\text{MeV})$
62.4 GeV	0-20%	18.44 ± 2.49	$206 \pm 31 \pm 35$
62.4 GeV	20-40%	6.77 ± 0.82	$196 \pm 37 \pm 47$
62.4 GeV	0-86%	6.59 ± 0.89	$214 \pm 26 \pm 45$
39 GeV	0-86%	6.76 ± 1.08	$176 \pm 27 \pm 70$

Table 12: The values of T_{AA} is obtained from [145]. T_{eff} is from Fig. (100), Fig. (101), Fig. (102) and Fig. (103).

Fig. 104 shows T_{eff} for the minimum bias system at $\sqrt{s_{NN}} = 62.4 \text{ GeV}$ and $\sqrt{s_{NN}} = 39 \text{ GeV}$, and the comparison with the inverse slope from the PHENIX preliminary result in Cu+Cu (0-94%) at $\sqrt{s_{NN}} = 200 \text{ GeV}$ along with the published results on T_{eff} from the PHENIX Au+Au (0-92%) at $\sqrt{s_{NN}} = 200 \text{ GeV}$ and ALICE Pb+Pb (0-20%) at $\sqrt{s_{NN}} = 2760 \text{ GeV}$. However, we should point out that for our systems at lower beam energies, contrary to the systems at the other two energies, we obtain the values of T_{eff} without subtracting the contribution of the hard processes from the invariant yield. Other details are shown in Fig. 104.

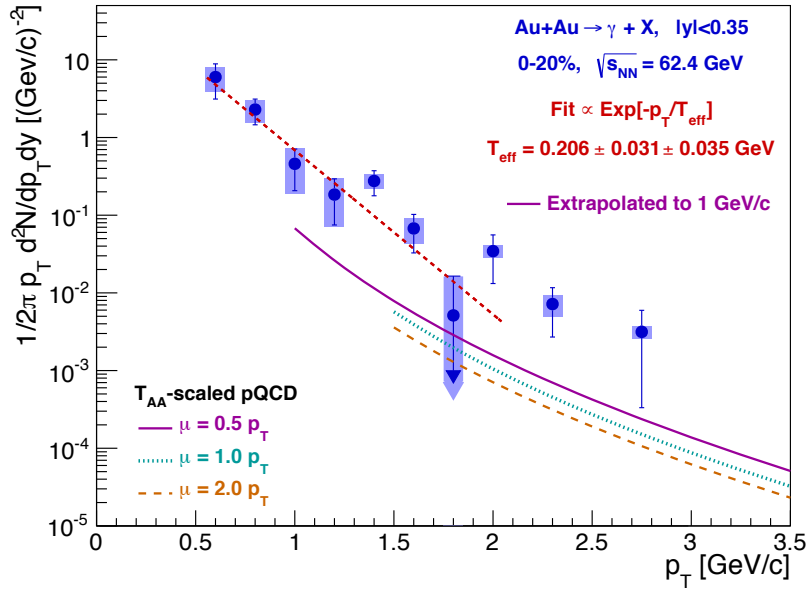


Figure 100: The invariant yield of direct photons at $\sqrt{s_{NN}} = 62.4 \text{ GeV}$ beam energy in the centrality bin of 0-20%. The inverse slope T_{eff} is obtained from fitting with the data in the p_T range of $0.55 \text{ GeV}/c - 2.05 \text{ GeV}/c$.

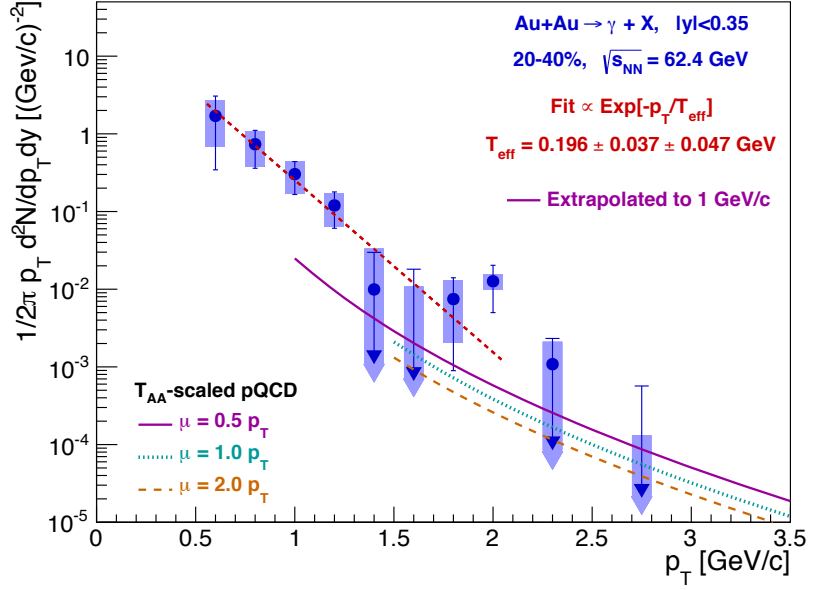


Figure 101: The invariant yield of direct photons at $\sqrt{s_{NN}} = 62.4$ GeV beam energy in the centrality bin of 20-40%. The inverse slope T_{eff} is obtained from fitting with the data in the p_T range of 0.55 GeV/c - 2.05 GeV/c.

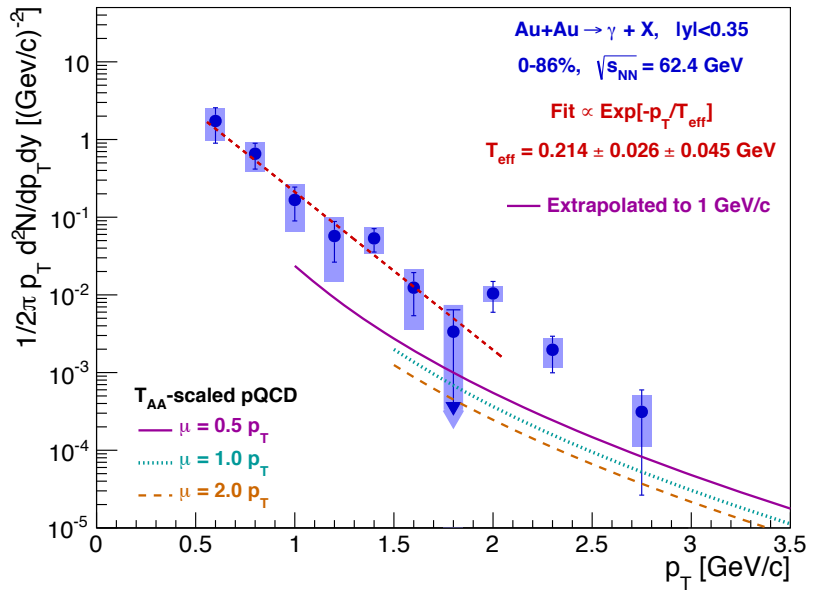


Figure 102: The invariant yield of direct photons at $\sqrt{s_{NN}} = 62.4$ GeV beam energy in the minimum bias 0-86%. The inverse slope T_{eff} is obtained from fitting with the data in the p_T range of 0.55 GeV/c - 2.05 GeV/c.

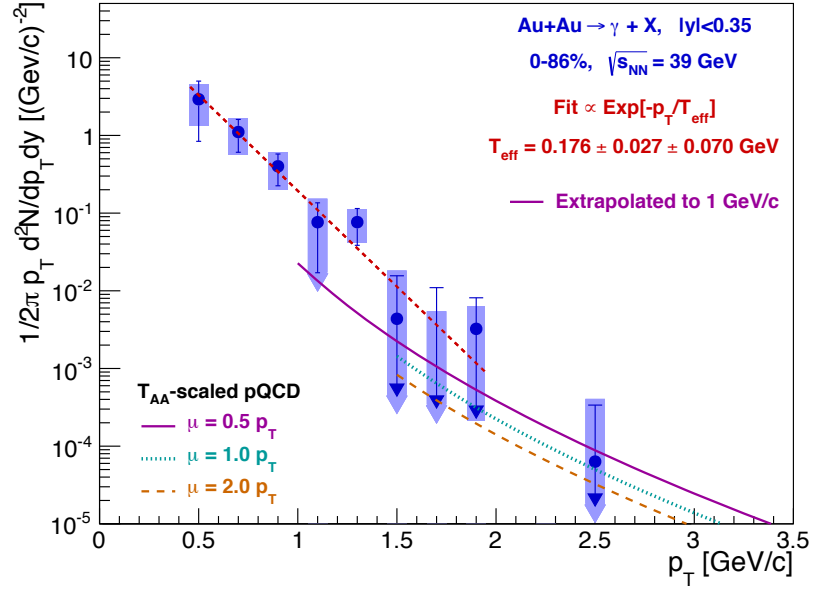


Figure 103: The invariant yield of direct photons at $\sqrt{s_{NN}} = 39$ GeV beam energy in the minimum bias 0-86%. The inverse slope T_{eff} is obtained from fitting with the data in the p_T range of 0.45 GeV/c - 1.95 GeV/c.

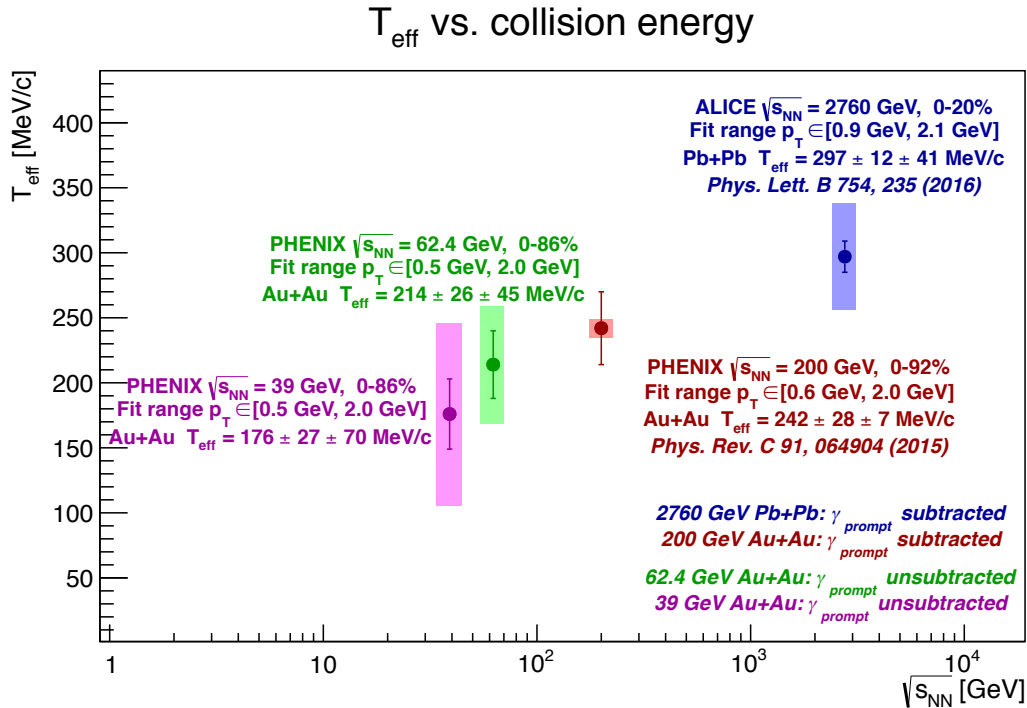


Figure 104: Data-extracted T_{eff} for four systems at four beam energies: 2760 GeV, 200 GeV and 62.4 GeV and 39 GeV.

7.2 Direct photon scaling

7.2.1 The scaling between number of binary collisions and charged particle multiplicity distribution

Before discussing the integrated yield, first we wish to focus on an interesting feature coming from a relation between the number of binary collisions, N_{coll} , and charged particle multiplicity, $dN_{ch}/d\eta$. It results in a trend with a power-law behavior, which can be seen in the following²¹.

- Fig. (105) shows the comparison of N_{coll} and $dN_{ch}/d\eta$ for Au+Au and Pb+Pb systems at four collision energies. We fit them individually by a power-law with vertical N_{coll} errors²², and extract four powers shown in the plot.

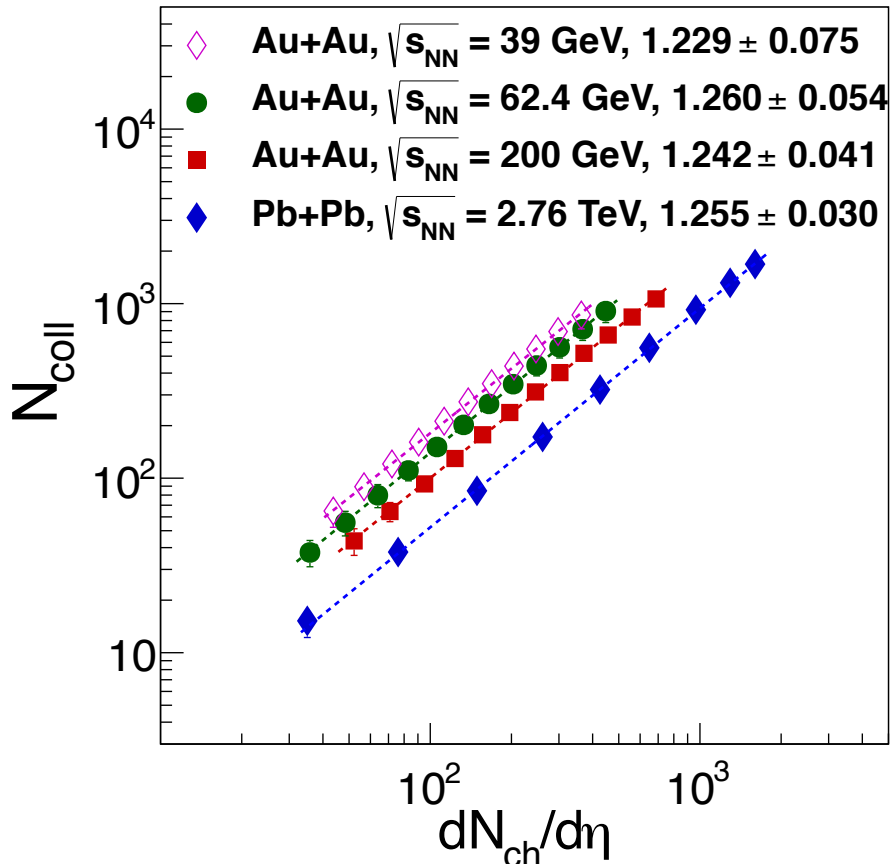


Figure 105: The number of binary collisions, N_{coll} , vs. charged particle multiplicity, $dN_{ch}/d\eta$, for four datasets, individually fitted by a power-law with vertical errors, leading to four extracted powers.

²¹Here we use the data tables of Sec. (15.1).

²²The N_{coll} values and uncertainties are from [146, 147, 148].

- Fig. (106) shows the comparison of N_{coll} and $dN_{ch}/d\eta$ for Au+Au and Pb+Pb systems at four collision energies. We fit them individually by a power-law with vertical and horizontal errors, and extract four powers shown in the plot. These powers are very similar, in fact consistent within errors, both in Fig. (105) and Fig. (106).

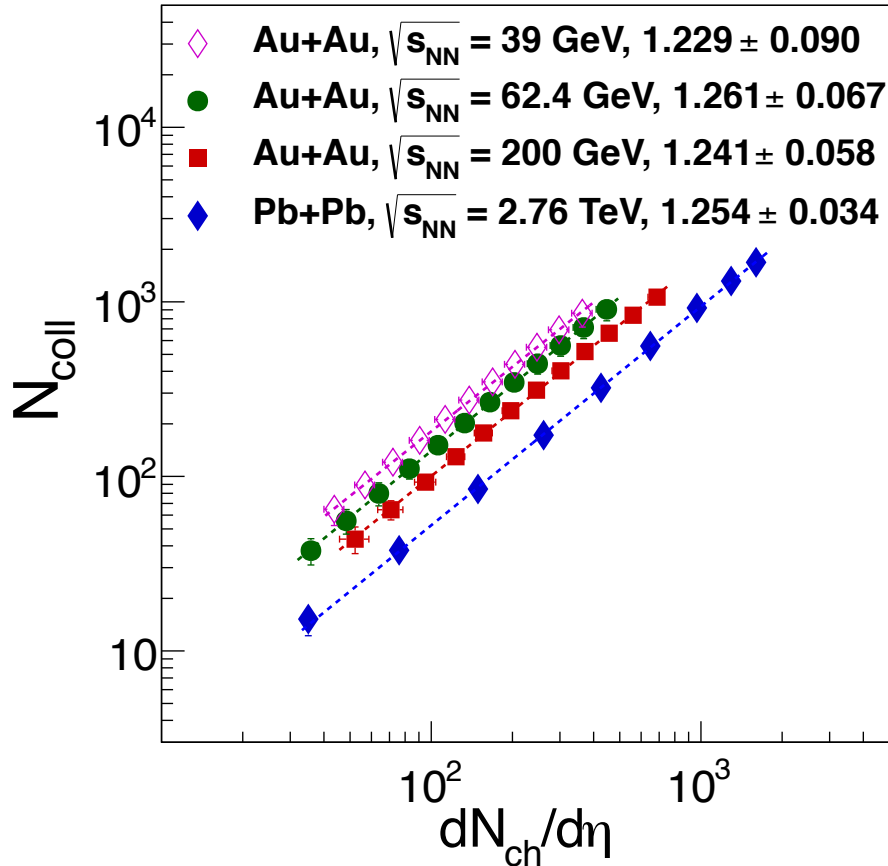


Figure 106: The number of binary collisions, N_{coll} , vs. charged particle multiplicity, $dN_{ch}/d\eta$, for four datasets, individually fitted by a power-law with vertical and horizontal errors, leading to four extracted powers.

- Therefore we attempt to use a common fit. We normalize all the results on top of each other and merge them, using the constants from the individual fits. Fig.(107) shows the comparison of N_{coll} and $dN_{ch}/d\eta$ for Au+Au and Pb+Pb systems at four collision energies. We fit them with a common fit by a power-law with vertical errors, and extract a power shown in the plot. So the slope is 1.250 ± 0.019 when we use only the vertical N_{coll} errors.

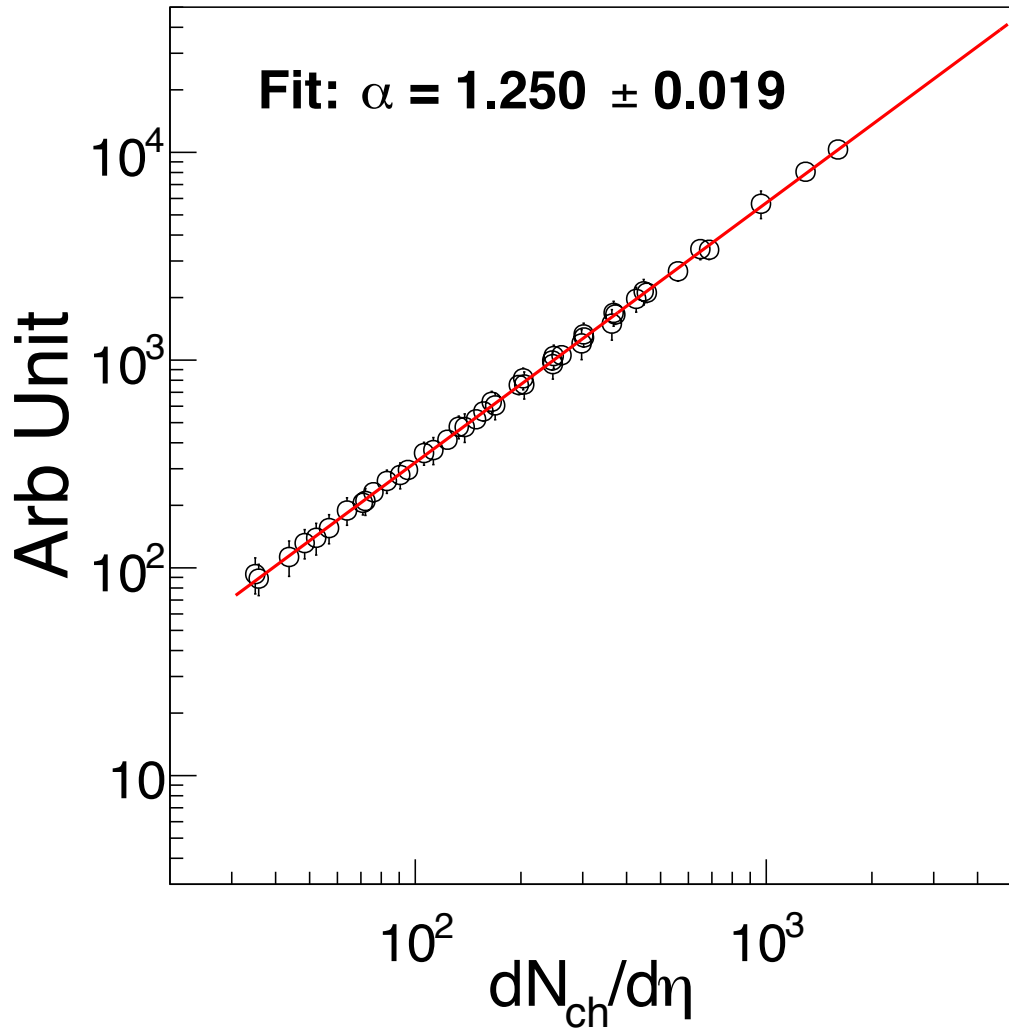


Figure 107: The number of binary collisions, N_{coll} , vs. charged particle multiplicity, $dN_{ch}/d\eta$, for four normalized and merged datasets, simultaneously fitted by a power-law with vertical errors, leading to one extracted power.

- One can again add the horizontal $dN_{ch}/d\eta$ errors. Then Fig. (108) shows the comparison of N_{coll} and $dN_{ch}/d\eta$ for Au+Au and Pb+Pb systems at four collision energies, fitted by a power-law with a common fit (with vertical and horizontal errors), which gives a power equal to 1.251 ± 0.024 .

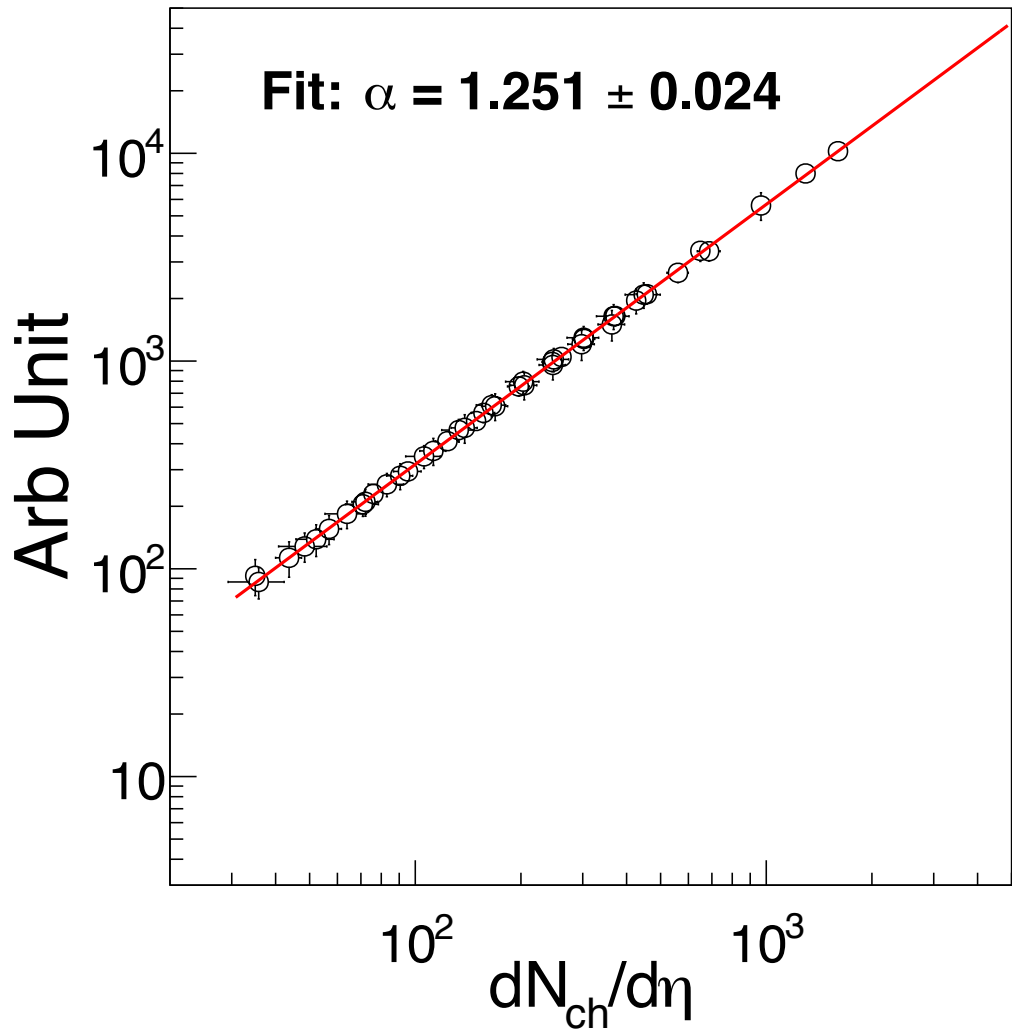


Figure 108: The number of binary collisions, N_{coll} , vs. charged particle multiplicity, $dN_{ch}/d\eta$, for four normalized and merged datasets, simultaneously fitted by a power-law with vertical and horizontal errors, leading to one extracted power.

- Fig. (109) and Fig. (110) show the ratios of the data to the common fit obtained with horizontal errors, and with vertical and horizontal errors, respectively. The fits in both plots are very consistent within the error bars.

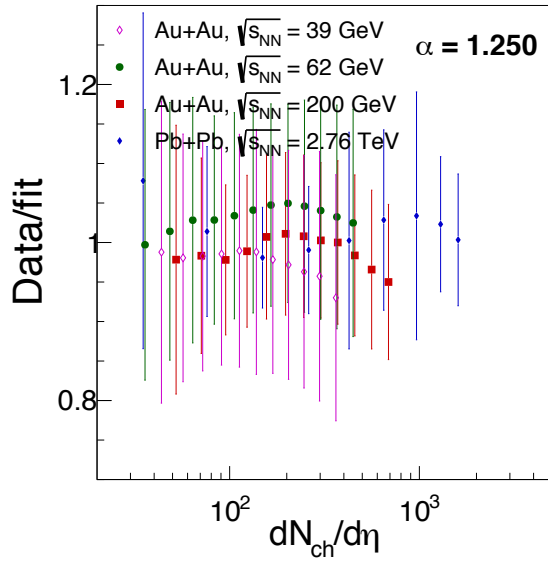


Figure 109: The ratio of the data to the simultaneous fit obtained with horizontal errors.

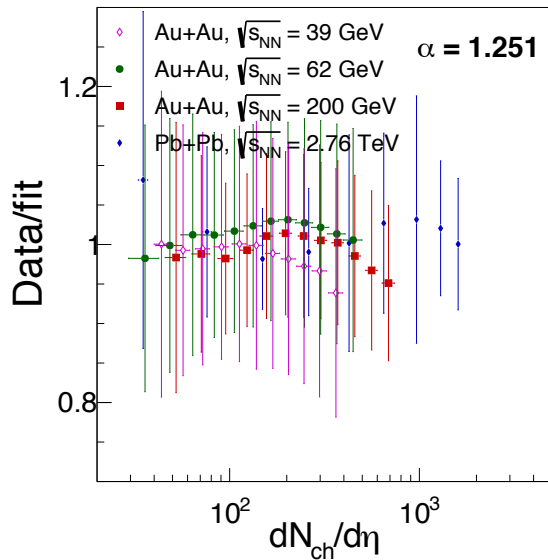


Figure 110: The ratio of the data to the simultaneous fit obtained with vertical and horizontal errors.

- Thus one can choose the power 1.25 from the simultaneous fitting, as shown in Fig. (111) below. So the data exhibit a remarkable scaling between N_{coll} and $dN_{ch}/d\eta$, which takes the form:

$$N_{coll} = \frac{1}{SY(\sqrt{s_{NN}})} \left(\frac{dN_{ch}}{d\eta} \right)^\alpha. \quad (130)$$

Here we introduce the specific yield SY, which logarithmically increases with $\sqrt{s_{NN}}$:

$$SY(\sqrt{s_{NN}}) = 1.02 \log(\sqrt{s_{NN}}) - 1.94. \quad (131)$$

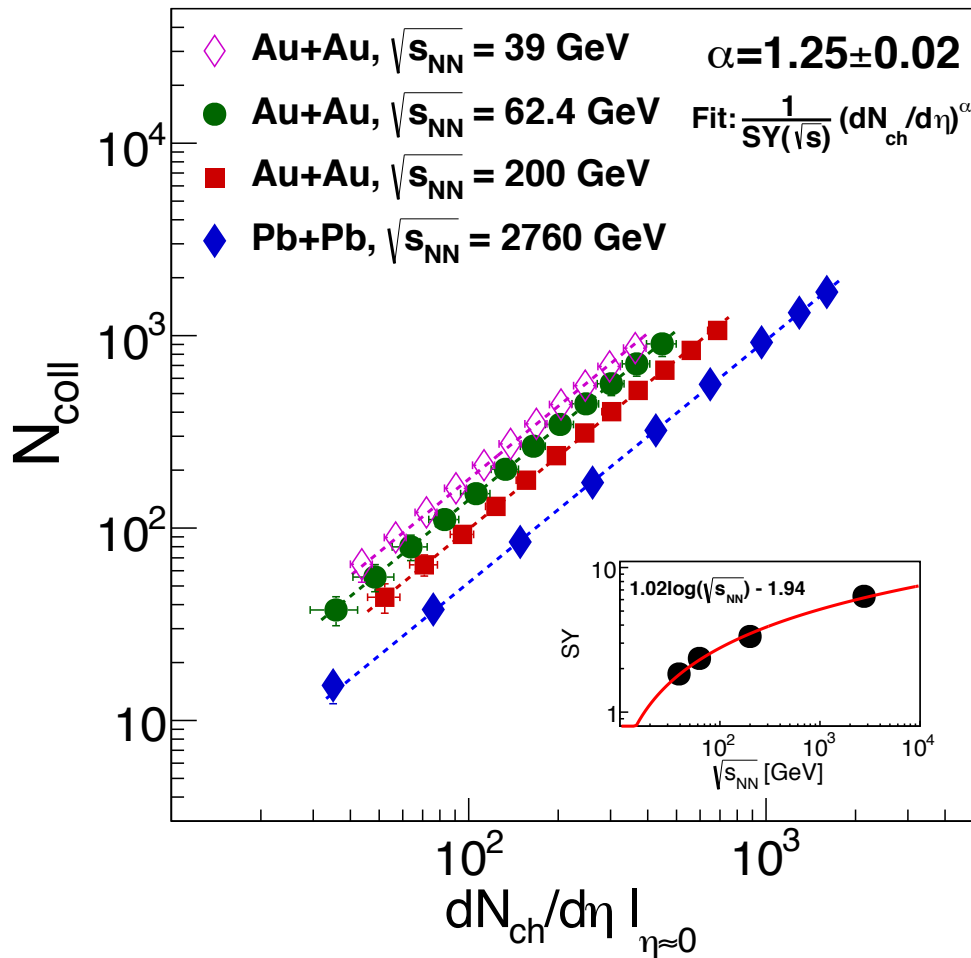


Figure 111: The number of binary collisions, N_{coll} , vs. charged particle multiplicity, $dN_{ch}/d\eta$, for four datasets, simultaneously fitted by a power-law (with vertical errors) with the power $\alpha = 1.25$.

7.2.2 Calculation of the charged hadron multiplicity for peripheral A+A systems

In Tables 63, 64, 65, 66 and in Tables 67, 68, 69 one can see the values of $dN_{ch}/d\eta$ at which the integrated invariant yields of various centrality systems at different energies are shown (the details on the integrated yield are given in the next section). In fact most of the multiplicity numbers are calculated from the tables of Sec. (15.1). For example, the $dN_{ch}/d\eta$ value of the system Au+Au 0-20% at $\sqrt{s_{NN}} = 200$ GeV is calculated from Table 29: namely,

$$dN_{ch}/d\eta(0-20\%) = \quad (132)$$

$$= \frac{5 \cdot dN_{ch}/d\eta(0-5\%) + 5 \cdot dN_{ch}/d\eta(5-10\%) + 5 \cdot dN_{ch}/d\eta(10-15\%) + 5 \cdot dN_{ch}/d\eta(15-20\%)}{20} . \quad (133)$$

Similarly all the other centrality points in the aforementioned tables can be obtained using such a formula, except for the most peripheral and minimum bias points.

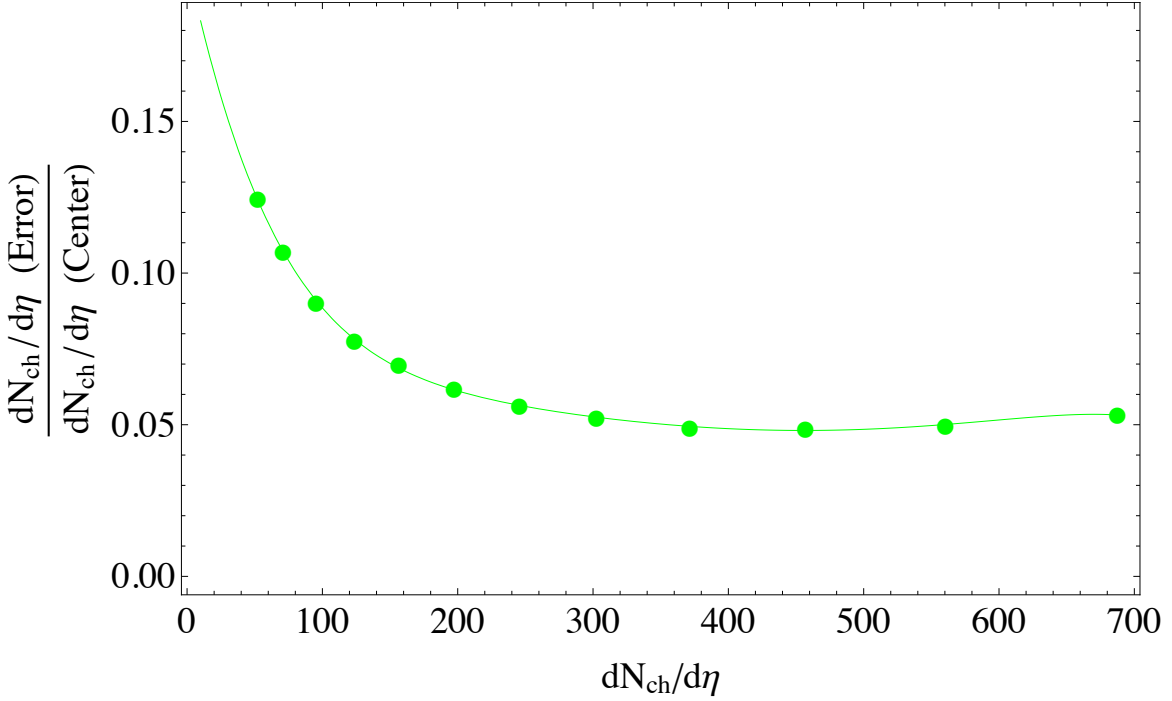


Figure 112: The ratio of the charged particle multiplicity error to its central value as a function of $dN_{ch}/d\eta$ at $\sqrt{s_{NN}} = 200$ GeV (see Table 29).

For the system Au+Au 60-92% at 200 GeV we extrapolate the multiplicity obtained from the data points of Table 29 to the low $dN_{ch}/d\eta$ region. This can be done using higher order polynomial functions. The extrapolated value will be $dN_{ch}/d\eta = 16.362$. Then we look at Fig. (112) and Fig. (113) (again obtained from Table 29), to get another extrapolated number, which is the error of $dN_{ch}/d\eta$ (for

Au+Au 60-92% at 200 GeV) obtained from the ratio of $dN_{ch}/d\eta(\text{Error}) / dN_{ch}/d\eta(\text{Center})$. Both extrapolated green curves in Fig.(112) and Fig.(113) give very close values for $dN_{ch}/d\eta(\text{Error})$. Ultimately we take 16.362 ± 2.814 .

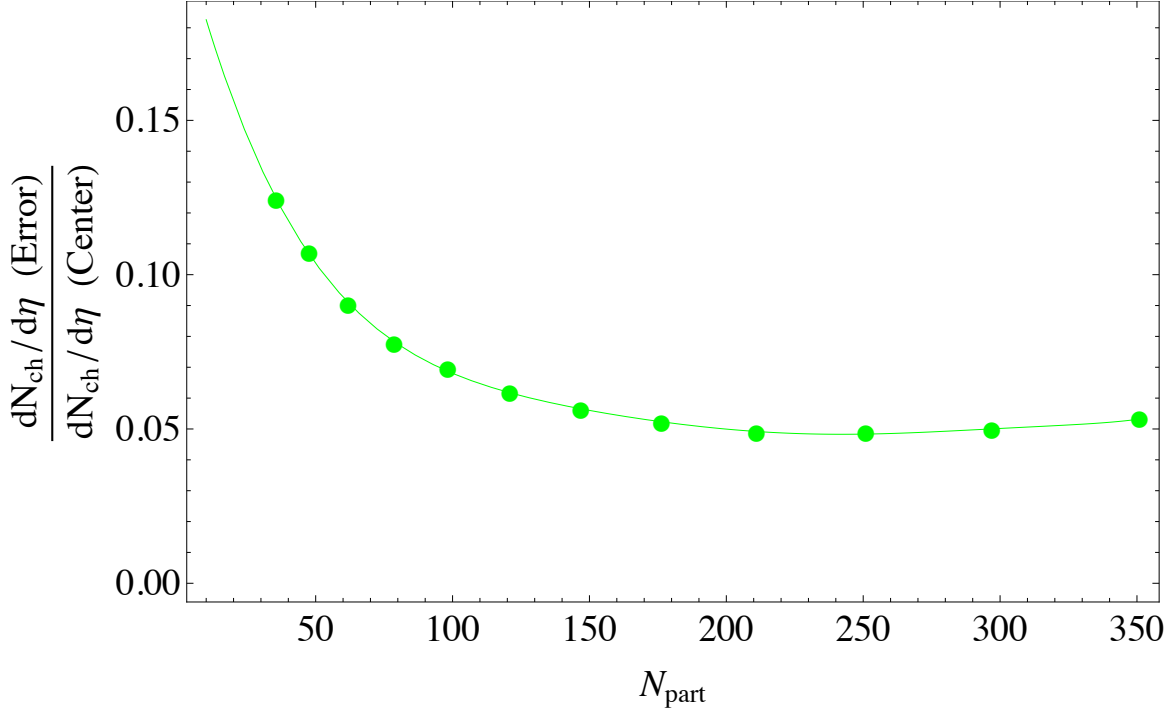


Figure 113: The ratio of the charged particle multiplicity error to its central value as a function of N_{part} at $\sqrt{s_{NN}} = 200$ GeV (see Table 29).

Then we can get the multiplicity for the system Au+Au 0-92% at 200 GeV from

$$dN_{ch}/d\eta(0-92\%) = \quad (134)$$

$$= \frac{20 \cdot dN_{ch}/d\eta(0-20\%) + 20 \cdot dN_{ch}/d\eta(20-40\%) + 20 \cdot dN_{ch}/d\eta(40-60\%) + 32 \cdot dN_{ch}/d\eta(60-92\%)}{92}. \quad (135)$$

We use this procedure described above to obtain the other multiplicity values for the systems Au+Au 0-86% at 62.4 GeV/39 GeV and Cu+Cu 0-94% at 200 GeV.

7.2.3 Integrated yield vs. charged particle multiplicity

One of the key observables to characterize the properties of the matter produced in (ultra)relativistic heavy ion collisions is the multiplicity distribution of the charged-particle pseudorapidity density, $dN_{ch}/d\eta$, at midrapidity. We can have understanding on the relative contributions to particle production from hard and soft processes by investigating the dependence of the charged-particle multiplicity

on the collision geometry, initial parton and energy densities of the produced matter. As the collision energy increases, the role of the hard processes also increases, which may provide insight into the partonic structure of the colliding nuclei.

PHENIX has measured the multiplicity distributions for a variety of collision systems from $\sqrt{s_{NN}} = 7.7 \text{ GeV}$ to 200 GeV [145]. ALICE in turn has measured the distributions in Pb+Pb collisions at $\sqrt{s_{NN}} = 2.76 \text{ TeV}$ and 5.02 TeV [149, 150]. PHENIX has also measured the midrapidity distributions of transverse energy, $dE_T/d\eta$, along with $dN_{ch}/d\eta$. Some interesting findings show that the production of E_T and N_{ch} in collisions of symmetric nuclei depends on the collision energy and is independent of the size of the colliding system, nevertheless, one should also take into account their dependence on the mean p_T of charged particles. The ratio of $dE_T/d\eta$ to $dN_{ch}/d\eta$ is found to be constant as a function of centrality for all collision systems and energies. Besides, a weak dependence of this ratio as a function of $\sqrt{s_{NN}}$ is observed too.

We know that the high- p_T direct photon nuclear modification factor, R_{AA} , is unity at all centralities and energies [151], which would also mean that the high- p_T direct photon yield would scale with $(dN_{ch}/d\eta)^\alpha$, where $\alpha = 1.25$. Fig.(114)²³ shows the spectra of direct photons normalized by $(dN_{ch}/d\eta)^{1.25}$, for Au+Au data in five centrality classes at $\sqrt{s_{NN}} = 200 \text{ GeV}$ and for Cu+Cu data in two centrality classes at $\sqrt{s_{NN}} = 200 \text{ GeV}$ (left panel), as well as for Pb+Pb 0-20% data at $\sqrt{s_{NN}} = 2.76 \text{ TeV}$, Au+Au 0-20% data at $\sqrt{s_{NN}} = 200 \text{ GeV}$, Au+Au 0-20% and 0-86% data at $\sqrt{s_{NN}} = 62.4 \text{ GeV}$ and Au+Au 0-86% data at $\sqrt{s_{NN}} = 39 \text{ GeV}$. The statistical and systematic errors combined in quadrature, along with all upper limits are shown too.

Thereby, in the left panel of Fig. (114) we see that the high- p_T direct photon invariant yield scales as expected in Au+Au collisions [151]. Meanwhile, on top of that we surprisingly see the same scaling behavior for the low- p_T region. On the other hand, in the right panel we actually see how at low- p_T the same scaling occurs across different centrality systems and center-of-mass energies when we compare with each other the direct photon data from Pb+Pb at 2.76 TeV and Au+Au at 200 GeV, 62.4 GeV, 39 GeV. Here at high- p_T the scaling seems to take place for various centrality systems but within a specific energy.

In Fig. (114) we have also other additions: first, the prompt photon p+p fit from Ref. [42] described by the purple band:

$$\text{Prompt photons: p+p fit} = T_{AA} \times \frac{A_{pp}}{(1 + p_T^2/p_0)^n}, \quad (136)$$

where the parameters are $A_{pp} = (8.3 \pm 7.5) \cdot 10^{-3} \text{ mb GeV}^{-2}$, $p_0 = 2.26 \pm 0.78 \text{ GeV}^2$ and $n = 3.45 \pm 0.08$. The systematic uncertainties of these quantities are highly correlated. The purple band is the uncertainty of the fit.

Second, we show prompt photon calculations at $\sqrt{s_{NN}} = 2760 \text{ GeV}$, 200 GeV , 62.4 GeV , which are

²³See also Fig. (115) and Fig. (116).

perturbative QCD (pQCD) calculations extrapolated down to $p_T = 1 \text{ GeV}/c$ at the scale $\mu = 0.5 p_T$ from [144]. Generally, the pQCD calculation with $\mu = 0.5 p_T$ is directly applicable for $p_T > 3 \text{ GeV}/c$. In the extrapolation procedure, below this $3 \text{ GeV}/c$, larger scales (up to $\mu = 8.0 p_T$) are used down to $p_T = 1 \text{ GeV}/c$, and then the result is rescaled such that it matches the calculation done with $\mu = 0.5 p_T$ at higher p_T . For a parton distribution function (PDF) and a fragmentation function (FF), the nCTEQ15-np as nuclear PDF and BFG-II as photon FF are used, respectively. We normalize the pQCD curves with the experimental $dN_{ch}/d\eta$ values from p+p collisions. We use the following $dN_{ch}/d\eta$ for normalization at the above three collision energies: $dN_{ch}/d\eta = 3.75 \pm 0.26$ at 2760 GeV [152], $dN_{ch}/d\eta = 2.38 \pm 0.17$ at 200 GeV [145] and $dN_{ch}/d\eta = 1.864$ at 62.4 GeV [152].

The direct photon integrated yield is actually the sum of the direct photon invariant yield (which has statistical and systematic errors):

$$\text{yield} = \frac{dN_\gamma}{dy} = \sum_{p_T(i)} \frac{d^3 N(i)}{d^2 p_T dy} \Delta p_T. \quad (137)$$

In this case the statistical error is the square root of the absolute errors added in quadrature:

$$\sigma_{\text{yield}}^{\text{stat}} = \sqrt{\sum_i (\sigma_{\text{yield}}^{\text{stat}}(i))^2}, \quad (138)$$

and the systematic error (if fully correlated) is just the sum of the absolute errors:

$$\sigma_{\text{yield}}^{\text{sys}} = \sum_i (\sigma_{\text{yield}}^{\text{sys}}(i)). \quad (139)$$

Since the direct photon spectra can be quantified by integrating the invariant yield above some p_T threshold value, now we can look at the scaling properties of direct photons when we plot the low- p_T and high- p_T integrated yields vs. $dN_{ch}/d\eta$. Similarly, in order to characterize the evolution of the excess photon yield with $dN_{ch}/d\eta$ (or centrality N_{part}) one can examine the p_T -integrated yield calculated from the measured invariant yield spectra with

$$\frac{dN_\gamma}{dy} = 2\pi \int_{p_{T,\min}}^{p_{T,\max}} dp_T p_T \left(\frac{1}{2\pi p_T} \frac{d^2 N}{dp_T dy} \right), \quad (140)$$

where we have the integral of the invariant yield from a minimal $p_{T,\min}$ up to the end $p_{T,\max}$ of the covered range. Taking into account that the photon spectra are steeply falling in photon p_T , it is obvious that any such integrated yield will be dominated by the behavior of the lowest p_T points, which contribute most of the yield. The values of $p_{T,\min}$ and $p_{T,\max}$ can be seen in the integrated yield plots and corresponding captions shown in Fig.(119), Fig.(120), Fig.(121), Fig.(122), and

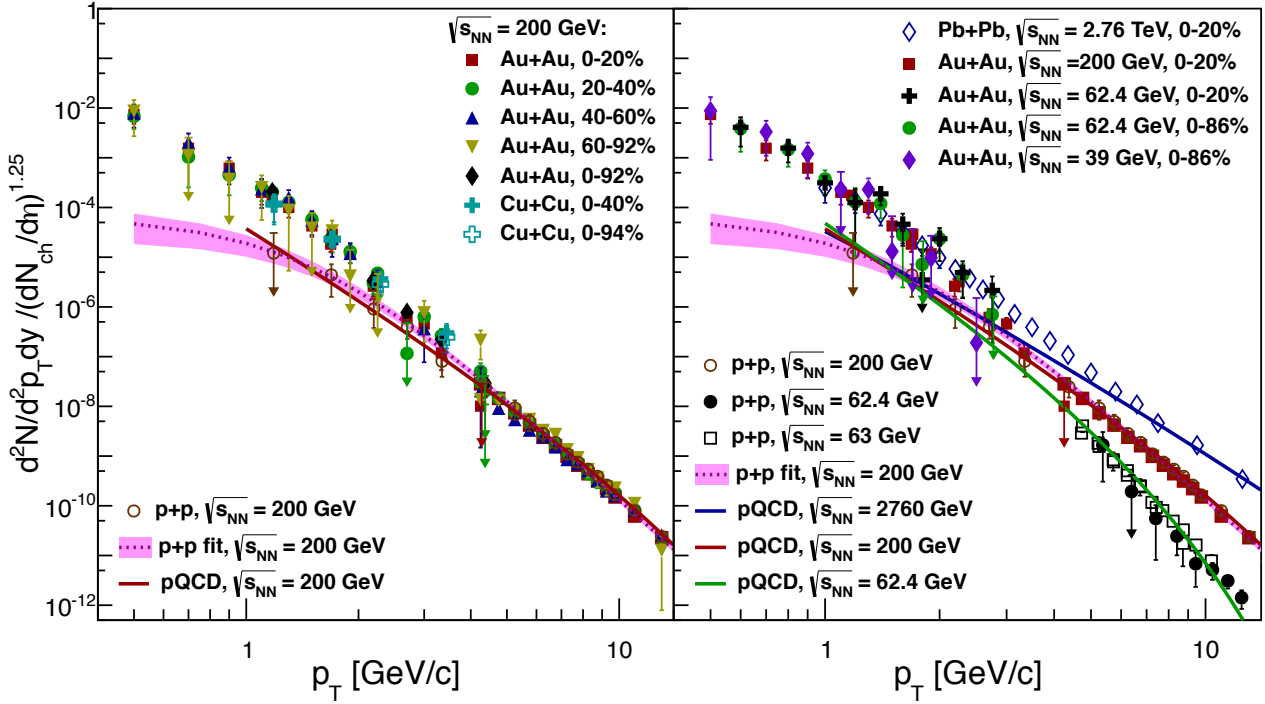


Figure 114: The direct photon spectra normalized by $(dN_{ch}/d\eta)^{1.25}$, for Au+Au and Cu+Cu datasets at 200 GeV collision energy (left panel), and for four A+A datasets at different collision energies (right panel). The data in Au+Au at 200 GeV are from [40, 42], in Cu+Cu at 200 GeV from [44], and in Pb+Pb at 2.76 TeV from [45]. The data in Au+Au at 62.4 GeV and 39 GeV are those from Fig. (100), Fig. (101), Fig. (102) and Fig. (103) (this analysis). The 200 GeV p+p data points are from [153], the 62.4 GeV p+p and 63 GeV p+p data points are from [154, 155, 156, 157]. The statistical and systematic errors combined in quadrature, along with all upper limits are shown as well. All the corresponding direct photon invariant yield data tables can be seen in Sec. (15.2).

in Fig. (123), Fig. (124), Fig. (125). In all these figures we plot the integrated excess photon yield dN_γ/dy as a function of the charged particle multiplicity $dN_{ch}/d\eta$, where the data are fitted with the power-law function $(dN_{ch}/d\eta)^\alpha$ with the same $\alpha = 1.25$ as in Fig. (111). A very interesting feature is that the N_{coll} scaled prompt photons seem to have a similar scaling trend as that from heavy ion direct photons.

Fig. (119), Fig. (120), Fig. (121), Fig. (122), and in Fig. (123), Fig. (124), Fig. (125) are made taking into account the bin-shift correction for the integrated yield. For example, when we wish to obtain the integrated yield, dN_γ/dy , by summing the bins of the invariant yield, we should first multiply the invariant yield and the statistical/systematic errors of the data points by the corresponding correction factor in each p_T bin. Then we can sum all the bins to get the integrated yield. For an exponential

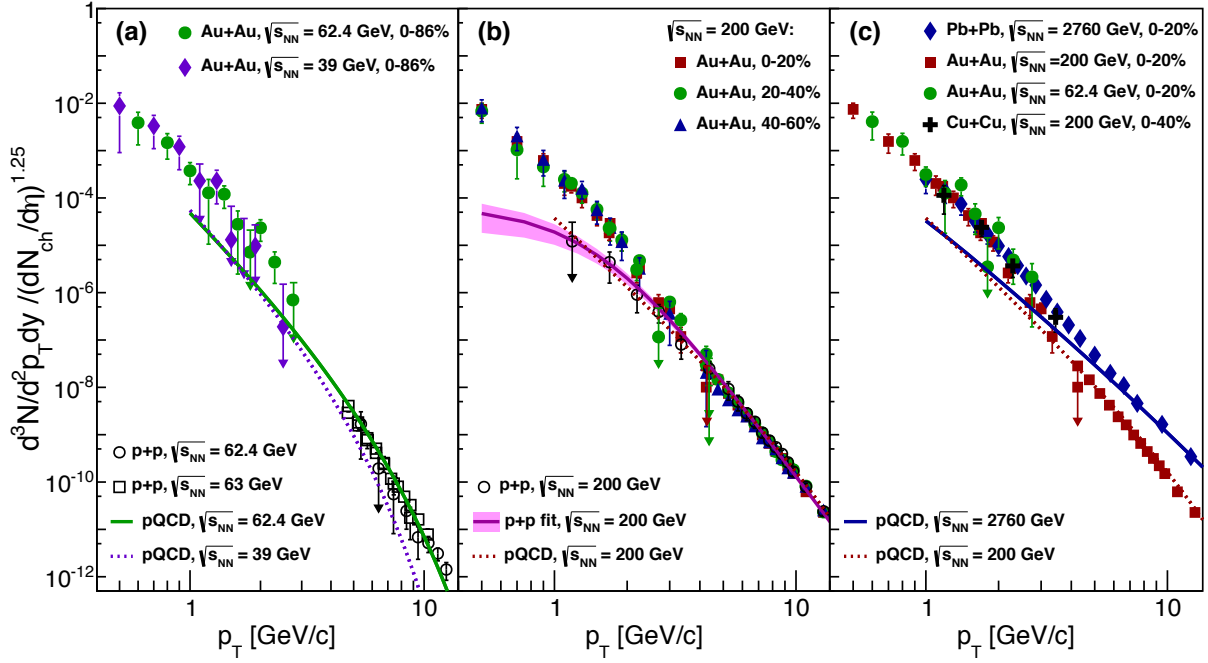


Figure 115: Another version of Fig. (114) with the same nomenclature.

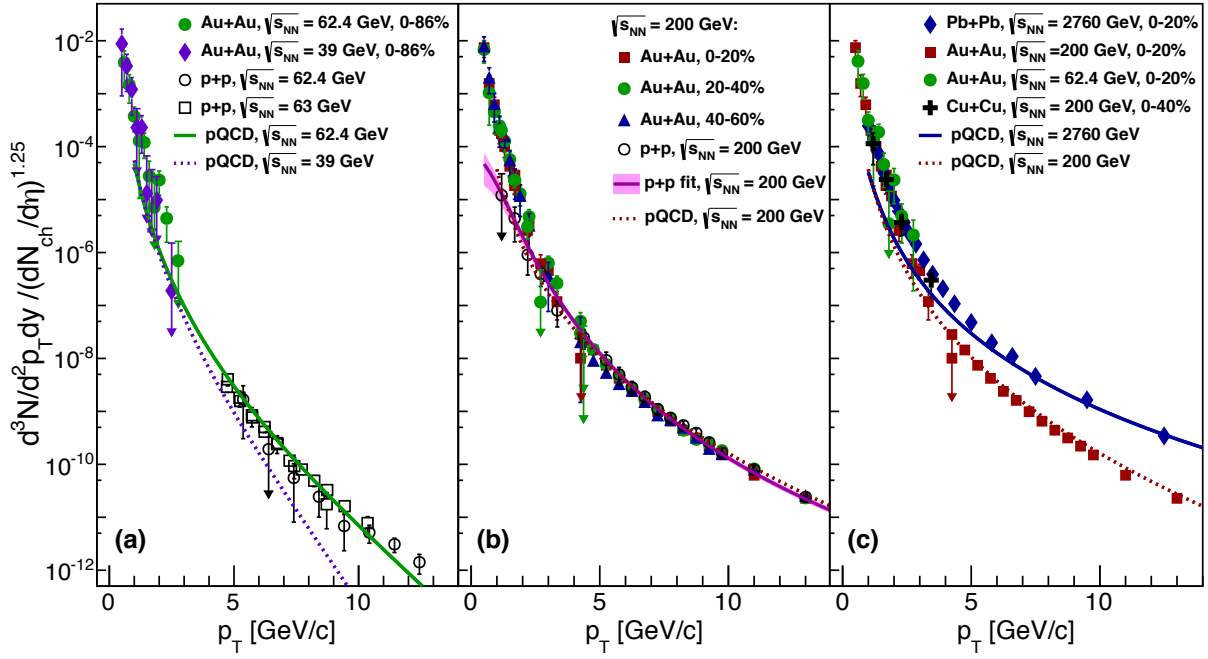


Figure 116: A linear-log version of Fig. (115) with the same nomenclature.

function at low- p_T region one can use

$$\text{Correction factor} = \frac{\text{Integral}(A \cdot \text{Exp}[-p_T/T_{\text{eff}}])}{A \cdot \text{Exp}[-p_{T,\text{center}}/T_{\text{eff}}] \Delta p_T}. \quad (141)$$

Fig. (117) and Fig. (118) show two cases for obtaining the integral correction when the data points are located at the center of p_T bin, and at the mean of p_T bin.

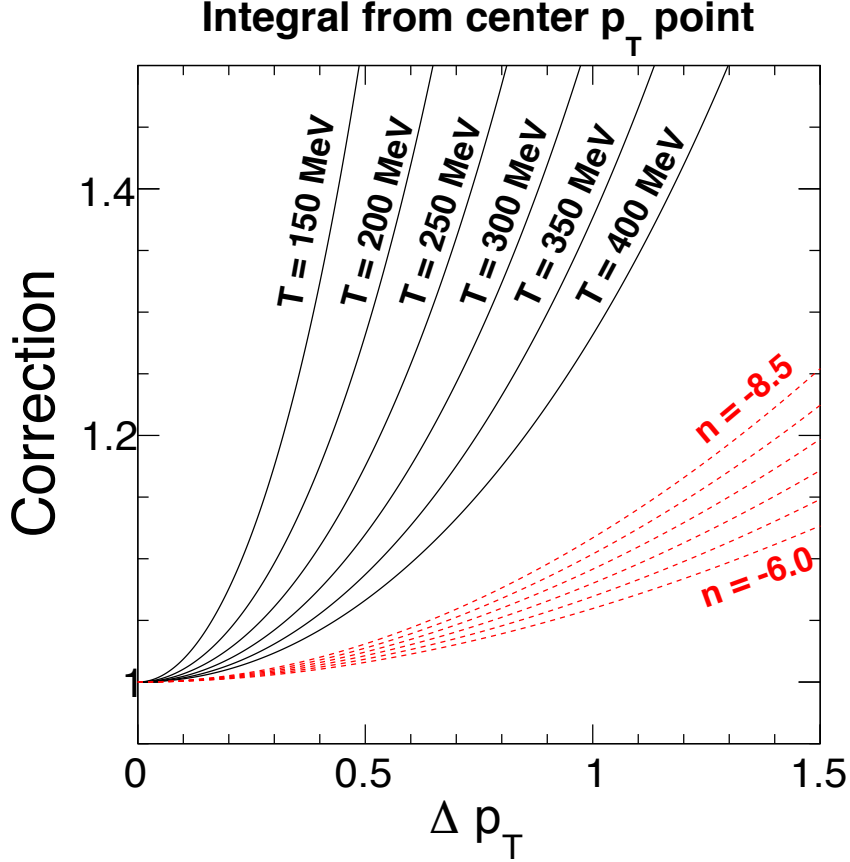


Figure 117: The integral correction using the center p_T point (correction upward). For the exponential we use minimum $p_T = 1 \text{ GeV}/c$, for the power-law we use minimum $p_T = 5 \text{ GeV}/c$. For the exponential, the correction is independent of p_T . For the power-law, the correction depends not only on n but also on p_T .

It is quite surprising that all the fits in these plots are described by a two-parameter power-law function. Furthermore, one can use another two-parameter function of the form

$$Fit = a \cdot (dN_{ch}/d\eta) + b \cdot (dN_{ch}/d\eta)^{4/3}, \quad (142)$$

where a and b are constants. Such a function would sort of suggest a two-component source, one linear with $dN_{ch}/d\eta$ (bremsstrahlung from charge creation), and the other smaller fraction going with

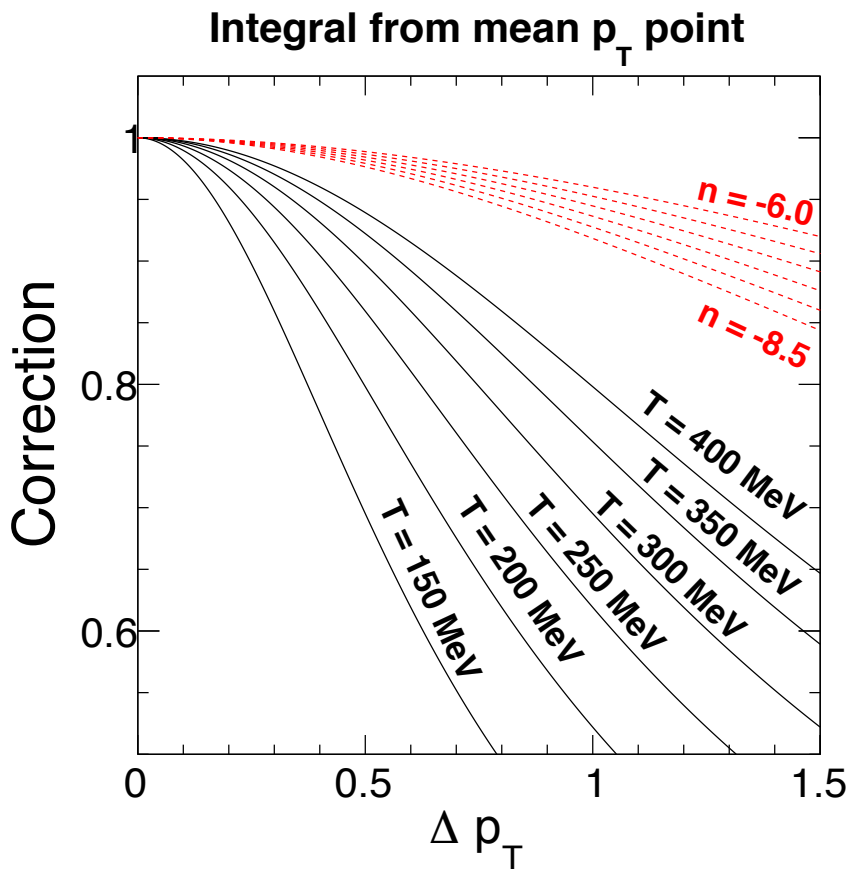


Figure 118: The integral correction using the mean p_T point (correction downward). For the exponential we use minimum $p_T = 1$ GeV/c, for the power-law we use minimum $p_T = 5$ GeV/c. For the exponential, the correction is independent of p_T . For the power-law, the correction depends not only on n but also on p_T .

$(dN_{ch}/d\eta)^{4/3}$ (thermal radiation from *volume* \times *time*). The comparison of Fig. (120) with Fig. (126) as well as Fig. (121) with Fig. (127) show that the two-parameter fits are actually quite close to each other.

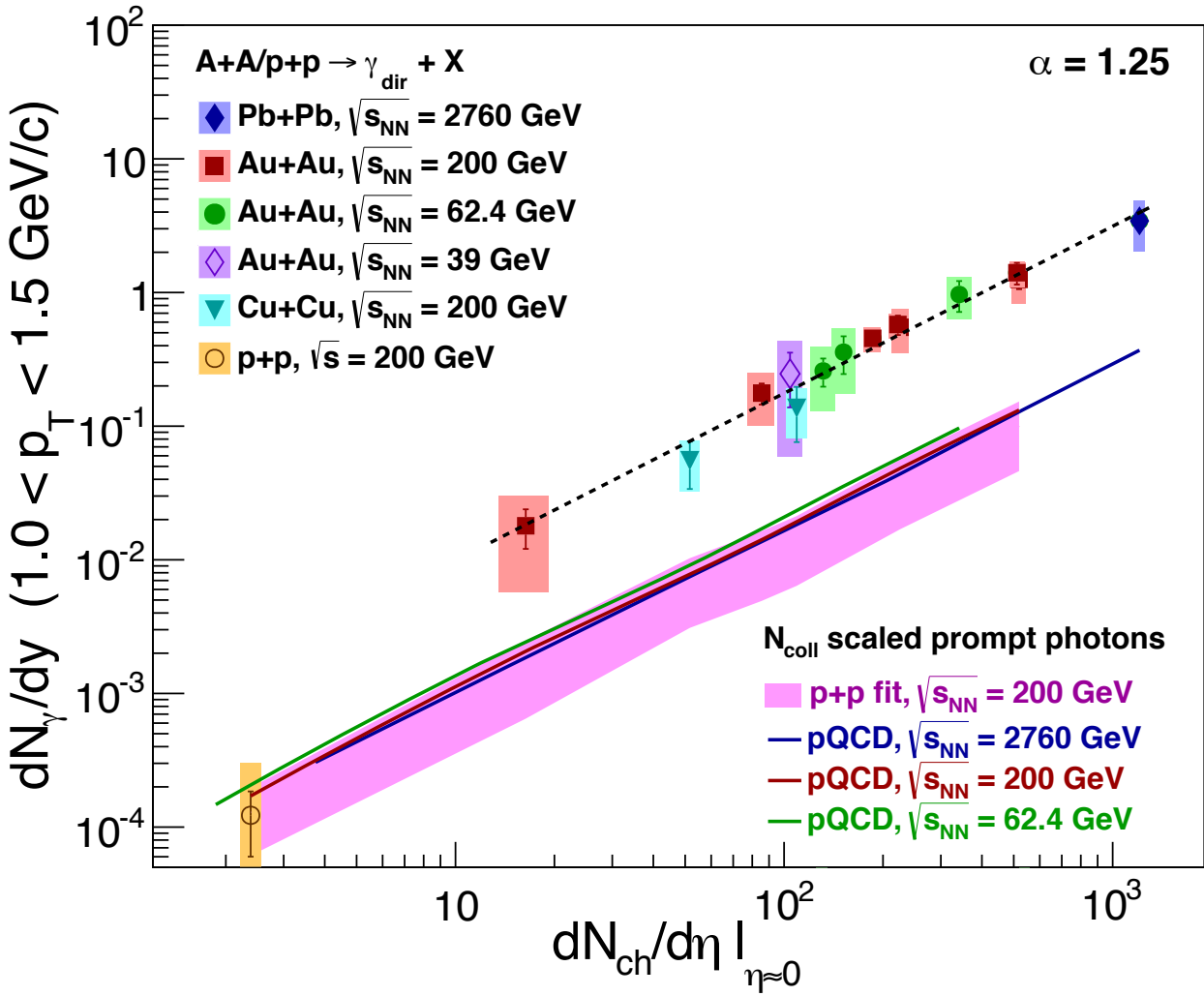


Figure 119: The direct photon integrated yield vs. charged particle multiplicity for p_T integrated from 1.0 GeV/c to 1.5 GeV/c, for five A+A datasets and one p+p dataset. The references for Pb+Pb, Au+Au and Cu+Cu systems are shown in Fig. (114). The p+p data are from [153]. The p+p fit describing the N_{coll} scaled prompt photons is obtained using a parameterization from [42] (see Eq. (136)). Each model curve also describing these N_{coll} scaled prompt photons is the (integrated) prompt photon yield extrapolated down to $p_T = 1.0$ GeV/c [144], at respective beam energy. All the corresponding direct photon integrated yield points can be seen in Table 63. The power $\alpha = 1.25$ is from Fig. (111). The black colored dashed fit is described by $Fit = 0.000557 \cdot dN_{ch}/d\eta^{1.25}$. If α were not fixed, it would be $\alpha = 1.184 \pm 0.040$.

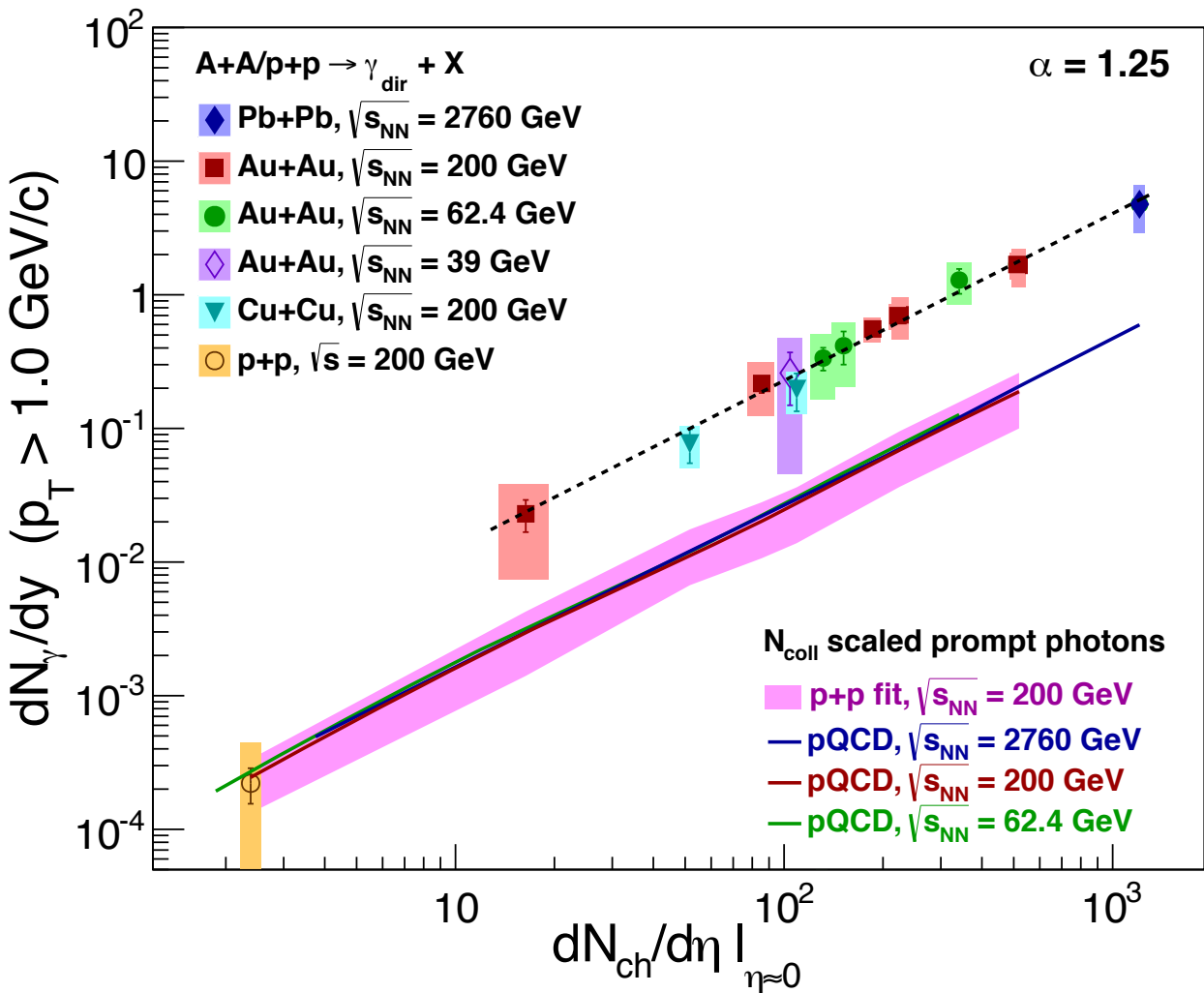


Figure 120: The direct photon integrated yield vs. charged particle multiplicity for p_T integrated from $1.0 \text{ GeV}/c$ to $5.0 \text{ GeV}/c$, for five A+A datasets and one p+p dataset. The nomenclature is the same as in Fig. 119. All the corresponding direct photon integrated yield points can be seen in Table 64. The power $\alpha = 1.25$ is from Fig. (111). The black colored dashed fit is described by $Fit = 0.000721 \cdot dN_{ch}/d\eta^{1.25}$. If α were not fixed, it would be $\alpha = 1.211 \pm 0.033$.

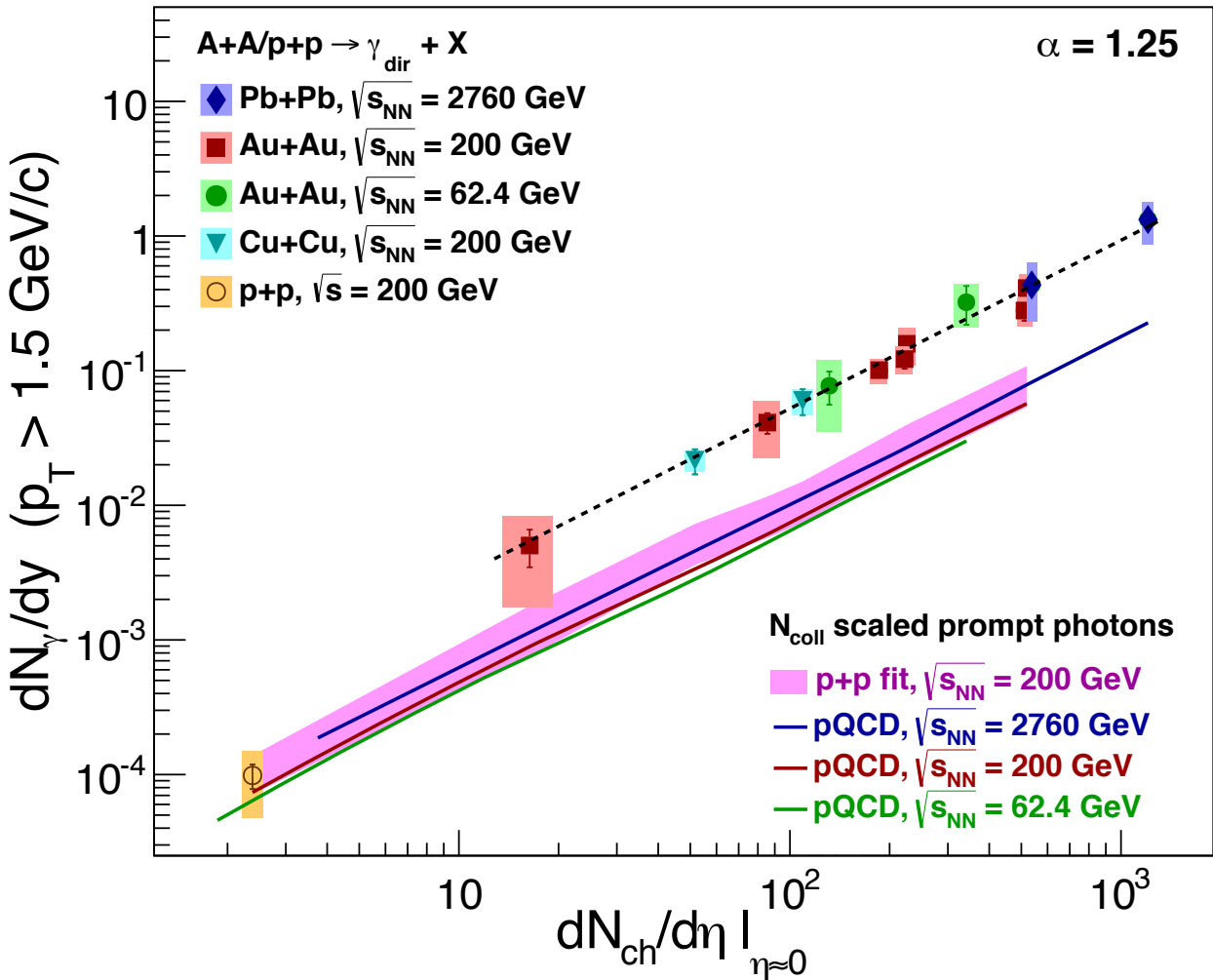


Figure 121: The direct photon integrated yield vs. charged particle multiplicity for p_T integrated from $1.5 \text{ GeV}/c$ to $5.0 \text{ GeV}/c$, for four A+A datasets and one p+p dataset. The nomenclature is the same as in Fig. 119. All the corresponding direct photon integrated yield points can be seen in Table 65. The power $\alpha = 1.25$ is from Fig. (111). The black colored dashed fit is described by $Fit = 0.000165 \cdot dN_{ch}/d\eta^{1.25}$. If α were not fixed, it would be $\alpha = 1.321 \pm 0.037$.

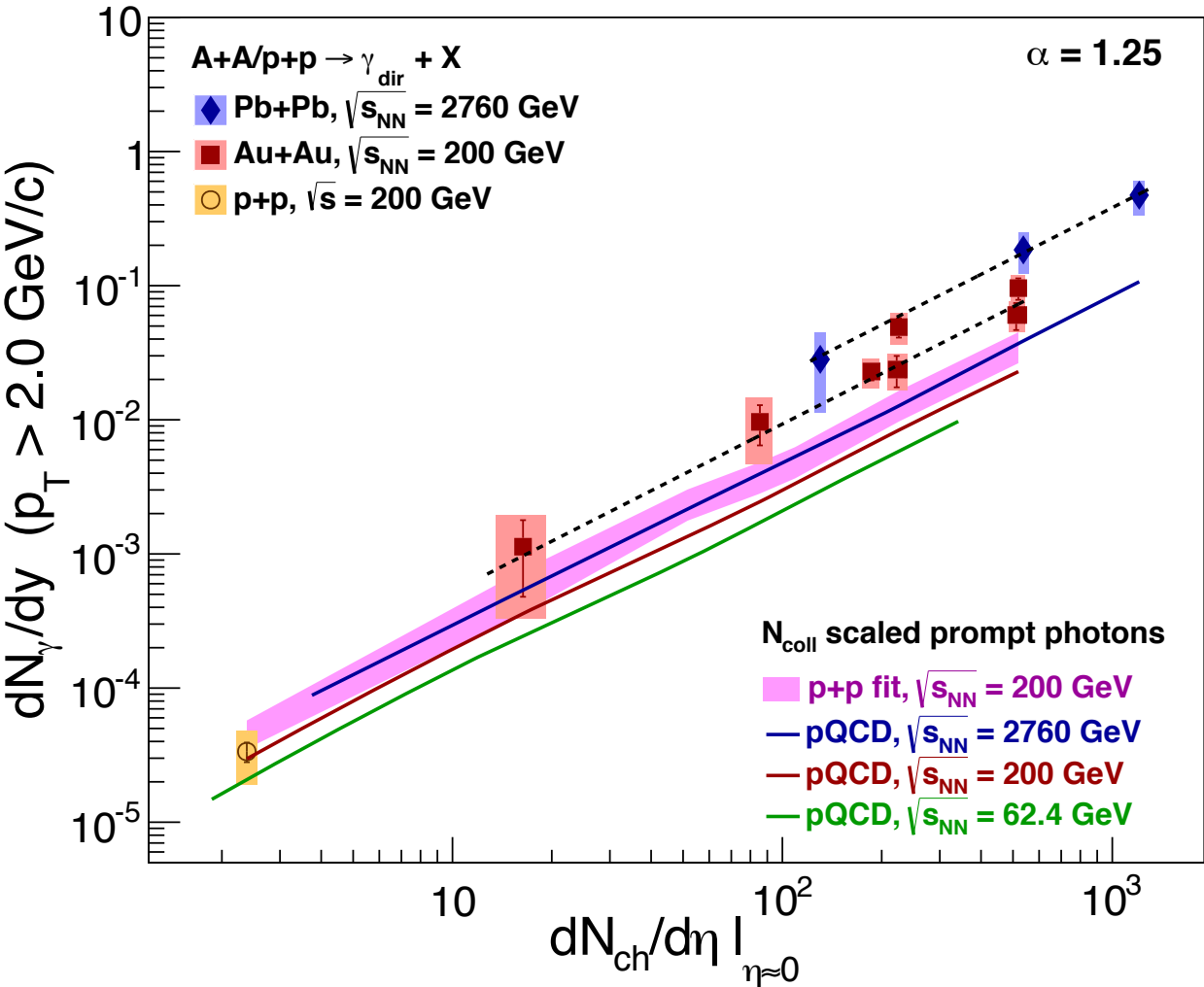


Figure 122: The direct photon integrated yield vs. charged particle multiplicity for p_T integrated from 2.0 GeV/c to 5.0 GeV/c, for two A+A datasets and one p+p dataset. The nomenclature is the same as in Fig. 119. Here we can see a trend for separation between different energy datasets. All the corresponding direct photon integrated yield points can be seen in Table 66. The power $\alpha = 1.25$ is from Fig. (111). The upper dashed fit (Pb+Pb) is described by $Fit = 0.0000659 \cdot dN_{ch}/d\eta^{1.25}$. If α were not fixed, it would be $\alpha = 1.255 \pm 0.031$. The lower dashed fit (Au+Au) is described by $Fit = 0.0000321 \cdot dN_{ch}/d\eta^{1.25}$. If α were not fixed, it would be $\alpha = 1.269 \pm 0.235$.

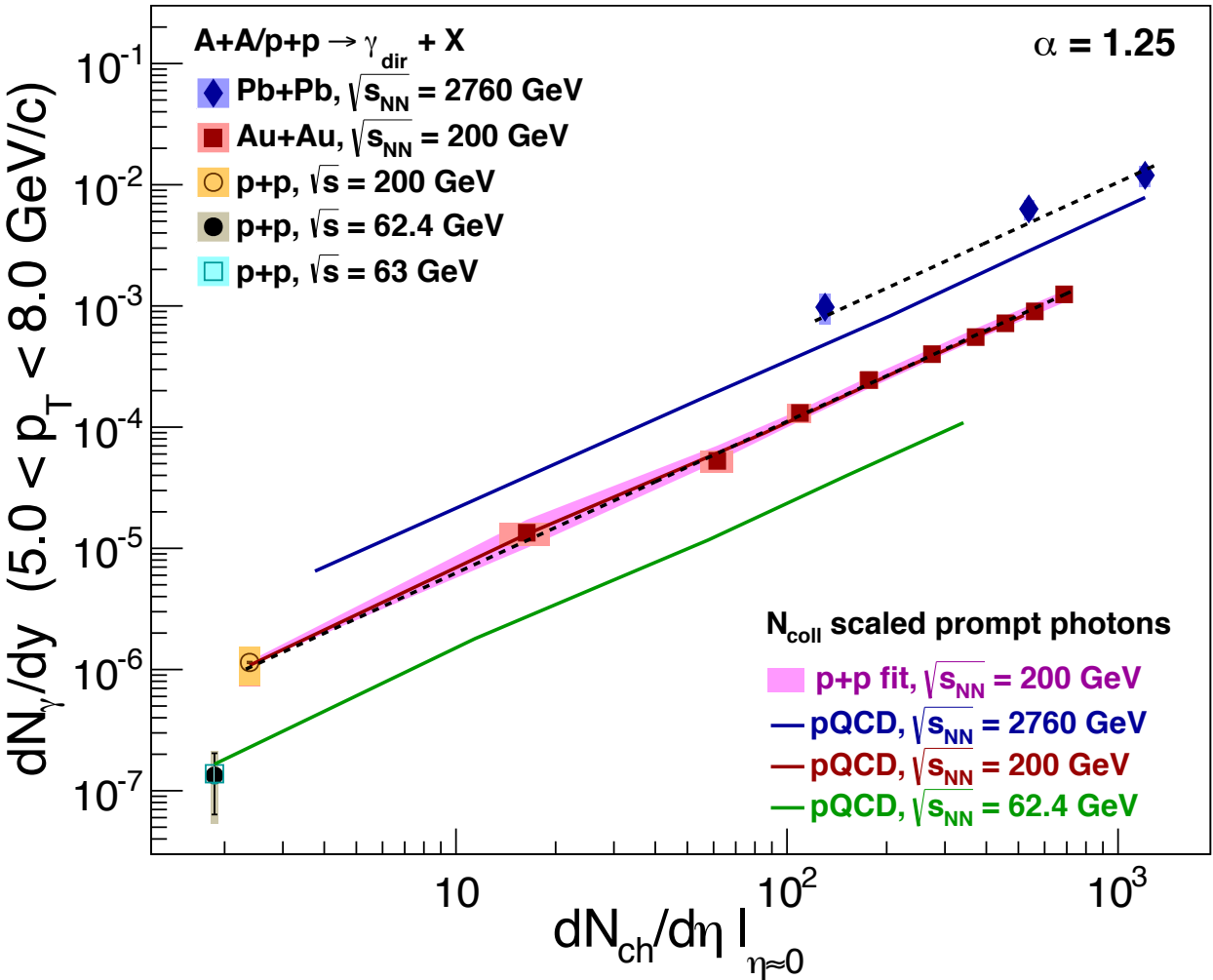


Figure 123: The direct photon integrated yield vs. charged particle multiplicity for p_T integrated from $5.0 \text{ GeV}/c$ to $8.0 \text{ GeV}/c$, for two A+A datasets and two p+p datasets. The data in Pb+Pb are from [45], in Au+Au from [151]. The 200 GeV p+p data points are from [153], the 62.4 GeV p+p and 63 GeV p+p data points are from [154, 155, 157]. The p+p fit has the same meaning as in Fig. (119). Each pQCD curve is the (integrated) prompt photon yield [144], at respective beam energy. The heavy ion photon data separation is very well visible in this plot. All the corresponding direct photon integrated yield points can be seen in Table 67. The power $\alpha = 1.25$ is from Fig. (111). The upper dashed fit (Pb+Pb) is described by $Fit = 6.064 \cdot 10^{-6} \cdot dN_{ch}/d\eta^{1.25}$. If α were not fixed, it would be $\alpha = 1.076 \pm 0.051$. The lower dashed fit (Au+Au) is described by $Fit = 3.883 \cdot 10^{-7} \cdot dN_{ch}/d\eta^{1.25}$. If α were not fixed, it would be $\alpha = 1.231 \pm 0.003$.

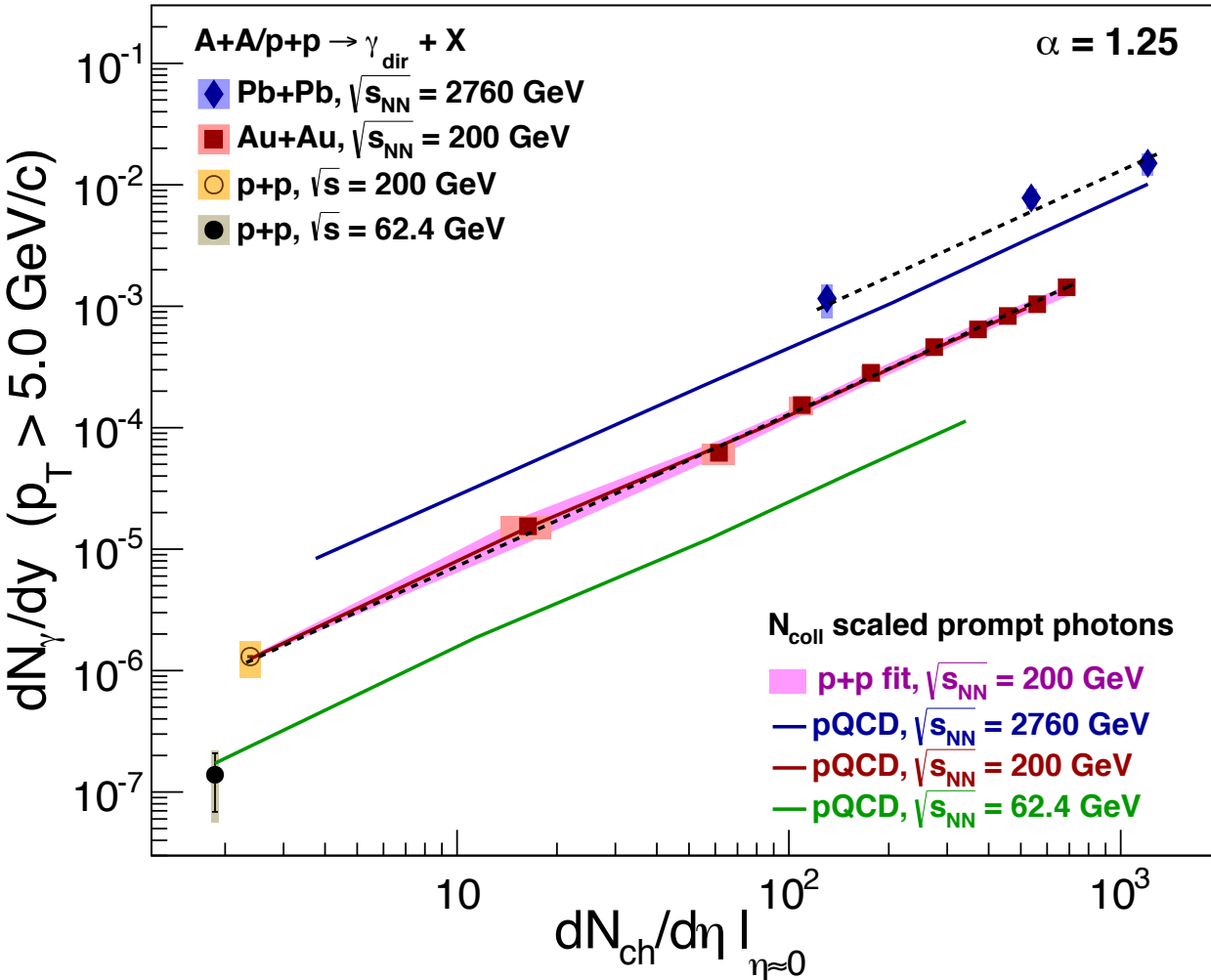


Figure 124: The direct photon integrated yield vs. charged particle multiplicity for p_T integrated from 5.0 GeV/c to 14.0 GeV/c, for two A+A datasets and two p+p datasets. The nomenclature is the same as in Fig. 123. All the corresponding direct photon integrated yield points can be seen in Table 68. The power $\alpha = 1.25$ is from Fig.(111). The upper dashed fit (Pb+Pb) is described by $Fit = 6.685 \cdot 10^{-6} \cdot dN_{ch}/d\eta^{1.25}$. If α were not fixed, it would be $\alpha = 1.094 \pm 0.048$. The lower dashed fit (Au+Au) is described by $Fit = 4.503 \cdot 10^{-7} \cdot dN_{ch}/d\eta^{1.25}$. If α were not fixed, it would be $\alpha = 1.231 \pm 0.003$.

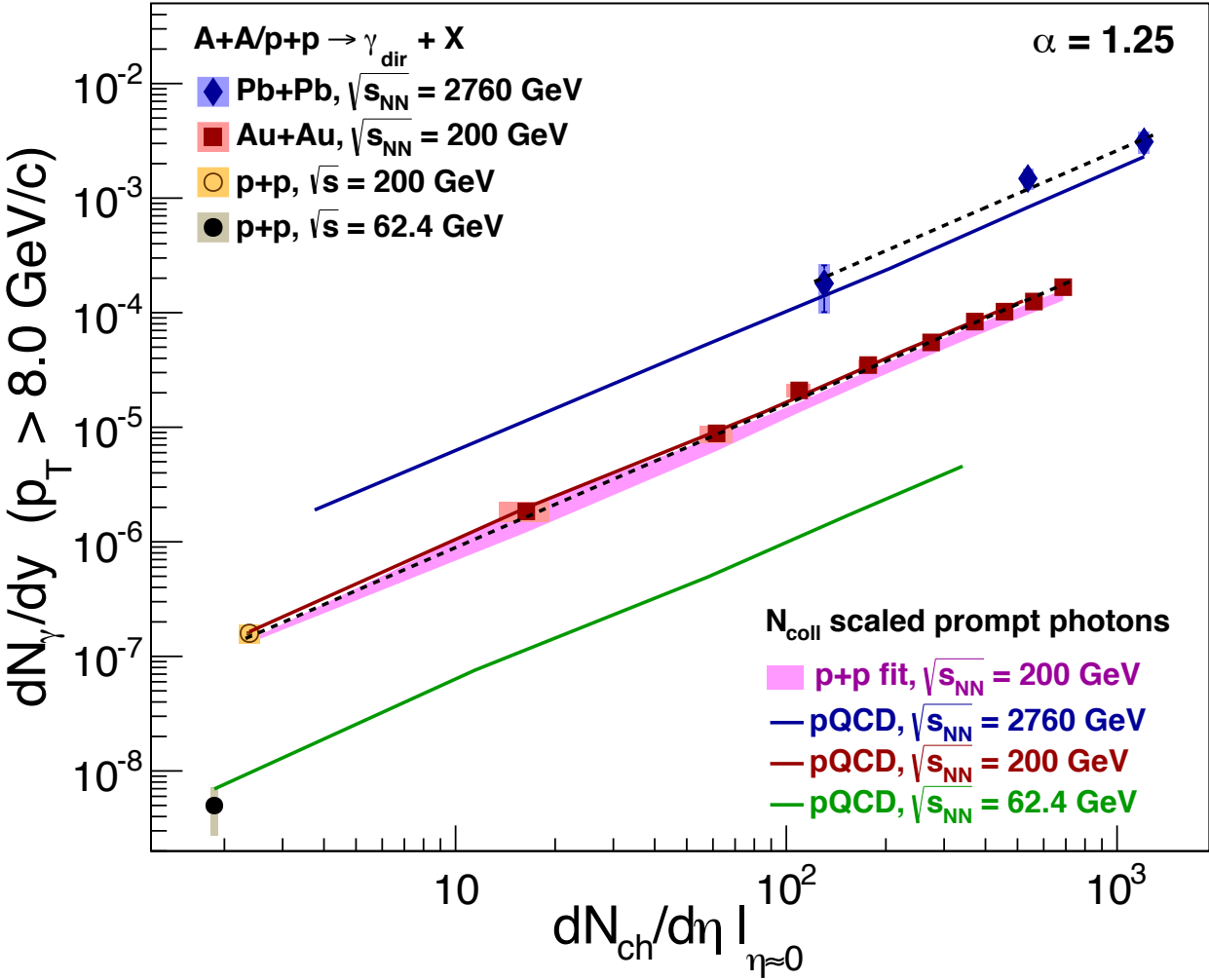


Figure 125: The direct photon integrated yield vs. charged particle multiplicity for p_T integrated from $8.0 \text{ GeV}/c$ to $14.0 \text{ GeV}/c$, for two A+A datasets and two p+p datasets. The nomenclature is the same as in Fig. 123. All the corresponding direct photon integrated yield points can be seen in Table 69. The power $\alpha = 1.25$ is from Fig. (111). The upper dashed fit (Pb+Pb) is described by $Fit = 7.695 \cdot 10^{-7} \cdot dN_{ch}/d\eta^{1.25}$. If α were not fixed, it would be $\alpha = 1.175 \pm 0.135$. The lower dashed fit (Au+Au) is described by $Fit = 5.581 \cdot 10^{-8} \cdot dN_{ch}/d\eta^{1.25}$. If α were not fixed, it would be $\alpha = 1.228 \pm 0.005$.

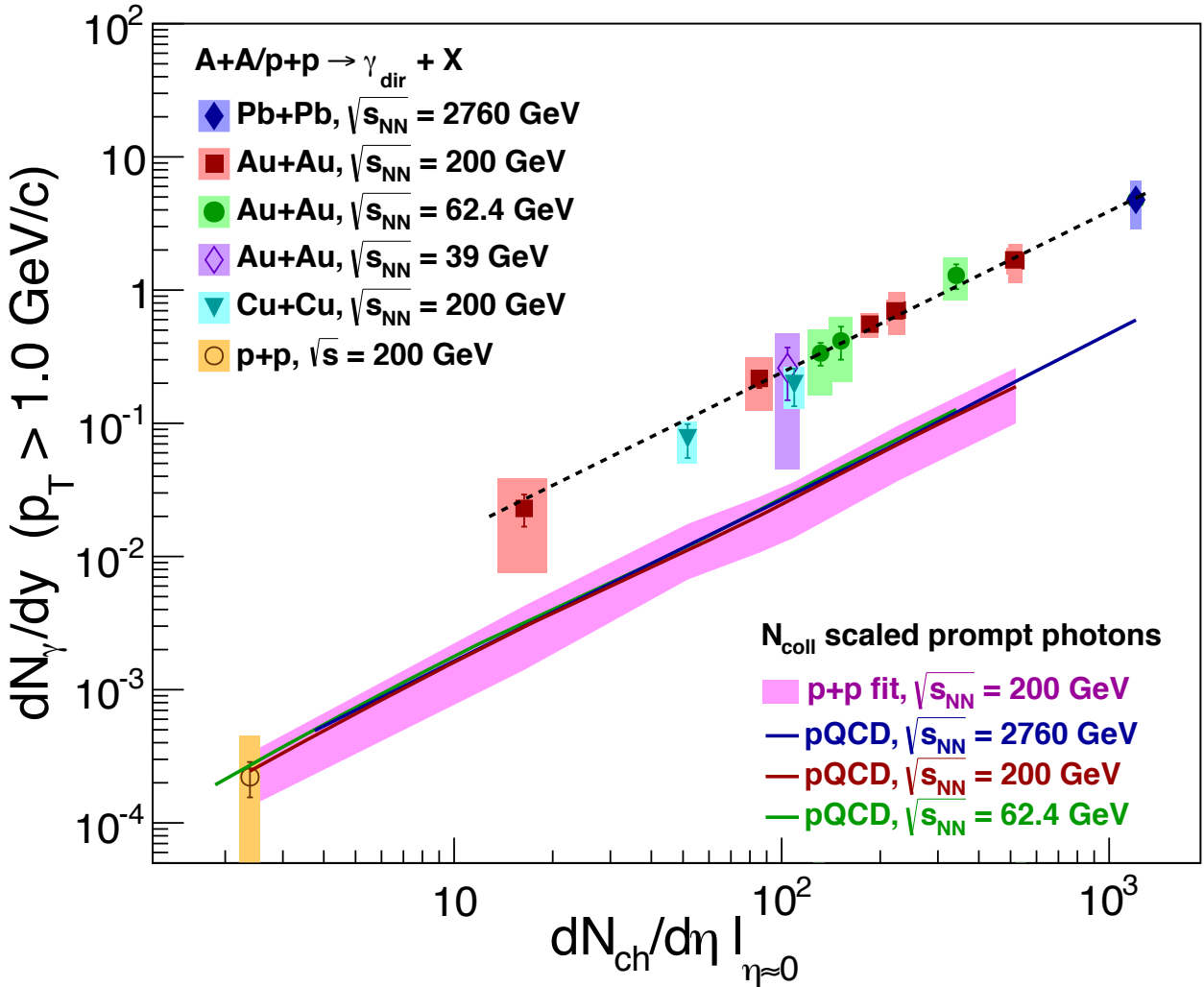


Figure 126: All the nomenclature is the same as in Fig. (120). However, now instead of the power-law fit (with $\alpha = 1.25$), the dashed fit is described by $Fit = 1.009 \cdot 10^{-3} \cdot (dN_{ch}/d\eta) + 2.938 \cdot 10^{-4} \cdot (dN_{ch}/d\eta)^{4/3}$.

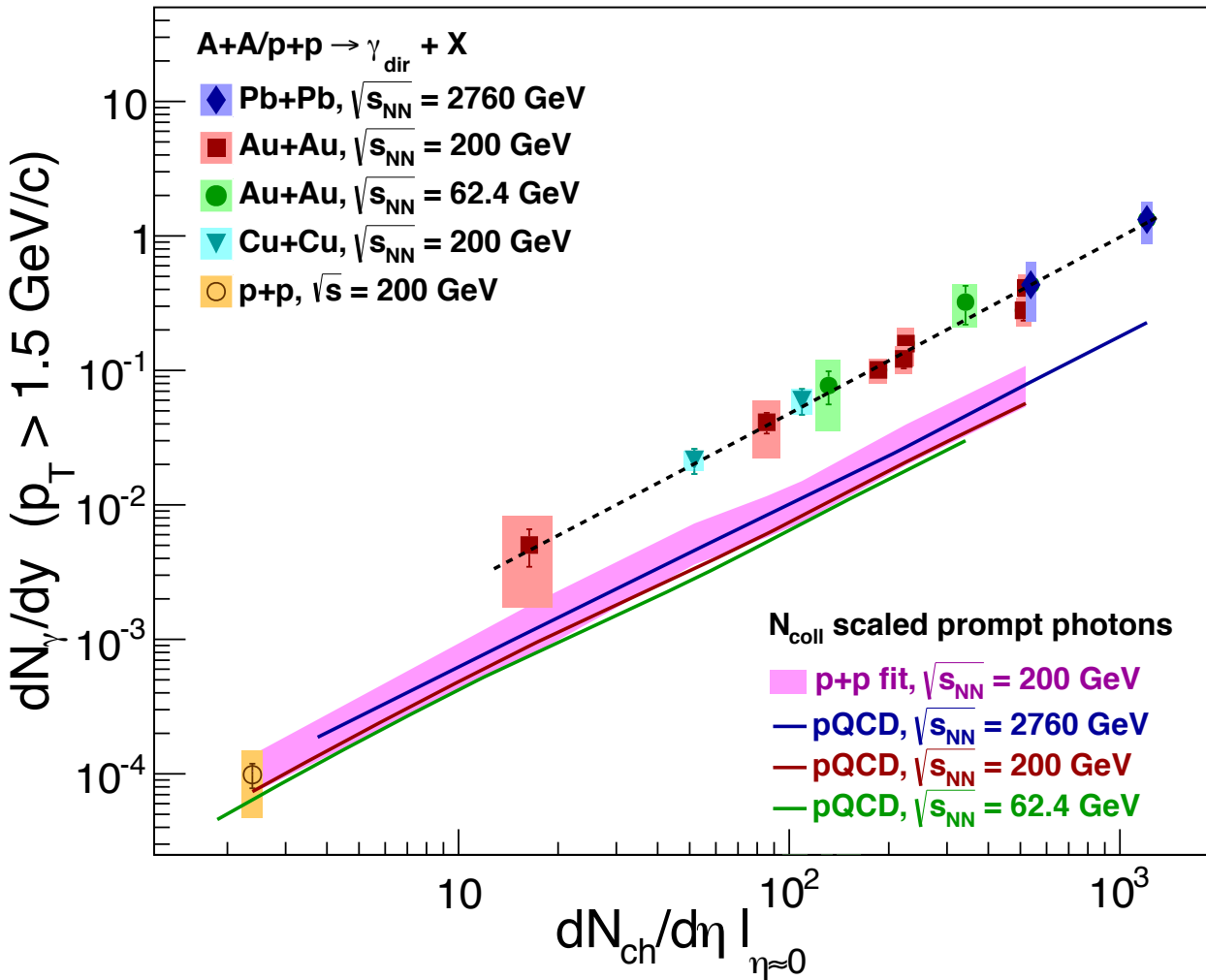


Figure 127: All the nomenclature is the same as in Fig. (121). However, now instead of the power-law fit (with $\alpha = 1.25$), the dashed fit is described by $Fit = 4.242 \cdot 10^{-5} \cdot (dN_{ch}/d\eta) + 9.362 \cdot 10^{-5} \cdot (dN_{ch}/d\eta)^{4/3}$.

8 Summary and conclusions

We have analyzed two data samples of 2.12×10^8 (at $\sqrt{s_{NN}} = 62.4$ GeV) and 7.79×10^7 (at $\sqrt{s_{NN}} = 39$ GeV) minimum bias Au+Au collisions at RHIC, which the PHENIX central arm spectrometers have recorded in 2010. The analysis is accomplished in the transverse momentum range of $0.4 \text{ GeV}/c < p_T < 3.0 \text{ GeV}/c$, and in the centrality bins of 0-20%, 20-40%, 40-60%, 60-86% and minimum bias 0-86% at $\sqrt{s_{NN}} = 62.4$ GeV and $\sqrt{s_{NN}} = 39$ GeV beam (center-of-mass) energies. We have measured low momentum direct photons via their external conversions to e^+e^- pairs in the backplane of the subsystem HBD of the PHENIX detector, and basically used the method utilized in [42] for the analysis of low momentum direct photons from Au+Au collisions at $\sqrt{s_{NN}} = 200$ GeV. This method has already proven to give a clean photon sample at 200 GeV analysis. In particular, we have measured the direct photon fraction, R_γ , through the double ratio of Eq. (98), canceling major sources of p_T -dependent uncertainties when forming each ratio in that double ratio. We have obtained results with good statistics in the centrality bins of 0-20%, 20-40% and minimum bias 0-86% at $\sqrt{s_{NN}} = 62.4$ GeV as well as in the minimum bias 0-86% at $\sqrt{s_{NN}} = 39$ GeV, shown in Fig. (96). From the plots in this figure we see that the data sample shows a clear direct photon signal for most of the p_T bins in the three centrality classes under consideration at $\sqrt{s_{NN}} = 62.4$ GeV. In the minimum bias sample of $\sqrt{s_{NN}} = 39$ GeV, we see the signal of direct photons at least in the lowest p_T bins.

Then by making use of Eq. (99) we have obtained the direct photon p_T spectra shown in Figs. (100)-(103). One can see the excess yield described by the data on top of the T_{AA} -scaled pQCD curves. We fitted the excess by an exponential function in the range of $\sim 0.5 \text{ GeV}/c - 2.0 \text{ GeV}/c$, and extracted the inverse slope T_{eff} . Fig. (104) shows the inverse slope for five systems, where T_{eff} seems to drop down from large to smaller collision energies. Nonetheless, the values of T_{eff} for the lower energies are obtained without subtracting the prompt photon contribution (T_{AA} -scaled pQCD) from the invariant yield.

We also presented the results of our studies on scaling properties of direct photons based on measured data from different heavy ion collision systems at various center-of-mass energies. First, in Fig. (111) we observe a power-law behavior with $\alpha = 1.25$ for the number of binary collisions as a function of charged-particle multiplicity. Second, when the direct photon spectra are being normalized by charged-particle multiplicity to the power of this α , we observe universal scaling trend at low transverse momentum region, as shown Fig. (114). In this region the data scale in all centralities and energies, which we got data for. We have additionally studied the integrated yield of direct

photons in order to have some insight in understanding of the thermal photon production from all heavy ion systems under our consideration. When we look at the integrated yield vs. charged particle multiplicity, we come to the above scaling picture. In this representation, we also found that the scaling of prompt photons is nearly the same as that of direct photons from heavy ion collisions (see Figs. (119)-(125)). One conclusion is that the underlying processes, which are responsible for the prompt photon production, can also be the source of direct photon production in heavy ion collisions. However, the ratio of their production rates can reach an order of magnitude.

Our current understanding is that in the intermediate transverse momentum range, the thermal photon yields from Au+Au at $\sqrt{s_{NN}} = 200 \text{ GeV}$ [41, 42] and from Pb+Pb at $\sqrt{s_{NN}} = 2760 \text{ GeV}$ [45] are due to processes occurring in the QGP phase of the evolution. The low- p_T region is dominated by the production from the hadronic phase. Then by looking at Fig. (119), Fig. (120) and Fig. (121) we can assume that within our experimental uncertainties the yields from Au+Au at $\sqrt{s_{NN}} = 62.4 \text{ GeV}$ and $\sqrt{s_{NN}} = 39 \text{ GeV}$ have also thermal origin based on the same QGP processes. However, we need to have more direct photon data from the systems p+p, Au+Au, Cu+Au, U+U, p+Au, p+Al, He³+Au, p+Pb, Pb+Pb at various beam energies, in order to understand the origin of the scaling properties of direct photons reported in this thesis. Furthermore, future studies of the scaling may help in resolving the “thermal photon puzzle”, at least in constraining its possible solutions.

9 Appendix A1

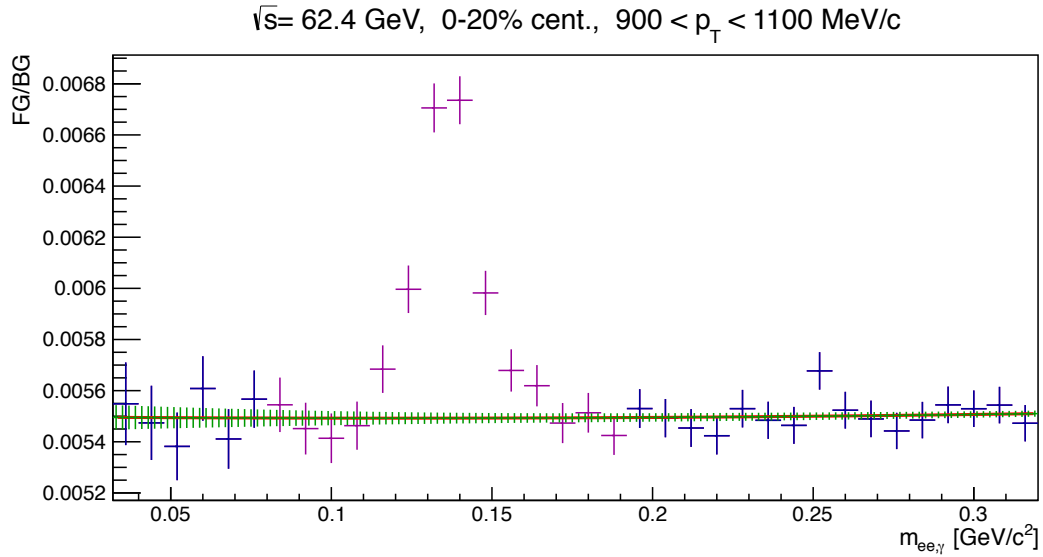


Figure 128: The converted di-photon foreground (FG) pair distribution in mass divided by the combinatorial mixed event background (BG) distribution for 0-20% centrality in the converted photon p_{Tee} bin of 0.9 - 1.1 GeV/c at $\sqrt{s_{NN}} = 62.4$ GeV. The region of the pion peak is excluded. The ratio is fitted with a second order polynomial (shown in red).

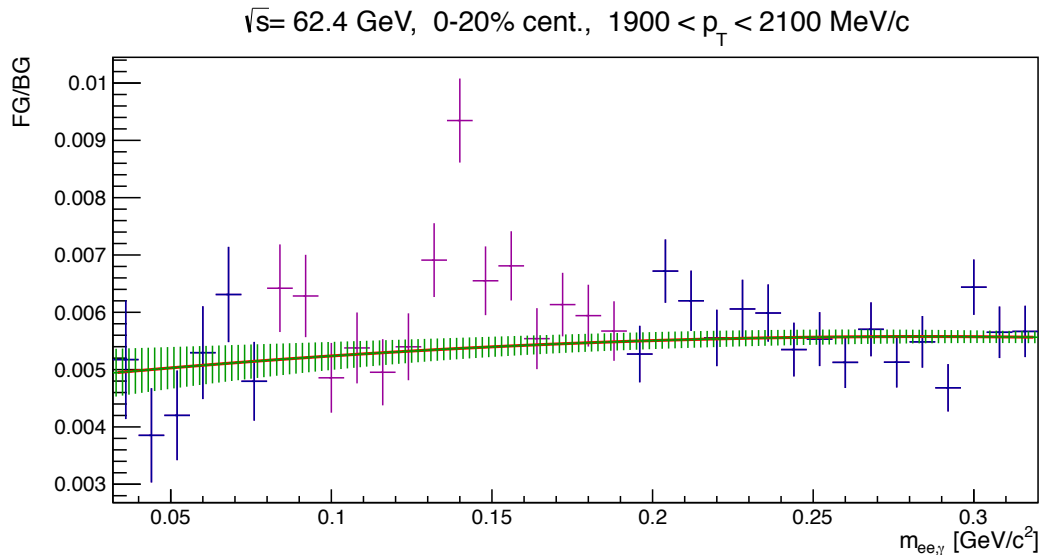


Figure 129: The FG pair distribution in mass divided by the combinatorial BG distribution for 0-20% centrality in the converted photon p_{Tee} bin of 1.9 - 2.1 GeV/c at $\sqrt{s_{NN}} = 62.4$ GeV.

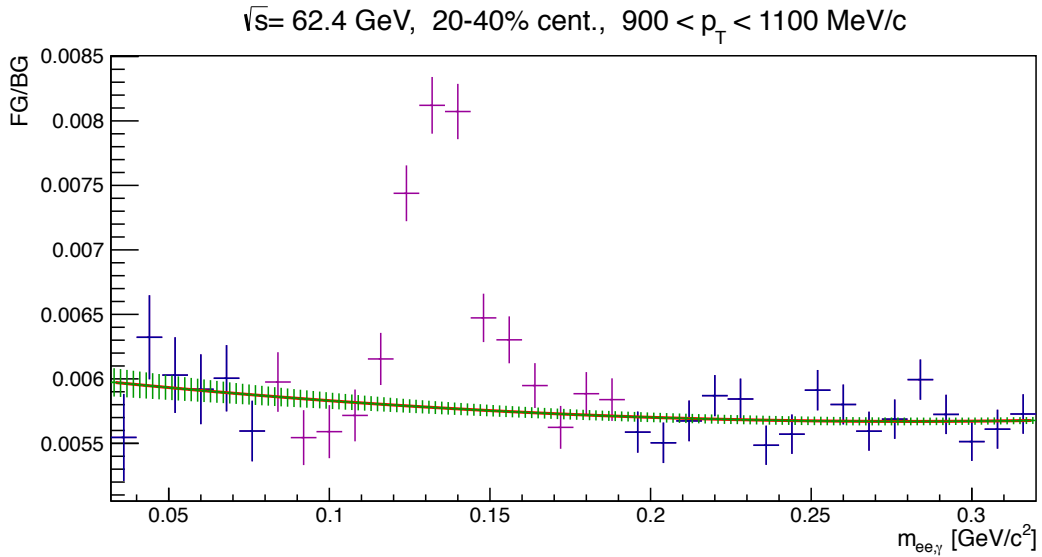


Figure 130: The converted di-photon foreground (FG) pair distribution in mass divided by the combinatorial mixed event background (BG) distribution for 20-40% centrality in the converted photon p_{Tee} bin of 0.9 - 1.1 GeV/c at $\sqrt{s_{NN}} = 62.4$ GeV. The region of the pion peak is excluded. The ratio is fitted with a second order polynomial (shown in red).

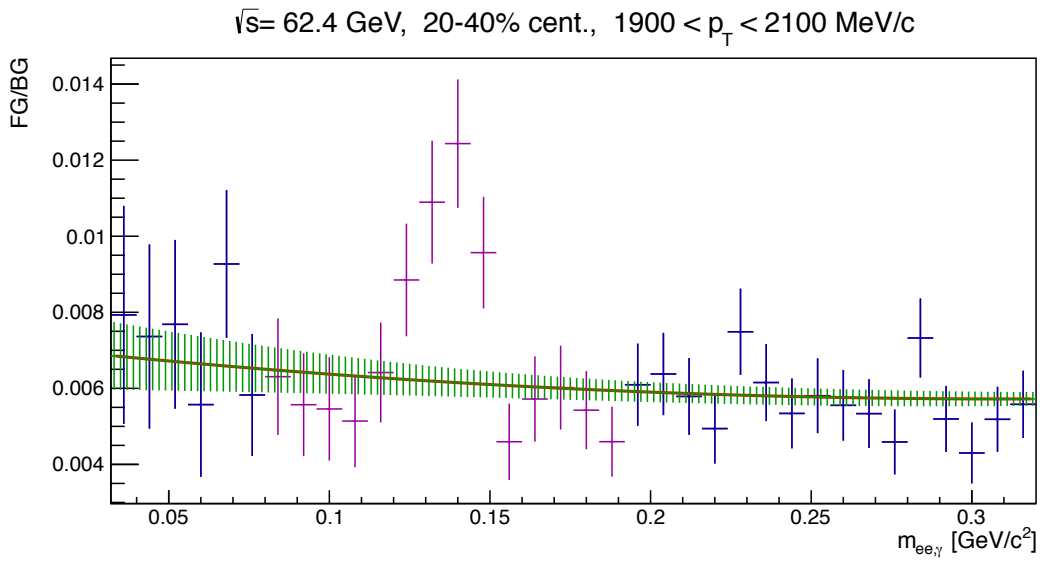


Figure 131: The FG pair distribution in mass divided by the combinatorial BG distribution for 20-40% centrality in the converted photon p_{Tee} bin of 1.9 - 2.1 GeV/c at $\sqrt{s_{NN}} = 62.4$ GeV.

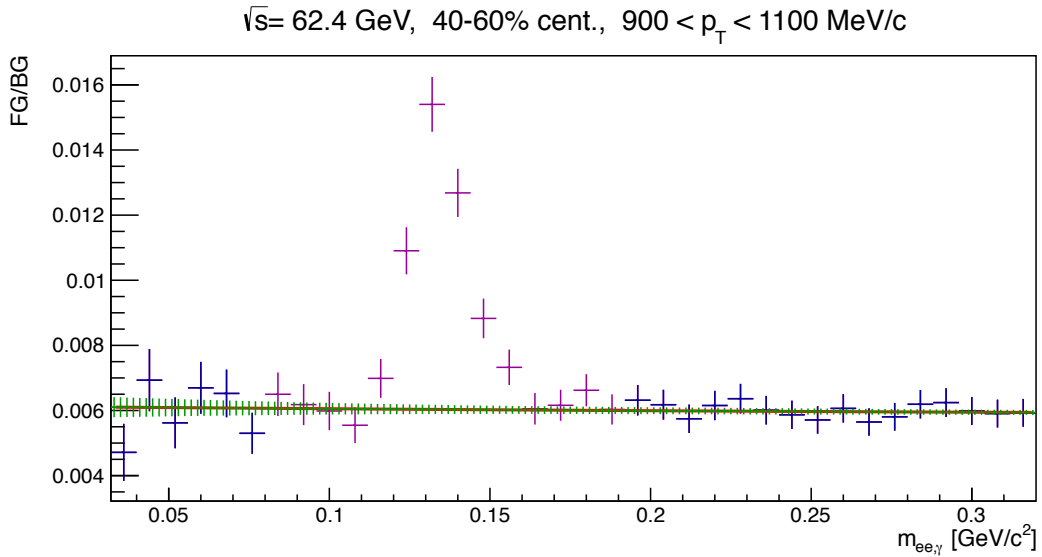


Figure 132: The converted di-photon foreground (FG) pair distribution in mass divided by the combinatorial mixed event background (BG) distribution for 40-60% centrality in the converted photon p_{Tee} bin of 0.9 - 1.1 GeV/c at $\sqrt{s_{NN}} = 62.4$ GeV. The region of the pion peak is excluded. The ratio is fitted with a second order polynomial (shown in red).

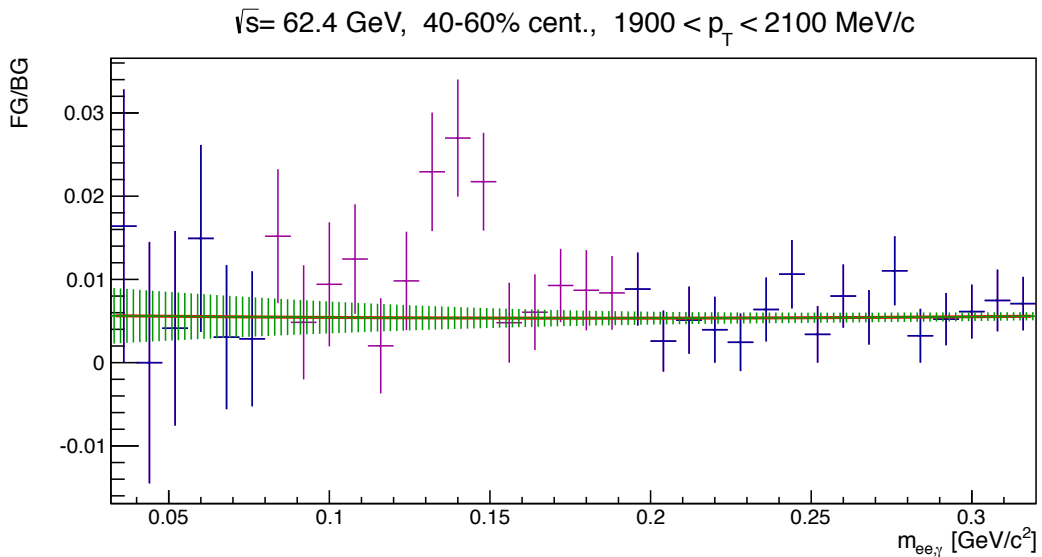


Figure 133: The FG pair distribution in mass divided by the combinatorial BG distribution for 40-60% centrality in the converted photon p_{Tee} bin of 1.9 - 2.1 GeV/c at $\sqrt{s_{NN}} = 62.4$ GeV.

$\sqrt{s} = 62.4 \text{ GeV}, 60\text{-}86\% \text{ cent.}, 700 < p_T < 900 \text{ MeV}/c$

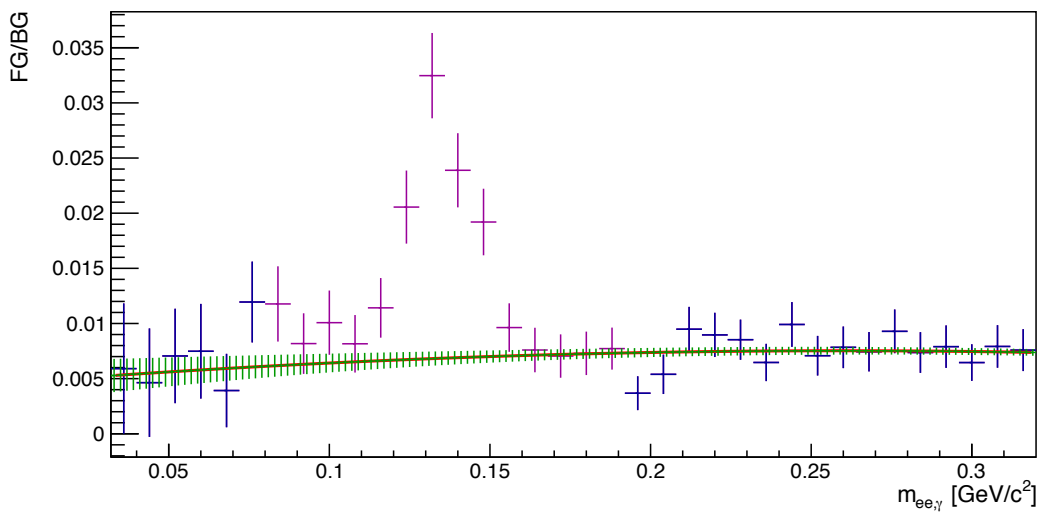


Figure 134: The converted di-photon foreground (FG) pair distribution in mass divided by the combinatorial mixed event background (BG) distribution for 60-86% centrality in the converted photon p_{Tee} bin of 0.7 - 0.9 GeV/c at $\sqrt{s_{NN}} = 62.4 \text{ GeV}$. The region of the pion peak is excluded. The ratio is fitted with a second order polynomial (shown in red).

$\sqrt{s} = 62.4 \text{ GeV}, 60\text{-}86\% \text{ cent.}, 1300 < p_T < 1500 \text{ MeV}/c$

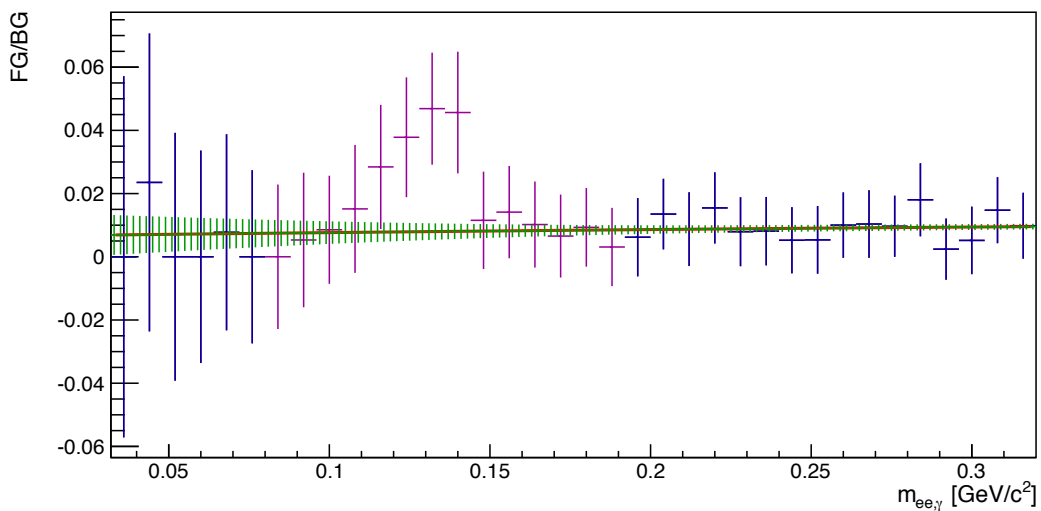


Figure 135: The FG pair distribution in mass divided by the combinatorial BG distribution for 60-86% centrality in the converted photon p_{Tee} bin of 1.3 - 1.5 GeV/c at $\sqrt{s_{NN}} = 62.4 \text{ GeV}$.

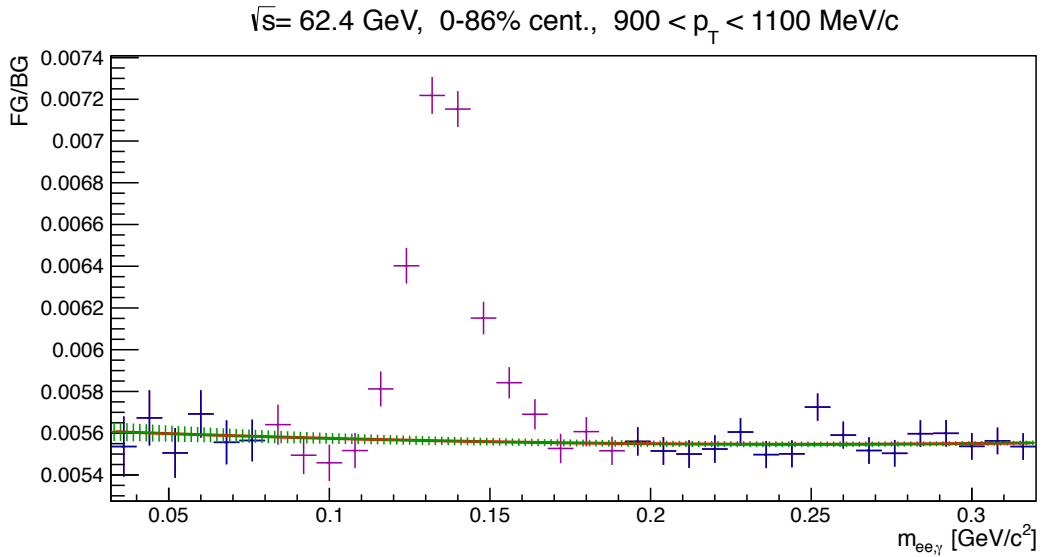


Figure 136: The converted di-photon foreground (FG) pair distribution in mass divided by the combinatorial mixed event background (BG) distribution for 0-86% centrality in the converted photon p_{Tee} bin of 0.9 - 1.1 GeV/c at $\sqrt{s_{NN}} = 62.4$ GeV. The region of the pion peak is excluded. The ratio is fitted with a second order polynomial (shown in red).

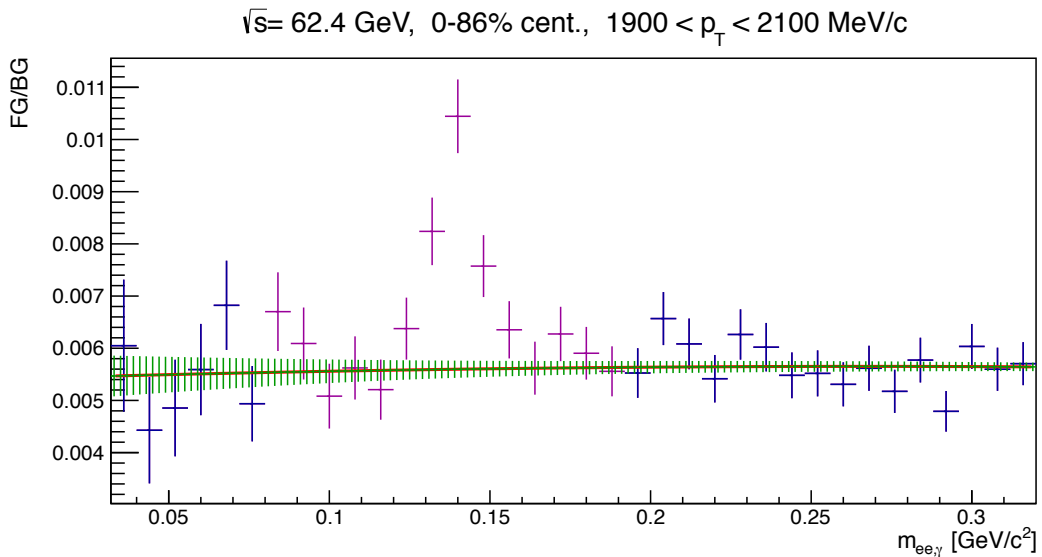


Figure 137: The FG pair distribution in mass divided by the combinatorial BG distribution for 0-86% centrality in the converted photon p_{Tee} bin of 1.9 - 2.1 GeV/c at $\sqrt{s_{NN}} = 62.4$ GeV.

10 Appendix A2

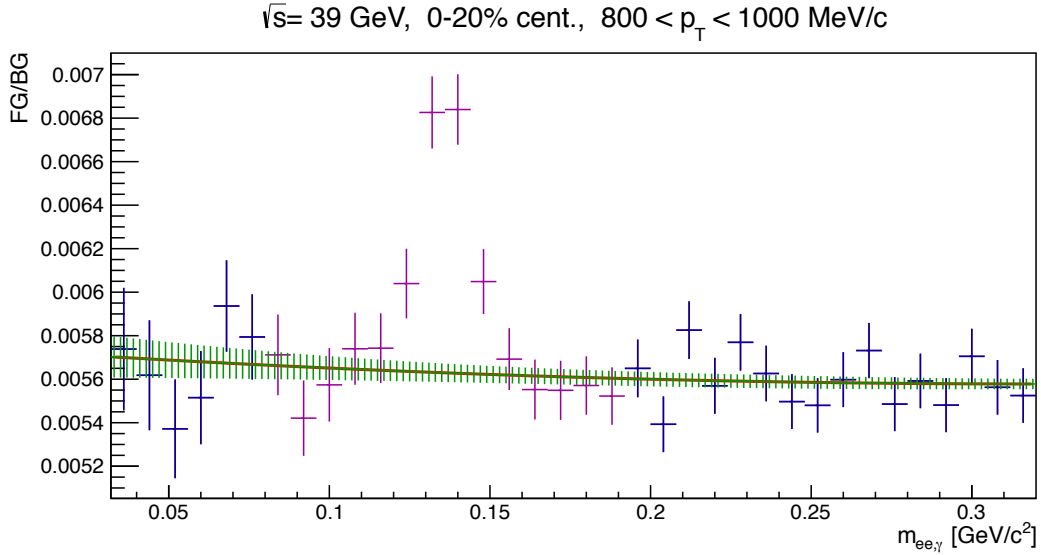


Figure 138: The converted di-photon foreground (FG) pair distribution in mass divided by the combinatorial mixed event background (BG) distribution for 0-20% centrality in the converted photon p_{Tee} bin of 0.8 - 1.0 GeV/c at $\sqrt{s_{NN}} = 39$ GeV. The region of the pion peak is excluded. The ratio is fitted with a second order polynomial (shown in red).

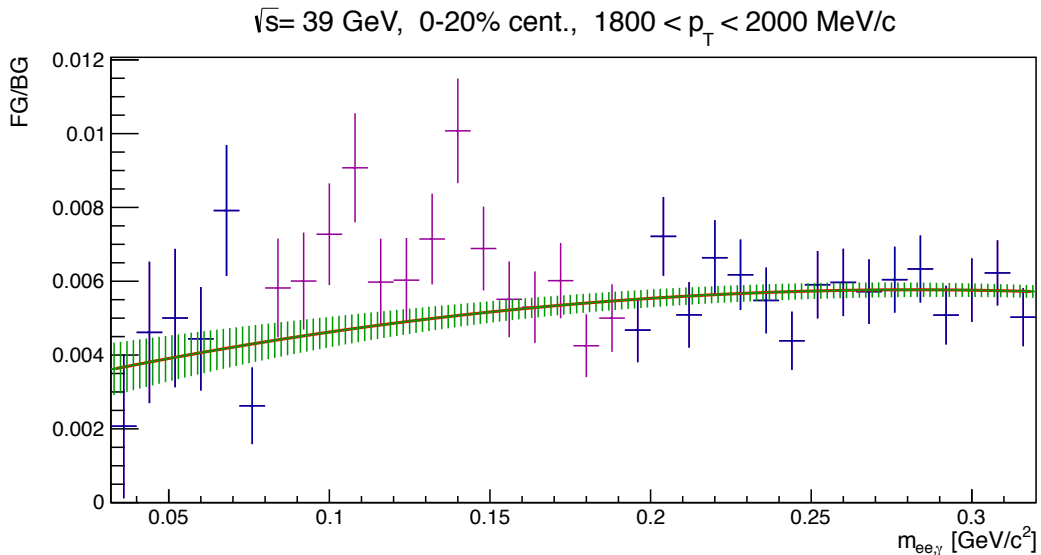


Figure 139: The FG pair distribution in mass divided by the combinatorial BG distribution for 0-20% centrality in the converted photon p_{Tee} bin of 1.8 - 2.0 GeV/c at $\sqrt{s_{NN}} = 39$ GeV.

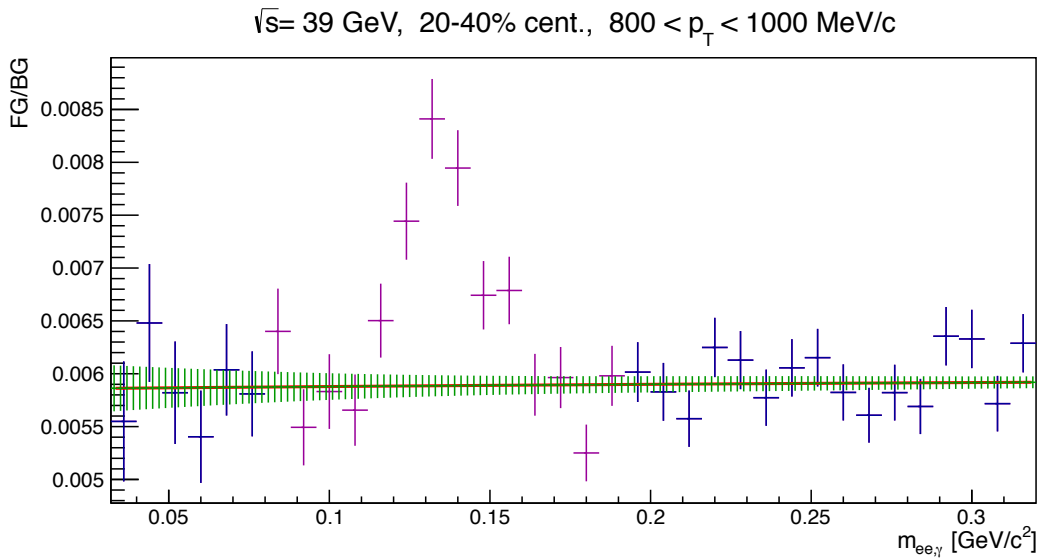


Figure 140: The converted di-photon foreground (FG) pair distribution in mass divided by the combinatorial mixed event background (BG) distribution for 20-40% centrality in the converted photon p_{Tee} bin of 0.8 - 1.0 GeV/c at $\sqrt{s_{NN}} = 39$ GeV. The region of the pion peak is excluded. The ratio is fitted with a second order polynomial (shown in red).

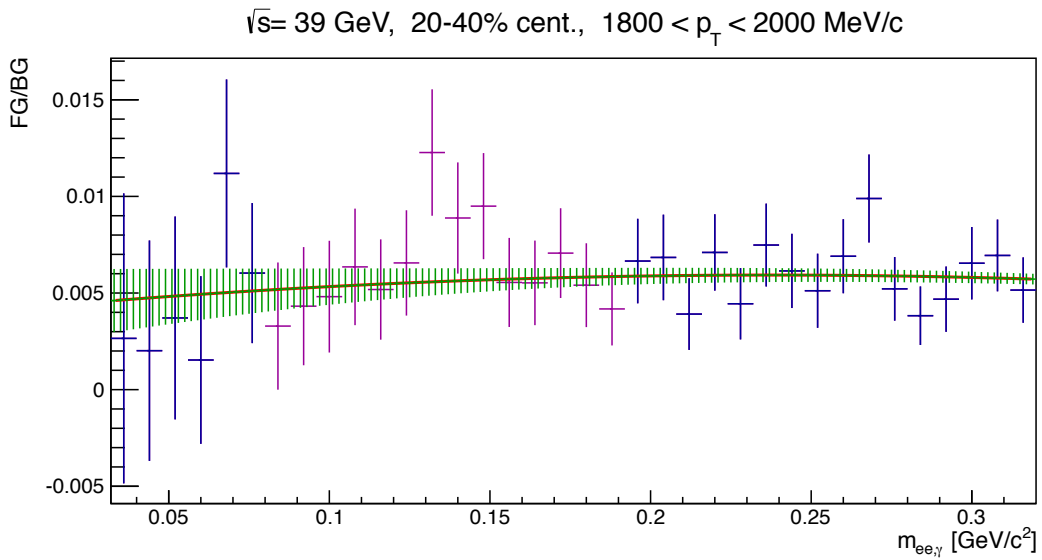


Figure 141: The FG pair distribution in mass divided by the combinatorial BG distribution for 20-40% centrality in the converted photon p_{Tee} bin of 1.8 - 2.0 GeV/c at $\sqrt{s_{NN}} = 39$ GeV.

$\sqrt{s} = 39 \text{ GeV}, 40\text{-}60\% \text{ cent.}, 600 < p_T < 800 \text{ MeV}/c$

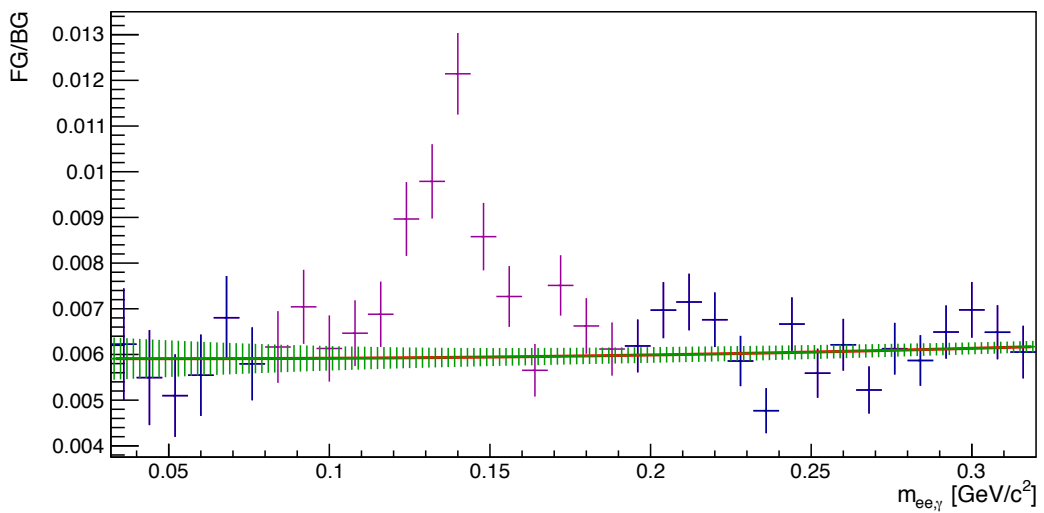


Figure 142: The converted di-photon foreground (FG) pair distribution in mass divided by the combinatorial mixed event background (BG) distribution for 40-60% centrality in the converted photon p_{Tee} bin of $0.6 - 0.8 \text{ GeV}/c$ at $\sqrt{s_{NN}} = 39 \text{ GeV}$. The region of the pion peak is excluded. The ratio is fitted with a second order polynomial (shown in red).

$\sqrt{s} = 39 \text{ GeV}, 40\text{-}60\% \text{ cent.}, 1200 < p_T < 1400 \text{ MeV}/c$

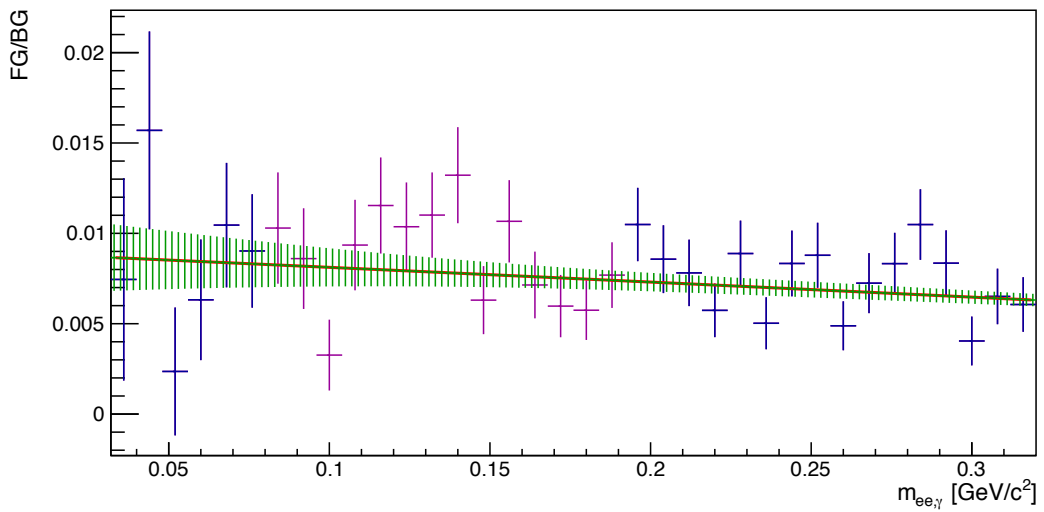


Figure 143: The FG pair distribution in mass divided by the combinatorial BG distribution for 40-60% centrality in the converted photon p_{Tee} bin of $1.2 - 1.4 \text{ GeV}/c$ at $\sqrt{s_{NN}} = 39 \text{ GeV}$.

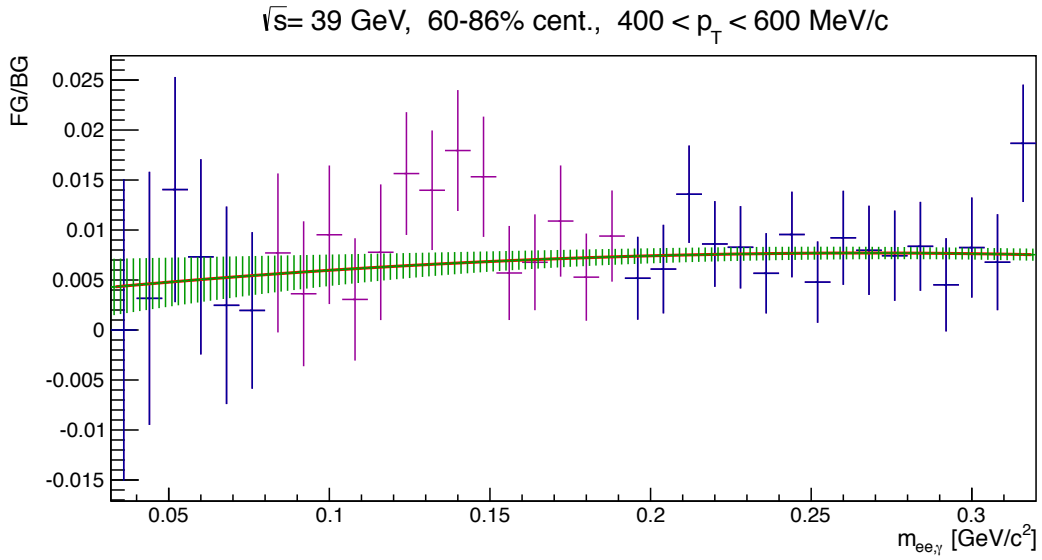


Figure 144: The converted di-photon foreground (FG) pair distribution in mass divided by the combinatorial mixed event background (BG) distribution for 60-86% centrality in the converted photon p_{Tee} bin of 0.4 - 0.6 GeV/c at $\sqrt{s_{NN}} = 39$ GeV. The region of the pion peak is excluded. The ratio is fitted with a second order polynomial (shown in red).

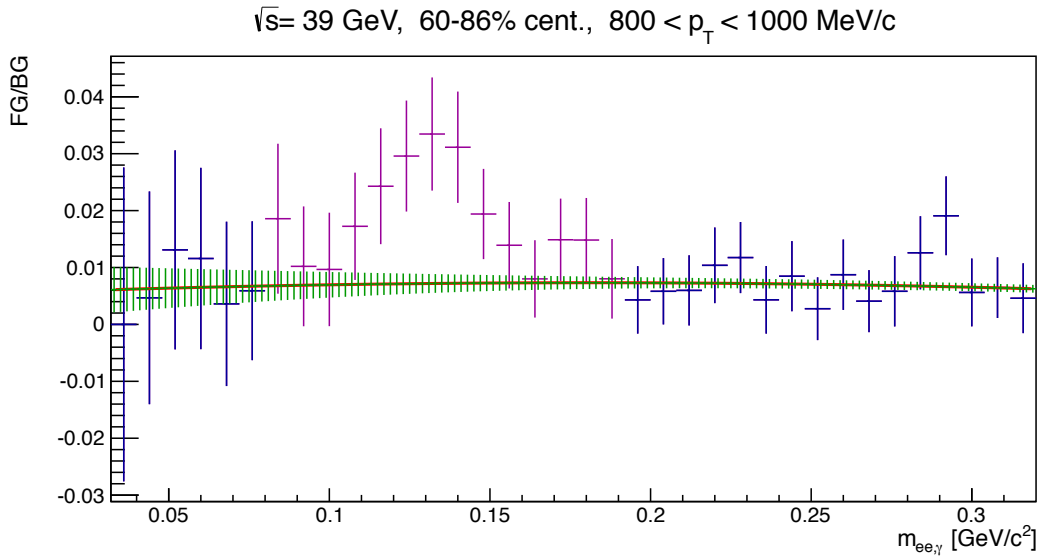


Figure 145: The FG pair distribution in mass divided by the combinatorial BG distribution for 60-86% centrality in the converted photon p_{Tee} bin of 0.8 - 1.0 GeV/c at $\sqrt{s_{NN}} = 39$ GeV.

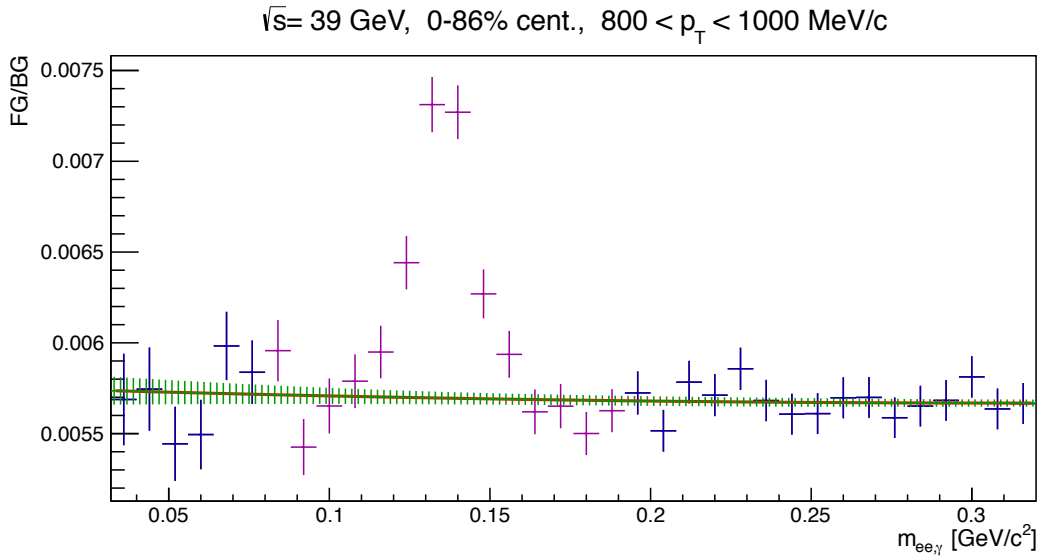


Figure 146: The converted di-photon foreground (FG) pair distribution in mass divided by the combinatorial mixed event background (BG) distribution for 0-86% centrality in the converted photon p_{Tee} bin of 0.8 - 1.0 GeV/c at $\sqrt{s_{NN}} = 39$ GeV. The region of the pion peak is excluded. The ratio is fitted with a second order polynomial (shown in red).

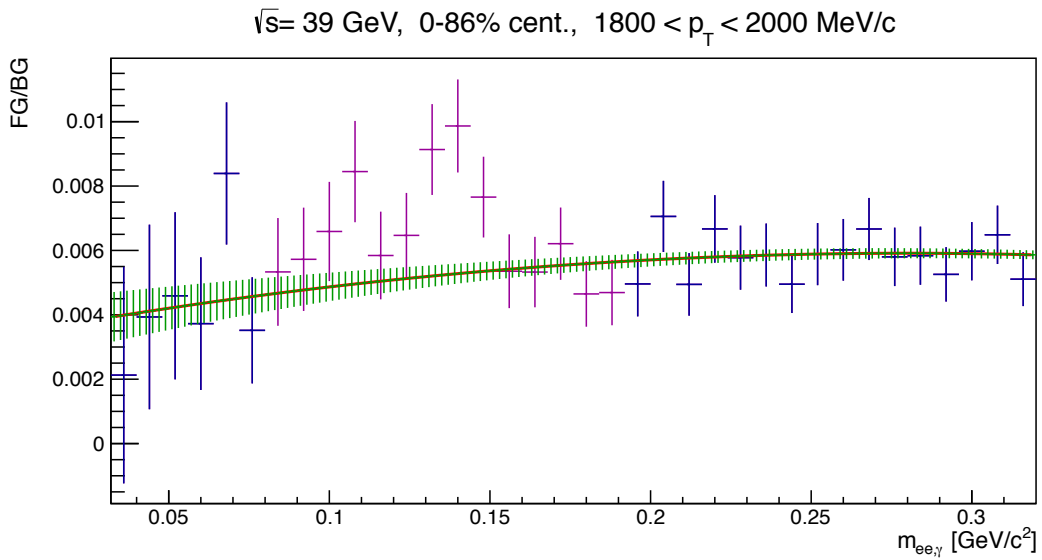


Figure 147: The FG pair distribution in mass divided by the combinatorial BG distribution for 0-86% centrality in the converted photon p_{Tee} bin of 1.8 - 2.0 GeV/c at $\sqrt{s_{NN}} = 39$ GeV.

11 Appendix B1

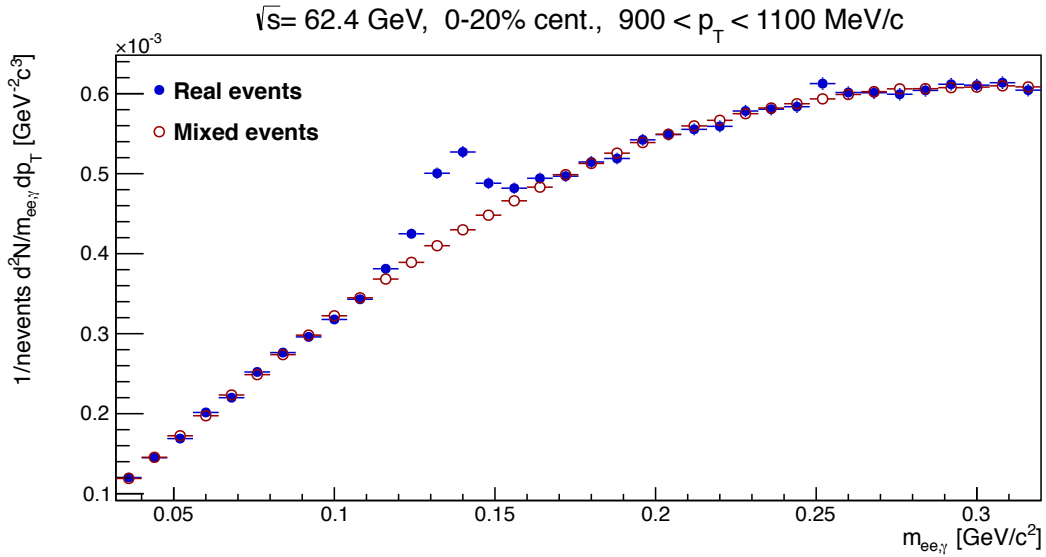


Figure 148: The di-photon foreground (blue) and normalized mixed event background (red) for 0-20% centrality in the converted photon p_{Tee} bin of $0.9 - 1.1 \text{ GeV}/c$ at $\sqrt{s_{NN}} = 62.4 \text{ GeV}$. The uncertainty on the background includes both background's statistical uncertainty and the uncertainty in the normalization with CL=0.66.

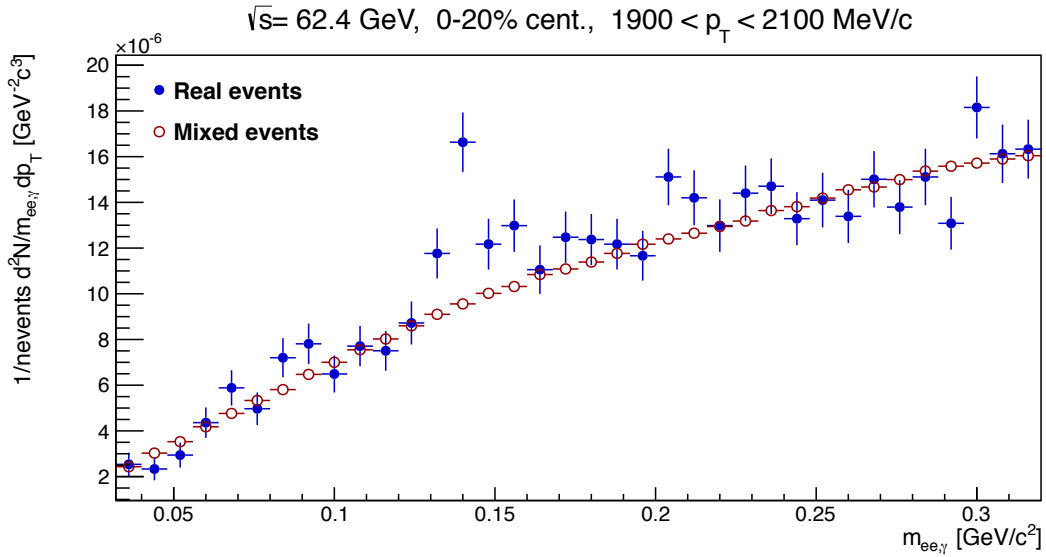


Figure 149: The foreground and normalized background for 0-20% centrality in the converted photon p_{Tee} bin of $1.9 - 2.1 \text{ GeV}/c$ at $\sqrt{s_{NN}} = 62.4 \text{ GeV}$.

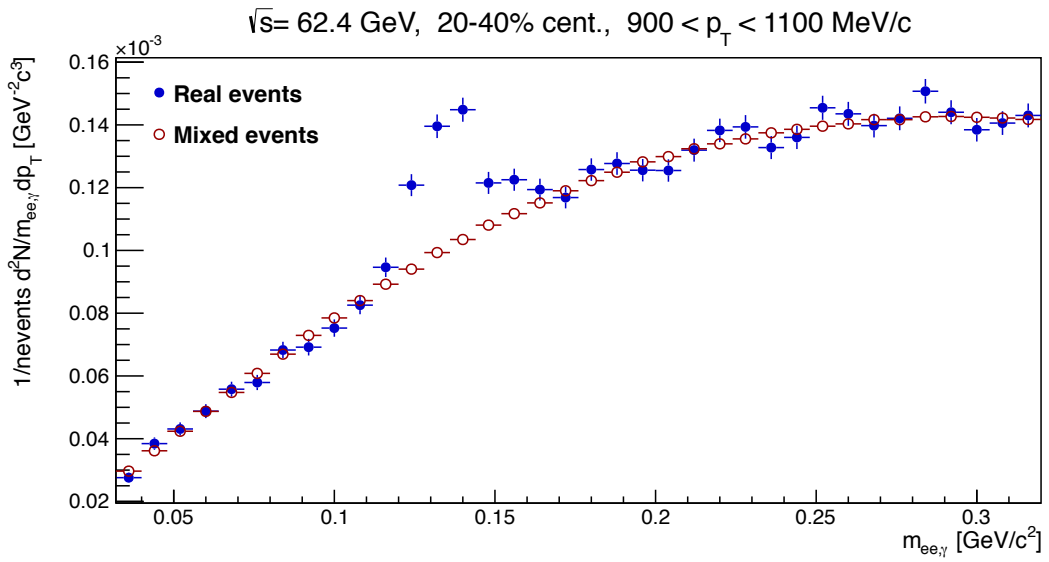


Figure 150: The di-photon foreground (blue) and normalized mixed event background (red) for 20-40% centrality in the converted photon p_{Tee} bin of 0.9 - 1.1 GeV/c at $\sqrt{s_{NN}} = 62.4$ GeV. The uncertainty on the background includes both background's statistical uncertainty and the uncertainty in the normalization with CL=0.66.

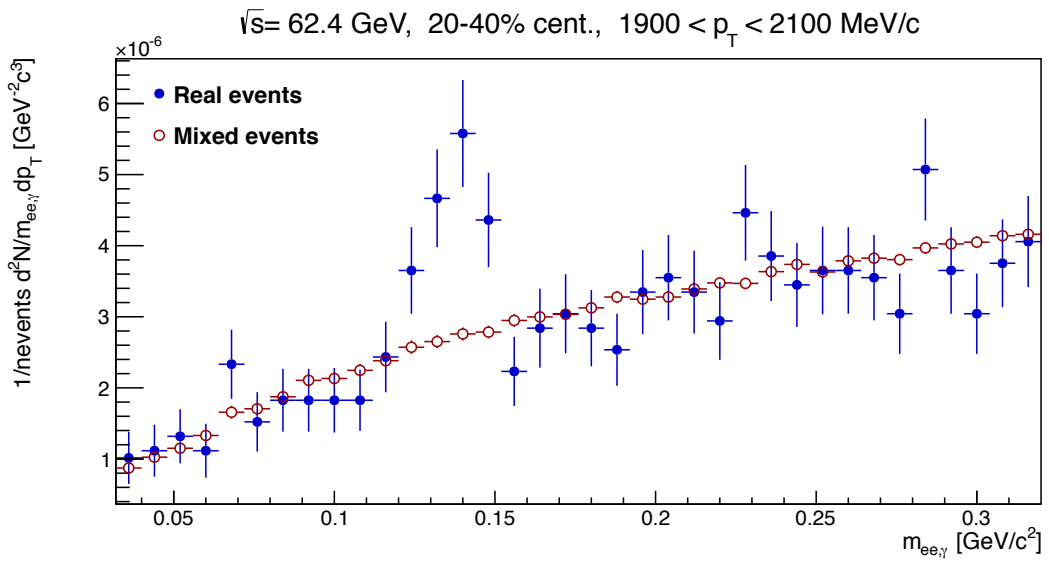


Figure 151: The foreground and normalized background for 20-40% centrality in the converted photon p_{Tee} bin of 1.9 - 2.1 GeV/c at $\sqrt{s_{NN}} = 62.4$ GeV.

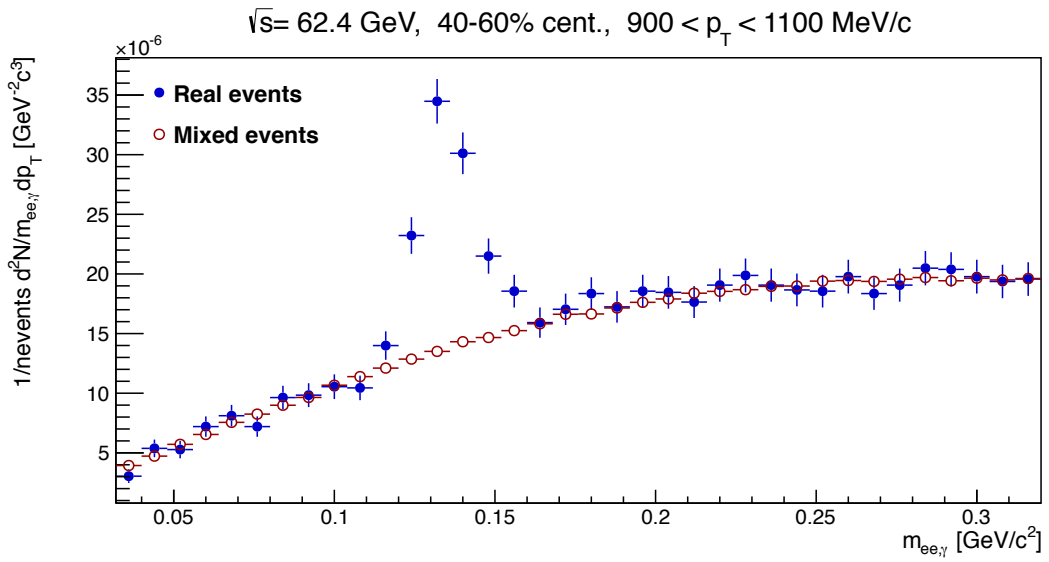


Figure 152: The di-photon foreground (blue) and normalized mixed event background (red) for 40-60% centrality in the converted photon p_{Tee} bin of $0.9 - 1.1 \text{ GeV}/c$ at $\sqrt{s_{NN}} = 62.4 \text{ GeV}$. The uncertainty on the background includes both background's statistical uncertainty and the uncertainty in the normalization with CL=0.66.

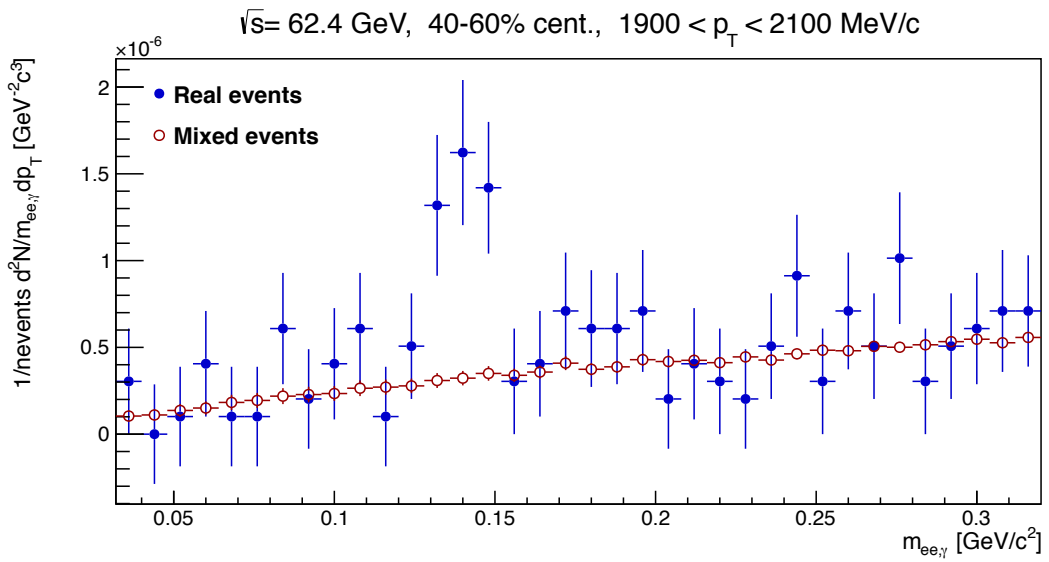


Figure 153: The foreground and normalized background for 40-60% centrality in the converted photon p_{Tee} bin of $1.9 - 2.1 \text{ GeV}/c$ at $\sqrt{s_{NN}} = 62.4 \text{ GeV}$.

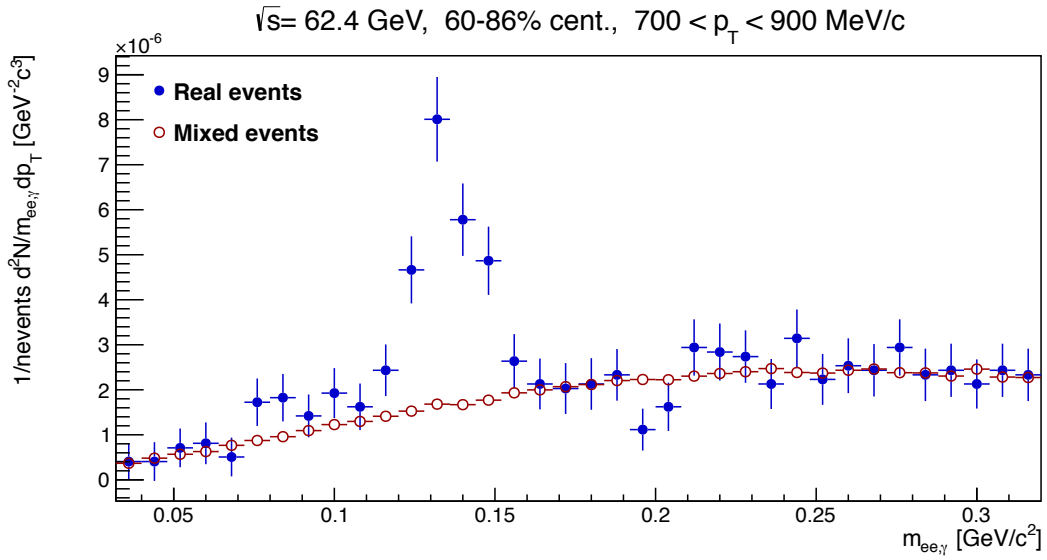


Figure 154: The di-photon foreground (blue) and normalized mixed event background (red) for 60-86% centrality in the converted photon p_{Tee} bin of 0.7 - 0.9 GeV/c at $\sqrt{s_{NN}} = 62.4$ GeV. The uncertainty on the background includes both background's statistical uncertainty and the uncertainty in the normalization with CL=0.66.

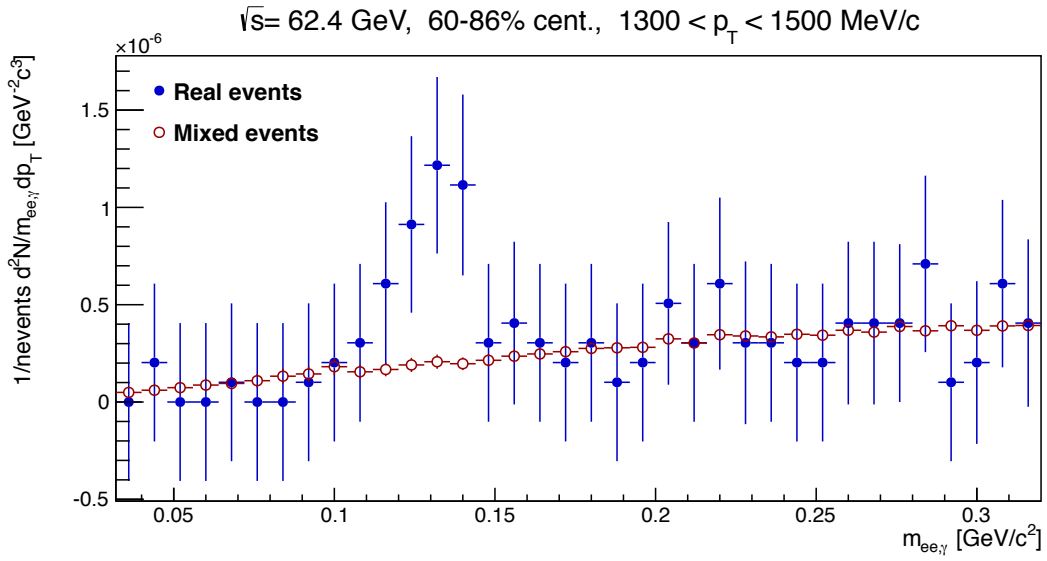


Figure 155: The foreground and normalized background for 60-86% centrality in the converted photon p_{Tee} bin of 1.3 - 1.5 GeV/c at $\sqrt{s_{NN}} = 62.4$ GeV.

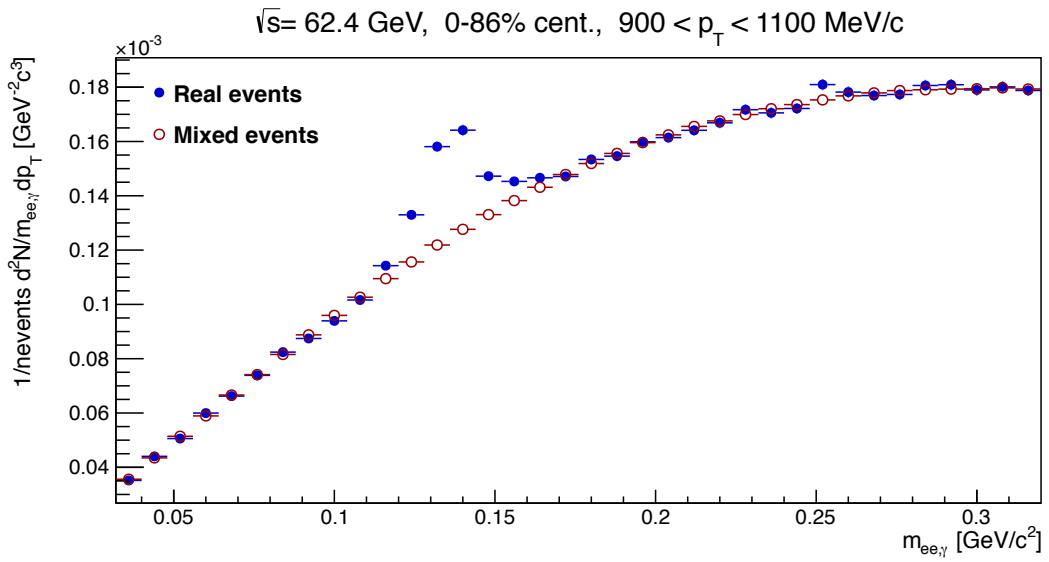


Figure 156: The di-photon foreground (blue) and normalized mixed event background (red) for 0-86% centrality in the converted photon p_{Tee} bin of 0.9 - 1.1 GeV/c at $\sqrt{s_{NN}} = 62.4$ GeV. The uncertainty on the background includes both background's statistical uncertainty and the uncertainty in the normalization with CL=0.66.

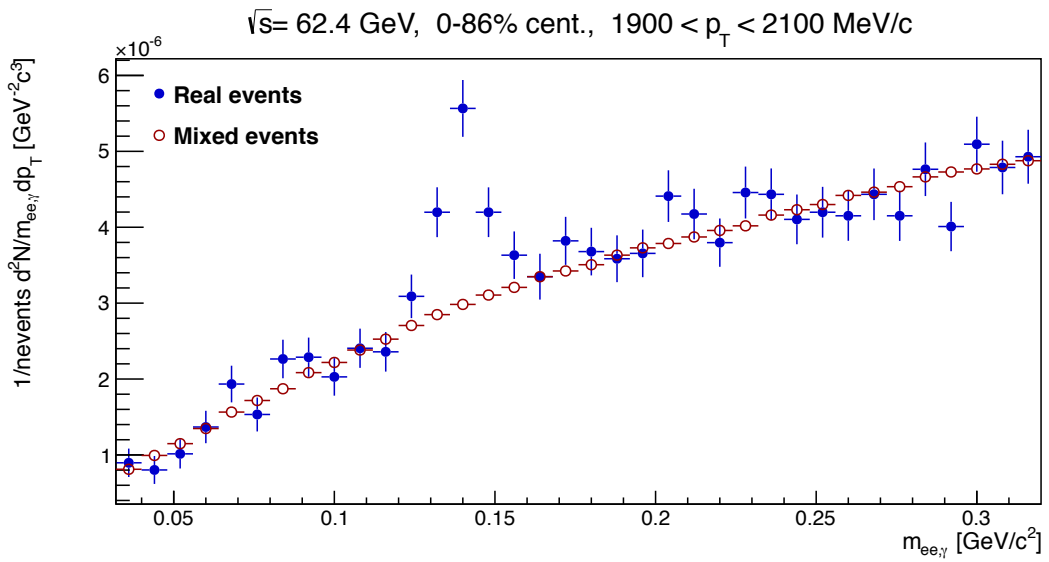


Figure 157: The foreground and normalized background for 0-86% centrality in the converted photon p_{Tee} bin of 1.9 - 2.1 GeV/c at $\sqrt{s_{NN}} = 62.4$ GeV.

12 Appendix B2

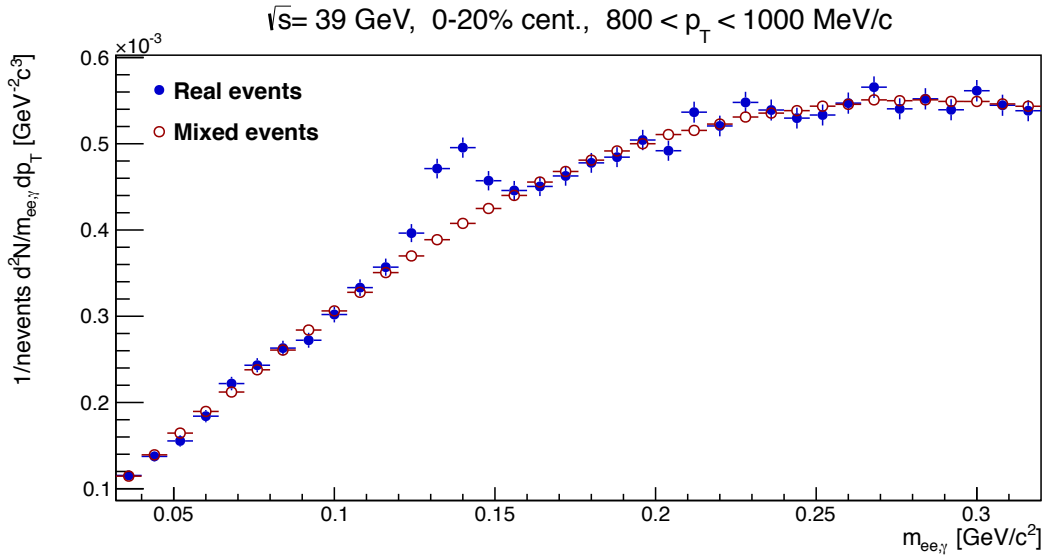


Figure 158: The di-photon foreground (blue) and normalized mixed event background (red) for 0-20% centrality in the converted photon p_{Tee} bin of 0.8 - 1.0 GeV/c at $\sqrt{s_{NN}} = 39$ GeV. The uncertainty on the background includes both background's statistical uncertainty and the uncertainty in the normalization with CL=0.66.

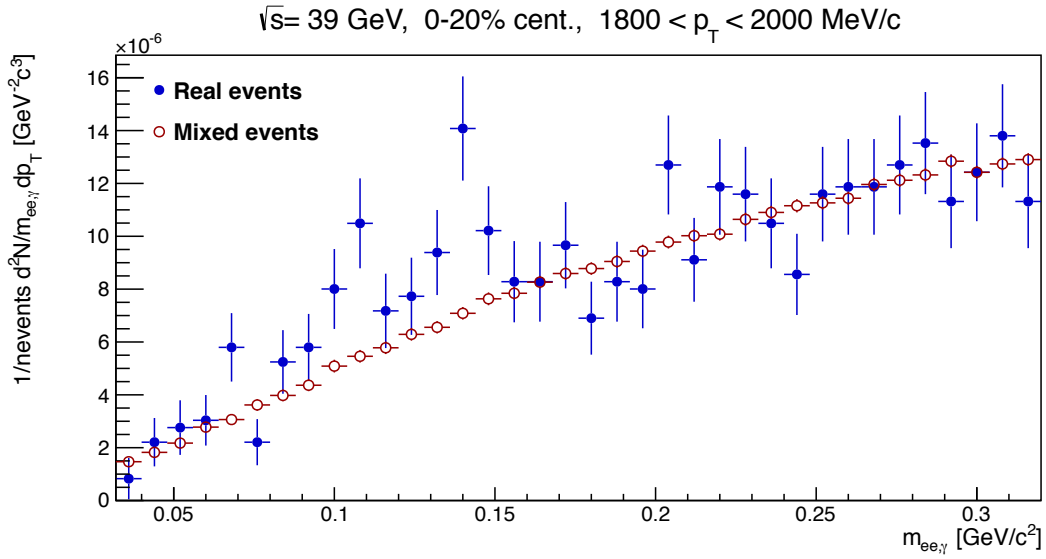


Figure 159: The foreground and normalized background for 0-20% centrality in the converted photon p_{Tee} bin of 1.8 - 2.0 GeV/c at $\sqrt{s_{NN}} = 39$ GeV.

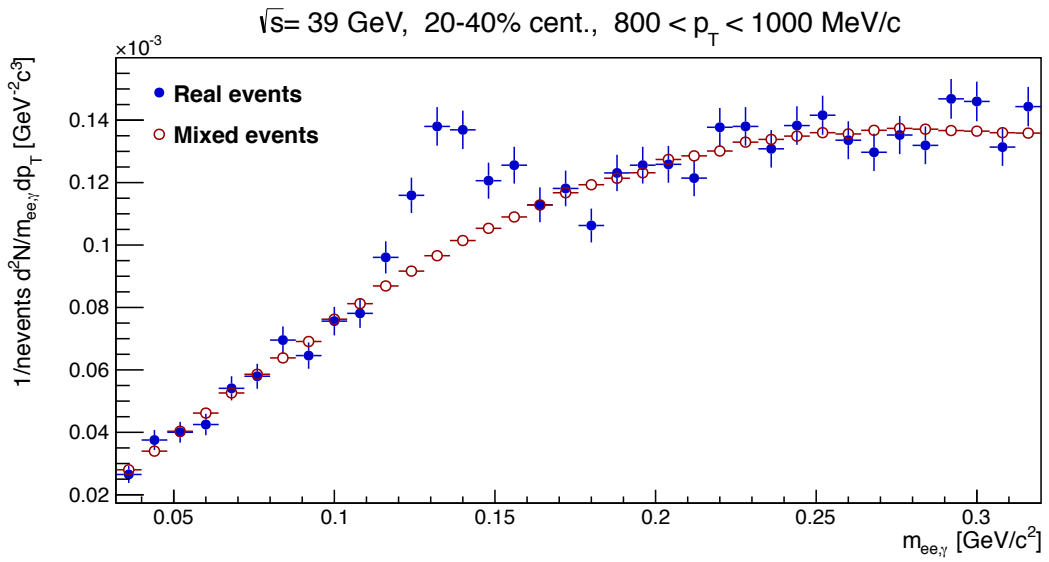


Figure 160: The di-photon foreground (blue) and normalized mixed event background (red) for 20-40% centrality in the converted photon p_{Tee} bin of $0.8 - 1.0 \text{ GeV}/c$ at $\sqrt{s_{NN}} = 39 \text{ GeV}$. The uncertainty on the background includes both background's statistical uncertainty and the uncertainty in the normalization with CL=0.66.

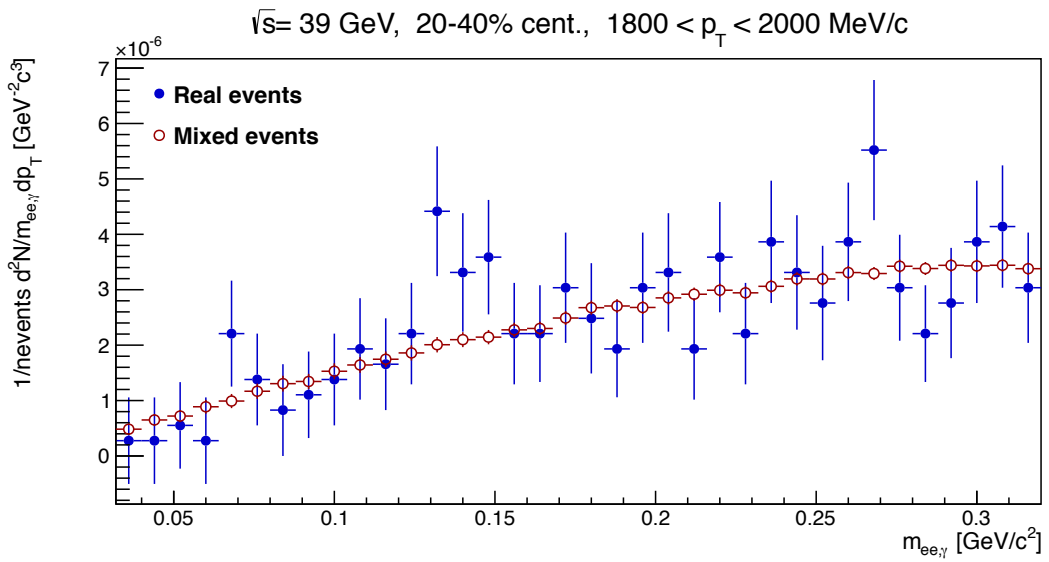


Figure 161: The foreground and normalized background for 20-40% centrality in the converted photon p_{Tee} bin of $1.8 - 2.0 \text{ GeV}/c$ at $\sqrt{s_{NN}} = 39 \text{ GeV}$.

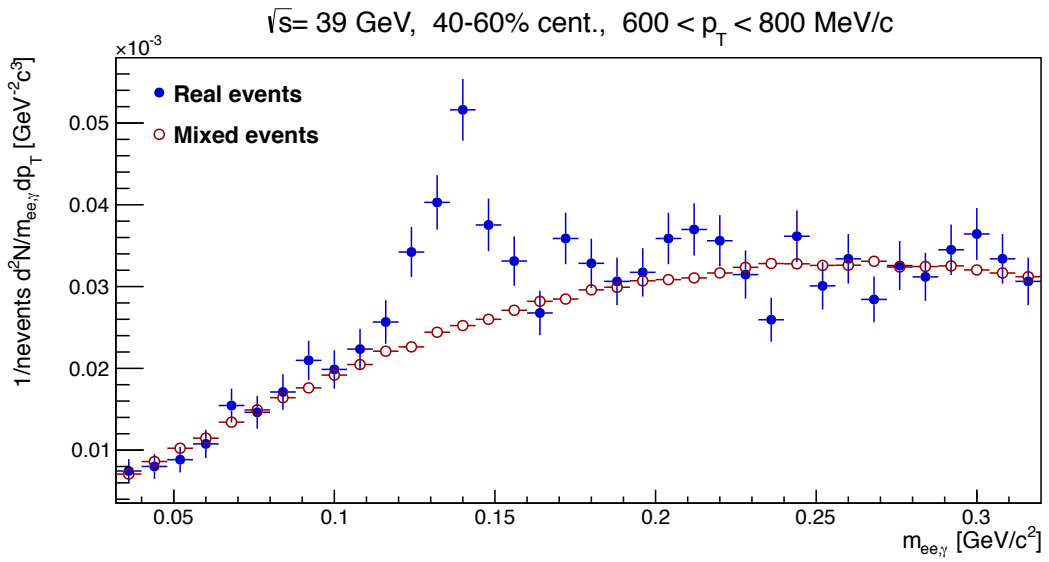


Figure 162: The di-photon foreground (blue) and normalized mixed event background (red) for 40-60% centrality in the converted photon p_{Tee} bin of $0.6 - 0.8 \text{ GeV}/c$ at $\sqrt{s_{NN}} = 39 \text{ GeV}$. The uncertainty on the background includes both background's statistical uncertainty and the uncertainty in the normalization with CL=0.66.

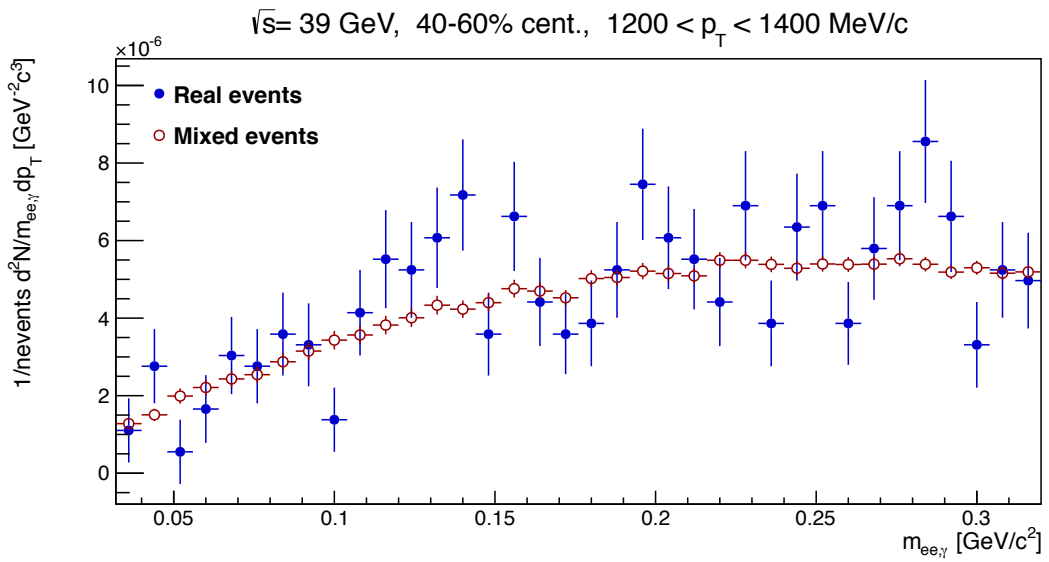


Figure 163: The foreground and normalized background for 40-60% centrality in the converted photon p_{Tee} bin of $1.2 - 1.4 \text{ GeV}/c$ at $\sqrt{s_{NN}} = 39 \text{ GeV}$.

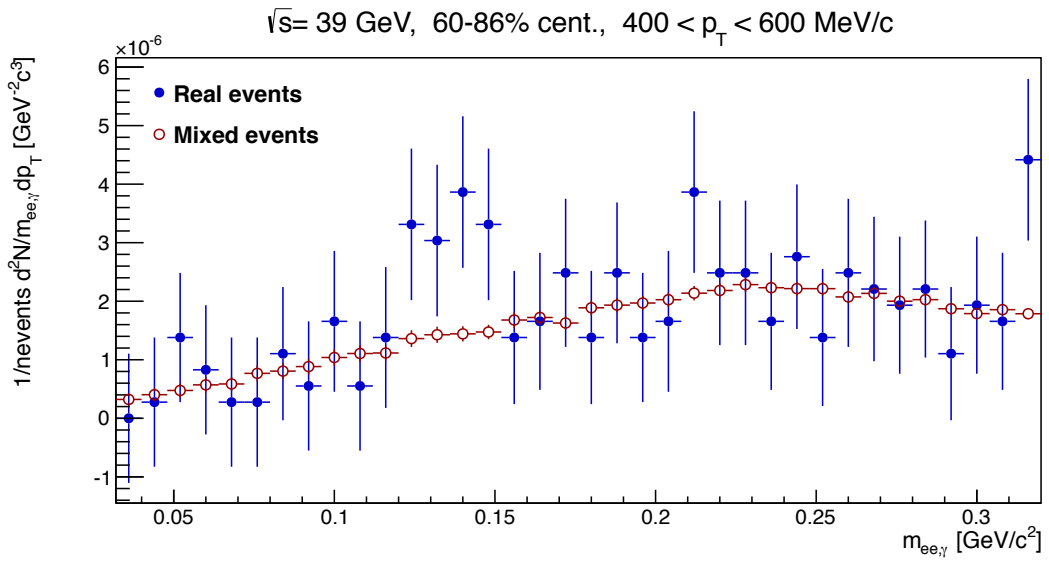


Figure 164: The di-photon foreground (blue) and normalized mixed event background (red) for 60–86% centrality in the converted photon p_{Tee} bin of $0.4\text{--}0.6 \text{ GeV}/c$ at $\sqrt{s_{NN}} = 39 \text{ GeV}$. The uncertainty on the background includes both background's statistical uncertainty and the uncertainty in the normalization with CL=0.66.

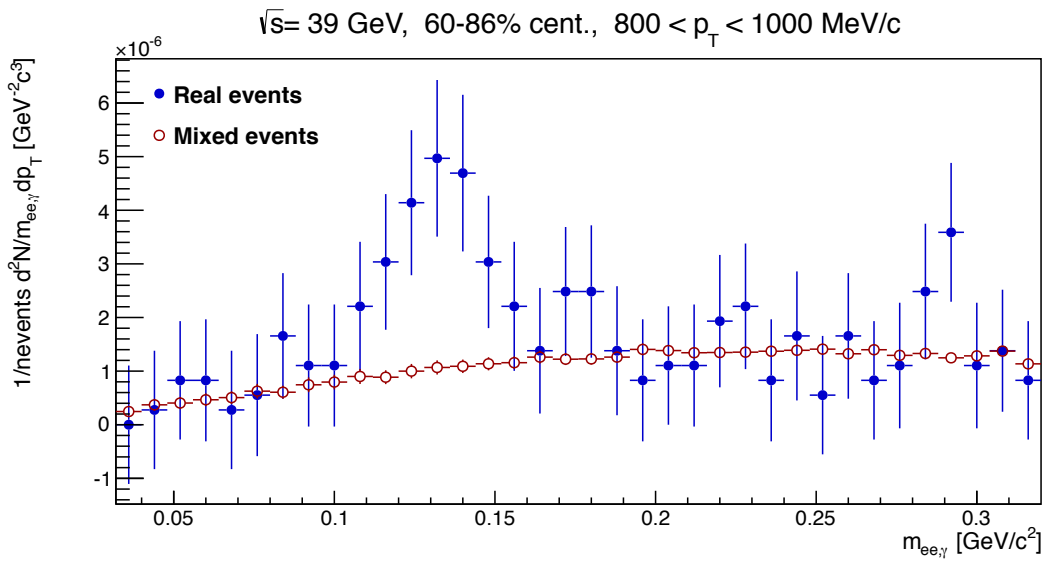


Figure 165: The foreground and normalized background for 60–86% centrality in the converted photon p_{Tee} bin of $0.8\text{--}1.0 \text{ GeV}/c$ at $\sqrt{s_{NN}} = 39 \text{ GeV}$.

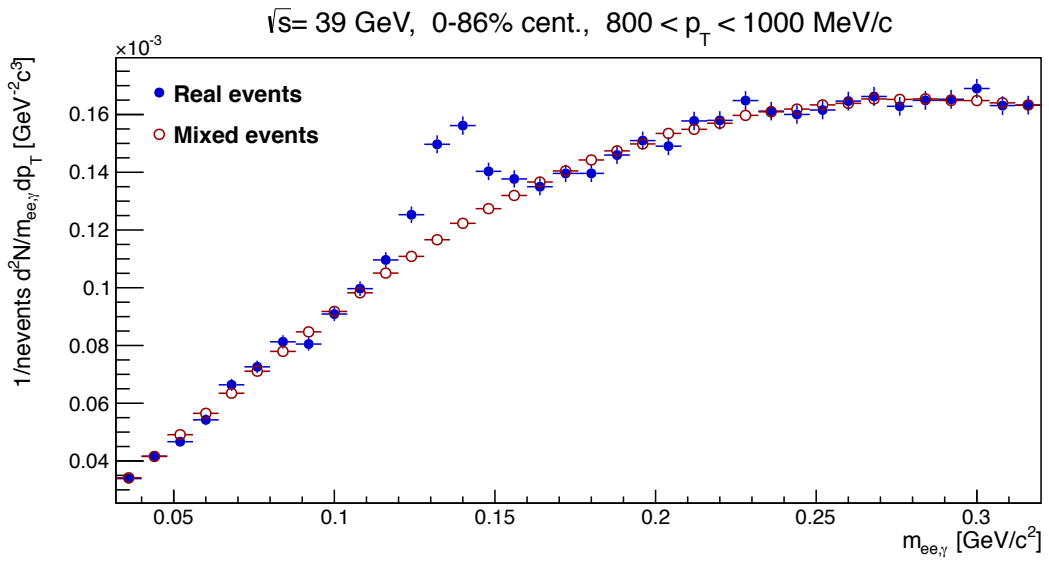


Figure 166: The di-photon foreground (blue) and normalized mixed event background (red) for 0-86% centrality in the converted photon p_{Tee} bin of 0.8 - 1.0 GeV/c at $\sqrt{s_{NN}} = 39$ GeV. The uncertainty on the background includes both background's statistical uncertainty and the uncertainty in the normalization with CL=0.66.

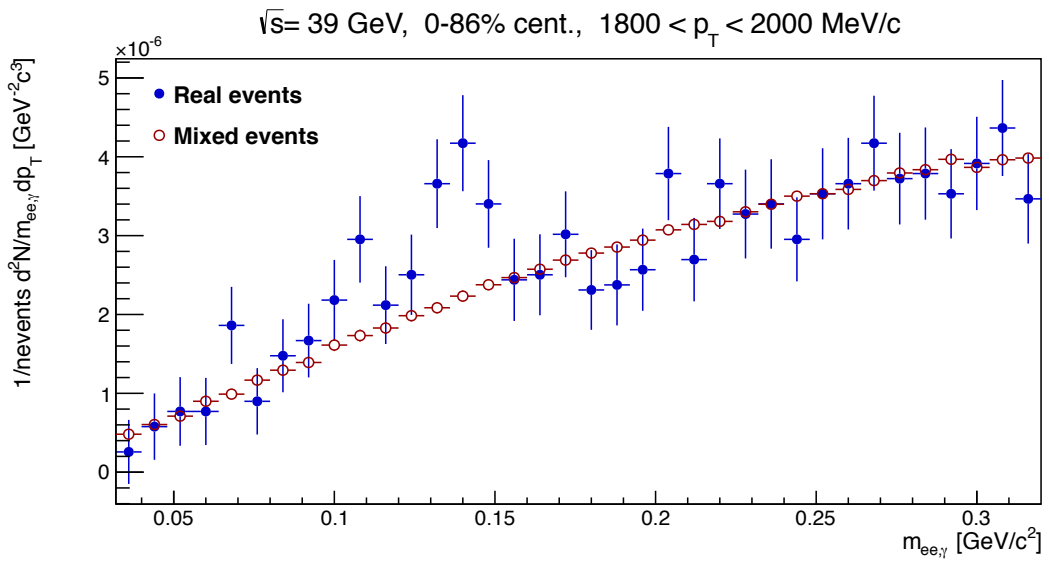


Figure 167: The foreground and normalized background for 0-86% centrality in the converted photon p_{Tee} bin of 1.8 - 2.0 GeV/c at $\sqrt{s_{NN}} = 39$ GeV.

13 Appendix C1

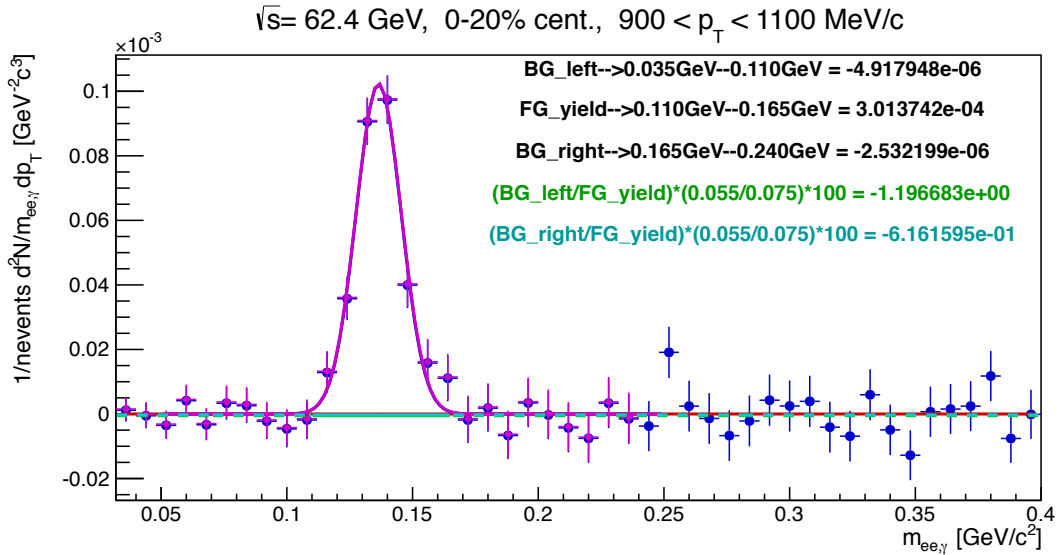


Figure 168: The π^0 yield extraction for 0-20% centrality in the converted photon p_{Tee} bin of 0.9 - 1.1 GeV/c at $\sqrt{s_{NN}} = 62.4$ GeV. The residual background is assumed to be described by averaging the sum of the green and cyan colored lines, which is subtracted from the original blue π^0 yield extraction (fitted by the blue Gaussian). The result is the purple histogram (fitted by the purple Gaussian).

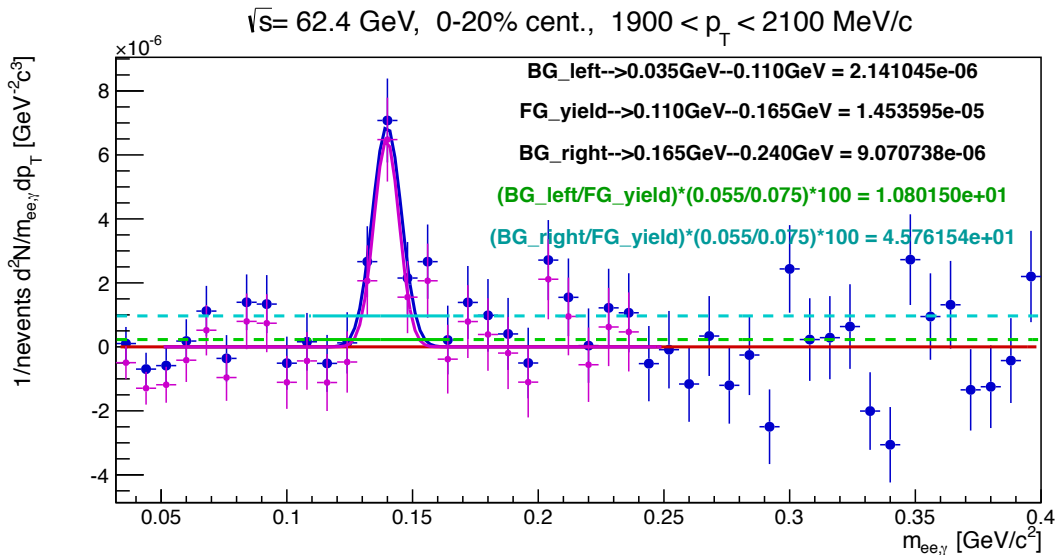


Figure 169: The π^0 yield extraction for 0-20% centrality in the converted photon p_{Tee} bin of 1.9 - 2.1 GeV/c at $\sqrt{s_{NN}} = 62.4$ GeV.

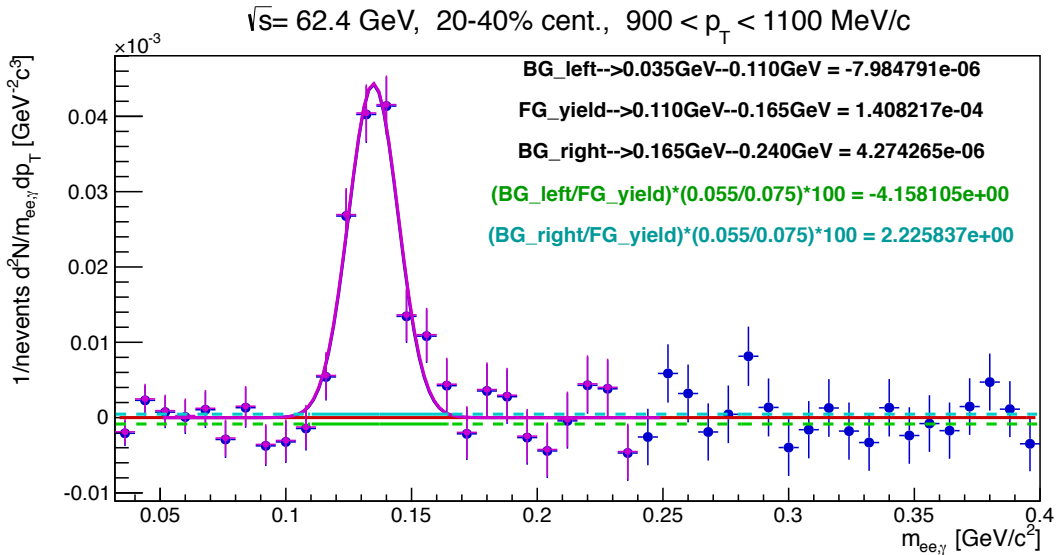


Figure 170: The π^0 yield extraction for 20-40% centrality in the converted photon p_{Tee} bin of 0.9 - 1.1 GeV/c at $\sqrt{s_{NN}} = 62.4$ GeV. The residual background is assumed to be described by averaging the sum of the green and cyan colored lines, which is subtracted from the original blue π^0 yield extraction (fitted by the blue Gaussian). The result is the purple histogram (fitted by the purple Gaussian).

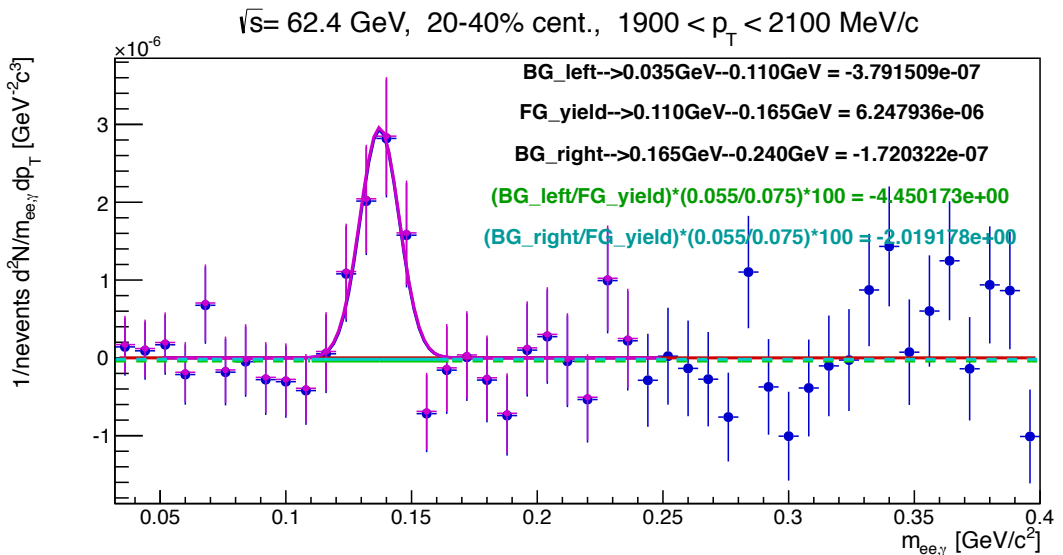


Figure 171: The π^0 yield extraction for 20-40% centrality in the converted photon p_{Tee} bin of 1.9 - 2.1 GeV/c at $\sqrt{s_{NN}} = 62.4$ GeV.

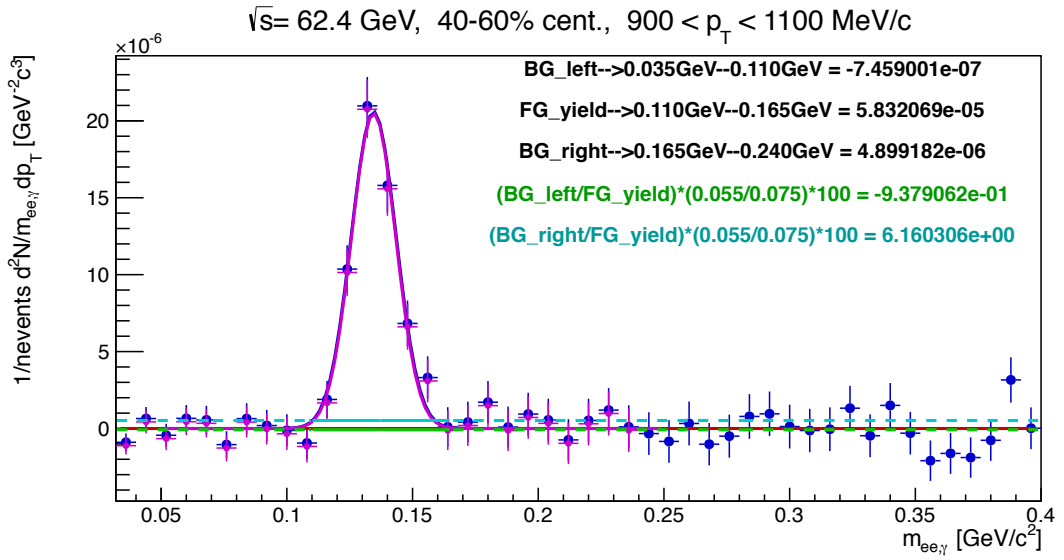


Figure 172: The π^0 yield extraction for 40-60% centrality in the converted photon p_{Tee} bin of 0.9 - 1.1 GeV/c at $\sqrt{s_{NN}} = 62.4$ GeV. The residual background is assumed to be described by averaging the sum of the green and cyan colored lines, which is subtracted from the original blue π^0 yield extraction (fitted by the blue Gaussian). The result is the purple histogram (fitted by the purple Gaussian).

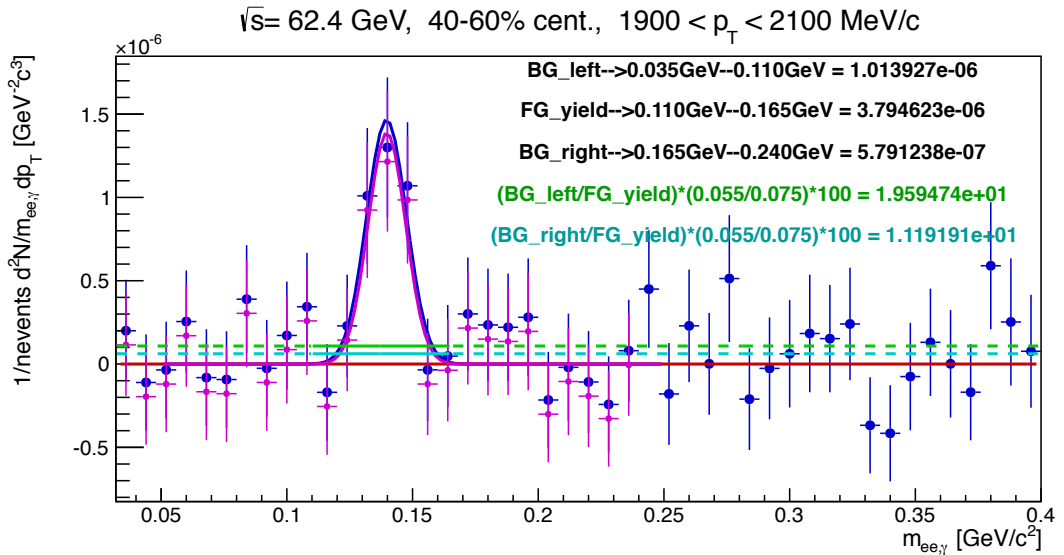


Figure 173: The π^0 yield extraction for 40-60% centrality in the converted photon p_{Tee} bin of 1.9 - 2.1 GeV/c at $\sqrt{s_{NN}} = 62.4$ GeV.

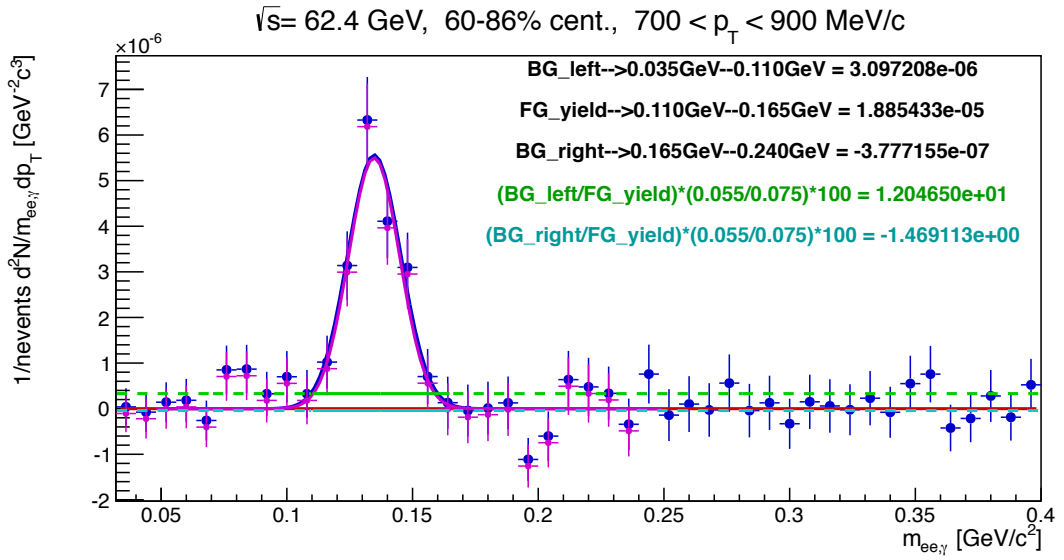


Figure 174: The π^0 yield extraction for 60-86% centrality in the converted photon p_{Tee} bin of 0.7 - 0.9 GeV/c at $\sqrt{s_{NN}} = 62.4$ GeV. The residual background is assumed to be described by averaging the sum of the green and cyan colored lines, which is subtracted from the original blue π^0 yield extraction (fitted by the blue Gaussian). The result is the purple histogram (fitted by the purple Gaussian).

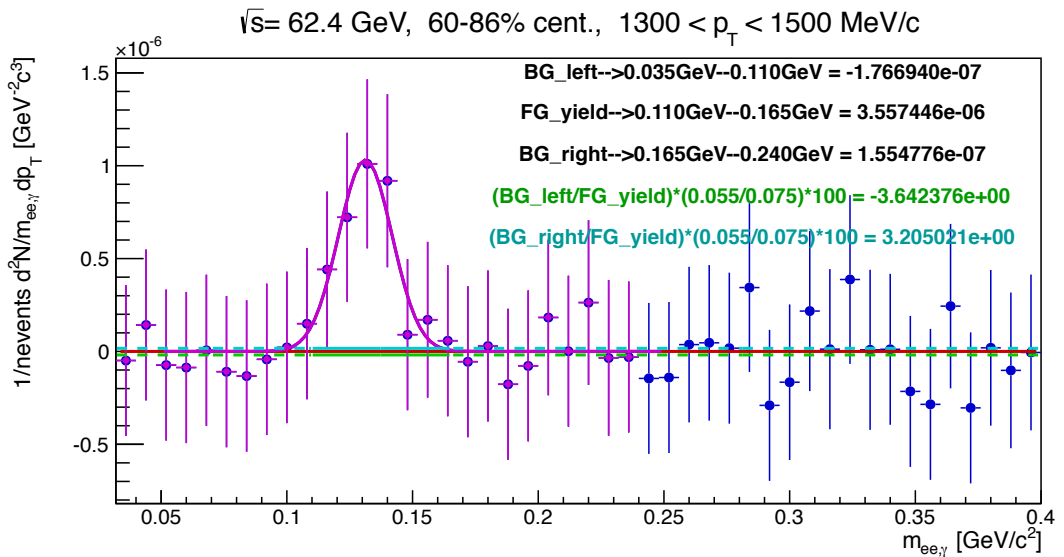


Figure 175: The π^0 yield extraction for 60-86% centrality in the converted photon p_{Tee} bin of 1.3 - 1.5 GeV/c at $\sqrt{s_{NN}} = 62.4$ GeV.

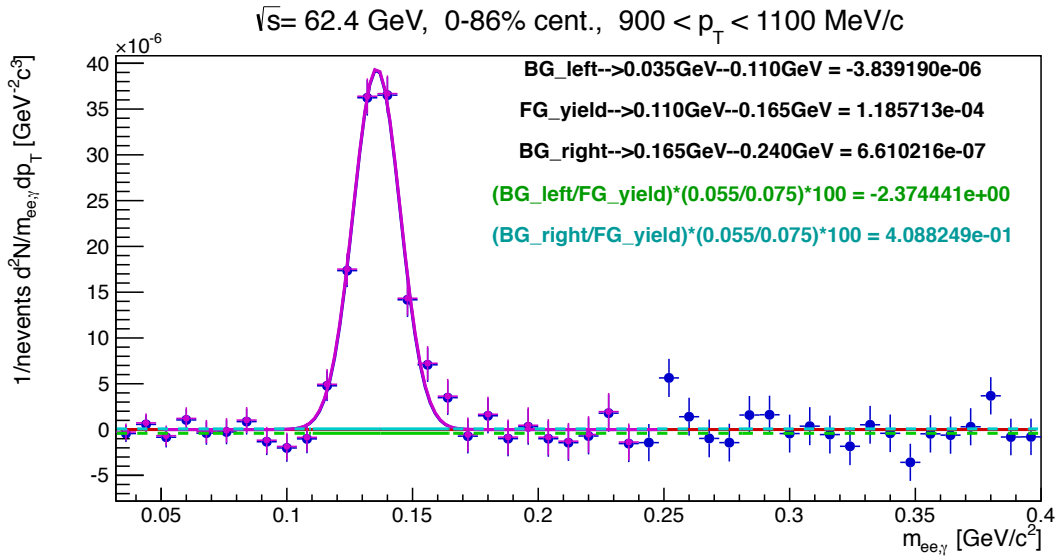


Figure 176: The π^0 yield extraction for 0-86% centrality in the converted photon p_{Tee} bin of 0.9 - 1.1 GeV/c at $\sqrt{s_{NN}} = 62.4$ GeV. The residual background is assumed to be described by averaging the sum of the green and cyan colored lines, which is subtracted from the original blue π^0 yield extraction (fitted by the blue Gaussian). The result is the purple histogram (fitted by the purple Gaussian).

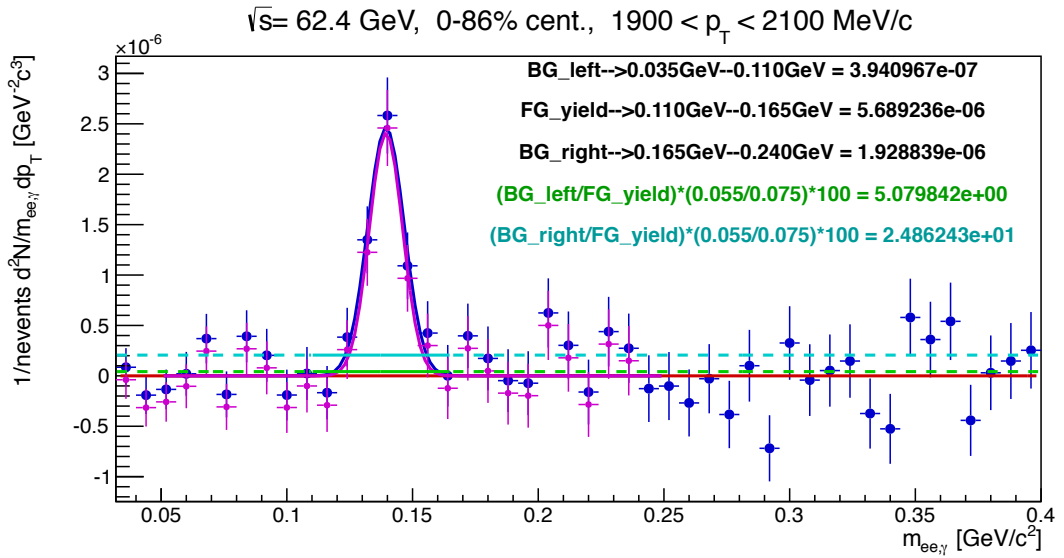


Figure 177: The π^0 yield extraction for 0-86% centrality in the converted photon p_{Tee} bin of 1.9 - 2.1 GeV/c at $\sqrt{s_{NN}} = 62.4$ GeV.

14 Appendix C2

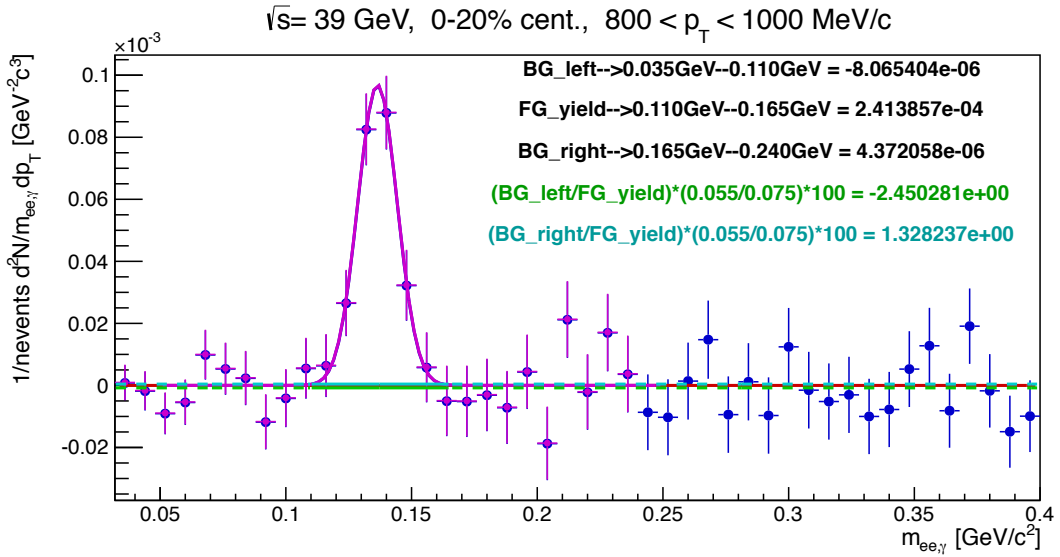


Figure 178: The π^0 yield extraction for 0-20% centrality in the converted photon p_{Tee} bin of 0.8 - 1.0 GeV/c at $\sqrt{s_{NN}} = 39$ GeV. The residual background is assumed to be described by averaging the sum of the green and cyan colored lines, which is subtracted from the original blue π^0 yield extraction (fitted by the blue Gaussian). The result is the purple histogram (fitted by the purple Gaussian).

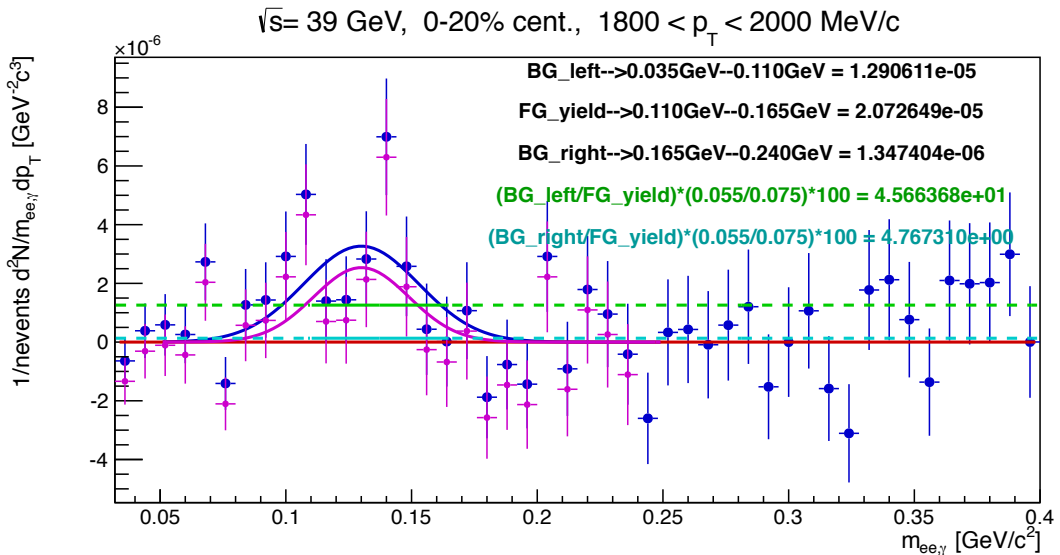


Figure 179: The π^0 yield extraction for 0-20% centrality in the converted photon p_{Tee} bin of 1.8 - 2.0 GeV/c at $\sqrt{s_{NN}} = 39$ GeV.

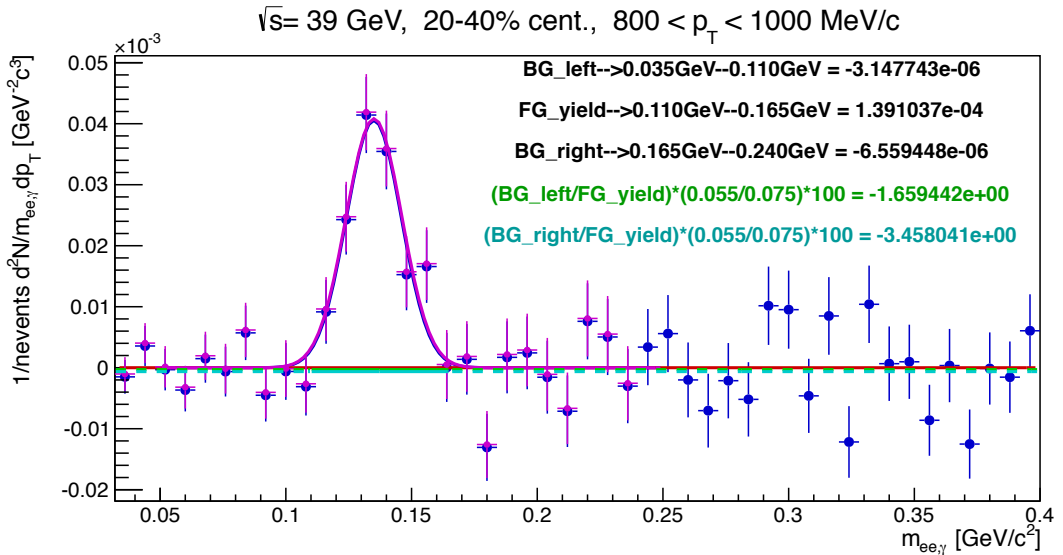


Figure 180: The π^0 yield extraction for 20-40% centrality in the converted photon p_{Tee} bin of 0.8 - 1.0 GeV/c at $\sqrt{s_{NN}} = 39$ GeV. The residual background is assumed to be described by averaging the sum of the green and cyan colored lines, which is subtracted from the original blue π^0 yield extraction (fitted by the blue Gaussian). The result is the purple histogram (fitted by the purple Gaussian).

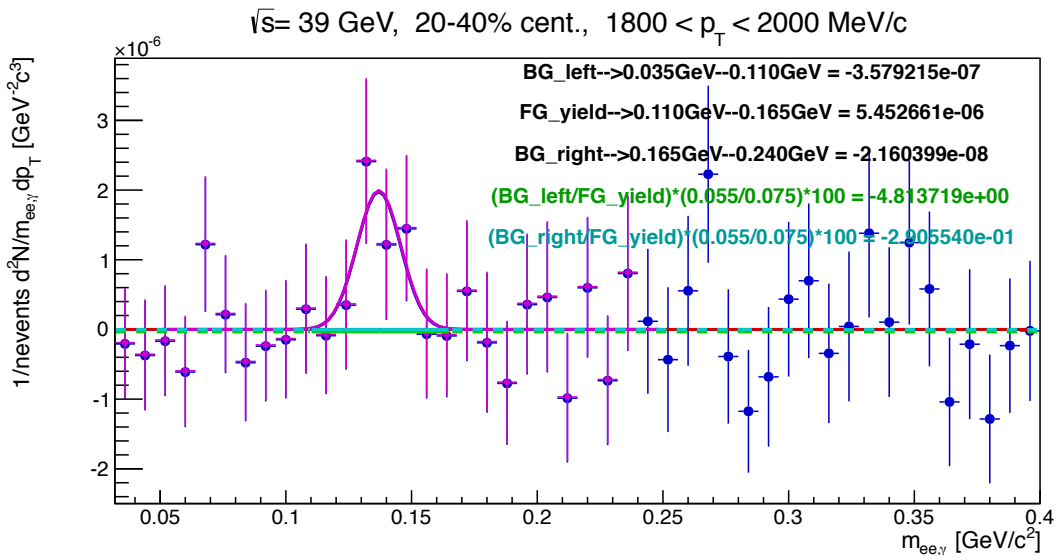


Figure 181: The π^0 yield extraction for 20-40% centrality in the converted photon p_{Tee} bin of 1.8 - 2.0 GeV/c at $\sqrt{s_{NN}} = 39$ GeV.

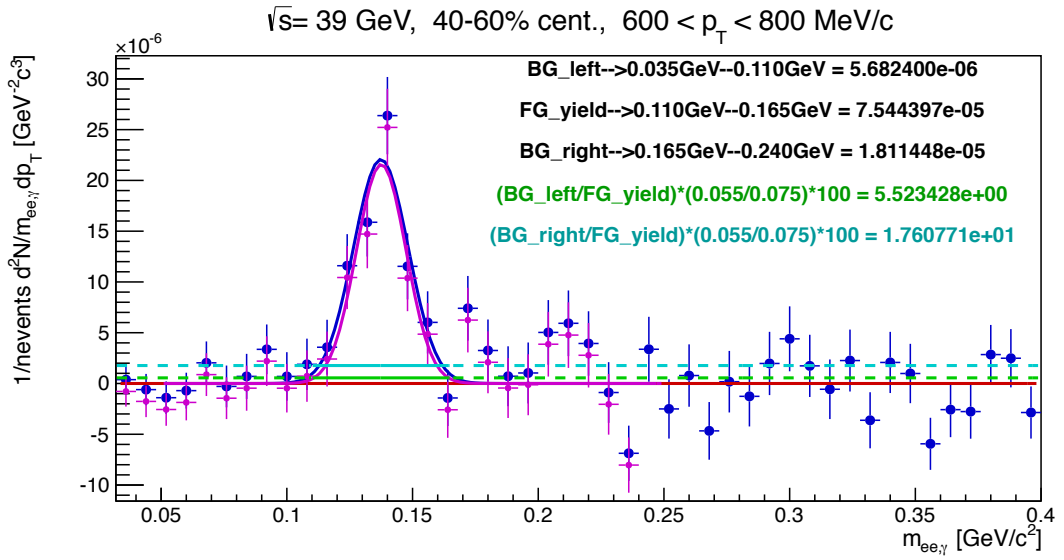


Figure 182: The π^0 yield extraction for 40-60% centrality in the converted photon p_{Tee} bin of 0.6 - 0.8 GeV/c at $\sqrt{s_{NN}} = 39$ GeV. The residual background is assumed to be described by averaging the sum of the green and cyan colored lines, which is subtracted from the original blue π^0 yield extraction (fitted by the blue Gaussian). The result is the purple histogram (fitted by the purple Gaussian).

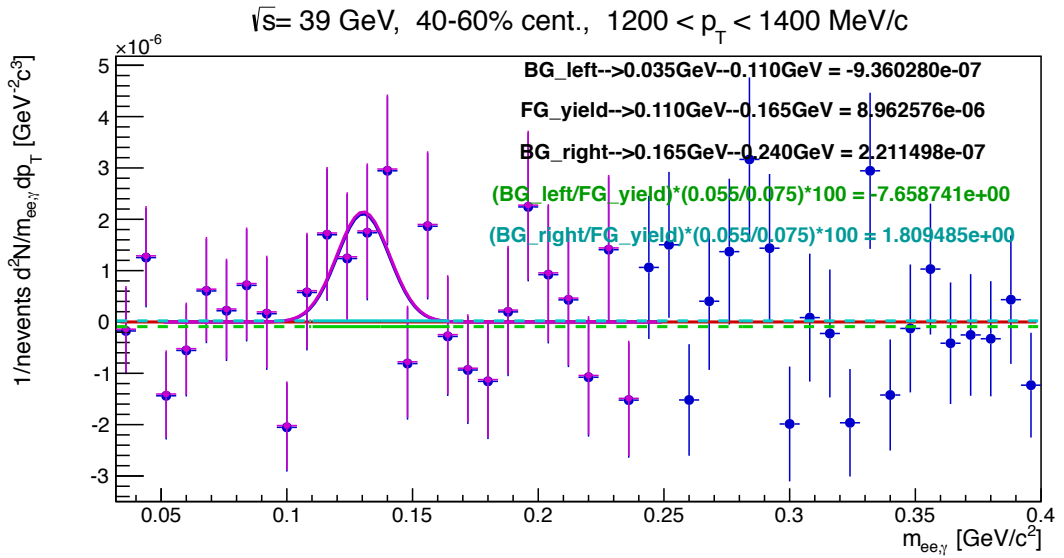


Figure 183: The π^0 yield extraction for 40-60% centrality in the converted photon p_{Tee} bin of 1.2 - 1.4 GeV/c at $\sqrt{s_{NN}} = 39$ GeV.

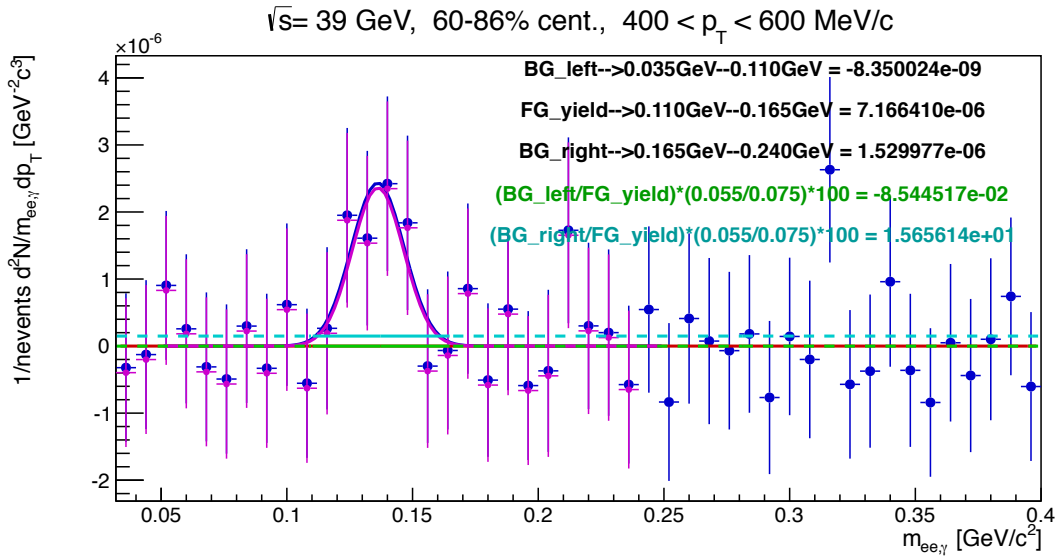


Figure 184: The π^0 yield extraction for 60-86% centrality in the converted photon p_{Tee} bin of 0.4 - 0.6 GeV/c at $\sqrt{s_{NN}} = 39$ GeV. The residual background is assumed to be described by averaging the sum of the green and cyan colored lines, which is subtracted from the original blue π^0 yield extraction (fitted by the blue Gaussian). The result is the purple histogram (fitted by the purple Gaussian).

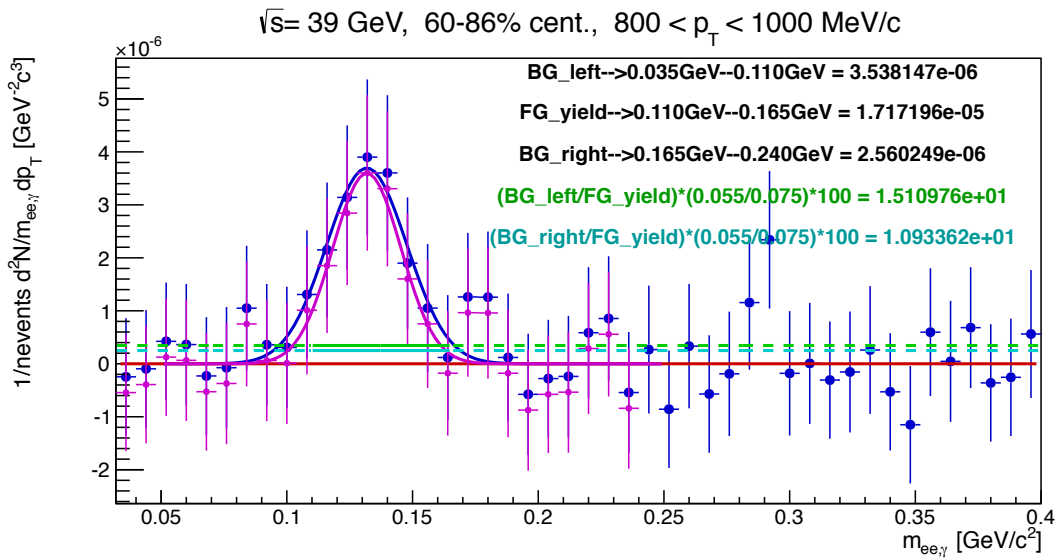


Figure 185: The π^0 yield extraction for 60-86% centrality in the converted photon p_{Tee} bin of 0.8 - 1.0 GeV/c at $\sqrt{s_{NN}} = 39$ GeV.

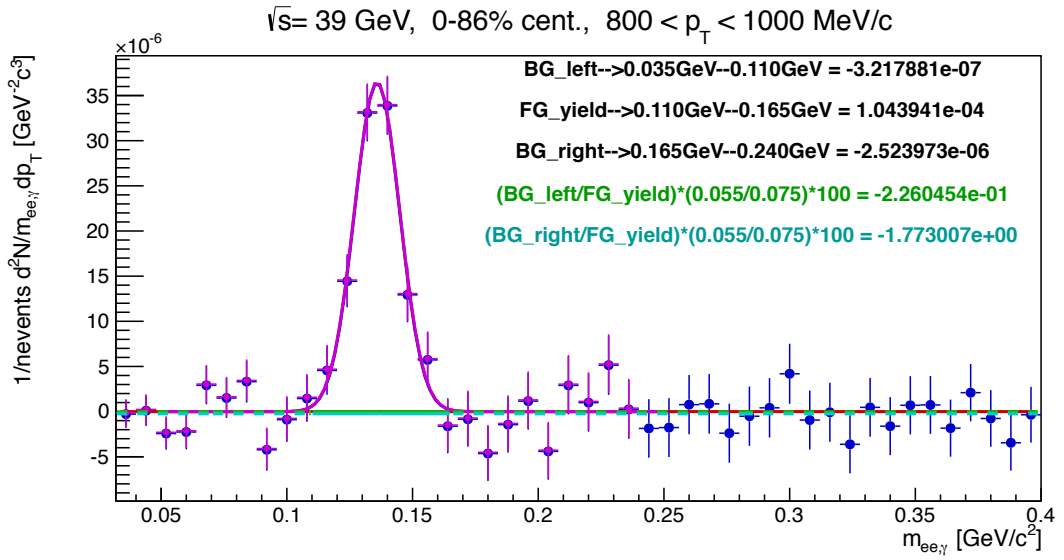


Figure 186: The π^0 yield extraction for 0-86% centrality in the converted photon p_{Tee} bin of 0.8 - 1.0 GeV/c at $\sqrt{s_{NN}} = 39$ GeV. The residual background is assumed to be described by averaging the sum of the green and cyan colored lines, which is subtracted from the original blue π^0 yield extraction (fitted by the blue Gaussian). The result is the purple histogram (fitted by the purple Gaussian).

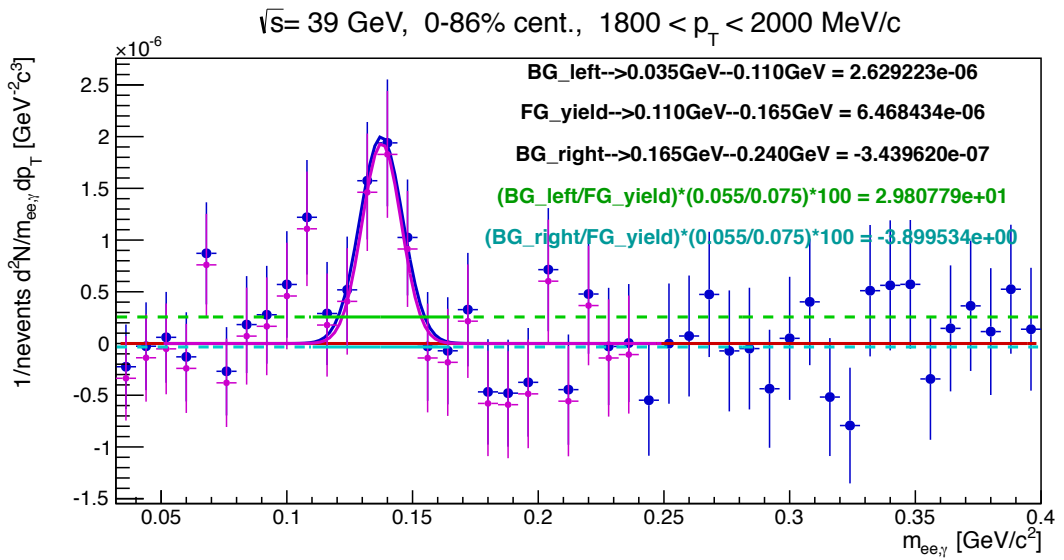


Figure 187: The π^0 yield extraction for 0-86% centrality in the converted photon p_{Tee} bin of 1.8 - 2.0 GeV/c at $\sqrt{s_{NN}} = 39$ GeV.

15 Data tables

15.1 The constituents of the relative direct photon yield, R_γ

p_T [GeV/c]	δp_T [GeV/c]	$\langle \varepsilon_\gamma f \rangle$	sys. error
0.60	0.10	0.104507	0.005225
0.80	0.10	0.117081	0.005854
1.00	0.10	0.126416	0.006321
1.20	0.10	0.134118	0.006706
1.40	0.10	0.141534	0.007077
1.60	0.10	0.149523	0.007476
1.80	0.10	0.158378	0.007919
2.00	0.10	0.167901	0.008395
2.30	0.20	0.182495	0.009125
2.75	0.25	0.201155	0.01006

Table 13: The table for 0-20% centrality binned conditional acceptance, $\langle \varepsilon_\gamma f \rangle$, at $\sqrt{s_{NN}} = 62.4$ GeV, shown in Fig. 81(a).

p_T [GeV/c]	δp_T [GeV/c]	$\langle \varepsilon_\gamma f \rangle$	sys. error
0.60	0.10	0.0974741	0.004874
0.80	0.10	0.111725	0.005586
1.00	0.10	0.123053	0.006153
1.20	0.10	0.133227	0.00667
1.40	0.10	0.143493	0.007175
1.60	0.10	0.154353	0.007718
1.80	0.10	0.165617	0.008281
2.00	0.10	0.17667	0.008833
2.30	0.20	0.191568	0.009578
2.75	0.25	0.208639	0.01043

Table 14: The conditional acceptance $\langle \varepsilon_\gamma f \rangle$ for 20-40% centrality at $\sqrt{s_{NN}} = 62.4$ GeV, shown in Fig. 81(b).

p_T [GeV/c]	δp_T [GeV/c]	$\langle \varepsilon_\gamma f \rangle$	sys. error
0.60	0.10	0.0990097	0.00495
0.80	0.10	0.11339	0.00567
1.00	0.10	0.124449	0.006222
1.20	0.10	0.134274	0.006714
1.40	0.10	0.144115	0.007206
1.60	0.10	0.15433	0.007716
1.80	0.10	0.164649	0.008232
2.00	0.10	0.174603	0.00873
2.30	0.20	0.188481	0.009424
2.75	0.25	0.208043	0.0104

Table 15: The conditional acceptance $\langle \varepsilon_\gamma f \rangle$ for the minimum bias 0-86% at $\sqrt{s_{NN}} = 62.4$ GeV, shown in Fig. 81(e).

p_T [GeV/c]	δp_T [GeV/c]	$\langle \varepsilon_\gamma f \rangle$	sys. error
0.50	0.10	0.105724	0.008458
0.70	0.10	0.115472	0.009238
0.90	0.10	0.121219	0.009698
1.10	0.10	0.126416	0.01011
1.30	0.10	0.132748	0.01062
1.50	0.10	0.14026	0.01122
1.70	0.10	0.148212	0.01186
1.90	0.10	0.155992	0.01248
2.50	0.50	0.179601	0.01437

Table 16: The conditional acceptance $\langle \varepsilon_\gamma f \rangle$ for the minimum bias 0-86% at $\sqrt{s_{NN}} = 39$ GeV, shown in Fig. 82(e).

p_T [GeV/c]	δp_T [GeV/c]	$Y_{cocktail}$	sys. error
0.60	0.10	1.14649	0.008333
0.80	0.10	1.16846	0.009403
1.00	0.10	1.18263	0.01007
1.20	0.10	1.1923	0.01052
1.40	0.10	1.19916	0.01083
1.60	0.10	1.20419	0.01106
1.80	0.10	1.2081	0.01123
2.00	0.10	1.211	0.01133
2.30	0.20	1.21447	0.01152
2.75	0.25	1.21837	0.01169

Table 17: The table for 0-20% centrality binned cocktail ratio, $Y_{cocktail}$, at $\sqrt{s_{NN}} = 62.4 \text{ GeV}$, shown in Fig. 84(a).

p_T [GeV/c]	δp_T [GeV/c]	$Y_{cocktail}$	sys. error
0.60	0.10	1.14225	0.008121
0.80	0.10	1.16515	0.009244
1.00	0.10	1.18047	0.00997
1.20	0.10	1.19107	0.01046
1.40	0.10	1.19864	0.01081
1.60	0.10	1.20437	0.01107
1.80	0.10	1.20865	0.01126
2.00	0.10	1.21216	0.01141
2.30	0.20	1.2155	0.01156
2.75	0.25	1.21946	0.01174

Table 18: The cocktail ratio $Y_{cocktail}$ for 20-40% centrality at $\sqrt{s_{NN}} = 62.4 \text{ GeV}$, shown in Fig. 84(b).

p_T [GeV/c]	δp_T [GeV/c]	$Y_{cocktail}$	sys. error
0.60	0.10	1.14441	0.008229
0.80	0.10	1.16695	0.00933
1.00	0.10	1.18169	0.01003
1.20	0.10	1.19178	0.01049
1.40	0.10	1.19894	0.01082
1.60	0.10	1.20425	0.01106
1.80	0.10	1.20831	0.01124
2.00	0.10	1.21144	0.01138
2.30	0.20	1.21488	0.01154
2.75	0.25	1.21884	0.01171

Table 19: The cocktail ratio $Y_{cocktail}$ for the minimum bias 0-86% at $\sqrt{s_{NN}} = 62.4 \text{ GeV}$, shown in Fig. 84(e).

p_T [GeV/c]	δp_T [GeV/c]	$Y_{cocktail}$	sys. error
0.50	0.10	1.14406	0.008212
0.70	0.10	1.16531	0.009251
0.90	0.10	1.1789	0.009897
1.10	0.10	1.18842	0.01034
1.30	0.10	1.19575	0.01068
1.50	0.10	1.20117	0.01092
1.70	0.10	1.20555	0.01112
1.90	0.10	1.209	0.01127
2.50	0.50	1.21484	0.01153

Table 20: The cocktail ratio $Y_{cocktail}$ for the minimum bias 0-86% at $\sqrt{s_{NN}} = 39 \text{ GeV}$, shown in Fig. 86(e).

p_T [GeV/c]	δp_T [GeV/c]	$N^{incl}/N^{\pi^0,tag}$	stat. error
0.60	0.10	13.5826	1.24979
0.80	0.10	12.9508	1.07953
1.00	0.10	10.9797	0.891311
1.20	0.10	10.5487	0.984142
1.40	0.10	14.4077	2.10538
1.60	0.10	11.3468	1.69769
1.80	0.10	8.1706	1.19436
2.00	0.10	14.8228	4.69579
2.30	0.20	11.174	2.81627
2.75	0.25	14.7179	7.74087

Table 21: The data table for 0-20% centrality binned $N^{incl}/N^{\pi^0,tag}$ ratio at $\sqrt{s_{NN}} = 62.4$ GeV, shown in Fig. 99(a).

p_T [GeV/c]	δp_T [GeV/c]	$N^{incl}/N^{\pi^0,tag}$	stat. error
0.60	0.10	13.2293	1.20466
0.80	0.10	12.4047	1.00577
1.00	0.10	11.8424	1.01781
1.20	0.10	11.1958	1.10868
1.40	0.10	8.79687	0.88732
1.60	0.10	7.17167	0.773866
1.80	0.10	8.88688	1.3972
2.00	0.10	12.3809	3.33833
2.30	0.20	7.65628	1.49631
2.75	0.25	5.69662	1.41744

Table 22: The $N^{incl}/N^{\pi^0,tag}$ ratio for 20-40% centrality at $\sqrt{s_{NN}} = 62.4$ GeV, shown in Fig. 99(b).

p_T [GeV/c]	δp_T [GeV/c]	$N^{incl}/N^{\pi^0,tag}$	stat. error
0.60	0.10	13.5886	0.977291
0.80	0.10	12.5754	0.833189
1.00	0.10	11.0776	0.732989
1.20	0.10	10.2418	0.735746
1.40	0.10	11.3291	1.00392
1.60	0.10	9.36672	0.881697
1.80	0.10	8.20372	0.873241
2.00	0.10	12.7937	2.5013
2.30	0.20	9.56863	1.54291
2.75	0.25	7.97255	1.93292

Table 23: The $N^{incl}/N^{\pi^0,tag}$ ratio for the minimum bias 0-86% at $\sqrt{s_{NN}} = 62.4 \text{ GeV}$, shown in Fig. 99(e).

p_T [GeV/c]	δp_T [GeV/c]	$N^{incl}/N^{\pi^0,tag}$	stat. error
0.50	0.10	13.0332	1.5759
0.70	0.10	12.6422	1.15186
0.90	0.10	12.3659	1.15876
1.10	0.10	10.7527	1.04741
1.30	0.10	12.4273	1.69954
1.50	0.10	9.03032	1.20284
1.70	0.10	8.08278	1.3515
1.90	0.10	9.53633	2.69989
2.50	0.50	7.08956	1.41

Table 24: The $N^{incl}/N^{\pi^0,tag}$ ratio for the minimum bias 0-86% at $\sqrt{s_{NN}} = 39 \text{ GeV}$, shown in Fig. 99(e).

p_T [GeV/c]	δp_T [GeV/c]	R_γ	stat. error	sys. error
0.60	0.10	1.2381	0.113981	0.0667
0.80	0.10	1.29768	0.10822	0.0698801
1.00	0.10	1.17366	0.0953233	0.0632018
1.20	0.10	1.18659	0.110767	0.0638976
1.40	0.10	1.7005	0.24858	0.0915719
1.60	0.10	1.40892	0.210909	0.0758704
1.80	0.10	1.07114	0.156713	0.057681
2.00	0.10	2.05513	0.651243	0.110669
2.30	0.20	1.67908	0.423571	0.0904186
2.75	0.25	2.42995	1.27878	0.130853

Table 25: The data table for 0-20% centrality binned relative direct photon yield, R_γ , at $\sqrt{s_{NN}} = 62.4 \text{ GeV}$, shown in Fig. 96(a).

p_T [GeV/c]	δp_T [GeV/c]	R_γ	stat. error	sys. error
0.60	0.10	1.12893	0.102867	0.0607927
0.80	0.10	1.18947	0.0965004	0.0640528
1.00	0.10	1.23446	0.106158	0.0664758
1.20	0.10	1.25231	0.124093	0.0674371
1.40	0.10	1.0531	0.106323	0.0567094
1.60	0.10	0.919128	0.313581	0.1399
1.80	0.10	1.21774	0.191634	0.0655751
2.00	0.10	1.8044	0.486769	0.0971668
2.30	0.20	1.20667	0.236257	0.0649787
2.75	0.25	0.97464	0.519643	0.114647

Table 26: R_γ for 20-40% centrality at $\sqrt{s_{NN}} = 62.4 \text{ GeV}$, shown in Fig. 96(b).

p_T [GeV/c]	δp_T [GeV/c]	R_γ	stat. error	sys. error
0.60	0.10	1.17563	0.0845764	0.0633075
0.80	0.10	1.22193	0.0809786	0.0658007
1.00	0.10	1.1667	0.0772161	0.0628231
1.20	0.10	1.1539	0.0829224	0.0621377
1.40	0.10	1.36178	0.120715	0.0733321
1.60	0.10	1.20038	0.113048	0.0646407
1.80	0.10	1.11787	0.119061	0.0601974
2.00	0.10	1.84393	0.360605	0.0992955
2.30	0.20	1.48451	0.239566	0.0799409
2.75	0.25	1.36083	0.33026	0.0732808

Table 27: R_γ for the minimum bias 0-86% at $\sqrt{s_{NN}} = 62.4$ GeV, shown in Fig. 96(c).

p_T [GeV/c]	δp_T [GeV/c]	R_γ	stat. error	sys. error
0.50	0.10	1.20441	0.145656	0.0993158
0.70	0.10	1.25273	0.114151	0.1033
0.90	0.10	1.27151	0.119158	0.104849
1.10	0.10	1.1438	0.111428	0.0943174
1.30	0.10	1.37964	0.188694	0.113765
1.50	0.10	1.05447	0.140477	0.0869513
1.70	0.10	0.993708	0.341904	0.171966
1.90	0.10	1.23043	0.348389	0.101461
2.50	0.50	1.04812	0.20865	0.0864278

Table 28: R_γ for the minimum bias 0-86% at $\sqrt{s_{NN}} = 39$ GeV, shown in Fig. 96(d).

15.2 Charged particle multiplicity data tables

Table 29: Charged particle multiplicity results for 200 GeV Au+Au collisions. The uncertainties include the total statistical and systematic uncertainties. The table is from [145] with the substitution $\langle N_{qp} \rangle \leftrightarrow \langle N_{coll} \rangle$, where $\langle N_{coll} \rangle$ is from [146].

Centrality	$\langle N_{part} \rangle$	$\langle N_{coll} \rangle$	$dN_{ch}/d\eta$	$(dN_{ch}/d\eta)/(0.5N_{part})$	$(dN_{ch}/d\eta)/(0.5N_{qp})$
0%–5%	350.9 ± 4.7	1064.1 ± 110.0	687.4 ± 36.6	3.92 ± 0.22	1.49 ± 0.08
5%–10%	297.0 ± 6.6	838.0 ± 87.2	560.4 ± 27.9	3.77 ± 0.21	1.43 ± 0.08
10%–15%	251.0 ± 7.3	661.1 ± 68.5	456.8 ± 22.3	3.64 ± 0.21	1.42 ± 0.08
15%–20%	211.0 ± 7.3	519.1 ± 53.7	371.5 ± 18.2	3.52 ± 0.21	1.39 ± 0.08
20%–25%	176.3 ± 7.0	402.6 ± 39.5	302.5 ± 15.8	3.43 ± 0.22	1.38 ± 0.08
25%–30%	146.8 ± 7.1	311.9 ± 31.8	245.6 ± 13.8	3.35 ± 0.25	1.38 ± 0.09
30%–35%	120.9 ± 7.0	237.8 ± 24.2	197.2 ± 12.2	3.26 ± 0.28	1.37 ± 0.10
35%–40%	98.3 ± 6.8	177.3 ± 18.3	156.4 ± 10.9	3.18 ± 0.31	1.36 ± 0.11
40%–45%	78.7 ± 6.1	129.6 ± 12.6	123.5 ± 9.6	3.14 ± 0.34	1.36 ± 0.12
45%–50%	61.9 ± 5.2	92.7 ± 9.0	95.3 ± 8.6	3.08 ± 0.38	1.35 ± 0.13
50%–55%	47.6 ± 4.9	64.4 ± 8.1	70.9 ± 7.6	2.98 ± 0.44	1.32 ± 0.16
55%–60%	35.6 ± 5.1	43.7 ± 7.6	52.2 ± 6.5	2.93 ± 0.56	1.35 ± 0.20

Table 30: Charged particle multiplicity results for 62.4 GeV Au+Au collisions. The uncertainties include the total statistical and systematic uncertainties. The table is from [145] with the substitution $\langle N_{qp} \rangle \leftrightarrow \langle N_{coll} \rangle$, where $\langle N_{coll} \rangle$ is from [148].

Centrality	$\langle N_{part} \rangle$	$\langle N_{coll} \rangle$	$dN_{ch}/d\eta$	$(dN_{ch}/d\eta)/(0.5N_{part})$	$(dN_{ch}/d\eta)/(0.5N_{qp})$
0%–5%	342.6 ± 4.9	906.0 ± 127.2	447.5 ± 38.9	2.61 ± 0.23	1.00 ± 0.09
5%–10%	291.3 ± 7.3	713.30 ± 97.82	367.4 ± 31.6	2.52 ± 0.23	1.01 ± 0.09
10%–15%	244.5 ± 8.9	562.20 ± 74.34	301.8 ± 25.8	2.47 ± 0.23	1.01 ± 0.09
15%–20%	205.0 ± 9.6	442.20 ± 56.77	248.0 ± 21.0	2.42 ± 0.23	1.01 ± 0.09
20%–25%	171.3 ± 8.9	345.50 ± 41.34	203.0 ± 17.1	2.37 ± 0.24	1.01 ± 0.10
25%–30%	142.2 ± 8.5	266.30 ± 32.57	165.1 ± 13.8	2.32 ± 0.24	1.01 ± 0.10
30%–35%	116.7 ± 8.9	202.00 ± 25.26	133.0 ± 11.1	2.28 ± 0.26	1.02 ± 0.10
35%–40%	95.2 ± 7.7	150.90 ± 19.04	105.9 ± 8.76	2.22 ± 0.26	1.02 ± 0.11
40%–45%	76.1 ± 7.7	110.70 ± 14.19	83.0 ± 6.83	2.18 ± 0.28	1.03 ± 0.12
45%–50%	59.9 ± 6.9	79.82 ± 12.06	63.9 ± 5.24	2.13 ± 0.30	1.03 ± 0.14
50%–55%	46.8 ± 5.2	55.63 ± 8.95	48.4 ± 3.95	2.07 ± 0.29	1.05 ± 0.15
55%–60%	35.8 ± 4.6	37.52 ± 6.45	35.8 ± 2.92	2.00 ± 0.30	1.06 ± 0.16

Table 31: Charged particle multiplicity results for 39 GeV Au+Au collisions. The uncertainties include the total statistical and systematic uncertainties. The table is from [145] with the substitution $\langle N_{qp} \rangle \leftrightarrow \langle N_{coll} \rangle$, where $\langle N_{coll} \rangle$ is from [148].

Centrality	$\langle N_{part} \rangle$	$\langle N_{coll} \rangle$	$dN_{ch}/d\eta$	$(dN_{ch}/d\eta)/(0.5N_{part})$	$(dN_{ch}/d\eta)/(0.5N_{qp})$
0%–5%	340.0 ± 7.4	861.1 ± 144.2	363.2 ± 31.6	2.14 ± 0.19	0.83 ± 0.08
5%–10%	289.6 ± 8.1	691.6 ± 114.1	297.8 ± 25.8	2.06 ± 0.19	0.82 ± 0.08
10%–15%	244.1 ± 6.4	549.50 ± 83.95	246.6 ± 21.3	2.02 ± 0.18	0.82 ± 0.08
15%–20%	206.5 ± 6.3	438.60 ± 65.42	204.4 ± 17.5	1.98 ± 0.18	0.82 ± 0.08
20%–25%	174.1 ± 6.3	347.90 ± 51.19	168.9 ± 14.4	1.94 ± 0.18	0.82 ± 0.08
25%–30%	145.8 ± 6.2	273.70 ± 42.94	138.3 ± 11.8	1.90 ± 0.18	0.82 ± 0.09
30%–35%	120.8 ± 7.5	212.00 ± 31.56	112.6 ± 9.6	1.86 ± 0.20	0.83 ± 0.09
35%–40%	98.6 ± 6.4	160.90 ± 22.97	90.6 ± 7.7	1.84 ± 0.20	0.83 ± 0.09
40%–45%	79.8 ± 6.0	120.60 ± 17.83	72.1 ± 6.1	1.81 ± 0.20	0.84 ± 0.10
45%–50%	63.9 ± 5.8	89.31 ± 14.28	56.8 ± 4.8	1.78 ± 0.22	0.85 ± 0.11
50%–55%	50.3 ± 5.5	64.83 ± 12.54	43.7 ± 3.7	1.73 ± 0.24	0.85 ± 0.13

Table 32: Charged particle multiplicity results for 2760 GeV Pb+Pb collisions. The table is from [149] with the addition of $\langle N_{coll} \rangle$, which is from [147].

Centrality	$dN_{ch}/d\eta$	$\langle N_{part} \rangle$	$\langle N_{coll} \rangle$	$(dN_{ch}/d\eta)/(0.5N_{part})$
0–5%	1601 ± 60	382.8 ± 3.1	1684 ± 140	8.4 ± 0.3
5–10%	1294 ± 49	329.7 ± 4.6	1316 ± 110	7.9 ± 0.3
10–20%	966 ± 37	260.5 ± 4.4	922.7 ± 140.0	7.4 ± 0.3
20–30%	649 ± 23	186.4 ± 3.9	558.4 ± 62.0	7.0 ± 0.3
30–40%	426 ± 15	128.9 ± 3.3	321.6 ± 44.0	6.6 ± 0.3
40–50%	261 ± 9	85.0 ± 2.6	172.25 ± 14.00	6.1 ± 0.3
50–60%	149 ± 6	52.8 ± 2.0	84.65 ± 5.50	5.7 ± 0.3
60–70%	76 ± 4	30.0 ± 1.3	37.725 ± 4.000	5.1 ± 0.3
70–80%	35 ± 2	15.8 ± 0.6	15.22 ± 3.00	4.4 ± 0.4

15.3 Direct photon invariant yield data tables

p_T [GeV/c]	δp_T [GeV/c]	Inv. Yield [GeV $^{-2}$ c 2]	stat. error	sys. error
0.60	0.10	5.99931	2.87194	2.06997
0.80	0.10	2.29087	0.832835	0.729238
1.00	0.10	0.458696	0.251777	0.269288
1.20	0.10	0.184247	0.109379	0.113876
1.40	0.10	0.275767	0.0978589	0.0569525
1.60	0.10	0.0675218	0.0348258	0.0245695
1.80	0.10	0.00512972	0.0112999	0.0111852
2.00	0.10	0.0344753	0.0212788	0.00635657
2.30	0.20	0.00718324	0.00448047	0.00216863
2.75	0.25	0.00314815	0.00281535	0.000563547

Table 33: The data table for 0-20% centrality binned direct photon invariant yield in Au+Au at $\sqrt{s_{NN}} = 62.4 \text{ GeV}$.

p_T [GeV/c]	δp_T [GeV/c]	Inv. Yield [GeV $^{-2}$ c 2]	stat. error	sys. error
0.60	0.10	1.70371	1.35934	1.02358
0.80	0.10	0.734522	0.374109	0.351029
1.00	0.10	0.302658	0.137036	0.134269
1.20	0.10	0.11977	0.0589058	0.0556901
1.40	0.10	0.00992831	0.0198798	0.0234726
1.60	0.10	<0.0211		
1.80	0.10	0.00746587	0.00657083	0.0054254
2.00	0.10	0.0126559	0.00765854	0.0029452
2.30	0.20	0.00108393	0.00123917	0.00102349
2.75	0.25	<0.0005829		

Table 34: The data table for 20-40% centrality binned direct photon invariant yield in Au+Au at $\sqrt{s_{NN}} = 62.4 \text{ GeV}$.

p_T [GeV/c]	δp_T [GeV/c]	Inv. Yield [GeV $^{-2}$ c 2]	stat. error	sys. error
0.60	0.10	1.73082	0.833506	0.782957
0.80	0.10	0.655536	0.239199	0.271139
1.00	0.10	0.166892	0.0773369	0.101878
1.20	0.10	0.0572293	0.030835	0.0425233
1.40	0.10	0.0534166	0.0178233	0.0197658
1.60	0.10	0.0123823	0.00698556	0.00886086
1.80	0.10	0.00319487	0.00322708	0.00423036
2.00	0.10	0.0104315	0.00445731	0.00232759
2.30	0.20	0.00196486	0.000971526	0.000813566
2.75	0.25	0.000312075	0.000285635	0.000200551

Table 35: The data table for 0-86% centrality binned direct photon invariant yield in Au+Au at $\sqrt{s_{NN}} = 62.4 \text{ GeV}$.

p_T [GeV/c]	δp_T [GeV/c]	Inv. Yield [GeV $^{-2}$ c 2]	stat. error	sys. error
0.50	0.10	2.92163	2.08184	1.58925
0.70	0.10	1.10691	0.499952	0.546521
0.90	0.10	0.400722	0.175866	0.203937
1.10	0.10	0.0764554	0.0592452	0.0770413
1.30	0.10	0.0765651	0.0380557	0.03484
1.50	0.10	0.00436177	0.0112497	0.0138846
1.70	0.10	<0.01226		
1.90	0.10	0.00323661	0.00489344	0.0030254
2.50	0.25	6.33147e-5	0.000274548	0.00034286

Table 36: The data table for 0-86% centrality binned direct photon invariant yield in Au+Au at $\sqrt{s_{NN}} = 39 \text{ GeV}$.

p_T [GeV/c]	δp_T [GeV/c]	Inv. Yield [GeV $^{-2}$ c 2]	stat. error	sys. error
0.50	0.10	18.384316	4.162295	4.963615
0.70	0.10	3.863694	0.908128	1.412782
0.90	0.10	1.531712	0.313389	0.499280
1.10	0.10	0.500764	0.119182	0.184227
1.30	0.10	0.248402	0.053970	0.077102
1.50	0.10	0.105543	0.025248	0.032901
1.70	0.10	0.071944	0.014094	0.016161
1.90	0.10	0.028950	0.007115	0.007324
2.25	0.25	0.007928	0.001929	0.002126
3.00	0.50	0.001125	0.000274	0.000242
4.25	0.75	0.000025	0.000033	0.000012

Table 37: The data table for 0-20% centrality binned direct photon invariant yield in Au+Au at $\sqrt{s_{NN}} = 200$ GeV from [42].

p_T [GeV/c]	δp_T [GeV/c]	Inv. Yield [GeV $^{-2}$ c 2]	stat. error	sys. error
0.50	0.10	5.954453	1.590491	2.116200
0.70	0.10	0.906468	0.350932	0.588297
0.90	0.10	0.396036	0.121966	0.209478
1.10	0.10	0.215631	0.050980	0.084104
1.30	0.10	0.110570	0.023209	0.036068
1.50	0.10	0.050032	0.011015	0.015939
1.70	0.10	0.019825	0.005521	0.007187
1.90	0.10	0.011294	0.003037	0.003575
2.25	0.25	0.004157	0.000919	0.001142
3.00	0.50	0.000554	0.000135	0.000135
4.25	0.75	0.000044	0.000018	0.000009

Table 38: The data table for 20-40% centrality binned direct photon invariant yield in Au+Au at $\sqrt{s_{NN}} = 200$ GeV from [42].

p_T [GeV/c]	δp_T [GeV/c]	Inv. Yield [GeV $^{-2}$ c 2]	stat. error	sys. error
0.50	0.10	2.064060	0.615983	0.794669
0.70	0.10	0.530987	0.141643	0.232527
0.90	0.10	0.168944	0.047410	0.080196
1.10	0.10	0.061615	0.018912	0.030895
1.30	0.10	0.041359	0.009241	0.013852
1.50	0.10	0.014628	0.004274	0.005990
1.70	0.10	0.006184	0.002196	0.002790
1.90	0.10	0.003108	0.001249	0.001383
2.25	0.25	0.000850	0.000359	0.000435
3.00	0.50	0.000095	0.000054	0.000052
4.25	0.75	0.000008	0.000007	0.000003

Table 39: The data table for 40-60% centrality binned direct photon invariant yield in Au+Au at $\sqrt{s_{NN}} = 200$ GeV from [42].

p_T [GeV/c]	δp_T [GeV/c]	Inv. Yield [GeV $^{-2}$ c 2]	stat. error	sys. error
0.50	0.10	0.283798	0.126140	0.148048
0.70	0.10	0.036460	0.025660	0.039574
0.90	0.10	0.012077	0.008446	0.013316
1.10	0.10	0.008213	0.003597	0.005268
1.30	0.10	0.002898	0.001647	0.002167
1.50	0.10	0.001267	0.000829	0.000971
1.70	0.10	0.001107	0.000481	0.000490
1.90	0.10	0.000137	0.000243	0.000222
2.25	0.25	0.000045	0.000076	0.000074
3.00	0.50	0.000025	0.000015	0.000011
4.25	0.75	0.000007	0.000004	0.000001

Table 40: The data table for 60-92% centrality binned direct photon invariant yield in Au+Au at $\sqrt{s_{NN}} = 200$ GeV from [42].

p_T [GeV/c]	δp_T [GeV/c]	Inv. Yield [GeV $^{-2}$ c 2]	stat. error	sys. error
1.17469	0.25	0.436558	0.0703609	0.0963735
1.68434	0.25	0.0454181	0.0089549	0.0106445
2.19076	0.25	0.00645965	0.00195587	0.00151032
2.69795	0.25	0.00152809	0.000560347	0.00045023
3.3357	0.50	0.000293534	0.000130004	9.57608e-05
4.36874	0.50	-1.2651e-07	2.59207e-05	7.75734e-06

Table 41: The data table for 0-20% centrality binned direct photon invariant yield in Au+Au at $\sqrt{s_{NN}} = 200$ GeV from [40].

p_T [GeV/c]	δp_T [GeV/c]	Inv. Yield [GeV $^{-2}$ c 2]	stat. error	sys. error
1.17837	0.25	0.178151	0.0257948	0.037387
1.68653	0.25	0.020263	0.00357599	0.00442041
2.19281	0.25	0.00268808	0.000867393	0.000707814
2.70075	0.25	0.000101284	0.000257483	0.000169881
3.33915	0.50	0.000229536	7.36712e-05	4.33705e-05
4.37018	0.50	1.78475e-05	1.70697e-05	5.60662e-06

Table 42: The data table for 20-40% centrality binned direct photon invariant yield in Au+Au at $\sqrt{s_{NN}} = 200$ GeV from [40].

p_T [GeV/c]	δp_T [GeV/c]	Inv. Yield [GeV $^{-2}$ c 2]	stat. error	sys. error
1.17606	0.25	0.141133	0.0153485	0.0299764
1.68542	0.25	0.0162162	0.00201327	0.00322704
2.19144	0.25	0.00231514	0.000460845	0.000569122
2.69754	0.25	0.000530275	0.000139415	0.000146452
3.33822	0.50	0.00015278	3.38111e-05	3.60054e-05
4.36991	0.50	2.00909e-05	8.14502e-06	4.01129e-06

Table 43: The data table for 0-92% centrality binned direct photon invariant yield in Au+Au at $\sqrt{s_{NN}} = 200$ GeV from [40].

p_T [GeV/c]	δp_T [GeV/c]	Inv. Yield [GeV $^{-2}$ c 2]	stat. error	sys. error
1.1875	0.25	4.020e-02	1.780e-02	1.624e-02
1.7008	0.25	8.452e-03	2.309e-03	1.906e-03
2.2898	0.50	1.296e-03	0.489e-03	0.264e-03
3.4450	0.50	1.063e-04	0.526e-04	0.149e-04

Table 44: The data table for 0-40% centrality binned direct photon invariant yield in Cu+Cu at $\sqrt{s_{NN}} = 200$ GeV from [44].

p_T [GeV/c]	δp_T [GeV/c]	Inv. Yield [GeV $^{-2}$ c 2]	stat. error	sys. error
1.1874	0.25	1.628e-02	0.630e-02	0.674e-02
1.7006	0.25	3.170e-03	0.812e-03	0.669e-03
2.2915	0.50	3.943e-04	1.638e-04	0.090e-04
3.4444	0.50	3.415e-05	1.700e-05	0.422e-05

Table 45: The data table for 0-94% centrality binned direct photon invariant yield in Cu+Cu at $\sqrt{s_{NN}} = 200$ GeV from [44].

p_T [GeV/c]	δp_T [GeV/c]	Inv. Yield [GeV $^{-2}$ c 2]	stat. error	sys. error
1.00	0.10	1.758	0.134	0.867
1.20	0.10	0.990	0.179	0.406
1.40	0.10	0.5289	0.0709	0.2091
1.60	0.10	0.2290	0.0274	0.0901
1.80	0.10	0.1227	0.0130	0.0453
2.00	0.10	0.06878	0.00718	0.02498
2.20	0.10	0.04118	0.00390	0.01344
2.40	0.10	0.02652	0.00213	0.00755
2.60	0.10	0.01595	0.00128	0.00441
2.85	0.15	0.010264	0.000683	0.002439
3.15	0.15	0.005143	0.000385	0.001287
3.50	0.20	0.002764	0.000216	0.000680
3.90	0.20	0.001472	0.000112	0.000339
4.35	0.25	0.0007660	0.0000603	0.0001550
5.00	0.40	0.0003399	0.0000277	0.0000644
5.80	0.40	0.0001405	0.0000141	0.0000300
6.60	0.40	0.00007766	0.00000811	0.00001654
7.50	0.50	0.00003262	0.00000455	0.00000785
9.50	1.50	0.00001174	0.00000135	0.00000246
12.50	1.50	0.000002448	0.000000557	0.000000614

Table 46: The data table for 0-20% centrality binned direct photon invariant yield in Pb+Pb at $\sqrt{s_{NN}} = 2760$ GeV from [45].

p_T [GeV/c]	δp_T [GeV/c]	Inv. Yield [GeV $^{-2}$ c 2]	stat. error	sys. error
1.00	0.10	<0.645		
1.20	0.10	<0.517		
1.40	0.10	0.1176	0.0274	0.0833
1.60	0.10	0.0627	0.0110	0.0389
1.80	0.10	0.03753	0.00542	0.02005
2.00	0.10	0.02488	0.00293	0.01070
2.20	0.10	0.01554	0.00158	0.00584
2.40	0.10	0.00982	0.00101	0.00358
2.60	0.10	0.006913	0.000608	0.002049
2.85	0.15	0.004183	0.000350	0.001150
3.15	0.15	0.002107	0.000196	0.000591
3.50	0.20	0.001152	0.000113	0.000327
3.90	0.20	0.0006705	0.0000641	0.0001630
4.35	0.25	0.0002859	0.0000365	0.0000747
5.00	0.40	0.0001542	0.0000176	0.0000323
5.80	0.40	0.00007859	0.00000948	0.00001430
6.60	0.40	0.00004143	0.00000573	0.00000715
7.50	0.50	0.00001718	0.00000347	0.00000354
9.50	1.50	0.000005002	0.000000975	0.000001140
12.50	1.50	0.000001731	0.000000403	0.000000281

Table 47: The data table for 20-40% centrality binned direct photon invariant yield in Pb+Pb at $\sqrt{s_{NN}} = 2760$ GeV from [45].

p_T [GeV/c]	δp_T [GeV/c]	Inv. Yield [GeV $^{-2}$ c 2]	stat. error	sys. error
1.00	0.10	<0.114		
1.20	0.10	<0.0862		
1.40	0.10	<0.0430		
1.60	0.10	<0.0217		
1.80	0.10	<0.0115		
2.00	0.10	0.003604	0.000698	0.002690
2.20	0.10	0.001844	0.000440	0.001610
2.40	0.10	0.001300	0.000259	0.000913
2.60	0.10	0.000867	0.000165	0.000576
2.85	0.15	0.0007610	0.0000935	0.0003300
3.15	0.15	0.0004454	0.0000570	0.0001760
3.50	0.20	0.0002491	0.0000338	0.0000928
3.90	0.20	0.0001502	0.0000209	0.0000478
4.35	0.25	0.0000757	0.0000128	0.0000245
5.00	0.40	0.00002846	0.00000634	0.00001040
5.80	0.40	0.00001604	0.00000324	0.00000428
6.60	0.40	0.00000599	0.00000198	0.00000205
7.50	0.50	<0.00000257		
9.50	1.50	0.000000504	0.000000329	0.000000301
12.50	1.50	0.000000287	0.000000147	0.000000072

Table 48: The data table for 40-80% centrality binned direct photon invariant yield in Pb+Pb at $\sqrt{s_{NN}} = 2760$ GeV from [45].

p_T [GeV/c]	δp_T [GeV/c]	Inv. Cross Sec. [mb GeV $^{-2}$ c 3]	stat. error	sys. error
p+p (virtual photon)				
1.18449	0.25	0.001489490	0.000758668	0.002163150
1.69126	0.25	0.000541715	0.000163956	0.000304584
2.19773	0.25	0.000111656	3.04992e-05	5.79046e-05
2.703640	0.25	4.84535e-05	1.18865e-05	1.65357e-05
3.34880	0.50	9.89977e-06	3.26577e-06	3.86545e-06
4.37494	0.50	3.03996e-06	1.01686e-06	6.28280e-07
p+p (real photon)				
4.25	0.25	4.38e-06	2.94e-07	3.19e-06
4.75	0.25	1.64e-06	1.74e-07	1.17e-06
5.25	0.25	1.14e-06	3.04e-08	4.78e-07
5.75	0.25	6.13e-07	1.92e-08	2.21e-07
6.25	0.25	3.48e-07	1.27e-08	1.04e-07
6.75	0.25	2.31e-07	8.50e-09	6.24e-08
7.25	0.25	1.36e-07	6.12e-09	3.13e-08
7.75	0.25	9.29e-08	4.41e-09	2.04e-08
8.25	0.25	6.70e-08	3.22e-09	1.34e-08
8.75	0.25	4.83e-08	2.45e-09	9.18e-09
9.25	0.25	3.21e-08	1.89e-09	6.10e-09
9.75	0.25	2.04e-08	1.46e-09	3.68e-09
11.0	1.00	9.81e-09	4.23e-10	1.67e-09
13.0	1.00	2.97e-09	1.89e-10	5.05e-10
15.0	1.00	1.06e-09	9.85e-11	1.69e-10
17.0	1.00	3.38e-10	5.51e-11	5.42e-11
19.0	1.00	1.73e-10	3.37e-11	2.77e-11

Table 49: The data table for direct photon invariant cross section in p+p at $\sqrt{s_{NN}} = 200 \text{ GeV}$ from [153].

p_T [GeV/c]	δp_T [GeV/c]	Inv. Yield [GeV $^{-2}$ c 2]	stat. error	sys. error
4.25	0.25	0.000116954	1.60975e-06	1.34033e-05
4.75	0.25	5.83475e-05	9.80658e-07	6.49107e-06
5.25	0.25	2.88562e-05	6.23192e-07	3.04366e-06
5.75	0.25	1.61336e-05	4.16639e-07	1.58296e-06
6.25	0.25	1.01012e-05	2.95356e-07	9.37348e-07
6.75	0.25	6.16622e-06	2.09733e-07	5.44603e-07
7.25	0.25	3.8088e-06	1.49424e-07	3.29777e-07
7.75	0.25	2.57191e-06	1.14391e-07	2.18454e-07
8.25	0.25	1.69332e-06	8.43162e-08	1.40698e-07
8.75	0.25	1.21861e-06	6.77061e-08	1.00004e-07
9.25	0.25	7.47592e-07	4.79592e-08	6.20874e-08
9.75	0.25	5.57775e-07	3.9572e-08	4.63225e-08
11.0	1.00	2.49881e-07	1.49383e-08	2.02793e-08
13.0	1.00	7.60635e-08	7.66556e-09	6.14284e-09
15.0	1.00	2.25637e-08	3.24545e-09	1.95479e-09
17.0	1.00	1.32184e-08	2.96705e-09	1.17735e-09
19.0	1.00	1.40508e-09	1.00846e-09	2.2868e-10

Table 50: The data table for 0-5% centrality binned direct photon invariant yield in Au+Au at $\sqrt{s_{NN}} = 200$ GeV from [151].

p_T [GeV/c]	δp_T [GeV/c]	Inv. Yield [GeV $^{-2}$ c 2]	stat. error	sys. error
4.25	0.25	7.66858e-05	1.48594e-06	9.78811e-06
4.75	0.25	3.88705e-05	8.82305e-07	4.65519e-06
5.25	0.25	2.08984e-05	5.54484e-07	2.35914e-06
5.75	0.25	1.17278e-05	3.61419e-07	1.24133e-06
6.25	0.25	7.09631e-06	2.47076e-07	7.10095e-07
6.75	0.25	4.52354e-06	1.75644e-07	4.3033e-07
7.25	0.25	2.87252e-06	1.27089e-07	2.67933e-07
7.75	0.25	1.8289e-06	9.15946e-08	1.6685e-07
8.25	0.25	1.27362e-06	6.97623e-08	1.13217e-07
8.75	0.25	7.76441e-07	4.99626e-08	6.98159e-08
9.25	0.25	6.64047e-07	4.39702e-08	5.85468e-08
9.75	0.25	4.32546e-07	3.43591e-08	3.85014e-08
11.0	1.00	1.72682e-07	1.19268e-08	1.48453e-08
13.0	1.00	7.12815e-08	6.59493e-09	6.13045e-09
15.0	1.00	2.04322e-08	2.83537e-09	1.9797e-09
17.0	1.00	7.56549e-09	2.19236e-09	7.06729e-10

Table 51: The data table for 5-10% centrality binned direct photon invariant yield in Au+Au at $\sqrt{s_{NN}} = 200$ GeV from [151].

p_T [GeV/c]	δp_T [GeV/c]	Inv. Yield [GeV $^{-2}$ c 2]	stat. error	sys. error
4.25	0.25	6.28528e-05	1.39305e-06	9.49766e-06
4.75	0.25	3.33525e-05	8.1875e-07	4.4554e-06
5.25	0.25	1.6183e-05	5.15954e-07	2.2243e-06
5.75	0.25	9.5348e-06	3.36085e-07	1.16367e-06
6.25	0.25	5.47867e-06	2.25907e-07	6.42743e-07
6.75	0.25	3.73572e-06	1.62582e-07	3.91199e-07
7.25	0.25	2.45665e-06	1.19735e-07	2.46295e-07
7.75	0.25	1.52844e-06	8.55338e-08	1.51147e-07
8.25	0.25	1.03702e-06	6.40454e-08	9.86335e-08
8.75	0.25	7.14338e-07	4.75651e-08	6.23233e-08
9.25	0.25	5.19401e-07	3.97804e-08	5.03585e-08
9.75	0.25	4.01509e-07	3.30788e-08	3.74842e-08
11.0	1.00	1.36873e-07	1.10376e-08	1.26538e-08
13.0	1.00	4.42117e-08	5.46094e-09	4.3288e-09
15.0	1.00	1.75484e-08	2.96093e-09	1.53246e-09
17.0	1.00	7.4544e-09	2.00331e-09	6.911e-10

Table 52: The data table for 10-15% centrality binned direct photon invariant yield in Au+Au at $\sqrt{s_{NN}} = 200$ GeV from [151].

p_T [GeV/c]	δp_T [GeV/c]	Inv. Yield [GeV $^{-2}$ c 2]	stat. error	sys. error
4.25	0.25	4.45373e-05	1.22006e-06	6.96911e-06
4.75	0.25	2.32439e-05	7.26442e-07	3.44847e-06
5.25	0.25	1.2883e-05	4.53074e-07	1.79457e-06
5.75	0.25	7.37365e-06	2.92545e-07	9.59495e-07
6.25	0.25	3.98987e-06	1.80917e-07	4.8499e-07
6.75	0.25	2.9025e-06	1.38625e-07	3.26481e-07
7.25	0.25	1.69987e-06	9.15359e-08	1.84079e-07
7.75	0.25	1.18828e-06	7.07613e-08	1.24759e-07
8.25	0.25	7.86036e-07	5.30156e-08	8.15658e-08
8.75	0.25	6.47622e-07	4.51108e-08	6.36648e-08
9.25	0.25	4.14053e-07	3.19705e-08	4.19296e-08
9.75	0.25	2.53339e-07	2.47409e-08	2.69507e-08
11.0	1.00	1.15775e-07	9.53894e-09	1.09099e-08
13.0	1.00	4.8379e-08	5.50433e-09	4.52241e-09
15.0	1.00	1.60957e-08	2.84193e-09	1.64319e-09
17.0	1.00	5.18422e-09	1.80625e-09	5.14353e-10

Table 53: The data table for 15-20% centrality binned direct photon invariant yield in Au+Au at $\sqrt{s_{NN}} = 200$ GeV from [151].

p_T [GeV/c]	δp_T [GeV/c]	Inv. Yield [GeV $^{-2}$ c 2]	stat. error	sys. error
4.25	0.25	3.46394e-05	8.53671e-07	6.07928e-06
4.75	0.25	1.69732e-05	4.97669e-07	2.82796e-06
5.25	0.25	9.00084e-06	3.05573e-07	1.415e-06
5.75	0.25	5.06519e-06	1.96963e-07	7.60167e-07
6.25	0.25	3.32498e-06	1.35377e-07	4.48527e-07
6.75	0.25	2.02399e-06	9.16576e-08	2.53446e-07
7.25	0.25	1.43337e-06	6.77395e-08	1.62912e-07
7.75	0.25	7.93705e-07	4.54546e-08	9.30628e-08
8.25	0.25	5.48496e-07	3.62092e-08	6.38647e-08
8.75	0.25	3.44139e-07	2.40442e-08	3.83038e-08
9.25	0.25	2.62537e-07	2.13504e-08	2.92942e-08
9.75	0.25	1.88953e-07	1.57911e-08	2.04244e-08
11.0	1.00	9.21147e-08	6.35004e-09	9.06303e-09
13.0	1.00	2.40771e-08	2.71582e-09	2.45799e-09
15.0	1.00	9.58996e-09	1.62042e-09	9.84859e-10
17.0	1.00	4.06645e-09	1.11433e-09	4.19356e-10

Table 54: The data table for 20-30% centrality binned direct photon invariant yield in Au+Au at $\sqrt{s_{NN}} = 200$ GeV from [151].

p_T [GeV/c]	δp_T [GeV/c]	Inv. Yield [GeV $^{-2}$ c 2]	stat. error	sys. error
4.25	0.25	2.12037e-05	6.82959e-07	4.16323e-06
4.75	0.25	1.0309e-05	3.92972e-07	1.94061e-06
5.25	0.25	5.38349e-06	2.32228e-07	9.34297e-07
5.75	0.25	3.48093e-06	1.55433e-07	5.48261e-07
6.25	0.25	1.95874e-06	9.82211e-08	2.8673e-07
6.75	0.25	1.19183e-06	6.60515e-08	1.64963e-07
7.25	0.25	7.3781e-07	4.54547e-08	9.82336e-08
7.75	0.25	5.21498e-07	3.66729e-08	6.88873e-08
8.25	0.25	3.04829e-07	2.5189e-08	4.11188e-08
8.75	0.25	2.05469e-07	1.87424e-08	2.72173e-08
9.25	0.25	1.86589e-07	1.58522e-08	2.16718e-08
9.75	0.25	1.37474e-07	1.32118e-08	1.60122e-08
11.0	1.00	5.85428e-08	5.07133e-09	6.22987e-09
13.0	1.00	1.70608e-08	2.49448e-09	1.75424e-09
15.0	1.00	2.71386e-09	9.26231e-10	4.85289e-10
17.0	1.00	3.3607e-09	9.63855e-10	3.65587e-10

Table 55: The data table for 30-40% centrality binned direct photon invariant yield in Au+Au at $\sqrt{s_{NN}} = 200$ GeV from [151].

p_T [GeV/c]	δp_T [GeV/c]	Inv. Yield [GeV $^{-2}$ c 2]	stat. error	sys. error
4.25	0.25	1.21646e-05	5.13252e-07	2.58363e-06
4.75	0.25	5.15193e-06	2.62342e-07	1.03381e-06
5.25	0.25	2.91477e-06	1.62094e-07	5.63155e-07
5.75	0.25	1.85243e-06	1.08675e-07	3.32143e-07
6.25	0.25	9.87378e-07	6.19445e-08	1.61107e-07
6.75	0.25	6.61613e-07	4.81838e-08	1.09481e-07
7.25	0.25	3.71109e-07	3.07966e-08	6.04011e-08
7.75	0.25	3.04036e-07	2.47586e-08	4.34567e-08
8.25	0.25	2.01695e-07	1.76078e-08	2.73726e-08
8.75	0.25	1.34564e-07	1.30854e-08	1.80047e-08
9.25	0.25	1.02416e-07	1.07832e-08	1.34865e-08
9.75	0.25	7.33905e-08	8.95641e-09	9.88662e-09
11.0	1.00	2.93353e-08	3.1114e-09	3.43701e-09
13.0	1.00	1.41389e-08	2.19254e-09	1.49375e-09
15.0	1.00	4.83388e-09	1.04094e-09	5.95905e-10

Table 56: The data table for 40-50% centrality binned direct photon invariant yield in Au+Au at $\sqrt{s_{NN}} = 200$ GeV from [151].

p_T [GeV/c]	δp_T [GeV/c]	Inv. Yield [GeV $^{-2}$ c 2]	stat. error	sys. error
4.25	0.25	3.89983e-06	2.38787e-07	8.982e-07
4.75	0.25	1.7624e-06	1.24723e-07	4.03866e-07
5.25	0.25	1.04854e-06	7.99737e-08	2.33108e-07
5.75	0.25	6.51204e-07	5.10421e-08	1.33572e-07
6.25	0.25	4.93095e-07	4.12218e-08	9.79837e-08
6.75	0.25	3.14902e-07	2.7141e-08	5.67833e-08
7.25	0.25	1.73194e-07	1.76744e-08	3.14917e-08
7.75	0.25	1.3582e-07	1.56215e-08	2.4501e-08
8.25	0.25	9.51495e-08	1.25248e-08	1.71595e-08
8.75	0.25	5.74914e-08	9.66547e-09	1.14876e-08
9.25	0.25	3.01671e-08	7.05211e-09	6.96739e-09
9.75	0.25	3.0439e-08	5.35387e-09	4.71519e-09
11.0	1.00	1.50293e-08	2.69105e-09	1.94994e-09
13.0	1.00	4.49946e-09	1.18698e-09	6.14329e-10
15.0	1.00	1.51949e-09	6.73752e-10	2.15139e-10

Table 57: The data table for 50-60% centrality binned direct photon invariant yield in Au+Au at $\sqrt{s_{NN}} = 200$ GeV from [151].

p_T [GeV/c]	δp_T [GeV/c]	Inv. Yield [GeV $^{-2}$ c 2]	stat. error	sys. error
4.25	0.25	4.46963e-07	3.49445e-08	1.135e-07
4.75	0.25	4.2342e-07	3.48975e-08	1.0612e-07
5.25	0.25	2.71855e-07	2.29255e-08	6.32866e-08
5.75	0.25	1.78894e-07	1.58339e-08	3.90637e-08
6.25	0.25	1.07392e-07	1.11953e-08	2.35367e-08
6.75	0.25	8.91867e-08	9.2992e-09	1.68618e-08
7.25	0.25	4.38758e-08	6.10301e-09	9.32671e-09
7.75	0.25	3.03131e-08	4.28895e-09	5.86636e-09
8.25	0.25	1.75572e-08	3.55333e-09	3.92924e-09
8.75	0.25	1.19083e-08	2.83409e-09	3.0365e-09
9.25	0.25	7.92141e-09	2.11595e-09	1.60848e-09
9.75	0.25	7.45956e-09	1.83994e-09	1.38181e-09
11.0	1.00	3.6448e-09	7.56859e-10	4.75681e-10
13.0	1.00	4.16854e-10	3.71647e-10	1.20631e-10

Table 58: The data table for 60-92% centrality binned direct photon invariant yield in Au+Au at $\sqrt{s_{NN}} = 200$ GeV from [151].

p_T [GeV/c]	δp_T [GeV/c]	Inv. Yield [GeV $^{-2}$ c 2]	stat. error	sys. error
4.25	0.25	2.37835e-05	2.19677e-07	2.96213e-06
4.75	0.25	1.2078e-05	1.3158e-07	1.41102e-06
5.25	0.25	6.25418e-06	8.42344e-08	6.97981e-07
5.75	0.25	3.67097e-06	5.69567e-08	3.88451e-07
6.25	0.25	2.22912e-06	3.98972e-08	2.2556e-07
6.75	0.25	1.42338e-06	2.90466e-08	1.37362e-07
7.25	0.25	8.97382e-07	2.11727e-08	8.44308e-08
7.75	0.25	5.92454e-07	1.58539e-08	5.47688e-08
8.25	0.25	3.97668e-07	1.20151e-08	3.58027e-08
8.75	0.25	2.72478e-07	9.32689e-09	2.39246e-08
9.25	0.25	1.99436e-07	7.50916e-09	1.69442e-08
9.75	0.25	1.41081e-07	5.94224e-09	1.1835e-08
11.0	1.00	5.92193e-08	1.93299e-09	5.10856e-09
13.0	1.00	1.98351e-08	9.75672e-10	1.6495e-09
15.0	1.00	6.72473e-09	4.87442e-10	5.57649e-10
17.0	1.00	2.86982e-09	3.11581e-10	2.58077e-10
19.0	1.00	1.10198e-09	1.76465e-10	1.33886e-10
21.0	1.00	3.99786e-10	1.44796e-10	1.33955e-10

Table 59: The data table for 0-92% centrality binned direct photon invariant yield in Au+Au at $\sqrt{s_{NN}} = 200$ GeV from [151].

p_T [GeV/c]	δp_T [GeV/c]	Inv. Cross Sec. [pb GeV $^{-2}$ c 3]	stat. error	sys. error
5.37	0.50	130.0e-09	80.0e-09	70.0e-09
6.39	0.50	15.0e-09	10.0e-09	14.0e-09
7.40	0.50	4.3e-09	1.1e-09	3.5e-09
8.41	0.50	1.9e-09	0.5e-09	1.0e-09
9.42	0.50	0.53e-09	0.16e-09	0.31e-09
10.43	0.50	0.40e-09	0.10e-09	0.11e-09
11.44	0.50	0.24e-09	0.06e-09	0.04e-09
12.44	0.50	0.11e-09	0.04e-09	0.02e-09

Table 60: The data table for direct photon invariant cross section in p+p at $\sqrt{s_{NN}} = 62.4$ GeV from [154, 157].

p_T [GeV/c]	δp_T [GeV/c]	Inv. Cross Sec. [pb GeV $^{-2}$ c 3]	stat. error	sys. error
5.22	0.25	141.0e-09	42.0e-09	21.15e-09
5.72	0.25	65.6e-09	24.2e-09	9.84e-09
6.23	0.25	39.4e-09	6.30e-09	5.91e-09
6.73	0.25	19.6e-09	6.10e-09	3.724e-09
7.42	0.50	7.21e-09	2.72e-09	1.37e-09

Table 61: The data table for direct photon invariant cross section in p+p at $\sqrt{s_{NN}} = 63$ GeV from [155, 157].

p_T [GeV/c]	δp_T [GeV/c]	Inv. Cross Sec. [pb GeV $^{-2}$ c 3]	combined stat. and sys. errors
5.25	0.25	122.0e-09	27.0e-09
5.73	0.25	59.6e-09	12.2e-09
6.23	0.25	32.0e-09	6.3e-09
6.74	0.25	18.7e-09	3.5e-09
7.23	0.25	9.1e-09	1.8e-09
7.72	0.25	6.2e-09	1.26e-09
8.22	0.25	3.81e-09	0.86e-09
8.74	0.50	2.54e-09	0.63e-09
9.44	0.50	1.26e-09	0.32e-09
10.36	0.50	0.605e-09	0.192e-09

Table 62: The data table for direct photon invariant cross section in p+p at $\sqrt{s_{NN}} = 63$ GeV from [156, 157].

15.4 Direct photon scaling (integrated yield) data tables

System	$dN_{ch}/d\eta$	Int. Yield (dN_γ/dy)	stat. error	sys. error
Pb+Pb 0-20% 2760 GeV [45]	1206.75 ± 45.750	3.43473	0.309451	1.41208
Au+Au 0-20% 200 GeV [42]	519.025 ± 26.250	1.25393	0.194687	0.4303885
Au+Au 20-40% 200 GeV [42]	225.425 ± 13.175	0.549455	0.0830612	0.1983059
Au+Au 40-60% 200 GeV [42]	85.475 ± 8.075	0.17673	0.0316599	0.0752544
Au+Au 60-92% 200 GeV [42]	16.362 ± 2.814	0.0179668	0.00589737	0.0122169
Au+Au 0-20% 200 GeV [40]	519.025 ± 26.250	1.40633	0.22667	0.310458
Au+Au 20-40% 200 GeV [40]	225.425 ± 13.175	0.576294	0.0834426	0.120942
Au+Au 0-92% 200 GeV [40]	186.11 ± 11.324	0.454133	0.0493879	0.096457
Au+Au 0-20% 62.4 GeV	341.175 ± 29.325	0.9667	0.251362	0.338253
Au+Au 20-40% 62.4 GeV	151.750 ± 12.690	0.357752	0.112394	0.182407
Au+Au 0-86% 62.4 GeV	131.525 ± 11.152	0.259011	0.061689	0.130462
Au+Au 0-86% 39 GeV	104.264 ± 8.882	0.246498	0.108381	0.1869953
Cu+Cu 0-40% 200 GeV [44]	109.263 ± 7.813	0.136318	0.0603598	0.0550699
Cu+Cu 0-94% 200 GeV [44]	51.654 ± 3.559	0.0552561	0.0213829	0.0228763
p+p 200 GeV [153]	2.38 ± 0.17	0.000122499	6.2397e-05	0.000177912

Table 63: The data table for the integrated yield, ($1.0 \text{ GeV/c} < p_T < 1.5 \text{ GeV/c}$, Fig. (119)), all shown in Tables 33, 34, 35, 36, 37, 38, 39, 40, 41, 42, 43, 44, 45, 46, 49.

System	$dN_{ch}/d\eta$	Int. Yield (dN_γ/dy)	stat. error	sys. error
Pb+Pb 0-20% 2760 GeV [45]	1206.75 ± 45.750	4.75876	0.316777	1.8749
Au+Au 0-20% 200 GeV [42]	519.025 ± 26.250	1.66115	0.202514	0.5339347
Au+Au 20-40% 200 GeV [42]	225.425 ± 13.175	0.707725	0.0863305	0.2478384
Au+Au 40-60% 200 GeV [42]	85.475 ± 8.075	0.217113	0.0329216	0.0936435
Au+Au 60-92% 200 GeV [42]	16.362 ± 2.814	0.0229508	0.00620148	0.01547068
Au+Au 0-20% 200 GeV [40]	519.025 ± 26.250	1.68592	0.231152	0.37753
Au+Au 20-40% 200 GeV [40]	225.425 ± 13.175	0.698072	0.0854467	0.149428
Au+Au 0-92% 200 GeV [40]	186.11 ± 11.324	0.554999	0.050432	0.117674
Au+Au 0-20% 62.4 GeV	341.175 ± 29.325	1.28873	0.271747	0.452504
Au+Au 20-40% 62.4 GeV	151.750 ± 12.690	0.415701	0.115494	0.210051
Au+Au 0-86% 62.4 GeV	131.525 ± 11.152	0.336163	0.0652705	0.172416
Au+Au 0-86% 39 GeV	104.264 ± 8.882	0.259703	0.110752	0.2140941
Cu+Cu 0-40% 200 GeV [44]	109.263 ± 7.813	0.196037	0.061724	0.0679816
Cu+Cu 0-94% 200 GeV [44]	51.654 ± 3.559	0.0767671	0.0218601	0.0265065
p+p 200 GeV [153]	2.38 ± 0.17	0.00022102	0.00006565	0.00022898

Table 64: The data table for the integrated yield, ($p_T > 1.0 \text{ GeV/c}$, Fig. (120)), all shown in Tables 33, 34, 35, 36, 37, 38, 39, 40, 41, 42, 43, 44, 45, 46, 49.

System	$dN_{ch}/d\eta$	Int. Yield (dN_γ/dy)	stat. error	sys. error
Pb+Pb 0-20% 2760 GeV [45]	1206.75 ± 45.750	1.32403	0.06773	0.46282
Pb+Pb 20-40% 2760 GeV [45]	537.50 ± 19.00	0.432949	0.027346	0.202246
Au+Au 0-20% 200 GeV [42]	519.025 ± 26.250	0.410514	0.0445818	0.1045702
Au+Au 20-40% 200 GeV [42]	225.425 ± 13.175	0.158227	0.0183634	0.0495187
Au+Au 40-60% 200 GeV [42]	85.475 ± 8.075	0.041134	0.00721706	0.0186967
Au+Au 60-92% 200 GeV [42]	16.362 ± 2.814	0.00502646	0.00156284	0.003286214
Au+Au 0-20% 200 GeV [40]	519.025 ± 26.250	0.279587	0.0453434	0.0670718
Au+Au 20-40% 200 GeV [40]	225.425 ± 13.175	0.121778	0.0183977	0.0284861
Au+Au 0-92% 200 GeV [40]	186.11 ± 11.324	0.100866	0.0102093	0.0212172
Au+Au 0-20% 62.4 GeV	341.175 ± 29.325	0.322118	0.103213	0.114251
Au+Au 0-86% 62.4 GeV	131.525 ± 11.152	0.0771521	0.0213238	0.0419544
Cu+Cu 0-40% 200 GeV [44]	109.263 ± 7.813	0.0597191	0.0129053	0.0129118
Cu+Cu 0-94% 200 GeV [44]	51.654 ± 3.559	0.021511	0.00454284	0.00363019
p+p 200 GeV [153]	2.38 ± 0.17	9.85144e-05	2.04277e-05	5.10682e-05

Table 65: The data table for the integrated yield, ($p_T > 1.5 \text{ GeV/c}$, Fig. (121)), all shown in Tables 33, 35, 37, 38, 39, 40, 41, 42, 43, 44, 45, 46, 47, 49.

System	$dN_{ch}/d\eta$	Int. Yield (dN_γ/dy)	stat. error	sys. error
Pb+Pb 0-20% 2760 GeV [45]	1206.75 ± 45.750	0.47253	0.016425	0.137683
Pb+Pb 20-40% 2760 GeV [45]	537.50 ± 19.00	0.18485	0.00713615	0.0623732
Pb+Pb 40-80% 2760 GeV [45]	130.25 ± 5.25	0.028229	0.00188865	0.0168614
Au+Au 0-20% 200 GeV [42]	519.025 ± 26.250	0.095896	0.0174649	0.0244592
Au+Au 20-40% 200 GeV [42]	225.425 ± 13.175	0.0491005	0.00809309	0.0128995
Au+Au 40-60% 200 GeV [42]	85.475 ± 8.075	0.00965084	0.00320873	0.00496369
Au+Au 60-92% 200 GeV [42]	16.362 ± 2.814	0.00113244	0.000653216	0.000802995
Au+Au 0-20% 200 GeV [40]	519.025 ± 26.250	0.0604352	0.0137472	0.0157099
Au+Au 20-40% 200 GeV [40]	225.425 ± 13.175	0.023697	0.00623442	0.00708956
Au+Au 0-92% 200 GeV [40]	186.11 ± 11.324	0.0229249	0.0032548	0.00570673
p+p 200 GeV [153]	2.38 ± 0.17	3.36123e-05	5.6071e-06	1.45755e-05

Table 66: The data table for the integrated yield, ($p_T > 2.0 \text{ GeV/c}$, Fig. (122)), all shown in Tables ,37, 38, 39, 40, 41, 42, 43, 46, 47, 48, 49.

References

- [1] W. Greiner, S. Schramm and E. Stein, “Quantum Chromodynamics”, Springer (2007). 1

System	$dN_{ch}/d\eta$	Int. Yield (dN_γ/dy)	stat. error	sys. error
Pb+Pb 0-20% 2760 GeV [45]	1206.75 ± 45.750	0.0119517	0.000595667	0.00236721
Pb+Pb 20-40% 2760 GeV [45]	537.50 ± 19.00	0.00631369	0.000419745	0.00115739
Pb+Pb 40-80% 2760 GeV [45]	130.25 ± 5.25	0.000976442	0.000128046	0.000278493
Au+Au 0-5% 200 GeV [151]	687.40 ± 36.59	0.0012647	1.55721e-05	0.000123449
Au+Au 5-10% 200 GeV [151]	560.4 ± 27.9	0.00091461	1.35041e-05	9.59367e-05
Au+Au 10-15% 200 GeV [151]	456.8 ± 22.3	0.000729335	1.25391e-05	8.9194e-05
Au+Au 15-20% 200 GeV [151]	371.5 ± 18.2	0.00056078	1.0753e-05	7.15915e-05
Au+Au 20-30% 200 GeV [151]	274.05 ± 14.80	0.000405796	7.35546e-06	5.80569e-05
Au+Au 30-40% 200 GeV [151]	176.80 ± 11.55	0.000248418	5.57067e-06	3.89176e-05
Au+Au 40-50% 200 GeV [151]	109.4 ± 9.1	0.000132576	3.84692e-06	2.3526e-05
Au+Au 50-60% 200 GeV [151]	61.55 ± 7.05	5.32919e-05	1.9954e-06	1.08283e-05
Au+Au 60-92% 200 GeV [151]	16.362 ± 2.814	1.35833e-05	5.90936e-07	2.95321e-06
p+p 200 GeV [153]	2.38 ± 0.17	1.14424e-06	1.69318e-08	3.9498e-07
p+p 62.4 GeV [154, 157]	1.864	1.33713e-07	7.0062e-08	7.9729e-08
p+p 63 GeV [155, 157]	1.864	1.38423e-07	2.32531e-08	2.15911e-08

Table 67: The data table for the integrated yield, ($5.0 \text{ GeV/c} < p_T < 8.0 \text{ GeV/c}$, Fig. (123)), all shown in Tables 46, 47, 48, 50, 51, 52, 53, 54, 55, 56, 57, 58, 49, 60, 61.

System	$dN_{ch}/d\eta$	Int. Yield (dN_γ/dy)	stat. error	sys. error
Pb+Pb 0-20% 2760 GeV [45]	1206.75 ± 45.750	0.015055	0.00067547	0.00304361
Pb+Pb 20-40% 2760 GeV [45]	537.50 ± 19.00	0.00779719	0.000477406	0.00146635
Pb+Pb 40-80% 2760 GeV [45]	130.25 ± 5.25	0.00115644	0.000150377	0.000360317
Au+Au 0-5% 200 GeV [151]	687.40 ± 36.59	0.00143165	1.61525e-05	0.000137183
Au+Au 5-10% 200 GeV [151]	560.4 ± 27.9	0.00103968	1.3954e-05	0.000106954
Au+Au 10-15% 200 GeV [151]	456.8 ± 22.3	0.000831428	1.29484e-05	9.87226e-05
Au+Au 15-20% 200 GeV [151]	371.5 ± 18.2	0.000644358	1.11083e-05	7.99094e-05,
Au+Au 20-30% 200 GeV [151]	274.05 ± 14.80	0.000460806	7.56005e-06	6.40234e-05
Au+Au 30-40% 200 GeV [151]	176.80 ± 11.55	0.00028329	5.73184e-06	4.30884e-05
Au+Au 40-50% 200 GeV [151]	109.4 ± 9.1	0.00015353	3.95786e-06	2.61958e-05
Au+Au 50-60% 200 GeV [151]	61.55 ± 7.05	6.21368e-05	2.10334e-06	1.23307e-05
Au+Au 60-92% 200 GeV [151]	16.362 ± 2.814	1.54268e-05	6.21928e-07	3.31787e-06
p+p 200 GeV [153]	2.38 ± 0.17	1.30325e-06	1.75546e-08	4.30564e-07
p+p 62.4 GeV [154, 157]	1.864	1.38699e-07	7.00663e-08	8.19705e-08

Table 68: The data table for the integrated yield, ($p_T > 5.0 \text{ GeV/c}$, Fig. (124)), all shown in Tables 46, 47, 48, 50, 51, 52, 53, 54, 55, 56, 57, 58, 49, 60.

System	$dN_{ch}/d\eta$	Int. Yield (dN_γ/dy)	stat. error	sys. error
Pb+Pb 0-20% 2760 GeV [45]	1206.75 ± 45.750	0.00310335	0.000318496	0.000676405
Pb+Pb 20-40% 2760 GeV [45]	537.50 ± 19.00	0.0014835	0.000227444	0.000308967
Pb+Pb 40-80% 2760 GeV [45]	130.25 ± 5.25	0.000180003	7.88521e-05	8.18241e-05
Au+Au 0-5% 200 GeV [151]	687.40 ± 36.59	0.000166958	4.29119e-06	1.37345e-05
Au+Au 5-10% 200 GeV [151]	560.4 ± 27.9	0.000125065	3.51471e-06	1.10173e-05
Au+Au 10-15% 200 GeV [151]	456.8 ± 22.3	0.000102093	3.22964e-06	9.5286e-06
Au+Au 15-20% 200 GeV [151]	371.5 ± 18.2	8.35779e-05	2.78715e-06	8.31792e-06
Au+Au 20-30% 200 GeV [151]	274.05 ± 14.80	5.50097e-05	1.7469e-06	5.96654e-06
Au+Au 30-40% 200 GeV [151]	176.80 ± 11.55	3.48722e-05	1.34975e-06	4.17074e-06
Au+Au 40-50% 200 GeV [151]	109.4 ± 9.1	2.09539e-05	9.30504e-07	2.66987e-06
Au+Au 50-60% 200 GeV [151]	61.55 ± 7.05	8.84494e-06	6.65168e-07	1.50235e-06
Au+Au 60-92% 200 GeV [151]	16.362 ± 2.814	1.8435e-06	1.9388e-07	3.64665e-07
p+p 200 GeV [153]	2.38 ± 0.17	1.5901e-07	3.54158e-09	2.95532e-08
p+p 62.4 GeV [154, 157]	1.864	4.98528e-09	7.91149e-10	2.24076e-09

Table 69: The data table for the integrated yield, ($p_T > 8.0$ GeV/c, Fig. (125)), all shown in Tables 46, 47, 48, 50, 51, 52, 53, 54, 55, 56, 57, 58, 49, 60.

System	N_{coll}
Pb+Pb 0-20% 2760 GeV [45, 147]	1210.85
Pb+Pb 20-40% 2760 GeV [45, 147]	438.40
Pb+Pb 40-60% 2760 GeV [45, 147]	127.70
Pb+Pb 60-80% 2760 GeV [45, 147]	26.71
Au+Au 0-20% 200 GeV [145, 146]	770.6
Au+Au 20-40% 200 GeV [145, 146]	282.4
Au+Au 40-60% 200 GeV [145, 146]	82.6
Au+Au 60-92% 200 GeV [145, 146]	12.1
Au+Au 0-92% 200 GeV [145, 146]	251.1
Au+Au 0-20% 62.4 GeV [145, 148]	656.59
Au+Au 20-40% 62.4 GeV [145, 148]	241.10
Au+Au 40-60% 62.4 GeV [145, 148]	70.69
Au+Au 60-86% 62.4 GeV [145, 148]	10.87
Au+Au 0-86% 62.4 GeV [145, 148]	228.50
Au+Au 0-86% 39 GeV [145, 148]	228.35

Table 70: The data table for the N_{coll} values used to obtain the model and pQCD calculations describing the N_{coll} scaled prompt photons, shown for example in Fig. (114), Fig. (120) and Fig. (124). No errors are shown.

- [2] T. Muta, ‘‘Foundation of Quantum Chromodynamics: an Introduction to Perturbative Methods in Gauge Theories’’, World Scientific Lecture Notes in Physics - Vol. 57, World Scientific Publishing Company (1998). 1
- [3] G. Dissertori, I. Knowles and M. Schmelling, ‘‘Quantum Chromodynamics: High Energy Experiments and Theory’’, International Series of Monographs on Physics • 115, Oxford Science Publications (2007). 1
- [4] D. Griffiths, ‘‘Introduction to Elementary Particles’’, Wiley-VCH (2008). 1
- [5] C. Patrignani *et al.* (Particle Data Group), ‘‘The Review of Particle Physics’’, Chin. Phys. C **40**, 100001 (2016). 2
- [6] B. Siegfried, Prog. Part. Nucl. Phys. **58**, 351 (2007). x, 7
- [7] M. G. Alford, A. Schmitt, K. Rajagopal and T. Schafer, Rev. Mod. Phys. **80**, 1455 (2008). x, 9
- [8] T. Csorgo, *Contributed to 5th International Workshop on Critical Point Conference*, PoS CPOD2009, 035 (2009) [arXiv:0911.5015 [nucl-th]]. x, 9
- [9] L. V. Gribov, E. M. Levin and M. G. Ryskin, Phys. Rept. **100**, 1 (1983); A. H. Mueller and J. W. Qiu, Nucl. Phys. B **268**, 427 (1986). 10
- [10] L. D. McLerran and R. Venugopalan, Phys. Rev. D **49**, 2233 (1994) [arXiv:hep-ph/9309289]; Phys. Rev. D **49**, 3352 (1994) [arXiv:hep-ph/9311205]; Phys. Rev. D **50**, 2225 (1994) [arXiv:hep-ph/9402335]. 10
- [11] A. Ayala, J. Jalilian-Marian, L. D. McLerran and R. Venugopalan, Phys. Rev. D **53**, 458 (1996) [arXiv:hep-ph/9508302]. 10
- [12] E. Iancu, A. Leonidov and L. McLerran, Nucl. Phys. A **692**, 583 (2001) [arXiv:hep-ph/0011241]. 10
- [13] E. Ferreiro, E. Iancu, A. Leonidov and L. McLerran, Nucl. Phys. A **703**, 489 (2002) [arXiv:hep-ph/0109115]. 10
- [14] E. Iancu and R. Venugopalan, In *Hwa, R.C. (ed.) et al.: Quark gluon plasma* 249-3363, (2003) [arXiv:hep-ph/0303204]; R. Venugopalan, Lectures given at Conference: C04-08-29.2, C04-06-22.2, C04-06-01.2, (2004) [arXiv:hep-ph/0412396]. 10
- [15] F. Gelis, T. Lappi and R. Venugopalan, Int. J. Mod. Phys. E **16**, 2595 (2007) [arXiv:0708.0047 [hep-ph]]. 10

- [16] F. Gelis, E. Iancu, J. Jalilian-Marian and R. Venugopalan, Ann. Rev. Nucl. Part. Sci. **60**, 463 (2010) [arXiv:1002.0333 [hep-ph]]. 10
- [17] F. Gelis, Int. J. Mod. Phys. A **28**, 1330001 (2013) [arXiv:1211.3327 [hep-ph]]. 10, 14
- [18] F. D. Aaron *et al.* [H1 and ZEUS Collaborations], JHEP **1001**, 109 (2010). x, 11, 12
- [19] CMS Collaboration, Phys. Lett. B **718**, 795 (2013) [arXiv:1210.5482 [nucl-ex]]. 14
- [20] CMS Collaboration, J. High Energy Phys. **09**, 091 (2010). 14
- [21] T. Lappi and L. McLerran, Nucl. Phys. A **772**, 200 (2006) [arXiv:hep-ph/0602189]. 14
- [22] L. McLerran, Prog. Theor. Phys. Suppl., 17 (2011) [arXiv:1011.3204 [hep-ph]]; Phys. Part. Nucl. Lett. **8**, 673 (2011); AIP Conf. Proc. **917**, 219 (2007). 14
- [23] F. Gelis, T. Lappi and L. McLerran, Nucl. Phys. A **828**, 149 (2009) [arXiv:0905.3234 [hep-ph]]. 14
- [24] A. Dumitru, F. Gelis, L. McLerran and R. Venugopalan, Nucl. Phys. A **810**, 91 (2008) [arXiv:0804.3858 [hep-ph]]. 15
- [25] K. Werner, I. Karpenko, T. Pierog, M. Bleicher and K. Mikhailov, Phys. Rev. C **82**, 044904 (2010) [arXiv:1004.0805 [nucl-th]]. 15
- [26] R. Baier, A. H. Mueller, D. Schiff and D. T. Son, Phys. Lett. B **502**, 51 (2001) [arXiv:hep-ph/0009237]. 16, 37
- [27] R. Baier, A. H. Mueller, D. Schiff and D. T. Son, Phys. Lett. **B539**, 46 (2002) [arXiv:hep-ph/0204211]; [arXiv:1103.1259 [nucl-th]]. x, 16, 17, 18, 37
- [28] J. Berges, K. Boguslavski, S. Schlichting and R. Venugopalan, Phys. Rev. D **89**, 074011 (2014) [arXiv:1303.5650 [hep-ph]]. 16, 35
- [29] J. Berges, K. Boguslavski, S. Schlichting and R. Venugopalan, Phys. Rev. D **89**, 114007 (2014) [arXiv:1311.3005 [hep-ph]]. 16, 35
- [30] J. Berges, K. Boguslavski, S. Schlichting and R. Venugopalan, JHEP **1405**, 054 (2014) [arXiv:1312.5216 [hep-ph]]. 16
- [31] J. Berges, B. Schenke, S. Schlichting, and R. Venugopalan, Nucl. Phys. A **931**, 348 (2014) [arXiv:1409.1638 [hep-ph]]. 16

- [32] J. Letessier and J. Rafelski, “Hadrons and Quark–Gluon Plasma”, Cambridge University Press (2002). 18
- [33] K. Yagi, T. Hatsuda and Y. Miake, “Quark-Gluon Plasma: From Big Bang to Little Bang”, Cambridge University Press (2008). 18
- [34] Yu. L. Dokshitzer, V. A. Khoze, A. H. Mueller and S. I. Troyan, “Basics of Perturbative QCD”, Editions Frontieres (1991). 20
- [35] P. Braun-Munzinger, D. Magestro, K. Redlich, and J. Stachel, Phys. Lett. B **518**, 41 (2001). 20
- [36] A. Andronic, P. Braun-Munzinger and J. Stachel, Nucl. Phys. A **772**, 167 (2006). 20
- [37] P. F. Kolb, J. Sollfrank and U. W. Heinz, Phys. Rev. C **62**, 054909 (2000). 20
- [38] A. Chodos, R. L. Jaffe, K. Johnson and C. B. Thorne, Phys. Rev. D **10**, 2599 (1974). 20
- [39] T. DeGrand, R. L. Jaffe, K. Johnson, J. Kiskis, Phys. Rev. D **12**, 2060 (1975). 20
- [40] A. Adare *et al.* (PHENIX Collaboration), Phys. Rev. Lett. **104**, 132301 (2010) [arXiv:0804.4168 [nucl-ex]]. x, xi, xii, xix, xxx, 22, 26, 30, 32, 40, 43, 44, 142, 201, 212, 213
- [41] A. Adare *et al.* (PHENIX Collaboration), Phys. Rev. C **81**, 034911 (2010) [arXiv:0912.0244 [nucl-ex]]. x, xi, 22, 30, 32, 102, 156
- [42] A. Adare *et al.* (PHENIX Collaboration), Phys. Rev. C **91** 6, 064904 (2015) [arXiv:1405.3940[nucl-ex]]. xi, xii, xix, xx, xxx, 22, 23, 26, 40, 45, 71, 91, 140, 142, 146, 155, 156, 199, 200, 212, 213
- [43] L. Adamczyk *et al.* (STAR Collaboration), Phys. Lett. B **770**, 451 (2017) [arXiv:1607.01447 [nucl-ex]]. 22
- [44] D. Sharma (for the PHENIX Collaboration), *PHENIX measurements of low momentum direct photons from large ion collisions as a function of beam energy and system size*, Quark Matter 2017. xix, xxx, 22, 142, 202, 212, 213
- [45] J. Adam *et al.* (ALICE Collaboration), Phys. Lett. B **754**, 235 (2016) [arXiv:1509.07324 [nucl-ex]]; M. Wilde *et al.* (ALICE Collaboration), Nucl. Phys. A **904-905**, 573 (2013) [arXiv:1210.5958 [hep-ex]]. xi, xii, xix, xxi, xxx, 22, 24, 40, 43, 44, 45, 46, 142, 150, 156, 202, 203, 204, 212, 213, 214, 215

- [46] S. Turbide, C. Gale, E. Frodermann and U. Heinz, Phys. Rev. C **77**, 024909 (2008) [arXiv:0712.0732 [hep-ph]]; S. Turbide, R. Rapp and C. Gale, Phys. Rev. C **69**, 014903 (2004) [arXiv:hep-ph/0308085]. x, 22, 44
- [47] A. Adare *et al.* (PHENIX Collaboration), Phys. Rev. D **86**, 072008 (2012) [arXiv:1205.5533[hep-ex]]. 23
- [48] A. Adare *et al.* (PHENIX Collaboration), Phys. Rev. C **94**, 064901 (2016) [arXiv:1509.07758 [nucl-ex]]; A. Adare *et al.* [PHENIX Collaboration], Phys. Rev.Lett. **109**, 122302 (2012) [arXiv:1105.4126 [nucl-ex]]. xi, xii, xiii, 23, 25, 26, 41, 42, 44, 46
- [49] D. Lohner *et al.* (ALICE Collaboration), J. Phys. Conf. Ser. **446**, 012028 (2013) [arXiv:1212.3995 [hep-ex]]. xi, xii, xiii, 23, 25, 26, 41, 42, 44, 46
- [50] M. Chiu, T. K. Hemmick, V. Khachatryan, A. Leonidov, J. Liao, L. McLerran, Nucl. Phys. A **900**, 16 (2013) [arXiv:1202.3679 [nucl-th]]. xi, 24, 26, 31, 32
- [51] L. McLerran, Acta Phys. Polon. B **45**, 2307 (2014) [arXiv:1411.1548 [hep-ph]]. 24, 26
- [52] L. McLerran and B. Schenke, Nucl. Phys. A **929**, 71 (2014) [arXiv:1403.7462 [hep-ph]]. 24, 26
- [53] C. Klein-Boesing and L. McLerran, Phys. Lett. B **734**, 282 (2014) [arXiv:1403.1174 [nucl-th]]. 24, 26
- [54] J. Berges, K. Reygers, N. Tanji and R. Venugopalan, Phys. Rev. C **95**, 054904 (2017) [arXiv:1701.05064 [nucl-th]]. xii, 24, 33, 38
- [55] K. Dusling and I. Zahed, Phys. Rev. C **82**, 054909 (2010) [arXiv:0911.2426 [nucl-th]]; K. Dusling, “*Hydrodynamic Description of Dilepton Production*”, PhD thesis, Stony Brook University (2008) [arXiv:0901.2027 [nucl-th]]. 24, 37, 39
- [56] C.-H. Lee and I. Zahed, Phys. Rev. C **90**, 025204 (2014) [arXiv:1403.1632 [hep-ph]]. 24, 37, 39
- [57] Y.-M. Kim, C.-H. Lee, D. Teaney and I. Zahed, Phys. Rev. C **96**, 015201 (2017) [arXiv:1610.06213 [nucl-th]]. xii, 24, 37, 40, 42
- [58] H. van Hees, C. Gale, and R. Rapp, Phys. Rev. C **84**, 054906 (2011) [arXiv:1108.2131 [hep-ph]]. 26, 43
- [59] R. Rapp, H. van Hees, M. He, Nucl. Phys. A **931**, 696 (2014) [arXiv:1408.0612 [nucl-th]]. 26, 43

- [60] H. van Hees, M. He, R. Rapp, Nucl. Phys. A **933**, 256 (2015) [arXiv:1404.2846 [nucl-th]]. xii, 26, 41, 43, 44
- [61] M. Dion, J.-F. Paquet, B. Schenke, C. Young, S. Jeon and C. Gale, Phys. Rev. C **84**, 064901 (2011) [arXiv:1109.4405 [hep-ph]]. 26
- [62] C. Shen, U. Heinz, J.-F. Paquet, and C. Gale, Phys. Rev. C **89**, 044910 (2014) [arXiv:1308.2440 [nucl-th]]. 26
- [63] J.-F. Paquet, C. Shen, G. S. Denicol, M. Luzum, B. Schenke, S. Jeon and C. Gale, Phys. Rev. C **93**, 044906 (2016), [arXiv:1509.06738 [hep-ph]]. xii, xiii, 26, 41, 44, 45, 46, 128
- [64] C. Shen, J.-F. Paquet, G. S. Denicol, S. Jeon and C. Gale, Phys. Rev. Lett. **116**, 072301 (2016) [arXiv:1504.07989 [nucl-th]]. 26
- [65] E. L. Bratkovskaya, S. M. Kiselev and G. B. Sharkov, Phys. Rev. C **78**, 034905 (2008) [arXiv:0806.3465 [nucl-th]]. 26
- [66] E. L. Bratkovskaya, Nucl. Phys. A **931**, 194 (2014) [arXiv:1408.3674 [hep-ph]]. 26
- [67] O. Linnyk, W. Cassing, E. Bratkovskaya, Phys. Rev. C **89**, 034908 (2014) [arXiv:1311.0279 [nucl-th]]. 26
- [68] O. Linnyk, V. Konchakovski, T. Steinert, W. Cassing, E. L. Bratkovskaya, Phys. Rev. C **92**, 054914 (2015) [arXiv:1504.05699 [nucl-th]]. 26
- [69] D. K. Srivastava and B. Sinha, Phys. Rev. C **64**, 034902 (2001). 26
- [70] P. Huovinen, P. V. Ruuskanen and S. S. Rasanen, Phys. Lett. B **535**, 109 (2002). 26
- [71] D. d'Enterria and D. Peressounko, Eur. Phy. J. C **46**, 451 (2006) [arXiv:nucl-th/0503054]. 26
- [72] B. Schenke and M. Strickland, Phys. Rev. D **76**, 025023 (2007) [arXiv:hep-ph/0611332]. 26
- [73] J. Alam, J. K. Nayak, P. Roy, A. K. Dutt-Mazumder and B. Sinha, J. Phys. G **34**, 871 (2007) [arXiv:nucl-th/0508043]; J. Alam, S. Sarkar, T. Hatsuda, T. K. Nayak and B. Sinha, Phys. Rev. C **63**, 021901 (2001) [arXiv:hep-ph/0008074]. 26
- [74] F. M. Liu, T. Hirano, K. Werner and Y. Zhu, Phys. Rev. C **79**, 014905 (2009) [arXiv:0807.4771 [hep-ph]]. 26
- [75] R. Chatterjee, H. Holopainen, T. Renk and K. J. Eskola, Phys. Rev. C **83**, 054908 (2011) [arXiv:1102.4706 [hep-ph]]. 26

- [76] G. Basar, D. Kharzeev and V. Skokov, Phys. Rev. Lett. **109**, 202303 (2012) [arXiv:1206.1334 [hep-ph]]. 26
- [77] F.-M. Liu and S.-X. Liu, Phys. Rev. C **89**, 034906 (2014) [arXiv:1212.6587 [nucl-th]]. 26
- [78] S. Campbell, Phys. Rev. C **92**, 014907 (2015) [arXiv:1504.01654 [nucl-ex]]. 26
- [79] C. Shen, J.-F. Paquet, U. Heinz and C. Gale, Phys. Rev. C **91**, 014908 (2015) [arXiv:1410.3404 [nucl-th]]. 26
- [80] M. Heffernan, P. Hohler and R. Rapp, Phys. Rev. C **91**, 027902 (2015) [arXiv:1411.7012 [hep-ph]]. 26, 44
- [81] L. Bhattacharya, R. Ryblewski and M. Strickland, Phys. Rev. D **93**, 065005 (2016) [arXiv:1507.06605 [hep-ph]]. 26
- [82] Y. Hidaka, S. Lin, R. D. Pisarski and D. Satow, JHEP **10**, 005 (2015) [arXiv:1504.01770 [hep-ph]]. 26
- [83] J. Liao, E. Shuryak, Phys. Rev. Lett. **101**, 162302 (2008) [arXiv:0804.0255 [hep-ph]]. 26
- [84] J. Liao, E. Shuryak, Phys. Rev. **C75**, 054907 (2007) [hep-ph/0611131]. 26
- [85] J.-P. Blaizot, F. Gelis, J. Liao, L. McLerran, R. Venugopalan, Nucl. Phys. A **873**, 68 (2012) [arXiv:1107.5296 [hep-ph]]. 27
- [86] J.-P. Blaizot, F. Gelis, J. Liao, L. McLerran, R. Venugopalan, Nucl. Phys. A **904-905**, 829 (2013) [arXiv:1210.6838 [hep-ph]]. 27
- [87] J. I. Kapusta, P. Lichard and D. Seibert, Phys. Rev. D **44**, 2774 (1991); [Erratum-ibid. D **47**, 4171 (1993)]. 28, 33
- [88] D. K. Srivastava, Pramana **57**, 235 (2001). 28, 33
- [89] L. McLerran and M. Praszalowicz, Acta Phys. Polon. B **41**, 1917 (2010) [arXiv:1006.4293 [hep-ph]]. 29
- [90] D. Kharzeev, E. Levin and M. Nardi, Nucl. Phys. A **747**, 609 (2005) [arXiv:hep-ph/0408050]. 31
- [91] D. Kharzeev and M. Nardi, Phys. Lett. B **507**, 121 (2001) [arXiv:nucl-th/0012025]. 31
- [92] P. Aurenche, F. Gelis, R. Kobes, and H. Zaraket, Phys. Rev. D **58**, 085003 (1998) [arXiv:hep-ph/9804224]. 34

[93] P. Aurenche, F. Gelis, and H. Zaraket, Phys. Rev. D **61**, 116001 (2000) [arXiv:hep-ph/9911367].

34

[94] P. Aurenche, F. Gelis, and H. Zaraket, Phys. Rev. D **62**, 096012 (2000) [arXiv:hep-ph/0003326].

34

[95] A. Krasnitz and R. Venugopalan, Phys. Rev. Lett. **86**, 1717 (2001); Nucl. Phys. A **727**, 427 (2003). 35

[96] T. Lappi, Phys. Rev. C **67**, 054903 (2003); Eur. Phys. J. C **55**, 285 (2008). 35, 36

[97] N. Tanji and R. Venugopalan, Phys. Rev. C **95**, 094009 (2017) [arXiv:1703.01372 [hep-ph]]. 35

[98] E. Lifshitz and L. Pitaevskii, *Physical Kinetics (Landau and Lifshitz Course of Theoretical Physics, vol 10)*, Pergamon, Oxford, (1981). 35

[99] P. Arnold, G. D. Moore, L. G. Yaffe, JHEP **11**, 001 (2000); JHEP **12**, 009 (2001); JHEP **05**, 051 (2003). 39

[100] J. Ghiglieri, J. Hong, A. Kurkela, E. Lu, G. D. Moore and D. Teaney, JHEP **1305**, 010 (2013) [arXiv:1302.5970 [hep-ph]]. 39

[101] M. He, R. J. Fries and R. Rapp, Phys. Rev. C **85**, 044911 (2012) [arXiv:1112.5894 [nucl-th]]. 43

[102] P. F. Kolb and U. W. Heinz, In *R. C. Hwa (ed.) et al.: Quark gluon plasma*, 634 [arXiv:nucl-th/0305084]. 43

[103] S. Ryu, J. F. Paquet, C. Shen, G. S. Denicol, B. Schenke, S. Jeon, and C. Gale, Phys. Rev. Lett. **115**, 132301 (2015). 44

[104] B. Schenke, P. Tribedy, and R. Venugopalan, Phys. Rev. Lett. **108**, 252301 (2012). 44

[105] K. Adcox *et al.* (PHENIX Collaboration), Nuclear Inst. and Methods in Physics Research A **499**, 469 (2003). 48

[106] Y. Akiba *et al.*, Nucl. Phys. A **638**, 565 (1998). 48

[107] PHENIX Conceptual Design Report, BNL 1993 (unpublished). 48

[108] K. Adcox *et al.* (PHENIX Collaboration), Nucl. Phys. A **757**, 184 (2005) [arXiv:nucl-ex/0410003]. 48

- [109] M. Harrison, S. Peggs and T. Roser, Annual Review of Nuclear and Particle Science **52**, 425 (2002). 50
- [110] M. Harrison, T. Ludlam and S. Ozaki, Nuclear Instruments and Methods in Physics Research A **499**, 235 (2003). 50
- [111] E. D Courant, Annual Review of Nuclear and Particle Science **53**, 1 (2003). 50
- [112] M. Blaskiewicz, J. M. Brennan and K. Mernick, Phys. Rev. Lett. **105**, 094801 (2010). 50
- [113] B. B. Blinov, Phys. Rev. Lett. **88**, 014801 (2002). 50
- [114] R. Tomas *et al.*, Physical Review Special Topics: Accelerators and Beams **8**, 024001 (2005). 50
- [115] R. Petti, “Low Momentum Direct Photons as a Probe of Heavy Ion Collisions”, PhD Thesis, Stony Brook University (2013). xiii, xvi, 51, 71, 85, 91, 92
- [116] M. Allen *et al.*, Nuclear Inst. and Methods in Physics Research A **499**, 549 (2003). 52
- [117] C. Adler *et al.*, Nuclear Inst. and Methods in Physics Research A **470**, 488 (2001). 53
- [118] E. Richardson *et al.* (PHENIX Collaboration), Nuclear Inst. and Methods in Physics Research A **636**, 99 (2001) [arXiv:1012.0873 [nucl-ex]]. 55
- [119] S. H. Aronson *et al.* (PHENIX Collaboration), Nuclear Inst. and Methods in Physics Research A **499**, 480 (2003). 57
- [120] K. Adcox *et al.* (PHENIX Collaboration), Nuclear Inst. and Methods in Physics Research A **499**, 489 (2003). 59, 61
- [121] A. Oskarsson *et al.*, Nuclear Inst. and Methods in Physics Research A **497**, 263 (2003). 61
- [122] M. Aizawa *et al.*, Nuclear Inst. and Methods in Physics Research A **499**, 508 (2003). 62
- [123] Y. Akiba *et al.*, Nuclear Inst. and Methods in Physics Research A **433**, 143 (1999). 62
- [124] W. Anderson *et al.*, Nuclear Inst. and Methods in Physics Research A **646**, 35 (2011) [arXiv:1103.4277 [physics.ins-det]]. 65
- [125] L. Aphecetche *et al.*, Nuclear Inst. and Methods in Physics Research A **499**, 521 (2003). 65
- [126] G. David *et al.*, IEEE Trans. Nucl. Sci. **43**, 1491 (1996). 66
- [127] J. Badier *et al.*, Nuclear Inst. and Methods in Physics Research A **348**, 74 (1994). 66

- [128] E. Tarkovsky, Nuclear Inst. and Methods in Physics Research A **379**, 515 (1996). 66
- [129] G. David, E. Kistenev, S. Stoll, S. N. White and C. Woody, IEEE Trans. Nucl. Sci. **42**, 306 (1995). 66
- [130] G. David *et al.*, IEEE Trans. Nucl. Sci. **45**, 705 (1998). 67
- [131] T. Awes, submitted to Nuclear Inst. and Methods in Physics Research A, (2002) [arXiv:nucl-ex/0202009]. 67
- [132] G. David *et al.*, IEEE Trans. Nucl. Sci. **45**, 692 (1998). 67
- [133] N. Novitzky, “Study of the neutral pion and direct photon production in Au+Au collisions at $\sqrt{s_{NN}} = 39\text{-}200 \text{ GeV}$ ”, PhD Thesis, Jyvaskyla University (2013). xv, 67, 70, 85, 86, 87, 88
- [134] R. Bannier, “Systematic studies of soft direct photon production in Au+Au collisions at $\sqrt{s_{NN}} = 200 \text{ GeV}$ ”, PhD Thesis, Stony Brook University (2014). xvii, xxviii, 71, 92, 95, 99, 107, 108, 114, 117
- [135] E. Atomssa, J. Sun, B. Bannier, V. Khachatryan, A. Drees, and T. Hemmick, “Dielectron analysis for Run 10 Au+Au 200 GeV data using HBD”, PHENIX analysis note AN1050. 73
- [136] J. T. Mitchell *et al.* (PHENIX Collaboration), Nuclear Inst. and Methods in Physics Research A **482**, 498 (2002). 85
- [137] A. Bazilevsky, V. Kochetkov, V. Semenov, S. White, and E. Kistenev, Instrum. Exp.Tech. **42**, 167 (1999). 86
- [138] T. Awes *et al.*, Nuclear Inst. and Methods in Physics Research A **311**, 130 (1992). 87
- [139] V. Khachatryan, N. Novitzky, A. Drees, T. Hemmick, G. David, “Analysis Note on Low Momentum Direct Photons in Au+Au Collisions at $\sqrt{s_{NN}} = 62.4 \text{ GeV}$ and $\sqrt{s_{NN}} = 39 \text{ GeV}$ Center-of-mass Energies”, PHENIX analysis note AN1283. 101, 114, 115
- [140] A. Dress, “Reference Spectra for π and η Mesons in $\sqrt{s_{NN}} = 62.4 \text{ GeV}$ Au+Au Collisions”, PHENIX analysis note AN1217. xvii, xxviii, 104, 113, 114
- [141] A. Adare *et al.* (PHENIX Collaboration), Phys. Rev. Lett. **109**, 152301 (2012) [arXiv:1204.1526 [nucl-ex]]. xvii, 113, 115
- [142] B. I. Abelev *et al.* (STAR Collaboration), Phys. Lett. B **655**, 104 (2007) [arXiv:nucl-ex/0703040]. xvii, 113

- [143] A. Dress, “Reference Spectra for π and η Mesons in $\sqrt{s_{NN}} = 39$ GeV Au+Au Collisions”, Stony Brook University (2016). xvii, xxviii, 104, 115, 116
- [144] J. F. Paquet, Private communication, (2017). xx, xxi, 128, 141, 146, 150
- [145] A. Adare *et al.* (PHENIX Collaboration), Phys. Rev. C **93**, 024901 (2016) [arXiv:1509.06727 [nucl-ex]]. xxviii, xxix, 129, 140, 141, 195, 196, 215
- [146] S. S. Adler *et al.* (PHENIX Collaboration), Phys. Rev. C **89**, 044905 (2014) [arXiv:1312.6676 [nucl-ex]]. xxix, 132, 195, 215
- [147] B. Abelev *et al.* (ALICE Collaboration), Phys. Rev. C **88**, 044909 (2013) [arXiv:1301.4361 [nucl-ex]]. xxix, 132, 196, 215
- [148] J. T. Mitchell, S. Bazilevsky, B. Fadem, P. Garg, and M. Tannenbaum, “Compilation of Charged Particle Multiplicity and Transverse Energy Production Results”, PHENIX analysis note AN1227. xxix, 132, 195, 196, 215
- [149] K. Aamodt *et al.* (ALICE Collaboration), Phys. Rev. Lett. **106**, 032301 (2011) [arXiv:1012.1657 [nucl-ex]]. xxix, 140, 196
- [150] J. Adam *et al.* (ALICE Collaboration), Phys. Rev. Lett. **116**, 222302 (2016) [arXiv:1512.06104 [nucl-ex]]. 140
- [151] S. Afanasiev *et al.* (PHENIX Collaboration), Phys. Rev. Lett. **109**, 152302 (2012) [arXiv:1205.5759 [nucl-ex]]. xxi, xxx, xxxi, 140, 150, 206, 207, 208, 209, 210, 214, 215
- [152] J. Adam *et al.* (ALICE Collaboration), Eur. Phys. J. C **77**, 33 (2017) [arXiv:1509.07541 [nucl-ex]]. 141
- [153] A. Adare *et al.* (PHENIX Collaboration), Phys. Rev. C **87**, 054907 (2013) [arXiv:1208.1234 [nucl-ex]]. xix, xx, xxi, xxx, 142, 146, 150, 205, 212, 213, 214, 215
- [154] A. L. S. Angelis *et al.* (CCOR Collaboration), Phys. Lett. B **94**, 106 (1980). xix, xxi, xxxi, 142, 150, 211, 214, 215
- [155] A. S. Angelis *et al.* (CMOR Collaboration), Nucl. Phys. B **327**, 541 (1989). xix, xxi, xxxi, 142, 150, 211, 214
- [156] T. Akesson *et al.* (AFS Collaboration), Sov. J. Nucl. Phys. **51**, 836 (1990). xix, xxxi, 142, 211
- [157] W. Vogelsang and M. R. Whalley, J. Phys. G.: Nucl. Part. Phys. **23**, A1 (1997). xix, xxi, xxxi, 142, 150, 211, 214, 215